CHARLES UNIVERSITY

Faculty of Science

Study Program: Biochemistry

Mgr. Barbora Kalousková

HARNESSING SOLUBLE FORMS OF NK CELL RECEPTORS AND THEIR LIGANDS FOR CANCER IMMUNOTHERAPY

Doctoral Thesis

Supervisor: RNDr. Ondřej Vaněk, Ph.D.

Prague 2021

PROHLÁŠENÍ

Prohlašuji, že jsem tuto závěrečnou práci zpracovala samostatně a že jsem uvedla všechny použité informační zdroje a literaturu. Tato práce ani její podstatná část nebyla předložena k získání jiného nebo stejného akademického titulu.

V Praze dne …………………   …………………………..

                                        Mgr. Barbora Kalousková

DECLARATION

I declare that I have worked on this thesis individually and that all sources of the previous knowledge are properly cited. No part of this work was used or will not be used for obtaining any other or the same academic degree.

Prague ………………… ………………………..

Mgr. Barbora Kalousková

DECLARATION OF AUTHORSHIP

I declare that Mgr. Barbora Kaloušková contributed significantly (30-90 %) to the experiments in all four scientific publications contained in this Ph.D. thesis. She performed most of the experiments, substantially contributed to their planning, and took a significant part in the primary data interpretation and preparation for the publication.

Prague ………………… ..…………………………..

RNDr. Ondřej Vaněk, Ph.D.

ACKNOWLEDGMENTS

I would like to thank my supervisor Ondřej Vaněk for his patience and help not only with finalizing my first author paper and this thesis but also for the mentoring and guidance through my studies and for supporting me in my scientific career.

I cannot forget to thank Jan Bláha for always being there with sound advice, Ondřej Skořepa and Celeste Abreu for being great colleagues, Mrs. Ammerová for being great technical support and other members of our lab for creating an inspiring working environment.

Special thanks to our collaborating partners, namely Valerie Grobárová, Jozef Janda, Marie Olšinová, Jan Dohnálek, Tereza Skálová, Michal Pechar, Robert Pola, Irena Sieglová, who kindly shared their expertise, provided material for our studies, or helped with the data analysis.

And also to my family and closest friends for the endless support.

ABSTRAKT

Přirozeně zabíječské buňky, také NK buňky (z angl. natural killer cells, NK cells) jsou skupinou lymfocytů s přirozenou schopností zabíjet infikované, poškozené nebo maligně transformované buňky. Jelikož jsou tyto lymfocyty součástí přirozené imunity, jsou cytotoxické mechanismy aktivovány po rozpoznání specifických buněčných znaků, avšak bez předchozího kontaktu s antigenem. Toto rozpoznání je důležité pro NK buněčnou funkci při udržování homeostázy a imunitního dohledu. NK buňky cílí přímo na maligně transformované buňky, účastní se však také komplexní imunitní odpovědi, a to produkcí cytokinů nebo komunikací s ostatními imunitními buňkami.

Na rakovinu můžeme nahlížet jako na prolomení imunitních bariér, kdy maligní buňky uniknou imunitě a zaplaví okolní tkáň, přičemž si kolem sebe vytváří mikroprostředí podporující růst nádoru. Tento proces může být zvrácen imunoterapií, tedy zásahem do formování imunitní odpovědi, což může vest k obnovení imunitního rozpoznávání. NK buňky jsou v imunoterapii důležitými efektorovými buňkami, mohou být použity pro adoptivní transfer, geneticky modifikovány pomocí chimerních antigenních receptorů nebo aktivovány příslušnými protilátkami. NK buněčné receptory, zodpovědné za rozpoznání cílových buněk a aktivaci cytotoxických mechanismů, jsou také jedním z cílů imunoterapie. Není však možné navrhovat imunoaktivní terapeutika cílící NK buněčné receptory bez přesné znalosti způsobu interakce receptorů a jejich ligandů.

Tato práce popisuje expresi rozpustných forem NK buněčných receptorů a jejich ligandů pro strukturní studie, s cílem poskytnout detailní biofyzikální charakterizaci NK buněčných imunokomplexů. Dále popisuje klastrování receptoru NKR-P1 přímo na buněčném povrchu, a to pomocí superrozlišovací mikroskopie. Vliv reorganizace receptoru na buněčnou signalizaci byl ověřen v cytotoxickém pokusu. Na závěr byl připraven aktivační ligand NK buněk B7-H6 s coiled coil motivem pro uchycení na polymerní nosič společně s fragmentem protilátky cílícím nádorové buňky. Biologická aktivita připraveného ligandu byla ověřena *in vitro*, může tak být součástí chimerních protein-polymerních částic pro cílenou aktivaci NK buněk.

ABSTRACT

Natural killer cells (NK cells) are a family of lymphocytes with a natural ability to kill infected, harmed, or malignantly transformed cells. As these cells are part of the innate immunity, the cytotoxic mechanisms are activated upon recognizing specific patterns without prior antigen sensitization. This recognition is crucial for NK cell function in the maintenance of homeostasis and immunosurveillance. NK cells not only act directly towards malignant cells but also participate in the complex immune response by producing cytokines or crosstalk with other immune cells.

Cancer may be seen as a break of all immune defenses when malignant cells escape the immunity and invade surrounding tissues creating a microenvironment supporting tumor progression. This process may be reverted by interventions into immune response shaping with immunotherapy, which may lead to restoration of immune recognition. NK cells are also effector cells important for immunotherapy, may be used for adoptive transfer, genetically modified with chimeric antigen receptors, or triggered with appropriate antibodies. NK cell receptors, responsible for target recognition and activation of cytotoxic machinery, may also be targeted in immunotherapy. However, this kind of immunoactive therapeutics may be designed only with the deep knowledge of NK cell receptor:ligand interaction.

This work describes the expression of soluble forms on NK cell receptors and their ligands and structural studies, providing detailed biophysical characteristics of NK cell immunocomplexes. Moreover, clustering of NKR-P1 receptor was described directly on the cell surface with superresolution microscopy, and the effect of receptor reorganization on signalization was verified by cytotoxic assay. Finally, NK cell-activating ligand B7-H6 was expressed with the coiled coil sequence enabling its attachment on the polymeric carrier, together with tumor-targeting scFv. The biological activity of this ligand was verified *in vitro*, which suggests the utilization of these chimeric protein-polymer particles for targeted NK cell activation.

LIST OF ABBREVIATIONS

ACT	adoptive cell transfer
ADCC	antibody-dependent cell-mediated cytotoxicity
aFGF	acidic fibroblast growth factor
AICL	activation-induced C-type lectin
APC	antigen-presenting cell
AUC	analytical ultracentrifugation
BiKE	bispecific killer engager
CAR	chimeric antigen receptor
CAR-NK	NK cells expressing chimeric antigen receptor
CD	cluster of differentiation
CTLA-4	cytotoxic T lymphocyte-associated protein
CTLD	C-type lectin-like domains
CTLR	C-type lectin-like receptor
DLS	dynamic light scattering
DSF	differential scanning fluorimetry
dSTORM	direct stochastical optical reconstruction microscopy
DLS	dynamic light scattering
EGFR	epidermal growth factor receptor
ELP	early lymphoid progenitor
EpCAM	epithelial cell adhesion molecule
FACS	flow cytometry (fluorescence-activated cell sorting)
Fc	fragment crystallizable
FPLC	fast protein liquid chromatography
GnTI$^-$	cells deficient in N-acetylglucosaminyltransferase I
GSD	ground state depletion
HEK293	human embryonic kidney cell line 293
HER2	human epidermal growth factor receptor
HLA-C	human leucocyte antigen (group of MHC I)
HPLC	high-performance liquid chromatography
ICAM-1	intercellular adhesion molecule 1
IDO	indoleamine-2,3-dioxygenase

IL	interleukin
INFγ	interferon gamma
ILC	innate lymphoid cell
IS	immune synapse
ITAM	immunoreceptor tyrosine-based activation motif
ITC	isothermal titration calorimetry
ITIM	immunoreceptor tyrosine-based inhibitory motif
K_D	dissociation constant
KIR	killer cell immunoglobulin-like receptor
LFA-1	leukocyte function-associated molecule 1
LLT1	lectin-like transcript 1
LRC	leukocyte receptor complex
HSC	hematopoietic stem cell
mAb	monoclonal antibody
MALS	multiangle light scattering
MHC I (II)	major histocompatibility complex glycoproteins class I (II)
MS	mass spectrometry
MST	microscale thermophoresis
Nb	nanobody
NCR	natural cytotoxicity receptor
NK	natural killer
NKC	natural killer complex
NKCE	natural killer cell engager
NKP	natural killer cell precursor
NKT	natural killer T cell
NKG2	natural-killer group 2
NKp30	natural killer cell protein 30 kDa
NKp44	natural killer cell protein 44 kDa
NKp46	natural killer cell protein 46 kDa
NKp65	natural killer cell protein 65 kDa
NKp80	natural killer cell protein 80 kDa
NKR-P1	natural killer receptor protein 1

p27	inhibitor of cyclin-dependent kinase
PB	piggyBac, transposon-based expression system
PBMC	peripheral blood mononuclear cells
PD-1	programmed death protein 1
PD-L1	programmed death-ligand 1
PDB	protein data bank
PGE2	prostaglandin E2
qSMM	quantitative single-molecule microscopy
RAG	recombination-activating gene
rtTA	reverse tetracycline transactivator
SAXS	small-angle X-ray scattering
scFv	single-chain fragment variable
SLB	supported lipid bilayer
SMAC	supramolecular activation cluster
SMIC	supramolecular inhibitory cluster
SMLM	single-molecule localization microscopy
STED	stimulated emission depletion microscopy
SPR	surface plasmon resonance
Tc	cytotoxic T cell
TCR	T cell receptor
Th17	T helper cell
TetraKE	tetraspecific killer engager
TGF-β	transforming growth factor-beta
TIR	total internal reflection
TLR	Toll-like receptor
TNF-β	tumor necrosis factor-beta
TME	tumor microenvironment
TRE	tetracycline response element
TriKE	trispecific killer engager
VHH	heavy-chain variable

LIST OF CONTENT

1 INTRODUCTION

1.1 NATURAL KILLER CELL BIOLOGY

Balancing between innate and adaptive immunity, natural killer cells (NK cells) are an armed force of our body. In the 1970s, several research groups reported spontaneous cytotoxicity of a distinct lymphocyte subset towards tumor cells [1–5]. These cells were neither B nor T lymphocytes and showed the ability to kill tumor cells without prior antigen sensitization, which was termed "natural" cellular cytotoxicity. The responsible effector cells were defined as natural killer cells [6]. NK cells were further studied and later described as separate lymphocyte lineage.

NK cell development can be divided into several stages, resulting in tissue-resident or NK cells circulating in peripheral blood (Figure 1, p. 14). NK cell precursors (NKPs) differentiate from hematopoietic stem cells (HSCs) or early lymphoid progenitor (ELPs) in the bone marrow and thymus. Their further development is not limited only to these sites but also to other tissues (also lymph nodes, spleen, and liver) [7]. NKPs develop into immature NK cells and later mature, educated, and competent NK cells, which means that NK cells acquired effector functions and also self-tolerance. Mature NK cells could remain in a resting state; activation of lytic competence is primed by the exposure to interferon gamma (INFγ), interleukin 2, or 15 (IL-2, or IL-15) [8].

Individual development stages are characterized by the expression of surface molecules [9,10]. Mature NK cell is characterized by the expression of CD56, CD94 and CD161 (more precisely $CD34^{-}/CD117^{+/-}/CD94^{+}/HLA\text{-}DR^{-}/CD10^{-}/CD122^{+}/CD94^{+}/NKp44^{low}/NKG2D^{+}/CD161^{+}$). Based on the expression of CD56, we can distinguish two main NK cell subsets: $CD56^{dim}$ ($CD56^{dim}/CD16^{pos}$, 90% of circulating NK cells) cells with cytotoxic activity and $CD56^{bright}$ ($CD56^{bright}/CD16^{neg}$) cells producing high amounts of cytokines and having regulatory function [11].

NK cells are close relatives of innate lymphoid cells (ILCs), sometimes listed as an independent group within ILCs [12]. ILCs are lymphocytes without surface molecules specific to other immune cell types. The primary role of ILCs is regulation of the immune response by secretion of cytokines; they are non-cytotoxic. In contrast, NK cells are primarily cytotoxic cells but have a secretory function ($CD56^{bright}$). NK cells and ILCs share common ancestors during cell development.
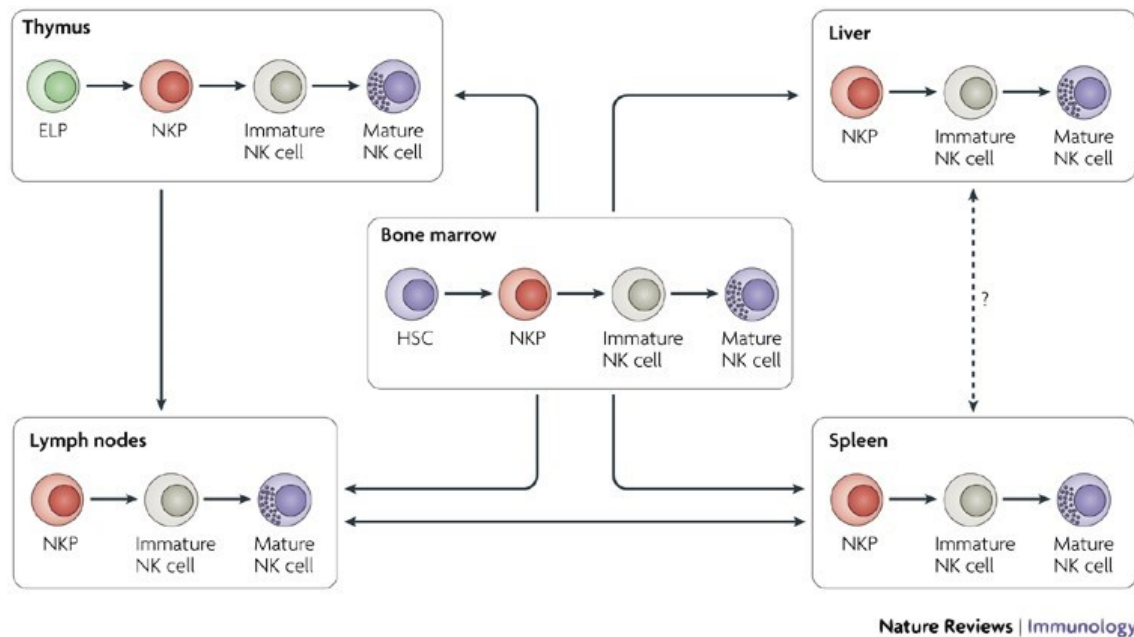
Figure 1: NK cell development. Bone marrow, thymus, lymph nodes, spleen, and liver are the primary sites for NK cell development. Several maturation stages could be distinguished – NK cell precursor (NKPs), immature NK cell, and mature NK cell. NKPs differentiate from hematopoietic stem cells (HSCs) or early lymphoid precursors (ELPs) [7].

1.1.1 FUNCTIONS OF NK CELLS

NK cells play several essential roles in our immunity. The most evident (hence their name) is the cytotoxicity towards stressed or transformed cells [13]. This cytotoxicity is independent of previous specific immunization (MHC-independent). On the other hand, NK cells must learn how to distinguish harmed cells from the healthy ones and ensure self-tolerance [14]. The killing is performed by inducing apoptosis in the target cell (by releasing cytotoxic granules containing perforin and granzyme, or by engaging death receptors by their ligands on NK cell surface) [15].

NK cells are part of a complex immune response; they communicate with other immune cells directly (e.g., killing immature dendritic cells or hyperactive macrophages) or by secretion of cytokines. Thus, they have the regulatory function, too [13,14]. NK cells produce both pro-inflammatory and immunosuppressive cytokines, such as IFNγ, tumor necrosis factor–α (TNF-α), IL-2 or IL-10, and various chemokines [16]. The overview of NK cell functions is represented in Figure 2, p. 15.

Recent studies revealed that NK cells also have an immunological memory [17,18]. Despite lacking the mechanism of RAG recombinase–dependent clonal antigen receptors,

being traditionally considered responsible for immunological memory (the case of B and T cells), NK cells are capable of fast and enhanced immune response upon rechallenge [19]. There are two types of NK cell immunological memory. The first is based on the interaction with antigens, resulting in a kind of antigen-specific memory; the second is non-antigen-specific, as NK cells can recognize known inflammatory cytokine milieus.
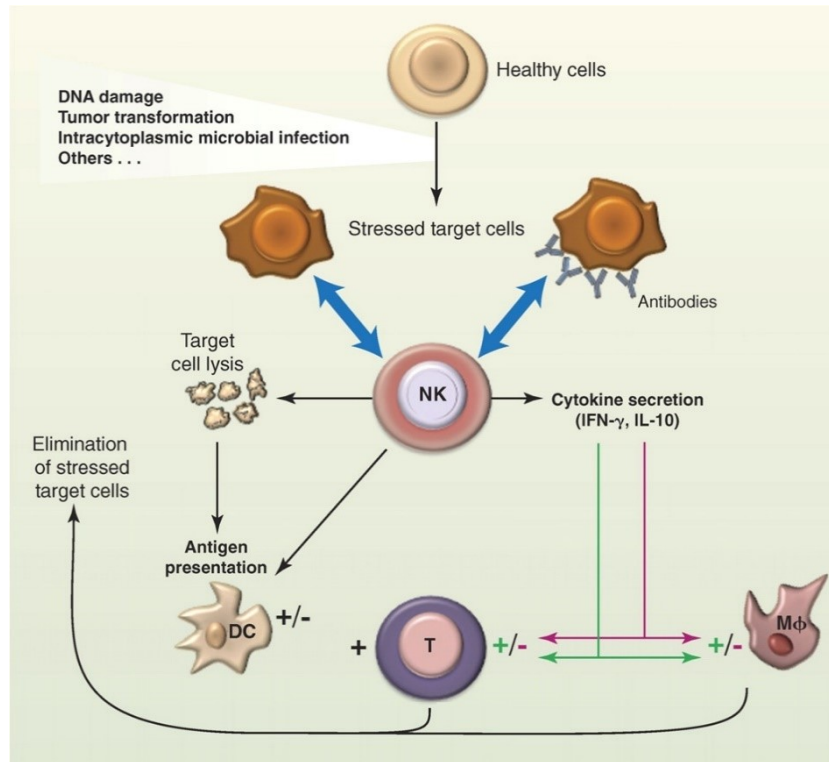

Figure 2: Representation of NK cell functions. NK cells have effector functions (lysis of harmed cells, blue arrows, but also tolerance of healthy cells) and regulatory function (secretion of cytokines, cross-talk with other immune cells) [13].

1.2 HUMAN NK CELL RECOGNITION

How do the NK cells recognize healthy cells from diseased ones? NK cells surfaces are decorated by the number of receptors both activating and inhibiting the cytotoxicity and having other physiological functions (receptors for cytokines or molecules of cellular adhesion) [13]. Activating and inhibitory receptors engage a broad range of health and cellular disease markers, resulting in two modes of recognition, termed as "missing-self" and "induced-self" [20]. This concept is represented in Figure 3, p. 16.

Major histocompatibility complex class I (MHC I) molecules are expressed on normal cells under physiological conditions and are considered as markers of good health and

determine the "self" phenotype; these molecules are ligands for inhibitory NK cell receptors [21]. The "missing-self" recognition results in the killing of the cells where inhibitory markers are missing [22,23]. On the other hand, "induced-self" recognition is based on the interaction with NK cell cytotoxicity activating ligands, typically expressed only under stress conditions [24]. NK cells learn to recognize self-MHC I molecules in the licensing process. Only licensed cells get inhibited by MHC I and become competent NK cells [25].
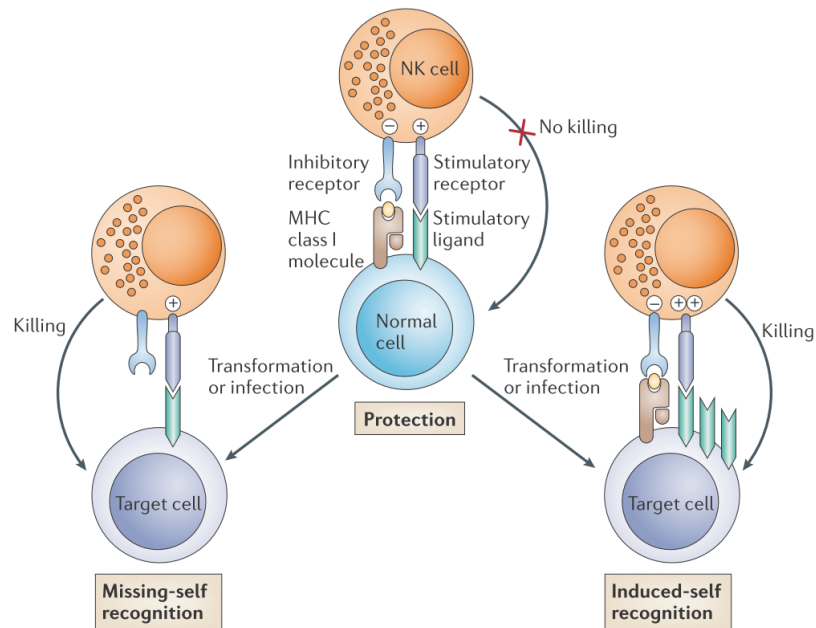
Figure 3: Examples of "missing-self" and "induced-self" NK cell recognition. Normal healthy cells (middle) present a balanced mixture of activating and inhibitory receptors on their surface, which results in self-tolerance. This equilibrium could be disrupted by the absence of inhibitory signals ("missing-self", left) or the presence of activating signals ("induced-self", right), both resulting in NK cell activation and cellular killing [26].

NK cell activation can also be mediated by antibodies (antibody-dependent cellular cytotoxicity, ADCC), as most circulating NK cells possess the CD16 receptor recognizing the Fc (fragment crystallizable) portion of an antibody [27]. NK cells eliminate cells opsonized with antibodies, demonstrating the complex cooperation of individual cell types within the immune system.

1.2.1 NK Cell Receptor Structural Families

NK cell receptors may be qualified into two groups based on the structure of the extracellular domain. These are C-type lectin-like receptors (CTLRs) and immunoglobulin-like receptors. Both groups consist of inhibitory as well as activating receptors [28]. The genes encoding receptor sequences are organized in two main clusters; in natural killer complex (CTLRs, chromosome 12p13.1) and leucocyte receptor complex (immunoglobulin molecules, chromosome 19q13.4).

CTLRs contain ligand binding C-type lectin-like domain (CTLD), whose structure is characterized by a double-loop, stabilized by highly conserved disulfide bonds (C1-C4 a C2-C3, with extra bond C0-C0' within the long receptor variant) [29]. C-type lectins primarily bind carbohydrate ligands in the presence of Ca^{2+} ions, but NK cell CTLRs also interact with protein ligands, independently from Ca^{2+} binding. The members of this structural group may be found in the NKG2 family (natural killer group 2; e.g., NKG2A, NKG2D, CD94) or in the NKR-P1 family (natural killer receptor protein 1; NKRP1, NKp80, NKp65) [30].

Receptors from the second structural group belong to the immunoglobulin (super)family and contain one or more immunoglobulin-like (Ig-like) domains. The immunoglobulin fold consists of 4 β-sheets in antiparallel orientation stabilized by the disulfide bond and connected via loops and other β-sheets [31]. NK cell receptors with the immunoglobulin-like structure are members of the KIRs family (killer cell immunoglobulin-like receptors) [32] and the NCRs family (natural cytotoxicity receptors) [33].

Most of the results and selected publications presented in this thesis focus on receptors NKp30 (natural killer protein 30) and NKR-P1 (natural killer receptor protein 1). For this reason, these receptors will be closely presented also in the introduction part.

1.2.2 Receptor NKp30

Receptor NKp30 (alternative names are CD337 or natural cytotoxicity receptor 3, NCR3) was first described in 1999 [34]. Together with NKp44 and NKp46, it belongs to the NCRs family of immunoglobulin-like receptors [35]. Structurally, NKp30 is part of the CD28 family of surface molecules (together with programmed cell death receptor 1, PD-1, or cytotoxic T lymphocyte antigen 4, CTLA-4) [36]. It is a type I transmembrane

protein with N-terminal immunoglobulin domain, stalk region, transmembrane helix, and C-terminal cytoplasmic domain. After ligand binding, charged arginine in position 143 is translocated deeply into the plasma membrane and mediates interaction with the CD3ζ chain enabling signals transduction [37].

Several cellular ligands expressed on the surface of tumor cells have been identified so far – B7-H6 [38], BAG-6 [39], and galectin-3 [40]. Membrane-bound BAG-6 and B7-H6 activate NK cell cytotoxicity, but their soluble forms as well as galectin-3 block it. Other ligands are viral or parasite antigens, pointing out the role of NK cells in infectious diseases [41].

The binding of NKp30 correlates with its glycosylation and oligomeric status [42,43]. In our recent publication (Publication no. 3, p. 85), we confirmed the importance of N-glycosylation for oligomer formation, as deglycosylation of NKp30 leads to their complete dissociation [44]. Moreover, the crystal structure of the NKp30:B7-H6 complex (PDB 6YJP) reveals the importance of one glycosylation site, at asparagine 42, in NKp30 dimerization. These data were measured using soluble forms of NKp30 in solution but reveal the question about the biological relevance of the NKp30 oligomerization on the cell surface, as the avidity effect may increase signal strength.

1.2.3   RECEPTOR NKR-P1

The expression of NKR-P1 (alternatively CD161, gene *klrb1*) is not limited only to the surface of NK cells but also to some populations of T cells [45,46]. This receptor was initially found also on both CD4$^+$ and CD8$^+$ TCRαβ$^+$ T cells [45], later on γδ T cells [47], natural killer T cells (NKT) [48], Th17 cells [49], and on Mucosal Associated Invariant T cells (MAIT) [50]. NKR-P1 is an inhibitory receptor, the only member with such function within the human NKR-P1 family [51]. Its ligand, lectin-like transcript 1 (LLT1, gene *clec2d*), genetically encoded in the proximity of NKR-P1 within the natural killer complex, is expressed on activated dendritic cells and B cells [52–54]. Suppression of immune response through the interaction of LLT1 with NKR-P1 is the tumor escape strategy of glioblastoma cells [55]. This interaction is also involved in some autoimmune disorders, such as lupus, rheumatoid arthritis, and multiple sclerosis [56–58].

The crystal structure of the NKR-P1:LLT1 complex (PDB 5MGT, Publication no. 4, p. 110) revealed an exciting organization into chain-like structures [59]. These structures enable receptor clustering on the cell surface, which was further studied by direct

stochastical optical reconstruction microscopy (dSTORM) and subsequent analysis of superresolution images. This organization may be a strategy to assure signal transduction despite the low affinity of this receptor:ligand interaction and deserves further investigation.

1.3 NK CELL IMMUNOLOGICAL SYNAPSE

As mentioned previously, activation of NK cells is driven by the overbalance of activating signals. However, tight cellular contact, involving the subsequent reorganization of many molecules, is needed to create functional immune synapse (IS) at the interface of NK and target cell [60]. This process is highly organized, initiated by the approximation and cell recognition, promoted by the engagement of adhesive molecules and accumulation of receptors in supramolecular activation clusters (SMAC), resulting in cell polarization and exocytosis of lytic granules [61]. An adhesive leukocyte function-associated molecule 1 (LFA-1, CD11a) recognizes the intercellular adhesion molecule 1 (ICAM-1, CD54) on target cells and initiates synapse formation as an early signal [62]. Next, reorganization of the cytoskeleton is needed to promote cellular spreading, strengthening the cellular contact [63]. A rearranged filament network also serves for the trafficking of vesicles containing perforin and granzymes towards the IS, as they must be secreted in direct proximity of the target cell membrane. Activating and inhibitory IS is described in Figure 4, p. 20.

Inhibitory KIRs accumulate at the cell membrane and induce HLA-C (human leucocyte antigen, group of MHC I) clustering on the target cell [64,65]. The accumulation is independent of cytoskeleton support, LFA-1 engagement, or signalization by the ITIM (immunoreceptor tyrosine-based inhibitory motif). Moreover, stimulation with KIRs (KIR2DL2 in this study [66] results in the suppression of activating receptor microclusters, the subsequent collapse of the peripheral actin network, and finally, the complete retraction of NK cell from the target cell, which is considered healthy, based on HLA-C identification. Massive KIRs engagement is essential for NK cell-mediated maintenance of self-tolerance. NK cells deficient in KIR expression are not hyperresponsive, but they fail in licensing, which results in their hyperresponsiveness [25]. NK cell function is tightly regulated by inhibitory regulation favoring.
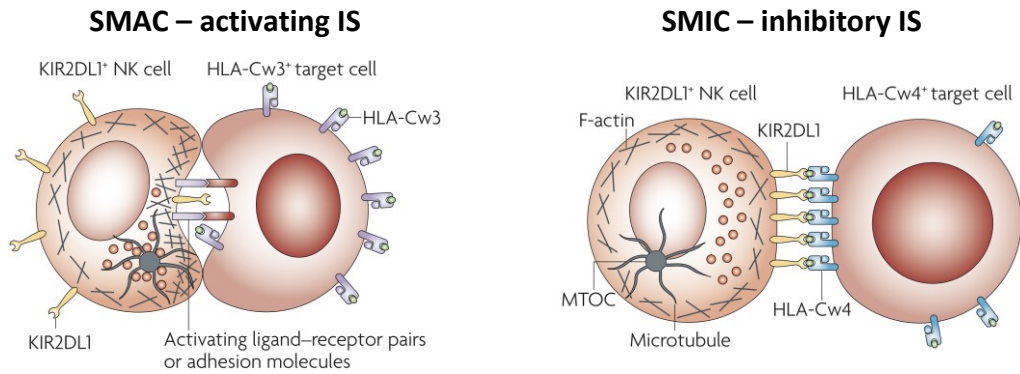
Figure 4: Immunological synapse in NK cells engages formation of the supramolecular activation clusters (SMAC) or is disrupted by supramolecular inhibitory cluster (SMIC) formation. SMAC (left) is required for the successful formation of the lytic synapse; it is driven by activating signals when excluding KIR receptors from the synapse. F-actin polymerizes and accumulates at the contact site, NK cell is polarized. SMIC (left) is characterized by the presence of KIR clusters recognizing MHC I on the target cell. As a result of this interaction, MHC I accumulate within the synapse, strengthening the inhibitory signal, F-actin does not accumulate on the periphery of the NK cell, and the cell does not polarize [67].

To answer the question, which are the minimal requirements for NK cell activation, experiments with primary resting human NK cells and insect cells expressing activating ligands, as model cells substituting target cells, were performed, combining signals for polarization and degranulation [68]. Activating receptors NKG2D, DNAM-1, 2B4, CD2 can induce inside-out signaling needed for LFA-1 mediated adhesion, but only CD16 can induce degranulation on its own [69]. Only collective engagement of activating and co-activating receptors (as well as signaling molecules, cytoskeleton, and other players) results in a successful NK cell lytic strike.

1.3.1   SUPERRESOLUTION MICROSCOPY AS A METHOD FOR REVEALING NK RECEPTOR ORGANIZATION ON THE CELL SURFACE

The IS is widely studied using fluorescent microscopy methods, but only the development of superresolution methods, overcoming limitations imposed by the diffraction limit, led to the research boom in this field [70]. Both technical progress in building microscopes with better resolution, and methodological progress in preparing artificial membrane mimicking cell surface, are essential for further understanding IS behavior. Monoclonal antibodies (mAbs) immobilized on the surface of the coverslips

are traditionally used to assure activating conditions when imaging NK cell IS [71]. In this approach, interacting molecules lack lateral mobility, and the rearrangement of the receptors and ligands is not entirely free, as it would be on the cellular interface. The alternative approach is a preparation of supported lipid bilayers (SLBs) as cell membrane mimicries maintaining fluidity, which can be easily functionalized with any cell-type-specific constituents to create tumor cell, antigen-presenting cell (APC), or any other cell type [72]. SLBs are used with 2D methods enhancing contrast by using total internal reflection (TIR) in combination with single-molecule localization microscopy (SMLM) [73] or stimulated emission depletion (STED) microscopy [74].

T cells, more precisely the nanoscale organization of TCR, are the most detailly studied immune cells by the methods of superresolution microscopy, but these data are both methodologically and biologically relevant also for the research of NK cells. It was found that TCRs reorganize upon engagement and activation by a peptide containing MHC; this finding is based on the different distribution of TCRs on the surface of naïve or activated T cells [75,76]. Although quantitative single-molecule microscopy (qSMM) revealed that antigen recognition is driven by monomeric TCRs [77], which are randomly distributed on the surface of naïve T cells [78], the global clustering occurs only upon activation and is reported for TCRs as well as its associating molecules [79–84].

Receptor clustering on NK cell surface was reported for KIRs and observed with standard confocal microscopy [64,85]. Later, KIRs clustering was also studied by localization microscopy methods in superresolution (particularly ground state depletion, GSD) [86]. This study revealed that activating KIR2DS1 receptors form clusters two-fold larger than inhibitory receptor KIR2DL1. The size of nanoclusters depends on the amino acids in the transmembrane part and influences the signaling. Further experiments focused on inhibitory KIRs found that the inhibitory receptors encoded by different genes also differ in their nanometer arrangement [87]. Moreover, the nanoscale organization is related to the abundance of the receptors (more abundant receptors form smaller clusters and vice versa), and the differences were also found in the downstream signalization. There is also evidence that activation of NK cells leads to changes in the nanoscale organization of inhibitory KIRs, as activation of NK cells via NKG2D results in reorganization of KIR2DL1 [88].

Not only KIRs are studied. Receptor NKp46 (NCR family) is also involved in the formation of IS [89]. It forms microcluster structures within the interaction interface and controls cytoskeletal rearrangement, resulting in polarization and NK cell degranulation.

The methods of SMLM may lead to overcounting of the labeled molecules and thus to incorrect data interpretation [90]. Based on the published data, it is difficult to tell if the nanoclusters are pre-existing on the surface of the cells or if clusters are only observed because of overcounting. Nevertheless, it was shown that the organization of the receptors (TCRs, KIRs) on the cell surface rearranges upon ligand binding. However, the IS formation is still an undiscovered process deserving our attention because functional immune synapses (both activating and inhibitory) are necessary for maintaining good health and homeostasis.

1.4 NK Cells as a Tool of Cancer Immunotherapy

1.4.1 Cancer Immunosurveillance

The hypothesis of "cancer immunosurveillance" was proposed in the 1950s by Sir Macfarlane Burnet and Lewis Thomas [91]. One by one, they presented the theory about the inevitable transformation of somatic cells towards malignant cells, which are recognized as immunogenic and eliminated from the body by immune cells. However, it took roughly another 50 years to prove this hypothesis, and we are trying to understand this process until these days.

As the immune system tries to identify the malignancies in our body, it sometimes fails because of the low immunogenicity of some tumor cells and thus suppresses the immune response permitting tumor growth [92]. The dual role of the immune system, the host-protective, and the tumor-promoting, is termed "cancer immunoediting", which is represented in Figure 5, p. 23. The mutual interaction between the immune system (not only cells, but humoral components are involved as well) and transformed cells may result in tumor elimination (immunosurveillance was successful), tumor escape (anti-tumor immune response failed), or may stay in the equilibrium (cancer cells are tolerated, not entirely eliminated, but further outgrowth is prevented) [93]. The equilibrium stage may be an outcome of immunoediting, when cancer cells are functionally dormant for the rest of their lives, without surrounding tissues' evasion [94]. The equilibrium phase explains a long period of latency for some tumors. On the other hand, tumor cells are under

constant pressure, which may result in the selection of clones with lower immunogenicity and thus tumor escape.
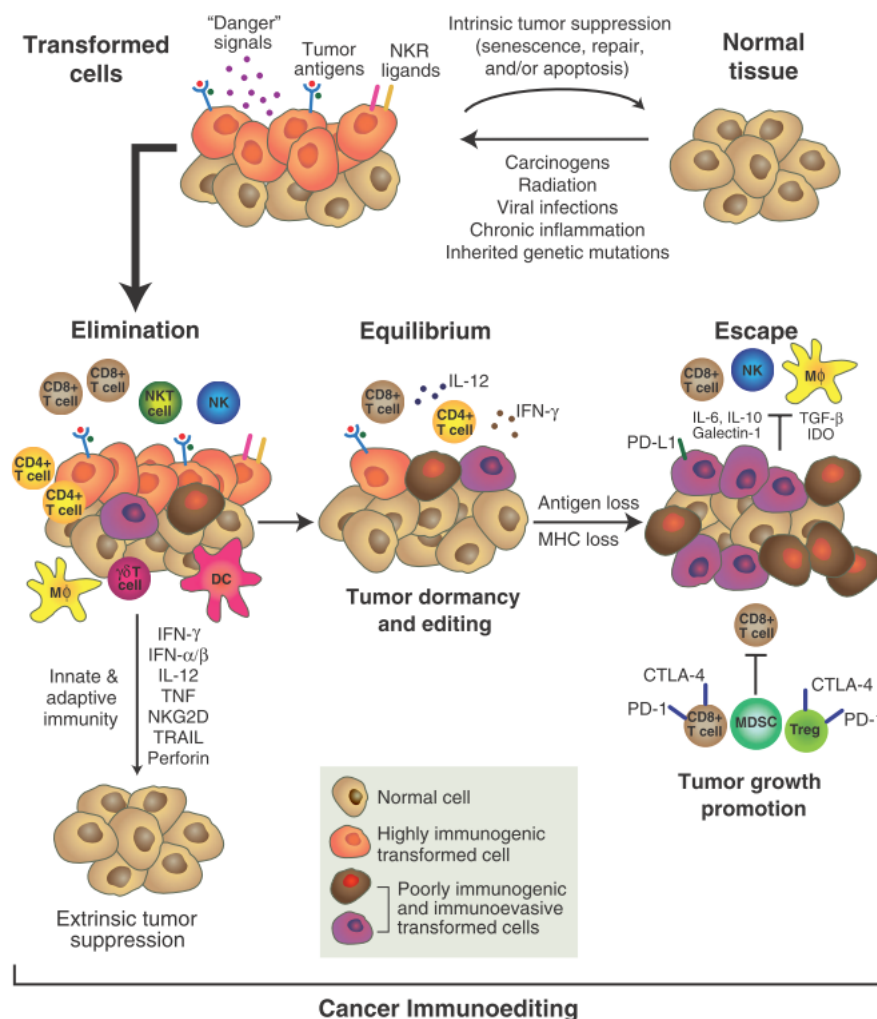

Figure 5: Cancer immunoediting. Based on the immunogenicity of transformed cells, the immune system could successfully eliminate the tumor (highly immunogenic cells), or tumor cells escape the immunosurveillance mechanisms (poorly immunogenic and immunoevasive cells). In a particular case, the immune system may be in equilibrium with cancer cells when cancer is temporarily tolerated and the editing process continues [95].

Tumor cells develop ingenious strategies for escaping immunity. There are three main tumor escape strategies – the loss of antigenicity, the loss of immunogenicity, and the creation of immune-suppressive tumor microenvironment (TME) [96]. Loss of antigenicity is represented by the selection of tumor cells deficient in molecules of immune recognition (downregulation of MHC I [97], alterations in antigen processing

machinery of MHC II [98], suppression of activating ligands [99]). Such cells are getting undetectable by the immune system. The loss of immunogenicity is represented by the upregulation of immune inhibitory molecules (such as PD-L1 [100] or HLA-G antigens [101]), leading in consequence to the silencing of the immune response. TME is a specific niche created by the cancer cells when evading healthy tissue. It is constantly shaped by cancer cell activity, contains molecules that inhibit mechanisms of anti-tumor immunity (immunosuppressive environment), and promotes tumor growth [102].

Cancer immunotherapy is a strategy to recruit endogenous anti-tumor mechanisms to restore the activity of immune cells against malignant cells [103]. Several approaches have been developed so far, including classical boosting of adaptive mechanisms with anti-cancer vaccines [104], adoptive cell transfer (ACT, administration of *ex vivo* re-educated immune cells) [105] and modulation of immune response by delivering artificial activating signals or by blocking inhibitory signals (e.g., by mAbs) [106–108]. Some viruses have an oncolytic function and thus could be modified for use in immunotherapy [109].

1.4.2   NATURAL KILLER CELL ROLE IN ONCOGENESIS

NK cells were described as lymphocytes with direct cytotoxic function towards tumor cells [6]. Although other NK cell functions were further discovered, their ability to eliminate malignant cells without prior antigen sensitization remains crucial in tumor immunosurveillance. Over the years, many studies have shown that NK cells are responsible for tumor rejection in experimental animal models [110]. Triggering of this immunity is driven by "missing-self" recognition mode, as the expression of MHC I is usually altered (mainly suppressed) on the surface of cancer cells [111]. KIRs inhibitory receptors are responsible for the discrimination of modified cells [112]. These receptors dampen cytotoxic responses towards healthy cells, but inhibition is absent in the case of cancer cells. Thus, these cells are attacked by NK cells. Apart from missing inhibition, NK cell cytotoxicity is also triggered directly by NK cell-activating receptors identifying specific cellular ligands expressed on tumor cells [36,113].

NK cells are tumor-infiltrating lymphocytes. Their presence in solid tumors is associated with a better prognosis [114]. However, it may be difficult for NK cells to reach some tumors, as these are surrounded by physical barriers and thus keeping specific physiological milieu, characterized by hypoxia, and affected by secretion of immune-

modulating molecules, such as transforming growth factor beta (TGF-β), IL-4, indoleamine 2,3-dioxygenase (IDO) or prostaglandin E2 (PGE2), suppressing NK cell function [115]. Tumor cells may also modify their MHC I repertoire (upregulation of inhibitory signals) to escape the recognition or express molecules preventing immunological synapse formation. Another possible strategy of tumor escape is the shedding of NK cell activating ligands, such as B7-H6 and MICA [116–118].

1.4.3 NK CELL-BASED IMMUNOTHERAPEUTICS

Although NK cells are tumor-killing effector lymphocytes, some tumor cells succeed in escaping. However, there are ways to restore NK cell activity and therapeutically modulate their natural function. The approaches of NK cell immunotherapy are schematically represented in Figure 6. All strategies are based on patterns of NK cell recognition or implement principles of NK cell activation or inhibition. NK cell-based immunotherapy is not just a concept, but there are already many therapeutics in different stages of clinical trials and also companies focusing mainly on NK cell harnessing, such as Innate Pharma or Affimed [119,120].
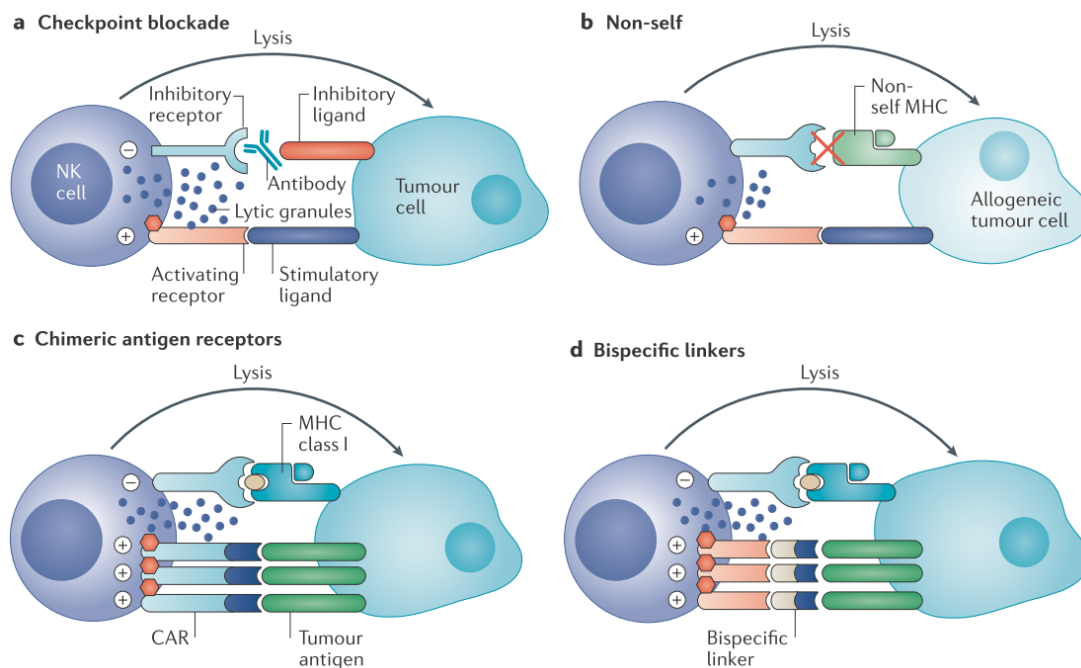

Figure 6: Therapeutical approaches based on NK cell anti-tumor potential. a) Restoring NK cell function by blocking inhibitory signals, **b)** introducing mismatch between donors KIRs and recipient MHC I, **c)** transducing NK cells with engineered CARs, **d)** bridging the cellular interaction with bispecific linkers [121].

One mostly classical therapeutical approach is using NK cells as "living drugs" [112]. These therapies use the adoptive transfer of NK cells, similar to the adoptive transfer of T cells, resulting in the administration of NK cells with enhanced anti-tumor properties. There are two types of transfer, autologous (*in vitro* proliferation and activation of patient's cells) or allogenic (transfer of blood cells from allogeneic donors, haploidentical or MHC-matched) [122]. In autologous transfer, the patient's blood cells are isolated, depleted from T cells, and the enriched NK cell portion is expanded and activated *ex vivo* (using IL-2 alone or combined with IL-12, IL-15, or IL-18, K562 feeder cells are also used to provide co-stimulatory signals). Activated NK cells are then administrated back into the patient's peripheral blood [123–125]. *Ex vivo* manipulations are similar for allogeneic NK cells, but this approach beneficiates from the mismatch between donor KIRs and recipient HLA antigens, promoting immune reaction [126].

Besides re-administration of phenotypically modified NK cells, there is a possibility of treatment with genetically modified NK cells. NK cells can be transfected with chimeric antigen receptors (CARs) similarly to T cells. It is believed that CAR-NK cells could overcome low persistency, low efficacy, and low tumor infiltration of NK cells. Moreover, CAR-NK cells could also be prepared from NK cell lines (e.g., NK92) and thus be used when needed [127]. The CAR constructs consist of extracellular domain recognizing tumor antigen (single-chain fragment variable, scFv antibody fragment), flexible hinge, a transmembrane region, and signaling domain (combination of co-stimulatory sequences and CD3ζ) [128]. CAR-NK-based therapy was reported successful for some types of lymphoid malignancies when CARs targeted CD19 surface antigen [129,130].

To assure self-tolerance, immune response activation is tightly regulated by robust inhibitory mechanisms, so-called immune checkpoint. However, malignant cells may upregulate the expression of checkpoint inhibitory receptor ligands and thus silence the immune response [131]. NK cells share common checkpoint receptors with other lymphocytes (PD-1, CTLA4, TIGIT, NKG2A/CD94, TIM-3, Lag-3, some KIR inhibitory receptors) [132,133]. A common approach to silence these receptors is the administration of mAbs, neutralizing these receptors or their ligands (or both) and preventing their interaction. The advantage is targeting NK cells and cytotoxic T-cells at the same time as well as blocking further inhibitory immune cell cross-talk.

Examples of mAbs targeting immune checkpoint are anti-PD-1 pembrolizumab [134], anti-PD-L1 avelumab [135], anti-NKG2A monalizumab [136], or lirilumab blocking the interaction of KIR2DL1/L2/L3 with its ligands [137]. The use of mAb to block inhibitory signals is not limited only to checkpoint receptors. Antibodies may also be used to neutralize immune-suppressive modulators within TME, such as anti-TGF-β fresolimumab [138].

Of course, NK cells may be triggered not only by blocking the inhibition but also directly by stimulation of activating pathways. Such activating pathway starts with the recruitment of receptor binding Fc region of antibodies (FcγR or CD16) [139]. Thus, NK cells can recognize cells decorated with antibodies. Approved monoclonal antibodies targeting classical tumor antigens HER2 (trastuzumab), EGFR (cetuximab), CD20 (rituximab), and others also provoke ADCC and thus stimulate NK cells [140].

Another approach to target specific NK cell ligands on the surface of cancer cells is the fusion of the Fc-domain with the extracellular part of NK cell receptors. The receptor part assures specificity, and the Fc part activates NK cells (or other $CD16^+$ cytotoxic cells). NKp30-Fc protein inhibited tumor growth in mice, resulting in complete tumor removal in 50 % of cases [141]. Another construct, NKp80-Fc, was successfully used to treat acute myeloid leukemia [142].

Fc fragment is a universal activating ligand for CD16. However, CD16 can also be targeted and activated by specific anti-CD16 antibodies [143]. Moreover, the tools of recombinant expression enable the combination of two or more scFv in one molecule, resulting in bispecific or polyspecific, respectively, synthetic antibodies. Fragment of anti-CD16 antibody is, in fusion with antibody fragment targeting tumor-associated antigens, part of bispecific killer engager (BiKE). Such tumor antigen is the CD33, a marker of myeloid-derived suppressor cells promoting the progress of myelodysplastic syndrome towards acute leukemia [144]. These molecules are bispecific, genetically engineered on the antibody platform. The activity of BiKE was improved by the insertion of a third targeting moiety and the generation of a tri-specific killer engager (TriKE). Such moiety might be another scFv or IL-15, which results in cytokine boosting of NK cell activity at the right time and place [145,146]. Construction of a tetraspecific engager (TetraKE), a fusion protein consisting of anti-CD16 scFv, IL-15, anti-EpCAM scFv, and anti-CD133 scFv, is also possible and induce NK degranulation *in vitro* [147]. To

conclude, synthetic molecules built from fragments of monoclonal antibodies designed to activate NK cell immune functions in cancer are generally termed natural killer cell engagers (NKCEs). This group currently shows promising results in preclinical or even subsequent clinical trials [148].

Combining monoclonal antibody fragments into polyspecific molecules is not the only way to reestablish and boost NK cell immune recognition. Fusion proteins containing soluble NK cell receptor ligands to trigger NK cells or NK cell receptor ectodomain to recognize tumor cells are also an emerging group of promising therapeutics, such in the case of molecules based on NKG2D and NKG2DL [149]. For example, NKG2D in fusion with Fc fragment, anti-CD16 scFv, or anti-CD3 scFv enhance the cytotoxic activity of CD16$^+$ cells or the number of effector T cells, respectively [150]. MICA activating ligand in fusion with CD24 targeting antibody mediates anti-tumor efficacy towards hepatoma carcinoma cells, both *in vitro* and *in vivo* [151]. Engaging NKG2D or NKp30 with proteins ULBP:7D8 or B7-H6:7D8 (where 7D8 is an scFv targeting CD20) also resulted in higher NK cell cytotoxicity, which was synergistically augmented when combined with antiCD20 mAb rituximab or antiCD38 mAb daratumumab [152]. Artificial coating of lymphoma cells with B7-H6 results in increased NK cell cytotoxicity [153]. In the targeted therapy for HER2$^+$ breast cancer, fusion proteins B7-H6:HER2-scFv (activating NKp30), AICL:HER2-scFv (NKp80), and PVR:HER2-scFv (DNAM-1) enhanced NK cell cytotoxicity [154]. This strategy was recently improved using an affinity matured version of the B7-H6 ligand, firmly binding NKp30, which replaced one arm of anti-EGFR mAb cetuximab [155].

The approach to enhance NK cell-mediated cytotoxicity is complex and comprises a variety of fusion proteins that combine different functional segments (e.g., soluble NK cell receptors to target cancer cells selectively, soluble NK cell-activating ligands, scFv fragments of mAb, Fc portion of mAbs, cytokines). These proteins are usually bivalent, but polyvalent molecules are also a strategy. Polymeric carriers might be used to broaden the repertoire of NK cell enhancers as a versatile tool for assembling polyvalent particles using specific anchors. Part of mAbs may be replaced with smaller fragments; for example, nanobodies (Nbs, VHHs) derived from camelid antibodies, consisting only of the heavy-chain variable domain of IgG2 and IgG3, with the size of about 14 kDa [156]. Thus the range of potentially beneficial molecules might be even broader.

2   AIMS OF THIS THESIS

- Cloning and expression of NK cell-activating ligands

- Binding studies and characterization of the interaction of expressed ligands with NK cell receptors

- Developing a strategy to combine NK cell-activating ligands with the moieties targeting tumor antigens and verification of binding on the target cell lines

- Optimization of rapid *in vitro* assays to test the biological activity of expressed recombinant proteins

- Optimization of cellular cytotoxicity assays to evaluate the capacity of recombinant proteins to influence NK cell-mediated cell lysis

- Structural studies of NK cell receptor organization on the cell surface using superresolution microscopy

3 METHODS

The methods used in this work are listed below. The detailed description of experimental procedures with all technical parameters is always part of the relevant publication.

- Cell culture
  - Cultivation and maintenance of suspension and adherent mammalian cell lines (HEK293, HeLa, HT-29, C33, SKBR3, BT-474, K562, Ramos, NK-92MI)
  - Transfection and its optimization
  - Isolation of PBMC and primary NK cells

- Protein expression and purification
  - Vector design and gene cloning
  - Chromatography techniques (affinity chromatography, size-exclusion chromatography)
  - Electrophoresis and western blot analysis

- Protein characterization
  - Analytical ultracentrifugation (AUC)
  - Mass spectrometry (MS)
  - Differential scanning fluorimetry (DSF, nanoDSF)
  - Dynamic light scattering (DLS)

- Characterization of protein-protein interactions
  - Isothermal titration calorimetry (ITC)
  - Surface plasmon resonance (SPR)
  - Microscale thermophoresis (MST)

- Structural techniques
  - Protein crystallization
  - Small-angle X-ray scattering (SAXS)

- Fluorescent techniques
  - Protein labeling
  - Flow cytometry (FACS)
  - Fluorescent microscopy (wide-field fluorescent microscopy, superresolution microscopy techniques – dSTORM)

4 RESULTS AND DISCUSSION

4.1 EXPRESSION OF SOLUBLE LIGANDS AND NK CELL RECEPTOR ECTODOMAINS

4.1.1 HEK293 EXPRESSION SYSTEM AND ITS OPTIMIZATION

In order to study the structure of NK cell receptors and their ligands, they must first be expressed. Protein quality requirements are high, but there is also a question of cost-effectiveness and feasibility. Moreover, such manipulations as crystallization or affinity measurements of low K_D complexes require high sample amounts (roughly milligrams of protein). Although the *E. coli* expression system is still often used, it has severe limitations for expressing immune receptors [157]. In the case of immune recognition, a native glycosylation pattern is essential [158].

For this reason, we used human embryonic kidney cells 293 (HEK293) for protein expression. These cells are a very versatile system, also having the potential to express therapeutical proteins [159]. Moreover, some NK cell receptors or ligands are simply not expressible in *E. coli* or form inclusion bodies and must be *in vitro* refolded [160].

Despite the glycosylation relevance for the recognition within immune receptors, complex branched glycans may be problematic for structural studies, for example, crystallization. Thus, we used two different variants of HEK293 cells, HEK293T (expressing the SV40 large T antigen; proteins possess wild-type, complex mammalian glycosylation and were used mainly for biological studies) and HEK293S GnTI⁻ (N-acetyl-glucosaminyltransferase I-deficient cell line; produced proteins have uniform glycosylation with $GlcNAc_2Man_5$ pattern, this glycosylation may be cleaved with EndoH or EndoF1 endoglycosidases, proteins are suitable for structural studies) [161,162].

HEK293 cells are initially adherent cells, which is not practical when working with large cell numbers and scaling up the protein expression. To overcome this technical issue, cells were adapted for cultivation in suspension in our group (Publication no. 2, p. 68) [163,164]. Cells were transferred into serum-free commercial medium EX-CELL293 (Sigma, St. Louis, MT, USA) supplemented with an additional 4 mM L-glutamine. Cells were placed in squared-shape glass flasks with gas permeable caps on an orbital shaker (135 rpm, 37 °C, and 5 % CO_2) to keep the suspension equally mixed.

Linear polyethyleneimine (lPEI 25 kDa; Polysciences, Warrington, PA, USA) was chosen as the transfection reagent, based on the cost/efficiency ratio. We optimized the transfection conditions, resulting in the use of 1 μg of the DNA per 10^6 cells, the ratio between the DNA and transfection reagent lPEI was 1:4 for HEK293T (but this ratio may vary between the cell lines and is always subject to optimization in case of new lPEI batch). We used the high-density protocol and added the DNA and lPEI directly to the cell suspension (20×10^6 cells/ml in EX-CELL293, without pre-incubation of DNA:lPEI complexes), cells were diluted to a final density of 2×10^6 cells/ml after 2 hours. Protein expression yield was further enhanced by adding 2 mM valproic acid as a histone deacetylase inhibitor and thus the cell cycle blocker [164]. Cell-culture supernatant was harvested 5-7 days post-transfection. The described protocol results from long-term optimization and is valid for my first-author publication, the most recent one among the selected publications (Publication no. 5, p. 149) [165].

The protein expression yield can be enhanced by prolonging the survival of transfected cells [166], which may be achieved by inhibition of apoptosis [167], modulation of the cell cycle (keeping the cell in the most productive G1 phase) [168] or introduction of growth factors [169]. This strategy was proven in the thesis of Edita Poláchová [170]. First, vector encoding for the protein interest, based on the pTT5 backbone (vector with the cytomegalovirus promotor [171]), was modified by the insertion of an extra WPRE sequence (woodchuck post-transcriptional regulatory element sequence [172]) and named pTW5 vector. After that, a DNA mixture was optimized to finally contain 88 % of the pTW5 plasmid encoding gene of interest, 10 % of pTW5_aFGF (vector with acidic fibroblast growth factor), and 2 % of pTW5_p27 (vector with an inhibitor of cyclin-dependent kinase), which led to the highest protein yields in HEK293S GnTI⁻ cell line.

As mentioned above, when using a simple transient expression, the yields of expressed protein may be highly enhanced by further interventions into cell well-being. Unfortunately, even this enhancement may not be sufficient for the expression of some specific proteins, such in the case of the ectodomain of human NKR-P1 (Publication no. 1, p. 59). The protein construct was systematically optimized but without successful expression; only the switch from transiently to a stably transfected pool of cells led to reasonable expression yields [173]. NKR-P1 construct (G90-S225) was subcloned into the pOPINTTGneo vector (obtained from the Oxford Protein Production Facility,

University of Oxford, UK [174]) containing neomycin resistance as a selection marker and thus enabling generation of stably transfected mammalian cells. These constitutively expressing pools produced enough protein (2.5 mg per liter of cell culture) for structural studies (SEC, AUC, crystallization).

Another strategy used to generate stably transfected cells and express NK cell receptors was the transposon-based system piggyBac (PB). This system uses PB transposase (PBase) to actively insert DNA fragments into the chromosomal DNA of the mammalian cell [175,176]. Moreover, the expression is regulated by the tetracycline response element (TRE) promoter and thus silenced by the reverse tetracycline transactivator (rtTA). The transactivator is carried by the helper plasmid co-transfected with the plasmid bearing the gene of interest and also incorporated by the PBase. Protein expression is then induced by adding doxycycline only when cell culture reaches appropriate viability and cell density. PiggyBac system was used for the production of NKp80 (human activating receptor from NKR-P1 family [177]) and Clrb (ligand of mouse NKR-P1B [178]).

4.1.2 CONSTRUCT OPTIMIZATION RESPECTING STRUCTURAL PATTERNS

Proper protein folding is necessary for correct protein function. For this reason, structural patterns, as functional domains, must be respected when designing the expression construct. There is a conserved disulfide motif within CTLD, which must be followed. For example, as in the case of LLT1, there is one "missing" cysteine at a conserved site in the wild-type sequence. Mutation of amino acid at this position, histidine 176 to cysteine, led to the expression of a stable protein (Figure 7a, p. 34) [162]. In the case of B7-H6, there is one disulfide bond in each Ig domain plus one odd cysteine residue (C212) in the membrane-proximal region. This cysteine forms unwanted covalent dimerization between two B7-H6 molecules. The mutation of cysteine 212 to serine highly enhanced the expression yields (Figure 7b, p. 34) [44].
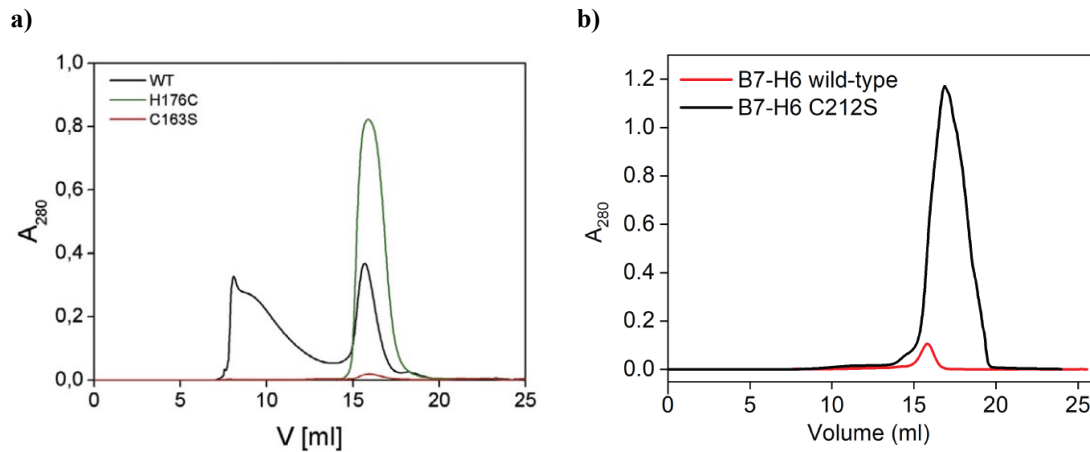
a)   **b)**

Figure 7: Design of stable protein constructs with respect to disulfide motif. a) Expression of three variants of LLT1, only mutation H176C, re-constituting disulfide bonds within CTLD stabilizes the protein, **b)** mutation of odd cysteine in the stalk domain of B7-H6 enhances the expression yield.

Some NK cell receptors from the NKR-P1 family or their ligands may form covalent dimers on the cell surface (e.g., human NKR-P1, LLT1, NKp80, KACL), usually by the interaction of odd cysteine present in the membrane-proximal domain (so-called stalk domain). The functional role of these dimers is not clearly revealed in humans but was studied in rodents. Although the published results are not directly comparable because of the different methodology or protein constructs, they suggest complex regulation of receptor function (ligand recognition, signalization). Murine NKR-P1 receptor variants c1, c2, and f1 form predominantly dimers or even higher oligomeric structures on the surface of lymphoid cells, but on the contrary, NKR-P1a is mainly present in the monomeric form [179]. Also, the dimerization is not exclusively driven by the presence of unpaired cysteine but is more likely regulated by the precise positioning of the cysteine residue. Murine NKR-P1b monomers and dimers are formed irrespective of the stalk domain, but only monomeric receptors interact with its ligands [180]. On the other hand, the crystal structure of NKR-P1b:Clr-b (PDB 6E7D) complex revealed head-to-head interaction between receptor and ligand homodimers. Moreover, there is a cross-linking of neighboring molecules by NKR-P1b non-classical homodimer [181]. Only the dimeric form of NKR-P1b transduced signals into the cell, suggesting an avidity-based mechanism of NKR-P1b receptor function.

To contribute to the study of rodent NKR-P1:Clr interaction, we produced functional dimeric constructs of CTLD ectodomains in the HEK293 system (Publication no. 2, p. 68)

[163]. This system beneficiates from the nature of the Fc fragment of human IgG, which forms covalently linked dimers and thus assures dimerization of the attached construct (Figure 8). Expressed proteins were secreted into the cell culture medium as soluble (no need for the refolding from inclusion bodies after *E. coli* expression) and carried mammalian glycosylation patterns. Furthermore, the protease-cleavable Fc fragment leaves the intact receptor ectodomain resulting in a stable covalent dimer, non-covalent dimer, or mixture of dimers and monomers, which may be separated using size exclusion chromatography.
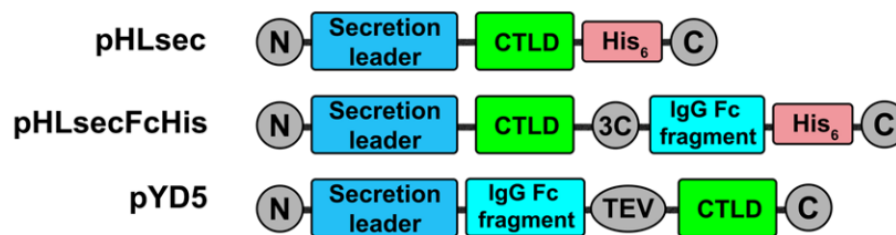

Figure 8: Schematical representation of the receptor NKR-P1b and Crl-11 construct design. Three vectors were designed – pHLsec (only secreted CTLD with histidine tag), pHLsec FcHis (secreted CTLD, cleavage site for 3C protease followed by Fc fragment and histidine tag), and pYD5 (secretion leader followed directly by Fc fragment, TEV protease cleavage site and CTLD on the C-terminus).

Although covalent dimers might be relevant for cellular signalization and thus the expression of such receptor constructs is also relevant, receptor NKp30 forms dimers and higher oligomers in the solution, without any covalent bond (Publication no. 3, p. 85) [44]. The formation of higher oligomeric species depends on receptor structural patterns, precisely on the presence of the membrane-proximal region – the stalk domain, and glycosylation (Figure 9abc, p. 36). Two receptor variants were compared, NKp30 with stalk domain (NKp30_Stalk) and NKp30 consisting of ligand-binding domain only (NKp30_LBD). Besides, NKp30 variants and glycovariants have different binding properties, the K_D of NKp30:B7-H6 interaction varies (Figure 9d, p. 36). The K_D also differs according to the method of measurement. We can see different results when measured by SPR (a method based on surface immobilization of one interaction partner) or ITC (a method measuring the thermodynamic interaction parameters directly in solution), which suggests the influence of the avidity effect. Nevertheless, the direct quantification of NKp30 oligomers on the cell surface or their trafficking during interaction with its ligands and NK cell activation remains undiscovered.
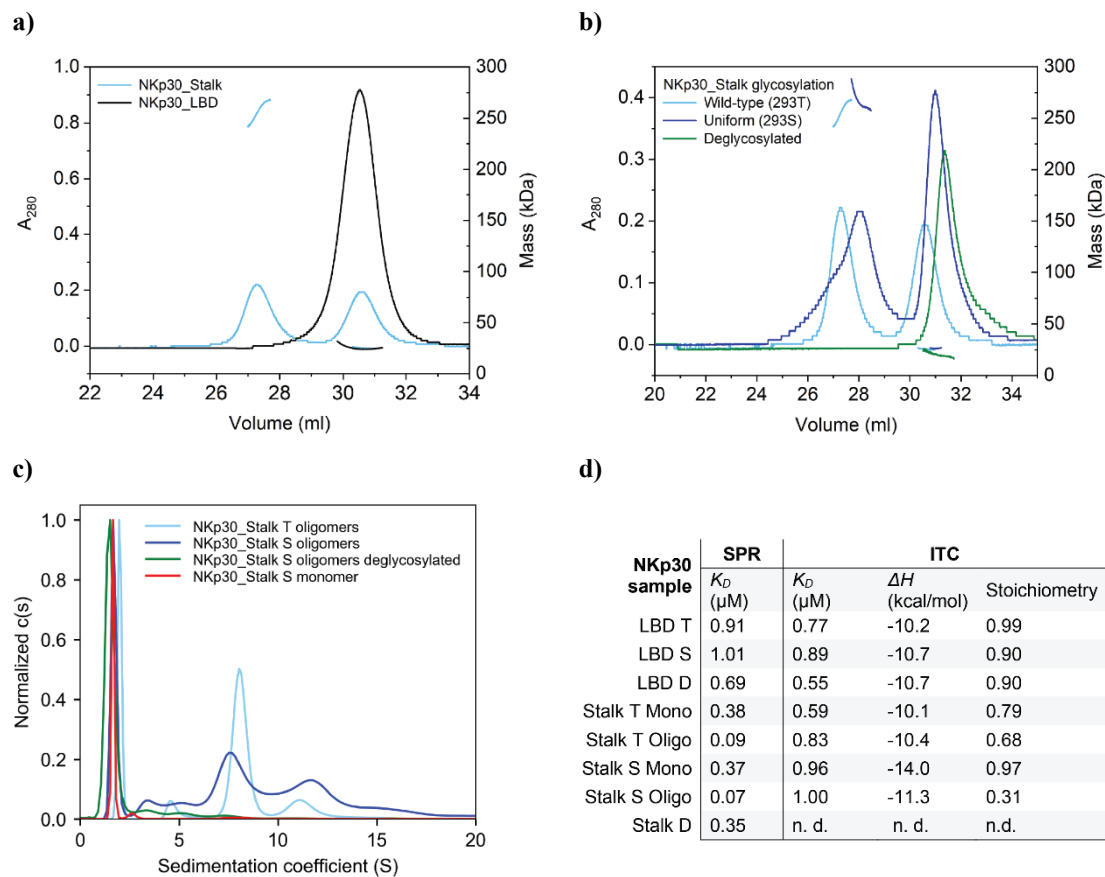
Figure 9: Oligomeric state of NKp30 variants and B7-H6 binding affinities. a) MALS data comparison of NKp30_Stalk and NKp30_LBD oligomeric state, **b)** MALS data for NKp30_Stalk glycovariants with wild-type glycosylation (T), uniform glycosylation (S), and deglycosylated, **c)** sedimentation coefficient distribution of particles analyzed by AUC comparing abundancy of higher species within an oligomeric or monomeric fraction of NKp30_Stalk protein, **d)** comparison of K_D values of NKp30:B7-H6 interaction measured by SPR and ITC [44].

4.1.3   EXPRESSION OF SOLUBLE PROTEINS FOR NK CELL ENGAGEMENT

Expression of soluble, stable, and pure proteins, especially NK cell-activating ligands, is a prerequisite for using such proteins as part of immunoactive therapeutics and the generation of so-called NK cell engagers (NKCE) [147]. As described previously (1.4.3 NK Cell-Based Immunotherapeutics, p. 25), there are many strategies for generating these molecules. However, altogether, they usually combine targeting moiety (for tumor recognition) and NK cell-activating moiety (ligand for triggering receptor) in one molecule. This strategy is not versatile, as it requires new cloning for every change of the construct, and the number of moieties is limited by the final protein size (and thus limited expression efficiency).

For this reason, we used HPMA-based polymer with coiled coil anchors as a carrier for NKp30 activating ligand B7-H6 and scFv targeting tumor marker carbonic anhydrase IX (CAIX). Both cargoes were modified with a complementary coiled coil sequence (CC). My first-author publication describes the expression of modified B7-H6CC (Publication no. 5, p. 149) [165]. The sequence of B7-H6 (C212S) was modified with four (VAALKEK) coiled coil peptide repeats. We also prepared a B7-H6 variant with mutations in the N-terminal domain (S60Y, F82W, L129Y), which were described to enhance receptor binding [154]. B7-H6 variants were expressed in the HEK293T cell line to maintain a natural glycosylation pattern. The quality control of expressed proteins is shown in Figure 10.
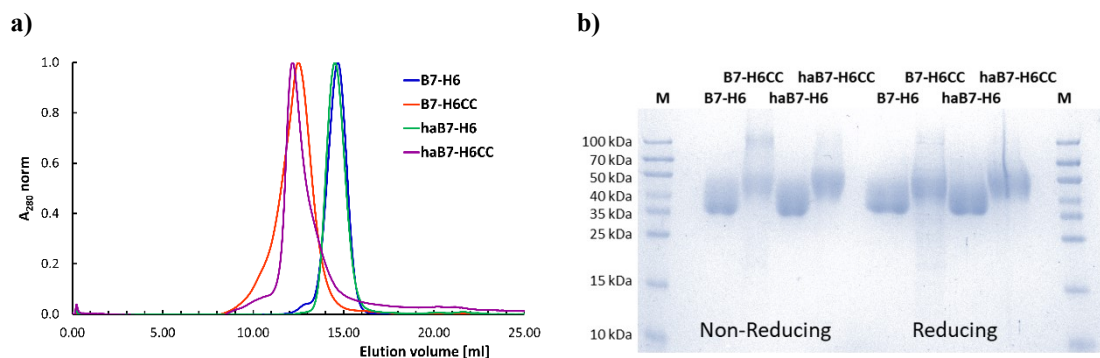

Figure 10: Expression of B7-H6 coiled coil variants. a) Comparison of size-exclusion chromatography elution profiles, **b)** SDS PAGE electrophoresis of expressed proteins.

Although the expression of both B7-H6CC and CAIX scFvCC was successful, the coiled coil motif is generally problematic for protein modification because it is highly charged. Moreover, the interaction of coiled coil complementary motifs is non-covalent, which may lead to complete dissociation of protein-polymer particles in low concentrations, typical for immunotherapeutic administration. This problem may be overcome using different anchors with specific transpeptidases, forming a covalent bond between the carrier and the decorating proteins. For example, transpeptidase sortase (Srt) from *S. aureus* recognizes short C-terminal amino acid sequence -LPXTG- (where X is any amino acid, glycine cannot be the very last amino acid) of the first partner and connects it with polyglycine at N-terminus of the second partner, resulting in covalent peptide bond between the two [182]. Currently, under optimization in our group, this

strategy may be used to generate fusion proteins, decorate polymeric carriers with immunoactive moieties, or label proteins.

Nanobodies (Nb) are an emerging group of targeting molecules as an alternative to scFv, thanks to their small size and easy expression. Successful expression of nanobodies in fusion with NK cell-activating ligands was described in the thesis of Denis Cmunt [183]. Fusion proteins consisting of Nb targeting receptor HER2, CD20, or aFGFR connected with activating ligands MICA or B7-H6 via (GS$_4$)$_4$ linker were prepared. Both orientations of protein were tested, Nb at N-terminus and ligand at C-terminus and vice versa, to find the best variant respecting structural patterns of the recognition. As an important part of the immunoligand characterization, binding to the NK cell receptor and the target cell line expressing tumor antigen was verified (only for immunoligand consisting of anti-HER2 Nb and MICA ligand in the thesis of Denis Cmunt). Fusion proteins are also a strategy to express immunoactive molecules that trigger NK cell cytotoxicity, which is currently being studied in our group.

4.2 TESTING OF B7-H6 COILED COIL BIOLOGICAL ACTIVITY IN VITRO

To prove that B7-H6CC protein is suitable for NK cell activation and coiled coil motif does not interfere with the protein function, we measured the binding affinity with NKp30 receptor and protein capacity to induce NK cell degranulation. Finally, we also tested binding to the polymeric carrier and the surface of target cell lines. The detailed methodology and all results are described in my first-author publication (Publication no. 5, p. 149) [165].

Two B7-H6 variants were considered in this study, the wild-type (with C212S mutation, for simplicity referred to as B7-H6) and its high-affinity version (S60Y, F82W, L129Y, C212S; haB7-H6). Both proteins were expressed with or without the coiled coil sequence. Affinity towards NKp30_LBD construct was measured by ITC when the injections of NKp30_LBD titrated B7-H6 in the cell. The thermodynamic parameters of the interaction with B7-H6 are summarized in Table 1, p. 39. The K_D = 668 nM for NKp30_LBD:B7-H6 interaction is in good accordance with our previously published data [44], and thus accurate value for further comparison.

Table 1: Thermodynamic parameters of NKp30_LBD:(ha)B7-H6(CC) interaction.

		K_D	ΔH	ΔS	N
NKp30_LBD	**B7-H6**	668 nM	-11.5 kcal/mol	-10.4 cal/mol/K	0.88
	B7-H6CC	787 nM	-11.2 kcal/mol	-9.6 cal/mol/K	0.74
	haB7-H6	115 nM	-12.7 kcal/mol	-10.8 cal/mol/K	0.91
	haB7-H6CC	259 nM	-11.8 kcal/mol	-9.5 cal/mol/K	0.65

The coiled coil (CC) sequence does not interfere with NKp30 binding (K_D = 668 nM for B7-H6 interaction vs. K_D = 787 nM for B7-H6CC and K_D = 115 nM for haB7-H6 interaction vs. K_D = 259 nM for haB7-H6CC, respectively), although minor differences in the parameters are evident, notably, the interaction stoichiometry is lower in case of the CC variants. This may be due to the homodimerization of the CC motif, as the molecules of (ha)B7-H6CC are not freely diffusing independent monomers but form dimers. The K_D of haB7-H6(CC) is increased compared to wild-type, but the difference is much lower than previously reported (K_D = 9.06 nM, 45-fold improvement compared to wild-type variant in this study [154]). This difference may be caused by the different methodology (BLI measurement in the study), different NKp30 construct used (construct with truncated stalk domain), or most likely by the differences in haB7-H6 construct (one arm of mAb cetuximab was replaced by the N-terminal domain of haB7-H6, whole fusion construct was used for the affinity measurements).

Next, the binding of the B7-H6CC to the polymeric carrier (PolCC) was verified by sedimentation velocity analysis in an analytical centrifuge. Coiled coil (VAALKEK)4 motif forms weak homodimers, as measured previously for scFv with the same anchor [184]. However, heterodimers are preferably formed in a mixture with complementary coiled coil sequence (VAALEKE)4. This behavior was verified for B7-H6CC as well, as B7-H6CC homodimer was completely absent when mixed with PolCC in equimolar ratio. When titrating the PolCC with a higher molar excess of B7-H6CC, shift to higher stoichiometries was observable (binding 1:2, 1:3, and 1:4). Moreover, B7-H6CC bound to polymer is still accessible for interaction with NKp30.

The capacity of B7-H6CC and haB7-H6CC to induce NK cell degranulation was also confirmed. The surface of the Ni-NTA coated well-plate was decorated with NK cell ligands using histidine tag, creating a very simple artificial activating milieu. Primary NK cells were stimulated overnight with a high dose of IL-2 and then incubated for 4 hours on the decorated surface. NK cell activation was detected by flow cytometry as cells

expressing CD107a, a marker of degranulation. Based on the percentage of CD107a^{+} cells, we concluded that expressed B7-H6, B7-H6CC, and haB7-H6CC activate NK cells. B7-H6CC bound to the PolCC also activates NK cells. Thus, NKp30 recognition is neither disrupted by the coiled coil motif nor by PolCC binding (as indicated previously by the affinity measurements and analytical ultracentrifugation). The high-affinity variant of B7-H6CC exhibited slightly higher activating potential than the wild-type.

Finally, we investigated the binding of polymer:protein complexes to the cell line expressing CAIX. Targeting molecule M75 derived scFvCC was labeled with AlexaFluor488, B7-H6CC was labeled with AlexaFluor647, and proteins were mixed with PolCC in 1:2:2 molar ratio (PolCC:B7-H6CC:scFvCC). These complexes were incubated with HT-29 cells. Cells were analyzed by fluorescent cytometry, and the result is shown in Figure 11. To study the binding directly, both two-color particles (both B7-H6CC and scFvCC fluorescently labeled) and single-color particles were prepared (both CC proteins were used, but only one with the label). As a control, we tested that B7-H6CC does not bind to the HT-29. Only the chimeric PolCC:protein particles containing both B7-H6CC and scFvCC emit a signal in the channel corresponding to the B7-H6CC label. This means that particles containing PolCC and B7-H6CC together with scFvCC were formed and targeted the surface of CAIX^{+} cells.
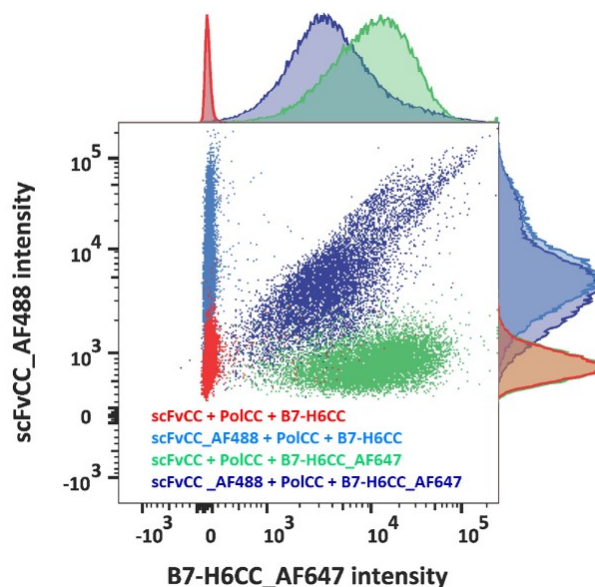

Figure 11: Binding of polymer:protein particles to the cell surface. HT-29 cells were decorated with particles always consisting of PolCC, B7-H6CC, and scFvCC; protein molecules were not fluorescently labeled (in red), only scFvCC was labeled (in light blue), only B7-H6CC was labeled (in green), both scFvCC and B7-H6CC were labeled using different dyes (in dark blue).

Taking together all these data about B7-H6CC, this modified NK cell-activating ligand can be a potent part of immunoactive particles based on pHPMA copolymers. The interaction of coiled coil complementary sequences is a versatile tool to decorate PolCC with various proteins, thus creating polyvalent species. However, best stoichiometry, stability of polymeric particles in low concentrations, and procedure of creating particles with uniform composition must be further investigated before cellular cytotoxicity assays with primary NK cells.

4.3 RECEPTOR ORGANIZATION ON THE CELL SURFACE

Interaction of NKR-P1 receptor with its ligand LLT1 was detailly studied in our group, mainly by Jan Bláha, Ph.D. First, LLT1 was expressed, and its crystal structure was solved [162,185]. Next, the NKR-P1 receptor was expressed using stable transfection of HEK293 GnTI⁻ cells [173]. Finally, we solved the structure of NKR-P1:LLT1 immunocomplex (PDB 5MGT), Publication no. 4, p. 110 [59]. This structure revealed interesting symmetry, facilitating the formation of chain-like structures on the cell surface. Two distinct interaction interfaces were identified, the primary mode, corresponding well with the structure of homologous NKp65:KACL complex (PDB 4IOP [187]), and the secondary mode, enabling interaction of two neighboring molecules. Because this interaction is quite unique, we decided to test the biological relevance of NKR-P1 clustering on the cell surface with superresolution fluorescent microscopy and explore this interaction's role in cell signaling in the cytotoxicity assay.

To test our hypotheses, we expressed the LLT1 variant with disturbed secondary interaction interface (LLT1^{SIM}, secondary interface mutant). We designed an experiment where the NKR-P1 receptor on the cell surface (transfected HEK293S GnTI⁻) interacts with soluble ligand LLT1 or LLT1^{SIM}, and the organization of the receptor on the cell surface was studied with dSTORM [188]. Cells were fixed and labeled with an anti-NKR-P1 primary antibody with the AlexaFluor647 label. This label has unique optical blinking properties, as, under specific buffer conditions, the probability of the transition from the excited state to the ground state and emitting fluorescence is low, and most of the fluorophore is in the off state. For this reason, only a small portion of molecules is blinking at each imaging cycle, enabling its precise localization. At the end of the data

acquisition, localization maps were processed and evaluated by Voronoi tessellation in the ClusterViSu program [189].

The surface organization of the NKR-P1 receptor was studied under different conditions: without the ligand or after ligand binding (LLT1 or LLT1^{SIM}). Results summarizing the NKR-P1 surface distribution are presented in Figure 12, p. 43. The average area of non-bound NKR-P1 clusters does not significantly differ from the clusters of NKR-P1 treated with soluble LLT1^{SIM}, the same for the average cluster diameter. Contrarily, cluster area and cluster diameter differ when comparing NKR-P1 bound to LLT1 with two other conditions. As a control, the total density of events remained the same for all three conditions. Based on these results, respecting the methodology used, we cannot directly measure cluster size and thus estimate how many NKR-P1 molecules form these clusters (as label size and label density also play the role). However, if we directly compare NKR-P1 cluster parameters, when it interacts with LLT1 enabling both interaction modes or with LLT1^{SIM} providing the primary binding mode only, we can conclude that NKR-P1 receptor forms higher structures induced by ligand binding. Soluble LLT1 affects the surface distribution of NKR-P1.

Finally, we tested how does the NKR-P1 clustering influence the signalization and thus inhibition of cellular cytotoxicity. In the direct cytotoxicity assay, primary NK cells were mixed with the target cells K562, easily susceptible to the NK cell-mediated lysis. Similarly, as in the dSTORM experiment, interacting cells were treated with LLT1, with LLT1^{SIM}, or remained untreated, two concentrations of soluble ligand were used, and results were evaluated by flow cytometry as a percentage of living K562 cells after four hours of incubation (Figure 13, p. 44). Soluble LLT1 interferes with the natural cytotoxicity, resulting in higher survival of K562 cells, but the capacity of LLT1^{SIM} to induce the same inhibitory effect is limited. LLT1 lacking the secondary interaction mode, contributing to the receptor clustering, cannot inhibit the cellular cytotoxicity. The NKR-P1 clustering affects signalization.
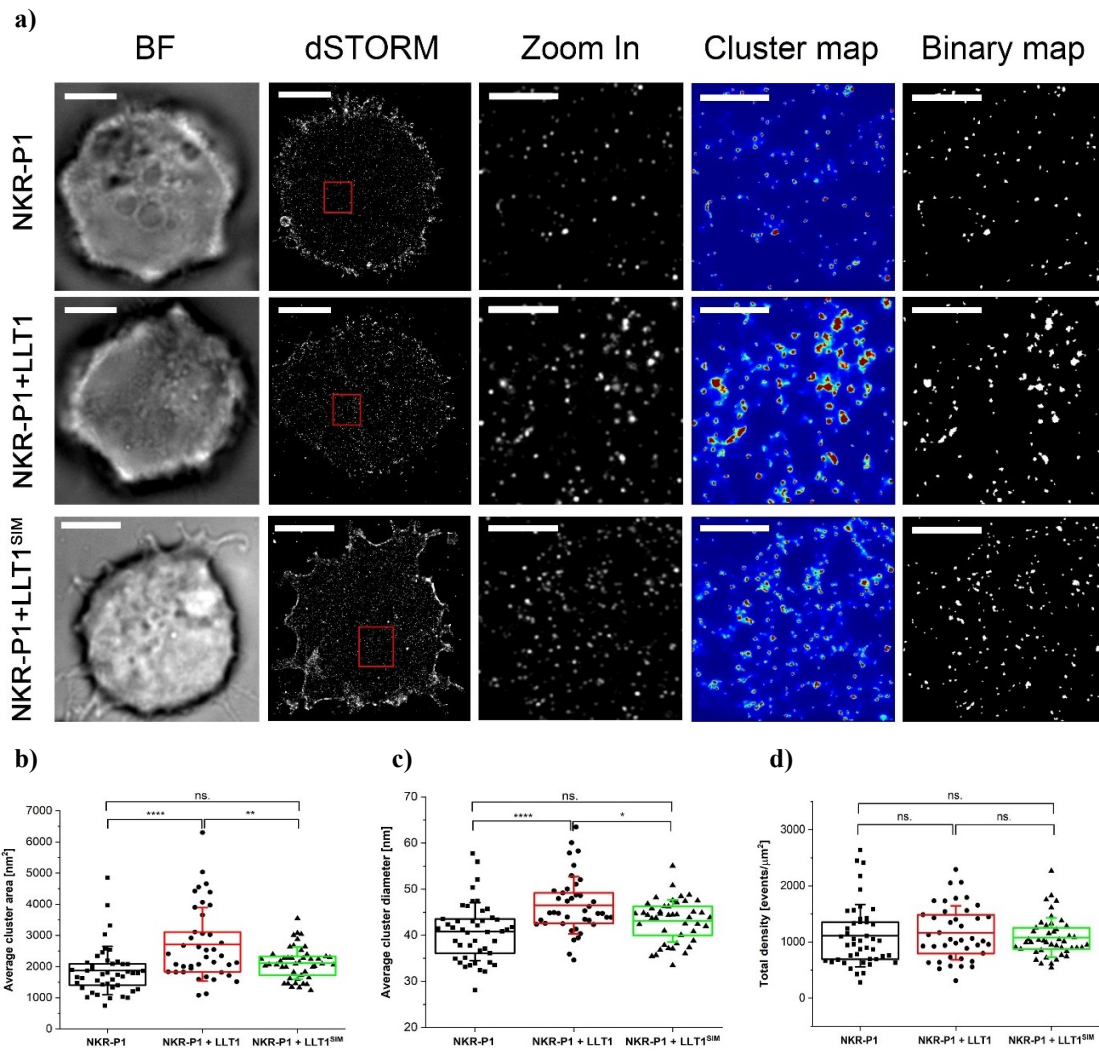
Figure 12: Superresolution microscopy reveals changes in the surface distribution of NKR-P1 upon binding of LLT1. a) Representative images of NKR-P1 clusters under three distinct conditions (without ligand, with LLT1, or with LLT1[SIM]), in brightfield (BF), after superresolution image reconstruction (dSTORM), scale bars represent 5 µm; red boxes in dSTORM images (10 µm²) were zoomed in and processed, resulting in cluster heatmap, and finally, in a binary map, scale bars represent 1 µm. b) Selected parameters of NKR-P1 clusters: average cluster area, average cluster diameter, and total density of events (horizontal bar corresponds to the mean value, box corresponds to the interquartile range, and error bars represent SD) [59].
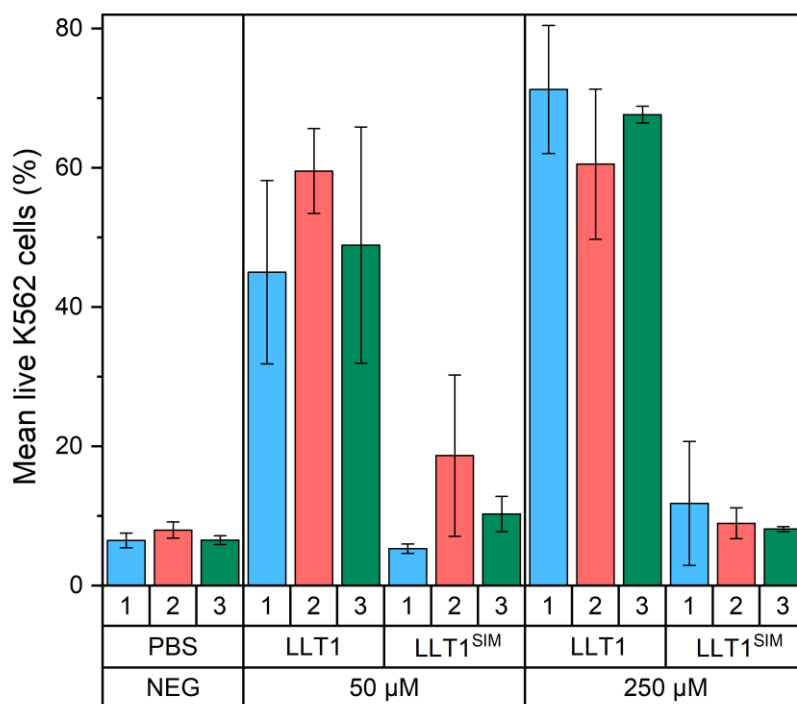
Figure 13: The effect of NKR-P1 clustering on signalization. The killing of K562 cells by primary NK cells is represented as a percentage of living cells. Cells were treated with LLT1, LLT1^{SIM} (in 50 µM and 250 µM concentration), or untreated. LLT1 blocks NK cell cytotoxicity, but this effect is not observable for LLT1^{SIM} [59].

Taken together, both superresolution microscopy and cytotoxicity assay results show the biological relevance of NKR-P1 clusters, which were initially observed in the crystal structure. Superresolution microscopy revealed the reorganization of NKR-P1 molecules upon ligand binding. Moreover, only LLT1 enabling such reorganization blocks the NK cell cytotoxicity in the killing assay. Signalization is affected by the cluster formation, most likely because of the avidity effect, which helps to overcome the low affinity of this interaction. This approach combining structural data, affinity measurements, and biological data (direct observations on the cell surface, activation assay) leads to conclusive results and reveals the biological relevance of NKR-P1 receptor oligomerization.

5 SUMMARY

- HEK293 expression system was shown to be suitable for expressing soluble NK cell receptors and their ligands, notably for NKR-P1, LLT1, NKp80, NKp30, B7-H6, rat receptors from the NKR-P1 family and its ligands.

- NKp30 activating ligand B7-H6 with coiled coil sequence and its variants were expressed in HEK293T cells.

- The interaction of B7-H6 variants to the soluble NKp30 receptor ectodomain was measured with isothermal titration calorimetry.

- pHPMA copolymer was decorated with both targeting moiety (scFv) and activating moiety (B7-H6) using coiled coil interaction, the binding of chimeric polymer-protein complexes to the surface of tumor cells confirmed by flow cytometry.

- The capacity of B7-H6 constructs to induce NK cell degranulation was tested in a simple *in vitro* assay, where functionalizes well-surface substitutes target cells; this assay may also be used for other activating NK cell ligands as control of the biological activity of expressed proteins.

- The organization of the NKR-P1 receptor on the cell surface was studied by the dSTORM technique, revealing ligand-induced receptor oligomerization.

- Direct NK cell cytotoxicity assay confirmed the importance of NKR-P1 clusters in the signalization; this assay was optimized and may also be modified for further studies of NK cell activation.

6 REFERENCES

1. Greenberg, A.H.; Playfair, J.H. Spontaneously Arising Cytotoxicity to the P-815-Y Mastocytoma in NZB Mice. *Clinical and experimental immunology* **1974**, *16*, 99–109.

2. Herberman, R.B.; Nunn, M.E.; Lavrin, D.H. Natural Cytotoxic Reactivity of Mouse Lymphoid Cells against Syngeneic and Allogeneic Tumors. I. Distribution of Reactivity and Specificity. *International Journal of Cancer* **1975**, *16*, 216–229.

3. Kiessling, R.; Klein, E.; Wigzell, H. „Natural" Killer Cells in the Mouse. I. Cytotoxic Cells with Specificity for Mouse Moloney Leukemia Cells. Specificity and Distribution According to Genotype. *European Journal of Immunology* **1975**, *5*, 112–117.

4. Kiessling, R.; Klein, E.; Pross, H.; Wigzell, H. „Natural" Killer Cells in the Mouse. II. Cytotoxic Cells with Specificity for Mouse Moloney Leukemia Cells. Characteristics of the Killer Cell. *European Journal of Immunology* **1975**, *5*, 117–121.

5. Greenberg, A.H. The Origins of the NK Cell, or a Canadian in King Ivan's Court. *Clinical and investigative medicine. Medecine clinique et experimentale* **1994**, *17*, 626–31.

6. Trinchieri, G. Biology of Natural Killer Cells. *Advances in Immunology* **1989**, *47*, 187–376.

7. Huntington, N.D.; Vosshenrich, C.A.J.; di Santo, J.P. Developmental Pathways That Generate Natural-Killer-Cell Diversity in Mice and Humans. *Nature Reviews Immunology* **2007**, *7*, 703–714.

8. Mak, T.W.; Saunders, M.E. Bridging Innate and Adaptive Immunity: NK, γδ T, and NKT Cells. In *The Immune Response*; Elsevier, 2006; Vol. 147, pp. 517–552.

9. Montaldo, E.; Zotto, G. del; Chiesa, M. della; Mingari, M.C.; Moretta, A.; Maria, A. de; Moretta, L. Human NK Cell Receptors/Markers: A Tool to Analyze NK Cell Development, Subsets and Function. *Cytometry Part A* **2013**, *83A*, 702–713.

10. di Vito, C.; Mikulak, J.; Mavilio, D. On the Way to Become a Natural Killer Cell. *Frontiers in Immunology* **2019**, *10*, 1812.

11. Cooper, M.A.; Fehniger, T.A.; Caligiuri, M.A. The Biology of Human Natural Killer-Cell Subsets. *Trends in Immunology* **2001**, *22*, 633–640.

12. Artis, D.; Spits, H. The Biology of Innate Lymphoid Cells. *Nature* **2015**, *517*, 293–301.

13. Vivier, E.; Raulet, D.H.; Moretta, A.; Caligiuri, M.A.; Zitvogel, L.; Lanier, L.L.; Yokoyama, W.M.; Ugolini, S. Innate or Adaptive Immunity? The Example of Natural Killer Cells. *Science* **2011**, *331*, 44–49.

14. Vivier, E.; Tomasello, E.; Baratin, M.; Walzer, T.; Ugolini, S. Functions of Natural Killer Cells. *Nature Immunology* **2008**, *9*, 503–510.

15. Smyth, M.J.; Cretney, E.; Kelly, J.M.; Westwood, J.A.; Street, S.E.A.; Yagita, H.; Takeda, K.; Dommelen, S.L.H. van; Degli-Esposti, M.A.; Hayakawa, Y. Activation of NK Cell Cytotoxicity. *Molecular Immunology* **2005**, *42*, 501–510.

16. Fu, B.; Tian, Z.; Wei, H. Subsets of Human Natural Killer Cells and Their Regulatory Effects. *Immunology* **2014**, *141*, 483–489.

17. Paust, S.; von Andrian, U.H. Natural Killer Cell Memory. *Nature Immunology* **2011**, *12*, 500–508.

18. von Andrian, U.H. NK Cell Memory: Discovery of a Mystery. *Nature Immunology* **2021**, *22*, 669–671.

19. Cerwenka, A.; Lanier, L.L. Natural Killer Cell Memory in Infection, Inflammation and Cancer. *Nature Reviews Immunology* **2016**, *16*, 112–123.

20. Vivier, E.; Ugolini, S. Natural Killer Cells: From Basic Research to Treatments. *Frontiers in Immunology* **2011**, *2*, 18.

21. Ljunggren, H.-G.; Kärre, K. In Search of the 'Missing Self': MHC Molecules and NK Cell Recognition. *Immunology Today* **1990**, *11*, 237–244.

22. Lanier, L.L. Up on the Tightrope: Natural Killer Cell Activation and Inhibition. *Nature Immunology* **2008**, *9*, 495–502.

23. Kärre, K. Natural Killer Cell Recognition of Missing Self. *Nature Immunology* **2008**, *9*, 477–480.

24. Malmberg, K.-J.; Carlsten, M.; Björklund, A.; Sohlberg, E.; Bryceson, Y.T.; Ljunggren, H.-G. Natural Killer Cell-Mediated Immunosurveillance of Human Cancer. *Seminars in Immunology* **2017**, *31*, 20–29.

25. Kim, S.; Poursine-Laurent, J.; Truscott, S.M.; Lybarger, L.; Song, Y.J.; Yang, L.; French, A.R.; Sunwoo, J.B.; Lemieux, S.; Hansen, T.H.; et al. Licensing of Natural Killer Cells by Host Major Histocompatibility Complex Class I Molecules. *Nature* **2005**, *436*, 709–713.

26. Raulet, D.H.; Vance, R.E. Self-Tolerance of Natural Killer Cells. *Nature Reviews Immunology* **2006**, *6*, 520–531.

27. Seidel, U.J.E.; Schlegel, P.; Lang, P. Natural Killer Cell Mediated Antibody-Dependent Cellular Cytotoxicity in Tumor Immunotherapy with Therapeutic Antibodies. *Frontiers in Immunology* **2013**, *4*, 76.

28. Kelley, J.; Walter, L.; Trowsdale, J. Comparative Genomics of Natural Killer Cell Receptor Gene Clusters. *PLoS Genetics* **2005**, *1*, e27.

29. Zelensky, A.N.; Gready, J.E. The C-Type Lectin-like Domain Superfamily. *FEBS Journal* **2005**, *272*, 6179–6217.

30. Li, Y.; Mariuzza, R.A. Structural Basis for Recognition of Cellular and Viral Ligands by NK Cell Receptors. *Frontiers in Immunology* **2014**, *5*, 123.

31. Bork, P.; Holm, L.; Sander, C. The Immunoglobulin Fold. *Journal of Molecular Biology* **1994**, *242*, 309–320.

32. Vitale, M.; Cantoni, C.; della Chiesa, M.; Ferlazzo, G.; Carlomagno, S.; Pende, D.; Falco, M.; Pessino, A.; Muccio, L.; de Maria, A.; et al. An Historical Overview: The Discovery of How NK Cells Can Kill Enemies, Recruit Defense Troops, and More. *Frontiers in Immunology* **2019**, *10*, 1415.

33. Kruse, P.H.; Matta, J.; Ugolini, S.; Vivier, E. Natural Cytotoxicity Receptors and Their Ligands. *Immunology & Cell Biology* **2014**, *92*, 221–229.

34. Pende, D.; Parolini, S.; Pessino, A.; Sivori, S.; Augugliaro, R.; Morelli, L.; Marcenaro, E.; Accame, L.; Malaspina, A.; Biassoni, R.; et al. Identification and Molecular Characterization of NKp30, a Novel Triggering Receptor Involved in Natural Cytotoxicity Mediated by Human Natural Killer Cells. *The Journal of Experimental Medicine* **1999**, *190*, 1505–1516.

35. Hudspeth, K.; Silva-Santos, B.; Mavilio, D. Natural Cytotoxicity Receptors: Broader Expression Patterns and Functions in Innate and Adaptive Immune Cells. *Frontiers in Immunology* **2013**, *4*, 69.

36. Li, Y.; Wang, Q.; Mariuzza, R.A. Structure of the Human Activating Natural Cytotoxicity Receptor NKp30 Bound to Its Tumor Cell Ligand B7-H6. *The Journal of Experimental Medicine* **2011**, *208*, 703–714.

37. Memmer, S.; Weil, S.; Beyer, S.; Zöller, T.; Peters, E.; Hartmann, J.; Steinle, A.; Koch, J. The Stalk Domain of NKp30 Contributes to Ligand Binding and Signaling of a Preassembled NKp30-CD3ζ Complex. *Journal of Biological Chemistry* **2016**, *291*, 25427–25438.

38. Brandt, C.S.; Baratin, M.; Yi, E.C.; Kennedy, J.; Gao, Z.; Fox, B.; Haldeman, B.; Ostrander, C.D.; Kaifu, T.; Chabannon, C.; et al. The B7 Family Member B7-H6 Is a Tumor Cell Ligand for the Activating Natural Killer Cell Receptor NKp30 in Humans. *Journal of Experimental Medicine* **2009**, *206*, 1495–1503.

39. Binici, J.; Koch, J. BAG-6, a Jack of All Trades in Health and Disease. *Cellular and Molecular Life Sciences* **2014**, *71*, 1829–1837.

40. Wang, W.; Guo, H.; Geng, J.; Zheng, X.; Wei, H.; Sun, R.; Tian, Z. Tumor-Released Galectin-3, a Soluble Inhibitory Ligand of Human NKp30, Plays an Important Role in Tumor Escape from NK Cell Attack. *Journal of Biological Chemistry* **2014**, *289*, 33311–33319.

41. Barrow, A.D.; Martin, C.J.; Colonna, M. The Natural Cytotoxicity Receptors in Health and Disease. *Frontiers in Immunology* **2019**, *10*, 909.

42. Hartmann, J.; Tran, T. van; Kaudeer, J.; Oberle, K.; Herrmann, J.; Quagliano, I.; Abel, T.; Cohnen, A.; Gatterdam, V.; Jacobs, A.; et al. The Stalk Domain and the Glycosylation Status of the Activating Natural Killer Cell Receptor NKp30 Are Important for Ligand Binding. *Journal of Biological Chemistry* **2012**, *287*, 31527–31539.

43. Herrmann, J.; Berberich, H.; Hartmann, J.; Beyer, S.; Davies, K.; Koch, J. Homo-Oligomerization of the Activating Natural Killer Cell Receptor NKp30 Ectodomain Increases Its Binding Affinity for Cellular Ligands. *Journal of Biological Chemistry* **2014**, *289*, 765–777.

44. Skořepa, O.; Pazicky, S.; Kalousková, B.; Bláha, J.; Abreu, C.; Ječmen, T.; Rosůlek, M.; Fish, A.; Sedivy, A.; Harlos, K.; et al. Natural Killer Cell Activation Receptor NKp30 Oligomerization Depends on Its N-Glycosylation. *Cancers* **2020**, *12*, 1998.

45. Lanier, L.L.; Chang, C.; Phillips, J.H. Human NKR-P1A. A Disulfide-Linked Homodimer of the C-Type Lectin Superfamily Expressed by a Subset of NK and T Lymphocytes. *The Journal of immunology* **1994**, *153*, 2417–28.

46. Fergusson, J.R.; Smith, K.E.; Fleming, V.M.; Rajoriya, N.; Newell, E.W.; Simmons, R.; Marchi, E.; Björkander, S.; Kang, Y.-H.; Swadling, L.; et al. CD161 Defines a Transcriptional and Functional Phenotype across Distinct Human T Cell Lineages. *Cell Reports* **2014**, *9*, 1075–1088.

47. Battistini, L.; Borsellino, G.; Sawicki, G.; Poccia, F.; Salvetti, M.; Ristori, G.; Brosnan, C.F. Phenotypic and Cytokine Analysis of Human Peripheral Blood Gamma Delta T Cells Expressing NK Cell Receptors. *The Journal of ImmunologyJ* **1997**, *159*, 3723–3730.

48. Exley, M.; Porcelli, S.; Furman, M.; Garcia, J.; Balk, S. CD161 (NKR-P1A) Costimulation of CD1d-Dependent Activation of Human T Cells Expressing Invariant Vα24JαQ T Cell Receptor α Chains. *Journal of Experimental Medicine* **1998**, *188*, 867–876.

49. Cosmi, L.; de Palma, R.; Santarlasci, V.; Maggi, L.; Capone, M.; Frosali, F.; Rodolico, G.; Querci, V.; Abbate, G.; Angeli, R.; et al. Human Interleukin 17–Producing Cells Originate from a CD161+CD4+ T Cell Precursor. *Journal of Experimental Medicine* **2008**, *205*, 1903–1916.

50. Martin, E.; Treiner, E.; Duban, L.; Guerri, L.; Laude, H.; Toly, C.; Premel, V.; Devys, A.; Moura, I.C.; Tilloy, F.; et al. Stepwise Development of MAIT Cells in Mouse and Human. *PLoS biology* **2009**, *7*, e54.

51. Yokoyama, W.M.; Plougastel, B.F.M. Immune Functions Encoded by the Natural Killer Gene Complex. *Nature Reviews Immunology* **2003**, *3*, 304–316.

52. Aldemir, H.; Prod'homme, V.; Dumaurier, M.-J.; Retiere, C.; Poupon, G.; Cazareth, J.; Bihl, F.; Braud, V.M. Cutting Edge: Lectin-like Transcript 1 Is a Ligand for the CD161 Receptor. *The Journal of Immunology* **2005**, *175*, 7791–7795.

53. Rosen, D.B.; Bettadapura, J.; Alsharifi, M.; Mathew, P.A.; Warren, H.S.; Lanier, L.L. Cutting Edge: Lectin-Like Transcript-1 Is a Ligand for the Inhibitory Human NKR-P1A Receptor. *The Journal of Immunology* **2005**, *175*, 7796–7799.

54. Rosen, D.B.; Cao, W.; Avery, D.T.; Tangye, S.G.; Liu, Y.-J.; Houchins, J.P.; Lanier, L.L. Functional Consequences of Interactions between Human NKR-P1A and Its Ligand LLT1 Expressed on Activated Dendritic Cells and B Cells. *The Journal of Immunology* **2008**, *180*, 6508–6517.

55. Roth, P.; Mittelbronn, M.; Wick, W.; Meyermann, R.; Tatagiba, M.; Weller, M. Malignant Glioma Cells Counteract Antitumor Immune Responses through Expression of Lectin-Like Transcript-1. *Cancer Research* **2007**, *67*, 3540–3544.

56. Brucklacher-Waldert, V.; Stuerner, K.; Kolster, M.; Wolthausen, J.; Tolosa, E. Phenotypical and Functional Characterization of T Helper 17 Cells in Multiple Sclerosis. *Brain* **2009**, *132*, 3329–3341.

57. Estrada-Capetillo, L.; Hernández-Castro, B.; Monsiváis-Urenda, A.; Alvarez-Quiroga, C.; Layseca-Espinosa, E.; Abud-Mendoza, C.; Baranda, L.; Urzainqui, A.; Sánchez-Madrid, F.; González-Amaro, R. Induction of Th17 Lymphocytes and Treg Cells by Monocyte-Derived Dendritic Cells in Patients with Rheumatoid Arthritis and Systemic Lupus Erythematosus. *Clinical and Developmental Immunology* **2013**.

58. Smith, J.A.; Colbert, R.A. Review: The Interleukin-23/Interleukin-17 Axis in Spondyloarthritis Pathogenesis: Th17 and Beyond. *Arthritis & Rheumatology* **2014**, *66*, 231–241.

59. Bláha, J.; Skálová, T.; Kalousková, B.; Skořepa, O.; Cmunt, D.; Pažický, S.; Poláchová, E.; Abreu, C.; Stránský, J.; Koval', T.; et al. Crystal Structure of the Human NKR-P1 Bound to Its Lymphocyte Ligand LLT1 Reveals Receptor Crosslinking in the Immune Synapse. *bioRxiv* **2021**, Preprint.

60. Orange, J.S. Formation and Function of the Lytic NK-Cell Immunological Synapse. *Nature Reviews Immunology* **2008**, *8*, 713–725.

61. Orange, J.S.; Harris, K.E.; Andzelm, M.M.; Valter, M.M.; Geha, R.S.; Strominger, J.L. The Mature Activating Natural Killer Cell Immunologic Synapse Is Formed in Distinct Stages. *Proceedings of the National Academy of Sciences* **2003**, *100*, 14151–14156.

62. Barber, D.F.; Faure, M.; Long, E.O. LFA-1 Contributes an Early Signal for NK Cell Cytotoxicity. *The Journal of Immunology* **2004**, *173*, 3653–3659.

63. Lagrue, K.; Carisey, A.; Oszmiana, A.; Kennedy, P.R.; Williamson, D.J.; Cartwright, A.; Barthen, C.; Davis, D.M. The Central Role of the Cytoskeleton in Mechanisms and Functions of the NK Cell Immune Synapse. *Immunological Reviews* **2013**, *256*, 203–221.

64. Davis, D.M.; Chiu, I.; Fassett, M.; Cohen, G.B.; Mandelboim, O.; Strominger, J.L. The Human Natural Killer Cell Immune Synapse. *Proceedings of the National Academy of Sciences of the United States of America* **1999**, *96*, 15062–7.

65. Kumar, S. Natural Killer Cell Cytotoxicity and Its Regulation by Inhibitory Receptors. *Immunology* **2018**, *154*, 383–393.

66. Abeyweera, T.P.; Merino, E.; Huse, M. Inhibitory Signaling Blocks Activating Receptor Clustering and Induces Cytoskeletal Retraction in Natural Killer Cells. *Journal of Cell Biology* **2011**, *192*, 675–690.

67. Orange, J.S. Formation and Function of the Lytic NK-Cell Immunological Synapse. *Nature Reviews Immunology* **2008**, *8*, 713–725.

68. Yenan T. Bryceson, Michael E. March, Hans-Gustaf Ljunggren, and E.O.L. Activation, Co–Activation, and Co–Stimulation of Resting Human NK Cells. *Immunological Reviews* **2006**, *29*, 997–1003.

69. Bryceson, Y.T.; Ljunggren, H.; Long, E.O. Minimal Requirement for Induction of Natural Cytotoxicity and Intersection of Activation Signals by Inhibitory Receptors. *Blood* **2009**, *114*, 2657–2666.

70. Hell, S.W.; Sahl, S.J.; Bates, M.; Zhuang, X.; Heintzmann, R.; Booth, M.J.; Bewersdorf, J.; Shtengel, G.; Hess, H.; Tinnefeld, P.; et al. The 2015 Super-Resolution Microscopy Roadmap. *Journal of Physics D: Applied Physics* **2015**, *48*, 443001.

71. Mace, E.M.; Orange, J.S. Visualization of the Immunological Synapse by Dual Color Time-Gated Stimulated Emission Depletion (STED) Nanoscopy. *Journal of Visualized Experiments* **2014**, 1–6.

72. Bertolet, G.; Liu, D. The Planar Lipid Bilayer System Serves as a Reductionist Approach for Studying NK Cell Immunological Synapses and Their Functions. In *Methods in Molecular Biology*; Somanchi, S.S., Ed.; Methods in Molecular Biology; Springer New York: New York, NY, 2016; Vol. 1441, pp. 151–165.

73. Axmann, M.; Schütz, G.J.; Huppa, J.B. Single Molecule Fluorescence Microscopy on Planar Supported Bilayers. *Journal of Visualized Experiments* **2015**, 1–16.

74. Zheng, P.; Bertolet, G.; Chen, Y.; Huang, S.; Liu, D. Super-Resolution Imaging of the Natural Killer Cell Immunological Synapse on a Glass-Supported Planar Lipid Bilayer. *Journal of Visualized Experiments* **2015**, 1–7.

75. Campi, G.; Varma, R.; Dustin, M.L. Actin and Agonist MHC–Peptide Complex–Dependent T Cell Receptor Microclusters as Scaffolds for Signaling. *Journal of Experimental Medicine* **2005**, *202*, 1031–1036.

76. Yokosuka, T.; Sakata-Sogawa, K.; Kobayashi, W.; Hiroshima, M.; Hashimoto-Tane, A.; Tokunaga, M.; Dustin, M.L.; Saito, T. Newly Generated T Cell Receptor Microclusters Initiate and Sustain T Cell Activation by Recruitment of Zap70 and SLP-76. *Nature Immunology* **2005**, *6*, 1253–1262.

77. Brameshuber, M.; Kellner, F.; Rossboth, B.K.; Ta, H.; Alge, K.; Sevcsik, E.; Göhring, J.; Axmann, M.; Baumgart, F.; Gascoigne, N.R.J.; et al. Monomeric TCRs Drive T Cell Antigen Recognition. *Nature Immunology* **2018**, *19*, 487–496.

78. Rossboth, B.; Arnold, A.M.; Ta, H.; Platzer, R.; Kellner, F.; Huppa, J.B.; Brameshuber, M.; Baumgart, F.; Schütz, G.J. TCRs Are Randomly Distributed on

the Plasma Membrane of Resting Antigen-Experienced T Cells. *Nature Immunology* **2018**, *19*, 821–827.

79. Lillemeier, B.F.; Mörtelmaier, M.A.; Forstner, M.B.; Huppa, J.B.; Groves, J.T.; Davis, M.M. TCR and Lat Are Expressed on Separate Protein Islands on T Cell Membranes and Concatenate during Activation. *Nature Immunology* **2010**, *11*, 90–96.

80. Sherman, E.; Barr, V.; Manley, S.; Patterson, G.; Balagopalan, L.; Akpan, I.; Regan, C.K.; Merrill, R.K.; Sommers, C.L.; Lippincott-Schwartz, J.; et al. Functional Nanoscale Organization of Signaling Molecules Downstream of the T Cell Antigen Receptor. *Immunity* **2011**, *35*, 705–720.

81. Williamson, D.J.; Owen, D.M.; Rossy, J.; Magenau, A.; Wehrmann, M.; Gooding, J.J.; Gaus, K. Pre-Existing Clusters of the Adaptor Lat Do Not Participate in Early T Cell Signaling Events. *Nature Immunology* **2011**, *12*, 655–662.

82. Rossy, J.; Owen, D.M.; Williamson, D.J.; Yang, Z.; Gaus, K. Conformational States of the Kinase Lck Regulate Clustering in Early T Cell Signaling. *Nature Immunology* **2013**, *14*, 82–89.

83. Pageon, S.V.; Tabarin, T.; Yamamoto, Y.; Ma, Y.; Bridgeman, J.S.; Cohnen, A.; Benzing, C.; Gao, Y.; Crowther, M.D.; Tungatt, K.; et al. Functional Role of T-Cell Receptor Nanoclusters in Signal Initiation and Antigen Discrimination. *Proceedings of the National Academy of Sciences of the United States of America* **2016**, *113*.

84. Hu, Y.S.; Cang, H.; Lillemeier, B.F. Superresolution Imaging Reveals Nanometer- and Micrometer-Scale Spatial Distributions of T-Cell Receptors in Lymph Nodes. *Proceedings of the National Academy of Sciences of the United States of America* **2016**, *113*, 7201–7206.

85. Schleinitz, N.; March, M.E.; Long, E.O. Recruitment of Activation Receptors at Inhibitory NK Cell Immune Synapses. *PLoS ONE* **2008**, *3*, 1–7.

86. Oszmiana, A.; Williamson, D.J.; Cordoba, S.-P.; Morgan, D.J.; Kennedy, P.R.; Stacey, K.; Davis, D.M. The Size of Activating and Inhibitory Killer Ig-like Receptor Nanoclusters Is Controlled by the Transmembrane Sequence and Affects Signaling. *Cell Reports* **2016**, *15*, 1957–1972.

87. Kennedy, P.R.; Barthen, C.; Williamson, D.J.; Pitkeathly, W.T.E.; Hazime, K.S.; Cumming, J.; Stacey, K.B.; Hilton, H.G.; Carrington, M.; Parham, P.; et al. Genetic Diversity Affects the Nanoscale Membrane Organization and Signaling of Natural Killer Cell Receptors. *Science Signaling* **2019**, *12*.

88. Pageon, S. v; Cordoba, S.-P.; Owen, D.M.; Rothery, S.M.; Oszmiana, A.; Davis, D.M. Superresolution Microscopy Reveals Nanometer-Scale Reorganization of Inhibitory Natural Killer Cell Receptors upon Activation of NKG2D. *Science Signaling* **2013**, *6*, ra62.

89. Hadad, U.; Thauland, T.J.; Martinez, O.M.; Butte, M.J.; Porgador, A.; Krams, S.M. NKp46 Clusters at the Immune Synapse and Regulates NK Cell Polarization. *Frontiers in Immunology* **2015**, *6*, 495.

90. Baumgart, F.; Arnold, A.M.; Rossboth, B.K.; Brameshuber, M.; Schütz, G.J. What We Talk about When We Talk about Nanoclusters. *Methods and Applications in Fluorescence* **2018**, *7*, 013001.

91. Dunn, G.P.; Bruce, A.T.; Ikeda, H.; Old, L.J.; Schreiber, R.D. Cancer Immunoediting: From Immunosurveillance to Tumor Escape. *Nature Immunology* **2002**, *3*, 991–998.

92. Zitvogel, L.; Tesniere, A.; Kroemer, G. Cancer despite Immunosurveillance: Immunoselection and Immunosubversion. *Nature Reviews Immunology* **2006**, *6*, 715–727.

93. Dunn, G.P.; Old, L.J.; Schreiber, R.D. The Three Es of Cancer Immunoediting. *Annual Review of Immunology* **2004**, *22*, 329–360.

94. Vesely, M.D.; Kershaw, M.H.; Schreiber, R.D.; Smyth, M.J. Natural Innate and Adaptive Immunity to Cancer. *Annual Review of Immunology* **2011**, *29*, 235–271.

95. Schreiber, R.D.; Old, L.J.; Smyth, M.J. Cancer Immunoediting: Integrating Immunity's Roles in Cancer Suppression and Promotion. *Science* **2011**, *331*, 1565–1570.

96. Beatty, G.L.; Gladney, W.L. Immune Escape Mechanisms as a Guide for Cancer Immunotherapy. *Clinical Cancer Research* **2015**, *21*, 687–692.

97. Khong, H.T.; Wang, Q.J.; Rosenberg, S.A. Identification of Multiple Antigens Recognized by Tumor-Infiltrating Lymphocytes from a Single Patient: Tumor Escape by Antigen Loss and Loss of MHC Expression. *Journal of Immunotherapy* **2004**, *27*, 184–190.

98. Sconocchia, G.; Eppenberger-Castori, S.; Zlobec, I.; Karamitopoulou, E.; Arriga, R.; Coppola, A.; Caratelli, S.; Spagnoli, G.C.; Lauro, D.; Lugli, A.; et al. HLA Class II Antigen Expression in Colorectal Carcinoma Tumors as a Favorable Prognostic Marker. *Neoplasia (United States)* **2014**, *16*, 31–42.

99. Stern-Ginossar, N.; Gur, C.; Biton, M.; Horwitz, E.; Elboim, M.; Stanietsky, N.; Mandelboim, M.; Mandelboim, O. Human MicroRNAs Regulate Stress-Induced Immune Responses Mediated by the Receptor NKG2D. *Nature Immunology* **2008**, *9*, 1065–1073.

100. Taube, J.M.; Anders, R.A.; Young, G.D.; Xu, H.; Sharma, R.; McMiller, T.L.; Chen, S.; Klein, A.P.; Pardoll, D.M.; Topalian, S.L.; et al. Colocalization of Inflammatory Response with B7-H1 Expression in Human Melanocytic Lesions Supports an Adaptive Resistance Mechanism of Immune Escape. *Science Translational Medicine* **2012**, *4*, 1–22.

101. Tripathi, P.; Agrawal, S. Non-Classical HLA-G Antigen and Its Role in the Cancer Progression. *Cancer Investigation* **2006**, *24*, 178–186.

102. Hui, L.; Chen, Y. Tumor Microenvironment: Sanctuary of the Devil. *Cancer Letters* **2015**, *368*, 7–13.

103. Farkona, S.; Diamandis, E.P.; Blasutig, I.M. Cancer Immunotherapy: The Beginning of the End of Cancer? *BMC Medicine* 2016, *14*, 73.

104. Yaddanapudi, K.; Mitchell, R.A.; Eaton, J.W. Cancer Vaccines: Looking to the Future. *OncoImmunology* **2013**, *2*, 37–41.

105. Hinrichs, C.S.; Rosenberg, S.A. Exploiting the Curative Potential of Adoptive T-Cell Therapy for Cancer. *Immunological Reviews* **2014**, *257*, 56–71.

106. Leach, D.R.; Krummel, M.F.; Allison, J.P. Enhancement of Antitumor Immunity by CTLA-4 Blockade. *Science* **1996**, *271*, 1734–1736.

107. Shin, J.H.; Park, H.B.; Choi, K. Enhanced Anti-Tumor Reactivity of Cytotoxic T Lymphocytes Expressing PD-1 Decoy. *Immune Network* **2016**, *16*, 134.

108. Peipp, M.; Wesch, D.; Oberg, H.-H.; Lutz, S.; Muskulus, A.; van de Winkel, J.G.J.; Parren, P.W.H.I.; Burger, R.; Humpe, A.; Kabelitz, D.; et al. CD20-Specific Immunoligands Engaging NKG2D Enhance Γδ T Cell-Mediated Lysis of Lymphoma Cells. *Scandinavian Journal of Immunology* **2017**, *86*, 196–206.

109. Tusell Wennier, S.; Liu, J.; McFadden, G. Bugs and Drugs: Oncolytic Virotherapy in Combination with Chemotherapy. *Current Pharmaceutical Biotechnology* **2012**, *13*, 1817–1833.

110. Vivier, E.; Ugolini, S.; Blaise, D.; Chabannon, C.; Brossay, L. Targeting Natural Killer Cells and Natural Killer T Cells in Cancer. *Nature Reviews Immunology* **2012**, *12*, 239–252.

111. Karre, K.; Ljunggren, H.G.; Piontek, G.; Kiessling, R. Selective Rejection of H-2-Deficient Lymphoma Variants Suggests Alternative Immune Defence Strategy. *Nature* **1986**, *319*, 675–678.

112. Shimasaki, N.; Jain, A.; Campana, D. NK Cells for Cancer Immunotherapy. *Nature Reviews Drug Discovery* **2020**, *19*, 200–218.

113. El-Gazzar, A.; Groh, V.; Spies, T. Immunobiology and Conflicting Roles of the Human NKG2D Lymphocyte Receptor and Its Ligands in Cancer. *The Journal of Immunology* **2013**, *191*, 1509–1515.

114. Habif, G.; Crinier, A.; André, P.; Vivier, E.; Narni-Mancinelli, E. Targeting Natural Killer Cells in Solid Tumors. *Cellular & Molecular Immunology* **2019**, *16*, 415–422.

115. Riggan, L.; Shah, S.; O'Sullivan, T.E. Arrested Development: Suppression of NK Cell Function in the Tumor Microenvironment. *Clinical & Translational Immunology* **2021**, *10*, 1–17.

116. Matta, J.; Baratin, M.; Chiche, L.; Forel, J.M.; Cognet, C.; Thomas, G.; Farnarier, C.; Piperoglou, C.; Papazian, L.; Chaussabel, D.; et al. Induction of B7-H6, a Ligand for the Natural Killer Cell-Activating Receptor NKp30, in Inflammatory Conditions. *Blood* **2013**, *122*, 394–404.

117. Schlecker, E.; Fiegler, N.; Arnold, A.; Altevogt, P.; Rose-John, S.; Moldenhauer, G.; Sucker, A.; Paschen, A.; von Strandmann, E.P.; Textor, S.; et al. Metalloprotease-Mediated Tumor Cell Shedding of B7-H6, the Ligand of the Natural Killer Cell-Activating Receptor NKp30. *Cancer research* **2014**, *74*, 3429–3440.

118. de Andrade, L.F.; En Tay, R.; Pan, D.; Luoma, A.M.; Ito, Y.; Badrinath, S.; Tsoucas, D.; Franz, B.; May, K.F.; Harvey, C.J.; et al. Antibody-Mediated Inhibition of MICA and MICB Shedding Promotes NK Cell-Driven Tumor Immunity. *Science* **2018**, *359*, 1537–1542.

119. Garber, K. Natural Killer Cells Blaze into Immuno-Oncology. *Nature biotechnology* **2016**, *34*, 219–220.

120. Khan, M.; Arooj, S.; Wang, H. NK Cell-Based Immune Checkpoint Inhibition. *Frontiers in Immunology* **2020**, *11*, 167.

121. Morvan, M.G.; Lanier, L.L. NK Cells and Cancer: You Can Teach Innate Cells New Tricks. *Nature Reviews Cancer* **2016**, *16*, 7–19.

122. Kundu, S.; Gurney, M.; O'Dwyer, M. Generating Natural Killer Cells for Adoptive Transfer: Expanding Horizons. *Cytotherapy* **2021**, *23*, 559–566.

123. Liu, M.; Meng, Y.; Zhang, L.; Han, Z.; Feng, X. High-Efficient Generation of Natural Killer Cells from Peripheral Blood with Preferable Cell Vitality and Enhanced Cytotoxicity by Combination of IL-2, IL-15 and IL-18. *Biochemical and Biophysical Research Communications* **2021**, *534*, 149–156.

124. Rezaeifard, S.; Heike, Y.; Masuyama, J.-I.; Rezvani, A.; Vojdani, R.; Erfani, N. Autologous Natural Killer Cell-Enrichment for Immune Cell Therapy: Preclinical

Setting Phase, Shiraz Experience. *Iranian Journal of Allergy, Asthma and Immunology* **2021**, *20*, 233–243.

125. Phan, M.-T.T.; Lee, S.-H.; Kim, S.-K.; Cho, D. Expansion of NK Cells Using Genetically Engineered K562 Feeder Cells. In *Methods in Molecular Biology*; 2016; Vol. 1441, pp. 167–174.

126. Ruggeri, L. Effectiveness of Donor Natural Killer Cell Alloreactivity in Mismatched Hematopoietic Transplants. *Science* **2002**, *295*, 2097–2100.

127. Bachiller, M.; Battram, A.M.; Perez-Amill, L.; Martín-Antonio, B. Natural Killer Cells in Immunotherapy: Are We Nearly There? *Cancers* **2020**, *12*, 3139.

128. Pfefferle, A.; Huntington, N.D. You Have Got a Fast CAR: Chimeric Antigen Receptor NK Cells in Cancer Therapy. *Cancers* **2020**, *12*, 706.

129. Romanski, A.; Uherek, C.; Bug, G.; Seifried, E.; Klingemann, H.; Wels, W.S.; Ottmann, O.G.; Tonn, T. CD19-CAR Engineered NK-92 Cells Are Sufficient to Overcome NK Cell Resistance in B-Cell Malignancies. *Journal of Cellular and Molecular Medicine* **2016**, *20*, 1287–1294.

130. Liu, E.; Marin, D.; Banerjee, P.; Macapinlac, H.A.; Thompson, P.; Basar, R.; Nassif Kerbauy, L.; Overman, B.; Thall, P.; Kaplan, M.; et al. Use of CAR-Transduced Natural Killer Cells in CD19-Positive Lymphoid Tumors. *New England Journal of Medicine* **2020**, *382*, 545–553.

131. Davis, Z.B.; Vallera, D.A.; Miller, J.S.; Felices, M. Natural Killer Cells Unleashed: Checkpoint Receptor Blockade and BiKE/TriKE Utilization in NK-Mediated Anti-Tumor Immunotherapy. *Seminars in Immunology* **2017**, *31*, 64–75.

132. Chauhan, S.K.S.; Koehl, U.; Kloess, S. Harnessing NK Cell Checkpoint-Modulating Immunotherapies. *Cancers* **2020**, *12*, 1807.

133. Nayyar, G.; Chu, Y.; Cairo, M.S. Overcoming Resistance to Natural Killer Cell Based Immunotherapies for Solid Tumors. *Frontiers in Oncology* **2019**, *9*, 1–28.

134. Kwok, G.; Yau, T.C.C.; Chiu, J.W.; Tse, E.; Kwong, Y. Pembrolizumab (Keytruda). *Human Vaccines & Immunotherapeutics* **2016**, *12*, 2777–2789.

135. Gil-Bazo, I. Avelumab—a New Programmed Death-Ligand 1 Inhibitor against Advanced Non-Small Cell Lung Cancer. *Translational Lung Cancer Research* **2017**, *6*, S35–S38.

136. André, P.; Denis, C.; Soulas, C.; Bourbon-Caillet, C.; Lopez, J.; Arnoux, T.; Bléry, M.; Bonnafous, C.; Gauthier, L.; Morel, A.; et al. Anti-NKG2A MAb Is a Checkpoint Inhibitor That Promotes Anti-Tumor Immunity by Unleashing Both T and NK Cells. *Cell* **2018**, *175*, 1731-1743.e13.

137. Yalniz, F.F.; Daver, N.; Rezvani, K.; Kornblau, S.; Ohanian, M.; Borthakur, G.; DiNardo, C.D.; Konopleva, M.; Burger, J.; Gasior, Y.; et al. A Pilot Trial of Lirilumab With or Without Azacitidine for Patients With Myelodysplastic Syndrome. *Clinical Lymphoma Myeloma and Leukemia* **2018**, *18*, 658-663.e2.

138. de Gramont, A.; Faivre, S.; Raymond, E. Novel TGF-β Inhibitors Ready for Prime Time in Onco-Immunology. *OncoImmunology* **2017**, *6*, e1257453.

139. Shevtsov, M.; Multhoff, G. Immunological and Translational Aspects of NK Cell-Based Antitumor Immunotherapies. *Frontiers in Immunology* **2016**, *7*, 1–9.

140. Kohrt, H.; Rajasekaran, N.; Chester, C.; Yonezawa, A.; Zhao, X. Enhancement of Antibody-Dependent Cell Mediated Cytotoxicity: A New Era in Cancer Treatment. *ImmunoTargets and Therapy* **2015**, *4*, 91–100.

141. Arnon, T.I.; Markel, G.; Bar-Ilan, A.; Hanna, J.; Fima, E.; Benchetrit, F.; Galili, R.; Cerwenka, A.; Benharroch, D.; Sion-Vardy, N.; et al. Harnessing Soluble NK

Cell Killer Receptors for the Generation of Novel Cancer Immune Therapy. *PLoS ONE* **2008**, *3*, e2150.

142. Deng, G.; Zheng, X.; Zhou, J.; Wei, H.; Tian, Z.; Sun, R. Generation and Preclinical Characterization of an NKp80-Fc Fusion Protein for Redirected Cytolysis of Natural Killer (NK) Cells against Leukemia. *Journal of Biological Chemistry* **2015**, *290*, 22474–22484.

143. Felices, M.; Lenvik, T.R.; Davis, Z.B.; Miller, J.S.; Vallera, D.A. Generation of BiKEs and TriKEs to Improve NK Cell-Mediated Targeting of Tumor Cells. *Methods in Molecular Biology* **2016**, *1441*, 333–346.

144. Gleason, M.K.; Ross, J.A.; Warlick, E.D.; Lund, T.C.; Verneris, M.R.; Wiernik, A.; Spellman, S.; Haagenson, M.D.; Lenvik, A.J.; Litzow, M.R.; et al. CD16xCD33 Bispecific Killer Cell Engager (BiKE) Activates NK Cells against Primary MDS and MDSC CD33+ Targets. *Blood* **2014**, *123*, 3016–3026.

145. Schmohl, J.U.; Felices, M.; Taras, E.; Miller, J.S.; Vallera, D.A. Enhanced ADCC and NK Cell Activation of an Anticarcinoma Bispecific Antibody by Genetic Insertion of a Modified IL-15 Cross-Linker. *Molecular Therapy* **2016**, *24*, 1312–1322.

146. Sarhan, D.; Brandt, L.; Felices, M.; Guldevall, K.; Lenvik, T.; Hinderlie, P.; Curtsinger, J.; Warlick, E.; Spellman, S.R.; Blazar, B.R.; et al. 161533 TriKE Stimulates NK-Cell Function to Overcome Myeloid-Derived Suppressor Cells in MDS. *Blood Advances* **2018**, *2*, 1459–1469.

147. Schmohl, J.U.; Felices, M.; Todhunter, D.; Taras, E.; Miller, J.S.; Vallera, D.A. Tetraspecific ScFv Construct Provides NK Cell Mediated ADCC and Self-Sustaining Stimuli via Insertion of IL-15 as a Cross-Linker. *Oncotarget* **2016**, *7*, 73830–73844.

148. Demaria, O.; Gauthier, L.; Debroas, G.; Vivier, E. Natural Killer Cell Engagers in Cancer Immunotherapy: Next Generation of Immuno-oncology Treatments. *European Journal of Immunology* **2021**, *51*, 1934–1942.

149. Ding, H.; Yang, X.; Wei, Y. Fusion Proteins of NKG2D/NKG2DL in Cancer Immunotherapy. *International Journal of Molecular Sciences* **2018**, *19*, 1–14.

150. Märklin, M.; Hagelstein, I.; Koerner, S.P.; Rothfelder, K.; Pfluegler, M.S.; Schumacher, A.; Grosse-Hovest, L.; Jung, G.; Salih, H.R. Bispecific NKG2D-CD3 and NKG2D-CD16 Fusion Proteins for Induction of NK and T Cell Reactivity against Acute Myeloid Leukemia. *Journal for ImmunoTherapy of Cancer* **2019**, *7*, 143.

151. Han, Y.; Sun, F.; Zhang, X.; Wang, T.; Jiang, J.; Cai, J.; Gao, Q.; Hezam, K.; Liu, Y.; Xie, J.; et al. CD24 Targeting Bi-Specific Antibody That Simultaneously Stimulates NKG2D Enhances the Efficacy of Cancer Immunotherapy. *Journal of Cancer Research and Clinical Oncology* **2019**, *145*, 1179–1190.

152. Kellner, C.; Günther, A.; Humpe, A.; Repp, R.; Klausz, K.; Derer, S.; Valerius, T.; Ritgen, M.; Brüggemann, M.; van de Winkel, J.G.; et al. Enhancing Natural Killer Cell-Mediated Lysis of Lymphoma Cells by Combining Therapeutic Antibodies with CD20-Specific Immunoligands Engaging NKG2D or NKp30. *OncoImmunology* **2016**, *5*, e1058459.

153. Kellner, C.; Maurer, T.; Hallack, D.; Repp, R.; van de Winkel, J.G.J.; Parren, P.W.H.I.; Valerius, T.; Humpe, A.; Gramatzki, M.; Peipp, M. Mimicking an Induced Self Phenotype by Coating Lymphomas with the NKp30 Ligand B7-H6

Promotes NK Cell Cytotoxicity. *The Journal of Immunology* **2012**, *189*, 5037–5046.

154.   Peipp, M.; Derer, S.; Lohse, S.; Staudinger, M.; Klausz, K.; Valerius, T.; Gramatzki, M.; Kellner, C. HER2-Specific Immunoligands Engaging NKp30 or NKp80 Trigger NK-Cell-Mediated Lysis of Tumor Cells and Enhance Antibody-Dependent Cell-Mediated Cytotoxicity. *Oncotarget* **2015**, *6*, 32075–32088.

155.   Pekar, L.; Klausz, K.; Busch, M.; Valldorf, B.; Kolmar, H.; Wesch, D.; Oberg, H.; Krohn, S.; Boje, A.S.; Gehlert, C.L.; et al. Affinity Maturation of B7-H6 Translates into Enhanced NK Cell–Mediated Tumor Cell Lysis and Improved Proinflammatory Cytokine Release of Bispecific Immunoligands via NKp30 Engagement. *The Journal of Immunology* **2021**, *206*, 225–236.

156.   de Marco, A. Recombinant Expression of Nanobodies and Nanobody-Derived Immunoreagents. *Protein Expression and Purification* **2020**, *172*.

157.   Nettleship, J.E.; Assenberg, R.; Diprose, J.M.; Rahman-Huq, N.; Owens, R.J. Recent Advances in the Production of Proteins in Insect and Mammalian Cells for Structural Biology. *Journal of Structural Biology* **2010**, *172*, 55–65.

158.   Pimlott, N.J.; Miller, R.G. The Use of Tunicamycin to Study the Role of Cell Surface Oligosaccharides in Lymphocyte Recognition. *The Journal of Immunology* **1986**, *137*, 2455–9.

159.   Pulix, M.; Lukashchuk, V.; Smith, D.C.; Dickson, A.J. Molecular Characterization of HEK293 Cells as Emerging Versatile Cell Factories. *Current Opinion in Biotechnology* **2021**, *71*, 18–24.

160.   Joyce, M.G.; Tran, P.; Zhuravleva, M. a; Jaw, J.; Colonna, M.; Sun, P.D. Crystal Structure of Human Natural Cytotoxicity Receptor NKp30 and Identification of Its Ligand Binding Site. *Proceedings of the National Academy of Sciences of the United States of America* **2011**, *108*, 6223–6228.

161.   Nettleship, J.E. Structural Biology of Glycoproteins. In *Glycosylation*; Petrescu, S., Ed.; IntechOpen, 2012.

162.   Grueninger-Leitch, F.; D'Arcy, A.; D'Arcy, B.; Chène, C. Deglycosylation of Proteins for Crystallization Using Recombinant Fusion Protein Glycosidases. *Protein Science* **1996**, *5*, 2617–2622.

163.   Bláha, J.; Pachl, P.; Novák, P.; Vaněk, O. Expression and Purification of Soluble and Stable Ectodomain of Natural Killer Cell Receptor LLT1 through High-Density Transfection of Suspension Adapted HEK293S GnTI⁻ Cells. *Protein Expression and Purification* **2015**, *109*, 7–13.

164.   Vaněk, O.; Celadova, P.; Skořepa, O.; Bláha, J.; Kalousková, B.; Dvorská, A.; Poláchová, E.; Pucholtová, H.; Kavan, D.; Pompach, P.; et al. Production of Recombinant Soluble Dimeric C-Type Lectin-like Receptors of Rat Natural Killer Cells. *Scientific Reports* **2019**, *9*, 17836.

165.   Backliwal, G.; Hildinger, M.; Kuettel, I.; Delegrange, F.; Hacker, D.L.; Wurm, F.M. Valproic Acid: A Viable Alternative to Sodium Butyrate for Enhancing Protein Expression in Mammalian Cell Cultures. *Biotechnology and Bioengineering* **2008**, *101*, 182–189.

166.   Kalouskova, B.; Skořepa, O.; Cmunt, D.; Abreu, C.; Krejčová, K.; Bláha, J.; Sieglová, I.; Král, V.; Fábry, M.; Pola, R.; et al. Tumor Marker B7-H6 Bound to the Coiled Coil Peptide-Polymer Conjugate Enables Targeted Therapy by Activating Human Natural Killer Cells. *Biomedicines* **2021**, *9*, 1597.

167. Jäger, V.; Büssow, K.; Schirrmann, T. Transient Recombinant Protein Expression in Mammalian Cells. In *Animal Cell Culture*; Al-Rubeai, M., Ed.; Springer, 2015; pp. 27–64.

168. Mastrangelo, A.J.; Betenbaugh, M.J. Overcoming Apoptosis: New Methods for Improving Protein-Expression Systems. *Trends in Biotechnology* **1998**, *16*, 88–95.

169. Peter, M.; Herskowitz, I. Joining the Complex: Cyclin-Dependent Kinase Inhibitory Proteins and the Cell Cycle. *Cell* **1994**, *79*, 181–184.

170. Backliwal, G.; Hildinger, M.; Chenuet, S.; DeJesus, M.; Wurm, F.M. Coexpression of Acidic Fibroblast Growth Factor Enhances Specific Productivity and Antibody Titers in Transiently Transfected HEK293 Cells. *New Biotechnology* **2008**, *25*, 162–166.

171. Poláchová, E. Optimization of HEK293 Cell Line Expression System by Regulation of Cell Cycle and Apoptosis, Master's thesis, Faculty of Science, Charles University, Prague, **2014**.

172. Durocher, Y. High-Level and High-Throughput Recombinant Protein Production by Transient Transfection of Suspension-Growing Human 293-EBNA1 Cells. *Nucleic Acids Research* **2002**, *30*, E9.

173. Zufferey, R.; Donello, J.E.; Trono, D.; Hope, T.J. Woodchuck Hepatitis Virus Posttranscriptional Regulatory Element Enhances Expression of Transgenes Delivered by Retroviral Vectors. *Journal of virology* **1999**, *73*, 2886–92.

174. Bláha, J.; Kalousková, B.; Skořepa, O.; Pažický, S.; Novák, P.; Vaněk, O. High-Level Expression and Purification of Soluble Form of Human Natural Killer Cell Receptor NKR-P1 in HEK293S GnTI⁻ Cells. *Protein Expression and Purification* **2017**, *140*, 36–43.

175. Nettleship, J.E.; Rada, H.; Owens, R.J. Overview of a high-throughput pipeline for streamlining the production of recombinant proteins. In *High-Throughput Protein Production and Purification*; Vincentelli, R., Ed.; Springer, 2019; Vol. 2025, pp. 33–49.

176. Li, Z.; Michael, I.P.; Zhou, D.; Nagy, A.; Rini, J.M. Simple PiggyBac Transposon-Based Mammalian Cell Expression System for Inducible Protein Production. *Proceedings of the National Academy of Sciences* **2013**, *110*, 5004–5009.

177. Yusa, K.; Zhou, L.; Li, M.A.; Bradley, A.; Craig, N.L. A Hyperactive PiggyBac Transposase for Mammalian Applications. *Proceedings of the National Academy of Sciences* **2011**, *108*, 1531–1536.

178. Kalousková, B. Preparation of Human NK Cell Receptor NKp80 and Its Ligand AICL, Master's thesis, Faculty of Science, Charles University, Prague, **2016**.

179. Skořepa, O. Structural Studies of Rat NK Cell Receptor NKR-P1B and Its Ligand Clrb, Master's thesis, Faculty of Science, Charles University, Prague, **2016**.

180. Adámková, L.; Kvíčalová, Z.; Rozbeský, D.; Kukačka, Z.; Adámek, D.; Cebecauer, M.; Novák, P. Oligomeric Architecture of Mouse Activating Nkrp1 Receptors on Living Cells. *International Journal of Molecular Sciences* **2019**, *20*, 1884.

181. Hernychová, L.; Rosůlek, M.; Kádek, A.; Mareška, V.; Chmelík, J.; Adámková, L.; Grobárová, V.; Šebesta, O.; Kukačka, Z.; Skála, K.; et al. The C-Type Lectin-like Receptor Nkrp1b: Structural Proteomics Reveals Features Affecting Protein Conformation and Interactions. *Journal of Proteomics* **2019**, *196*, 162–172.

182. Balaji, G.R.; Aguilar, O.A.; Tanaka, M.; Shingu-Vazquez, M.A.; Fu, Z.; Gully, B.S.; Lanier, L.L.; Carlyle, J.R.; Rossjohn, J.; Berry, R. Recognition of Host Clr-b

by the Inhibitory NKR-P1B Receptor Provides a Basis for Missing-Self Recognition. *Nature Communications* **2018**, *9*.

183. Jeong, H.-J.; Abhiraman, G.C.; Story, C.M.; Ingram, J.R.; Dougan, S.K. Generation of Ca2+-Independent Sortase A Mutants with Enhanced Activity for Protein and Cell Surface Labeling. *PLOS ONE* **2017**, *12*, e0189068.

184. Cmunt, D. Preparation of Fusion Domains of Human Immunoreceptors for Their Utilization in Immunotherapy, Master's thesis, Faculty of Science, Charles University, Prague, **2019**.

185. Pechar, M.; Pola, R.; Laga, R.; Ulbrich, K.; Bednárová, L.; Maloň, P.; Sieglová, I.; Král, V.; Fábry, M.; Vaněk, O. Coiled Coil Peptides as Universal Linkers for the Attachment of Recombinant Proteins to Polymer Therapeutics. *Biomacromolecules* **2011**, *12*, 3645–3655.

186. Skálová, T.; Bláha, J.; Harlos, K.; Dušková, J.; Koval', T.; Stránský, J.; Hašek, J.; Vaněk, O.; Dohnálek, J. Four Crystal Structures of Human LLT1, a Ligand of Human NKR-P1, in Varied Glycosylation and Oligomerization States. *Acta Crystallographica Section D Biological Crystallography* **2015**, *71*, 578–591.

187. Li, Y.; Wang, Q.; Chen, S.; Brown, P.H.; Mariuzza, R.A. Structure of NKp65 Bound to Its Keratinocyte Ligand Reveals Basis for Genetically Linked Recognition in Natural Killer Gene Complex. *Proceedings of the National Academy of Sciences* **2013**, *110*, 11505–11510.

188. van de Linde, S.; Löschberger, A.; Klein, T.; Heidbreder, M.; Wolter, S.; Heilemann, M.; Sauer, M. Direct Stochastic Optical Reconstruction Microscopy with Standard Fluorescent Probes. *Nature Protocols* **2011**, *6*, 991–1009.

189. Andronov, L.; Orlov, I.; Lutz, Y.; Vonesch, J.-L.; Klaholz, B.P. ClusterViSu, a Method for Clustering of Protein Complexes by Voronoi Tessellation in Super-Resolution Microscopy. *Scientific Reports* **2016**, *6*, 24084.

7 SELECTED PUBLICATIONS

7.1 PUBLICATION NO. 1

Bláha, J.; Kalousková, B.; Skořepa, O.; Pažický, S.; Novák, P.; Vaněk, O.

High-level expression and purification of soluble form of human natural killer cell receptor NKR-P1 in HEK293S GnTI⁻ cells.

My contribution to the publication:

Performing research (cell culture maintenance, transfection optimization, protein expression, protein purification, and quality control)

ELSEVIER

High-level expression and purification of soluble form of human natural killer cell receptor NKR-P1 in HEK293S GnTI⁻ cells

CrossMark

Jan Bláha [a], Barbora Kaloušková [a], Ondřej Skořepa [a], Samuel Pažický [a], Petr Novák [a, b], Ondřej Vaněk [a, *]

[a] Department of Biochemistry, Faculty of Science, Charles University, Hlavova 2030/8, 12840 Prague, Czech Republic
[b] Institute of Microbiology, The Czech Academy of Sciences, BIOCEV, Průmyslová 595, 25250 Vestec, Czech Republic

ARTICLE INFO

ABSTRACT

Human natural killer receptor protein 1 (NKR-P1, CD161, gene *klrb1*) is a C-type lectin-like receptor of natural killer (NK) cells responsible for recognition of its cognate protein ligand lectin-like transcript 1 (LLT1). NKR-P1 is the single human orthologue of the prototypical rodent NKR-P1 receptors. Naturally, human NKR-P1 is expressed on the surface of NK cells, where it serves as inhibitory receptor; and on T and NKT cells functioning as co-stimulatory receptor promoting secretion of IFNγ. Most notably, it is expressed on Th17 and Tc17 lymphocytes where presumably promotes targeting into LLT1 expressing immunologically privileged niches. We tested effect of different protein tags (SUMO, TRX, GST, MsyB) on expression of soluble NKR-P1 in *E. coli*. Then we optimized the expression construct of soluble NKR-P1 by preparing a library of expression constructs in pOPING vector containing the extracellular lectin-like domain with different length of the putative *N*-terminal stalk region and tested its expression in Sf9 and HEK293 cells. Finally, a high-level expression of soluble NKR-P1 was achieved by stable expression in suspension-adapted HEK293S GnTI⁻ cells utilizing pOPINGTTneo expression vector. Purified soluble NKR-P1 is homogeneous, deglycosylatable, crystallizable and monomeric in solution, as shown by size-exclusion chromatography, multi-angle light scattering and analytical ultracentrifugation.

© 2017 Elsevier Inc. All rights reserved.

1. Introduction

Natural killer (NK) cells are large granular lymphocytes described to be on the functional borderline of innate and adaptive immunity [1,2]. They are mainly recognized for their singular ability to provide defence against viral infection and tumour development without prior antigen sensitization [3], but they also contribute to the regulation of the adaptive system via secretion of cytokines [1] and are even able to form antigen specific immunologic memory [4—6]. NK cell activity is controlled by a fine balance of signals from its variety of inhibitory and activating receptors [3] that engage a broad range of health and disease markers in the accepted "missing-self" and "induced-self" modes of recognition,

respectively [7—11].

NK cell receptors are divided into the immunoglobulin-like [12] and the C-type lectin-like (CTL) structural classes [13,14]. C-type lectins bind calcium and carbohydrates; however, CTL receptors recognize protein ligands instead, despite the fact that they are homologous to C-type lectins [15,16]. The NKR-P1 receptor family, encoded in the Natural Killer Cell (NKC) gene complex (human chromosome 12), encompasses the prototypical NK cell receptors belonging to the CTL class [15]. Unlike many CTL NK receptors that are recognizing MHC class I glycoproteins [14,17,18], NKR-P1 receptors interact with a genetically and structurally highly related ligands from *clec2* gene subfamily [13].

Human NKR-P1 (CD161, gene *klrb1*) was identified in 1994 as a human orthologue of rodent NKR-P1 receptors [19] and up to now remains the only described human NKR-P1 receptor. However, human NK receptors from the *klrf* subfamily — i.e. NKp65 [20] and NKp80 [21] share distinct similarity to NKR-P1 and were proposed to represent activating counterparts of human NKR-P1 [13,22].

Apart from NK cells, human NKR-P1 was found to be expressed on NKT cells [23] and subpopulations of T lymphocytes [24]. Most

notably, human NKR-P1 is present on regulatory T cells [25] and is currently recognized to be a marker for all Th17 cells [26]. It was found also on some Tc17 cells [27] which are being more and more implicated in autoimmune diseases like multiple sclerosis [28], rheumatoid arthritis [29] and Crohn's disease [30]. It was proposed that NKR-P1 could play a role in targeting of these lymphocytes and promote transendothelial extravasation into immunologically privileged niches [26,31—34].

Under homeostasis NKR-P1 functions as inhibitory receptor of NK cells [19,35,36] and co-stimulatory receptor of NKT and T cells [35,37] promoting secretion of IFNγ. However, it was also described that the inhibitory function of human NKR-P1 is in an undesirable way exploited by glioblastomas [38] and B-cell Non-Hodgkin's lymphomas [39] which overexpress the NKR-P1 physiological ligand — lectin-like transcript 1 (LLT1, gene *clec2d*) [35,36,40,41] and thus escape immune response.

From a protein point of view, human NKR-P1 shares common CTL receptor features. It was identified as a homodimeric type II. transmembrane glycoprotein lacking O-linked glycosylation [19]. Its short intracellular portion contains an immunoreceptor tyrosine-based inhibitory motif that is noncanonical for the presence of alanine residue in the −2 position relative to the tyrosine residue [42]. A transmembrane helix is followed by 25 residues long stalk region that presumably functions as a flexible linker providing a scaffold for cystine homodimerization and a C-terminal CTL domain that itself contains 6 conserved cysteine residues stabilizing this domain by formation of three intramolecular disulphide bridges [14].

Although there have been recently promising results for refolding of murine NKR-P1 receptors from inclusion bodies produced in *E. coli* [43,44], so far only an unsuccessful renaturation of the human orthologue have been reported [45]. Mammalian cell lines were used previously to express full-length human NKR-P1 receptor or its extracellular part in low-scale for immunological studies [35,36,40,41] or surface plasmon resonance measurements [45], respectively. Here we present an optimization of the human NKR-P1 ectodomain expression in different expression systems and finally an utilization of HEK293S GnTI⁻ cells [46] for generation of stably transfected cell line that provides a high yield of soluble human NKR-P1 ectodomain usable for structural studies.

2. Material and methods

2.1. Vectors and NKR-P1 library cloning

A cDNA clone (GenBank accession no. BC114516) containing the entire coding sequence of *klrb1* gene was obtained from Source BioScience (GenomeCUBE IRCMp5012E0732D). A library of NKR-P1 stalk region deletion expression vectors was constructed by In-Fusion cloning at the Oxford Protein Production Facility (OPPF; Oxford, UK) as described before [47,48]. Primers used for amplification of the selected NKR-P1 constructs from the cDNA clone contained In-Fusion overlaps at the 5′ of the specific forward and the reverse primers as described in supplementary data, Table S1. For transient expression in HEK293 cells, NKR-P1 ectodomain (G90-S225) was amplified from the cDNA clone using 5′−AAAAAAACCGGTGGTCTCTTAAACTGCCCAATATATTG−3′ and 5′−AAAAAAGGTACCAGAGTCAGGATACACTTTATTTCTCAC−3′ and using *Age*I and *Kpn*I sites subcloned into pTT28 expression plasmid (kindly provided by Dr. Yves Durocher; a derivative of pTT5 [49] containing N-terminal secretion leader and C-terminal His₈-tag sequence, thus leaving ITG- and -GTKHHHHHHHHG at expressed protein N-and C-termini).

2.2. Small-scale NKR-P1 expression tests

Expression of the library of stalk region deletion constructs was performed at OPPF following standard OPPF protocols for high-throughput expression testing in *E. coli* [50] and Sf9 cells [51] as described before.

Briefly, for prokaryotic expression 150 μl of overnight cultures grown from selected colony of *E. coli* Rosetta2(DE3) pLysS or B834(DE3) strains (both Novagen) transformed with the given expression plasmid were used for inoculation of 3 ml of Power Broth (Molecular Dimensions) and Overnight Express Instant TB Medium (TBONEX; Novagen) with an appropriate antibiotic in 24-well deep well blocks. The blocks were shaken at 37 °C until an average OD_{595} reached ca 0.5. The Power Broth cultures were cooled to 20 °C and expression was induced by addition of IPTG to 1 mM final concentration and left to produce overnight. The TBO-NEX cultures were cooled to 25 °C and left to produce for 20 h.

Bacterial cultures were centrifuged and frozen until analysis. Defrosted cell pellets were resuspended in lysis buffer (50 mM NaH_2PO_4, 300 mM NaCl, 10 mM imidazole, 1% v/v Tween 20, pH 8.0) supplemented with lysozyme and DNAse I, incubated for 30 min and the lysates were cleared by centrifugation in deep-well block (6000 × g, 30 min, 4 °C). Expression levels were analysed by Coomassie stained reducing SDS-PAGE from soluble fraction of cell lysates [50].

For insect cell expression, to generate a P0 virus stock Sf9 cells were co-transfected with linearized bacmid DNA (Bac10:KO₁₆₂₉ [52]) and pOPIN vector from the stalk region deletion library as a transfer vector. For small-scale expression tests 3 ml of $1 × 10^6$ Sf9 cells/ml in 24-well deep blocks were infected with 3 and 30 μl of P1 virus stock and left to produce at 27 °C for 72 h. For scale up, 800 ml of Sf9 production culture in shaken Thompson flask was infected with 800 μl of P2 virus stock. Media were harvested and purified after 7 days.

For mammalian expression tests, 4 μg of the given expression plasmid and 10 μl of Lipofectamine 2000 (Invitrogen, USA) were each diluted into 25 μl of Freestyle F17 media (Invitrogen, USA), incubated for 5 min, mixed and incubated for 10 min again before addition to $2 × 10^6$ HEKT293T cells grown in 1 ml of Freestyle F17 medium on a shaken 24-well culture plate (Corning, USA) at 37 °C, 5% CO_2. After 4 h cell cultures were diluted with 1 ml of EX-CELL293 serum-free medium (Sigma, USA) and left to produce for 72 h.

Expression tests from insect and mammalian cell cultures were analysed by enriching the secreted products by IMAC on Ni-NTA magnetic beads (Qiagen and Biotool, USA) from 1 ml of the production media and either analysed by SDS-PAGE or by Western blot and immunodetection with primary mouse PentaHis anti-His-tag monoclonal antibody (Qiagen, USA) and secondary HRP or AP conjugated anti-mouse IgG antibody (R&D Systems, USA; Sigma, USA).

2.3. Transient NKR-P1 expression in HEK293T cells

HEK293 cell lines were grown in suspension as described in Ref. [41] in mixture of equal volumes of EX-CELL293 and Freestyle F17 media in shaken square-shaped glass bottles within humidified 37 °C, 5% CO2 incubator. For transient expression of soluble NKR-P1 ectodomain, 400 μg of the pTT28 expression plasmid were diluted in PBS, filter-sterilized and 25 kDa linear polyethylenimine (Polysciences, USA) was added in 1:3 (w/w) ratio to 4 ml final volume, the mixture was shaken and incubated for 5 min. Meanwhile, $400 × 10^6$ HEK293T cells were centrifuged and resuspended in 200 ml of Freestyle F17 and immediately transfected. Following 4 h incubation, the culture was diluted with 200 ml of EX-CELL293. 5—7 days post-transfection culture medium was harvested by

centrifugation (4000 × g, 30 min), filtered (0.22 μm Steritop filter; Millipore, USA), and stored at −20 °C or immediately processed.

2.4. Stable NKR-P1 expression in HEK293S GnTI⁻ cells

For generation of stably transfected HEK293S GnTI⁻ cell pool, 30×10^6 cells were transfected in high cell density [41] with 30 μg of pOPINGTTneo expression plasmid. For selection, Geneticin G418 was added two days post-transfection at 100 μg/ml. The culture was split and the medium was exchanged with fresh addition of the selection antibiotic every three days. Three weeks post-transfection healthy and growing pool of polyclonal stably transfected cell culture was established. The stable culture was maintained in 1:1 mixture of EX-CELL293 and Freestyle F17 with 100 μg/ml of the Geneticin G418. For protein production 400×10^6 cells were split into 400 ml of 1:1 mixture of EX-CELL293 and Expi293 (Invitrogen, USA) with 100 μg/ml of the selection antibiotic. Culture medium was harvested after 10—14 days by centrifugation (4000 × g, 30 min), filtered (0.22 μm Steritop filter; Millipore, USA), and stored at −20 °C or immediately processed.

2.5. Protein purification and crystallization

Medium was diluted twofold with 50 mM Na_2HPO_4, 300 mM NaCl, 10 mM NaN_3, pH 7.5 PBS buffer and pH was adjusted to 7.5 if necessary. The His-tagged protein was recovered by IMAC chromatography on HiTrap TALON crude column (GE Healthcare, USA) with subsequent SEC on Superdex 200 10/300 GL column (GE Healthcare, USA) in 10 mM HEPES, 150 mM NaCl, 10 mM NaN_3, pH 7.5 buffer and concentrated to 20 mg/ml on Amicon Ultra concentrator (10000 MWCO; Millipore, USA). The protein was crystallized using sitting drop vapour diffusion method. Drops (100 nl of protein solution and 100 nl of reservoir) were set up using a Cartesian Honeybee 961 robot (Genomic Solutions) at 294 K. The reservoir consisted of 30% w/v PEG 6000, 100 mM Bis-Tris propane pH 9.0 (PegRx screen, condition 39, Hampton Research).

2.6. Mass spectrometry

Disulphide bonds in soluble human NKR-P1 were determined according to the previously published protocol [53]. Briefly, the protein was separated by SDS-PAGE, N-linked glycans were cleaved off after the first GlcNAc unit by endoglycosidase Endo Hf (New England Biolabs, USA) and digested by trypsin (Sigma, USA) or Asp-N endoproteinase (Sigma, USA) under nonreducing conditions in the presence of 200 μM cystamine. The peptide mixtures were desalted on peptide MacroTrap and separated on reversed phase MAGIC C18 columns (both Michrom BioResources, USA) connected directly to an APEX-Q 9.4 T FT-ICR mass spectrometer (Bruker Daltonics, USA) using an electrospray ion source. Data were acquired using ApexControl 3.0.0 and processed with DataAnalysis 4.0. The disulphide bonds and saccharide moieties were identified using Links software [54].

2.7. Analytical ultracentrifugation

The oligomeric state of the produced protein was analysed in ProteomeLab XL-I analytical ultracentrifuge equipped with An-50 Ti rotor (Beckman Coulter, USA). For sedimentation velocity experiment, samples of NKR-P1 diluted to the desired concentration with the SEC buffer used for its purification were spun at 48000 rpm at 20 °C and 150 scans with 0.003 cm spatial resolution were recorded in 5 min interval using absorbance optics at 280—300 nm. The data were analysed using Sedfit [55] using a c(s) continuous size distribution model. For sedimentation equilibrium experiment, NKR-P1 at 0.11 mg/ml was spun at 12-15-18-21-24000 rpm at 4 °C and 1 scan with 0.001 cm spatial resolution at 280 nm was recorded after first 34 h and then consecutively after 18 h per each velocity. The data were analysed using Sedphat [56] using multi-speed sedimentation equilibrium and single ideal species model. Buffer density and protein partial specific volume were estimated in SEDNTERP (http://sednterp.unh.edu/), figures were prepared in GUSSI [57].

2.8. SEC-MALS

Molecular weight and polydispersity of NKR-P1 and LLT1(H176C) [41] were analysed by size exclusion chromatography using an HPLC system (Shimadzu, Japan) equipped with refractive index (RI), UV and multi-angle light scattering (MALS) DAWN8 EOS detectors (Wyatt Technology, USA). A microSuperose12 column (GE Healthcare, USA) was used with 10 mM HEPES, 150 mM NaCl, 10 mM NaN_3, pH 7.5 eluent at 0.1 ml/min. Weight-average molecular weights (Mw) were calculated from the light-scattering detector based on the known injected mass while assuming 100%
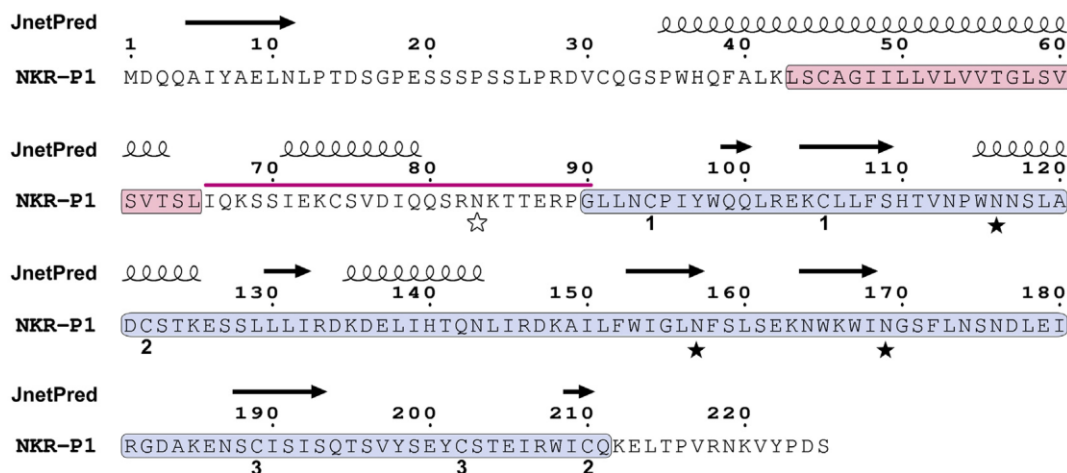

Fig. 1. The primary sequence of human NKR-P1 (CD161, *klrb1*). The transmembrane helix and C-type lectin-like domain predicted by Globplot 2 [59] are highlighted by red and blue rectangles, respectively. The stalk region optimized in this study is marked by magenta line above the sequence. JPred 4 [60] secondary structure prediction is depicted at the top. Identified cystic pairs and N-linked glycosylation sites are labelled by numbers and full stars, respectively. The empty star indicates the presumptive N-linked glycosylation site present within the stalk region. (For interpretation of the references to colour in this figure legend, the reader is referred to the web version of this article.)

Table 1
List of used expression plasmids with description of peptides flanking the expression construct.

Vector	N-terminal	C-terminal
pOPINS3C	His$_6$-SUMO-3C	—
pOPINTRX	His$_6$-TRX-3C	—
pOPINMSYB	His$_6$-MsyB-3C	—
pOPINJB	His$_6$-GST-3C	BAP
pOPINP	SS[PelB]	Lys-His$_6$
pOPING	SS[RPTPmu]	Lys-His$_6$
pOPINGTTneo	SS[RPTPmu]	Lys-His$_6$

His$_6$ —hexahistidine tag; SUMO — small ubiquitin-like modifier; 3C — cleavage site for 3C protease; TRX — E. coli thioredoxin; MsyB — E. coli MsyB; GST — glutathione S-transferase; SS[PelB] — PelB signal sequence; SS[RPTPmu] — receptor-like protein tyrosine phosphatase μ signal sequence; BAP — biotin acceptor peptide.

mass recovery. Number-average molecular weights (Mn) were determined by refractive index measurements and were calculated assuming a dn/dc value of 0.185 ml/g. Polydispersity is defined as (Mw/Mn).

3. Results and discussion

3.1. Transient expression of NKR-P1 in HEK293 cell lines

To our best knowledge, successful expression of soluble human NKR-P1 ectodomain has been previously reported only in transiently transfected HEK293 cells [45]. Although the authors haven't stated the production yield, the reported use for immobilization on SPR sensor chip doesn't necessarily suggest high yields. To evaluate this approach, we have performed transient expression of NKR-P1 ectodomain in suspension cultures of HEK293T and HEK293S GnTI$^-$ cells using the same expression construct G90-S225 as reported before [45]. This expression construct corresponds to the CTL domain of NKR-P1 (Fig. 1) and does not contain residues from the stalk region of the receptor. Similar constructs were previously successfully used within our hands for bacterial expression and refolding of mouse NKR-P1A, NKR-P1C, and Clrg ectodomains [43,44,58], as well as of human LLT1 ectodomain that was expressed in the same HEK293 cell lines [41]. However, in case of human NKR-P1 we have obtained on average yields of only about 0.1 mg of pure recombinant protein per litre of production culture from either HEK293 cell line. In contrast, we have recently reported ca 30-times higher yields in the same expression system for LLT1 [41]. Such low yields of NKR-P1 are neither sufficient nor economical for structural studies; therefore, we have attempted further optimization of its expression with regards to the expression system used and to the length of the putative N-terminal stalk region in its expression construct.

3.2. Screening of NKR-P1 expression in E. coli

In order to test the solubility effect of a protein tag fusion we
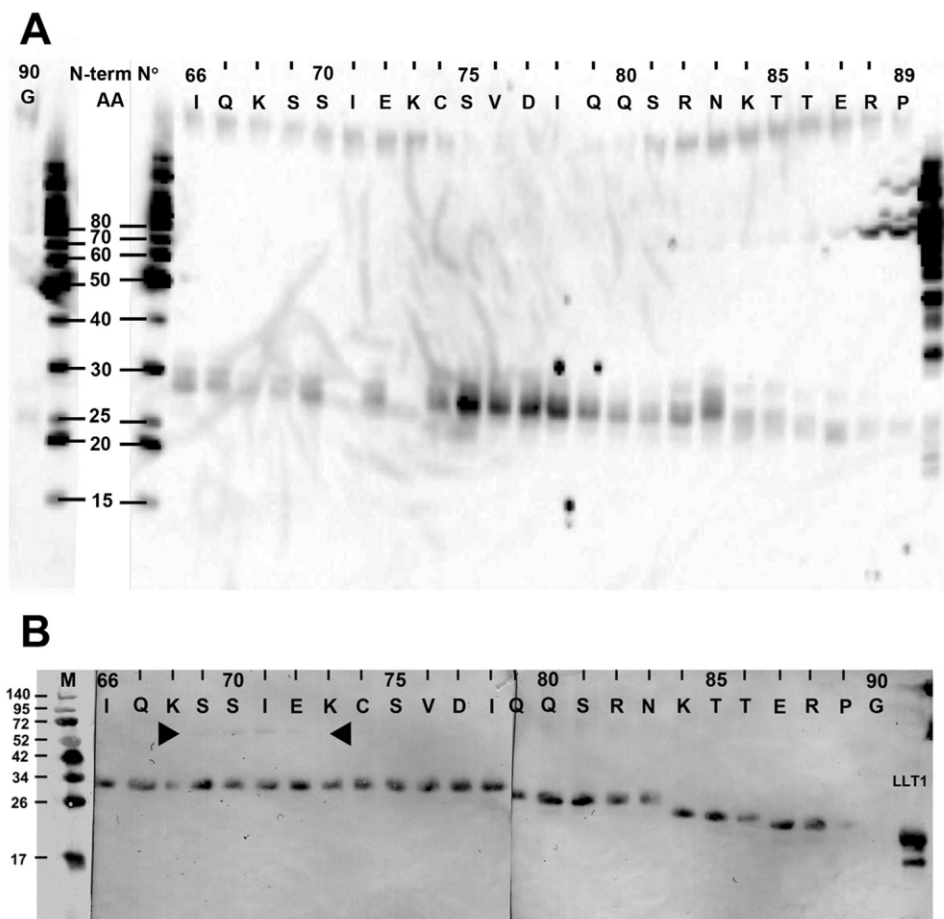
Fig. 2. Screening of the stalk region deletion library of NKR-P1 expression constructs. Western blots of His-tagged products enriched on Ni-NTA magnetic beads from small-scale expression tests of the NKR-P1 stalk region deletion library in pOPING (C-terminally His$_6$-tagged) in (A) Sf9 insect and (B) human HEK293T cell lines. The N-terminal residue of the stalk region included in the given construct is annotated at the top. Molecular weight standards are in kDa. Position of putative covalent dimer of NKR-P1 is marked by an arrow. Sample of NKR-P1 ligand, protein LLT1, was added for comparison.

have subcloned three expression constructs of human NKR-P1 differing in the length of the flexible *N*-terminal stalk region while containing the whole CTL domain (I66/Q80/G90-S225) (Fig. 1) into the pOPINS3C, pOPINTRX, pOPINMSYB, pOPINJB, and pOPINP expression vectors from OPPF's suite of pOPIN vectors [48] (see Table 1 for information about the expression cassettes). Expression tests were performed in *E. coli* B834(DE3) and *E. coli* Rosetta2(DE3) pLysS strains using two different production conditions – an overnight production at 20 °C after induction with 1 mM IPTG and a production in TBONEX auto-induction medium at 25 °C for 20 h. Products of 1 ml cultures were enriched using Ni-NTA magnetic beads from soluble fraction of cell lysate and analysed using Coomassie stained reducing SDS-PAGE [50] (Fig. S1). Unfortunately, we cannot report any improvement on expression of soluble human NKR-P1 in *E. coli* for any of the tested fusion constructs or conditions. It is possible that using strains with an oxidizing cytoplasm designed for expression of disulphide-containing proteins like SHuffle or Rosetta-gami would be more efficient; however, based on our previous experiences with these strains for similar constructs of mouse NKR-P1 receptors this seems unlikely, too (not shown).

3.3. Screening of stalk region deletion library in Sf9 and HEK293T cells

For simultaneous expression test in both insect cell baculoviral and mammalian expression systems, we have utilized OPPF's pOPING expression vector allowing for secreted expression with *C*-terminal His$_6$-tag flanking the protein of interest (Table 1). A series of 25 human NKR-P1 constructs with consecutively shortened *N*-terminal stalk region (I66-G90) (Fig. 1) ending at the CTL domain *C*-terminal S225 were subcloned into the pOPING vector. Expression tests were performed in 3 ml of Sf9 culture infected with P1 generation of baculoviruses and in 2 ml of transiently transfected suspension HEK293T cultures. Expression media were analysed for the presence of desired products 72 h post-transfection by anti-histidine tag immunodetection.

Although positive, only low expression signals were obtained from the insect cell expressions (Fig. 2A). However, a distinct region of best expressing constructs could be distinguished with the *N*-termini of NKR-P1 ranging from C74 to Q79. This could suggest stabilization of these constructs by secondary structure formation. Interestingly, a JPred 4 secondary structure prediction analysis suggests α-helix within this region (Fig. 1). Such structural stabilization could provide a scaffold for the formation of an intermolecular disulphide bridge via the C74 residue.

Analysis of the expression test in mammalian culture showed positive albeit similarly low level of expression for most of the tested constructs (Fig. 2B). Interestingly, a very low signal corresponding to the NKR-P1 covalent dimer could be detected within the range of S69-E72 *N*-terminal NKR-P1 constructs. Also, a sudden shift in the electrophoretic mobility between the N83 and K84 *N*-terminal constructs and presence of NKT consensus sequence suggest presence of *N*-linked glycan at the N83 (Fig. 1).

We have further attempted to scale-up the production of the S75-S225 construct in 800 ml of Sf9 culture infected with P2 generation of the virus. However, the low level of expression was confirmed with yield of only ca 0.4 mg of heavily contaminated protein per litre of production culture (contamination may have been caused by presence of misfolded protein aggregates). Therefore, we cannot report a suitable format of recombinant expression of soluble human NKR-P1 based on baculoviral transduction of Sf9 cells. We cannot exclude the possibility that the sequence following the signal peptide might have a negative impact on secretion in insect cells, rather than the construct itself.

3.4. High-level expression of soluble human NKR-P1 in stable HEK293S GnTI⁻ cell line

In parallel, we have attempted to express the original G90-S225 construct of human NKR-P1 ectodomain in stably transfected pool of HEK293S GnTI⁻ cells and thus test whether higher production yields might be reached by using stable instead of transient transfection. Although this construct performed poorly in the aforementioned transient expression test and may be suboptimal with respect to possible expression yield, based on our previous work on structural elucidation of CTL receptors [40,43,58,61] constructs lacking the *N*-terminal stalk region and containing only the well-defined CTL domain are the most suitable targets for further structural experiments. The expression construct was subcloned into OPPF's vector pOPINGTTneo containing neomycin selection marker. A pool of resistant HEK293S GnTI⁻ cells was selected on Geneticin G418. Following positive expression test (data not shown), the resistant pool was scaled to 300 ml of 1×10^6/ml cell suspension and left to produce for 10 days. The secreted product was purified by IMAC on HiTrap Talon column followed by SEC on Superdex 200 10/300 GL yielding on average 2.5 mg of pure protein per litre of production culture.

The HEK293S GnTI⁻ cell line provides uniform mammalian *N*-linked glycosylation of GlcNAc$_2$Man$_5$ type that is readily cleavable with endoglycosidase Endo F1 leaving only a single GlcNAc unit (Fig. 3A, lane D). Both under reducing and non-reducing conditions the soluble human NKR-P1 ectodomain migrates on SDS-PAGE as three distinct glycoforms corresponding to the theoretical weight of monomer with one (18.4 kDa), two (19.6 kDa) or three (20.9 kDa)
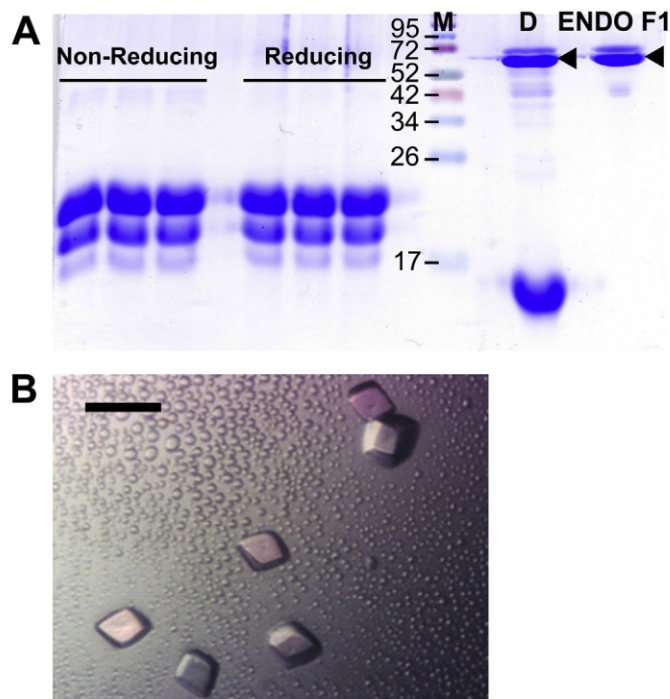

Fig. 3. Soluble NKR-P1 ectodomain forms distinct glycoforms, is easily deglycosylatable and crystallizable. (A) SDS-PAGE analysis of the final product of soluble NKR-P1 (G90-S225) with simple GlcNAc$_2$Man$_5$ *N*-linked glycosylation from HEK293S GnTI⁻ cells. Both under reducing and non-reducing conditions three distinct glycoforms of NKR-P1 are detectable, that migrate as a single band after cleavage of *N*-glycans with endoglycosidase Endo F1 (leaving single GlcNAc unit; lane D). M — molecular weight standard in kDa. ENDO F1 — endoglycosidase F1 (arrow). (B) Crystals of NKR-P1 produced in HEK293S GnTI⁻ cells grown by sitting drop vapour diffusion method. The black scale bar represents 100 μm.
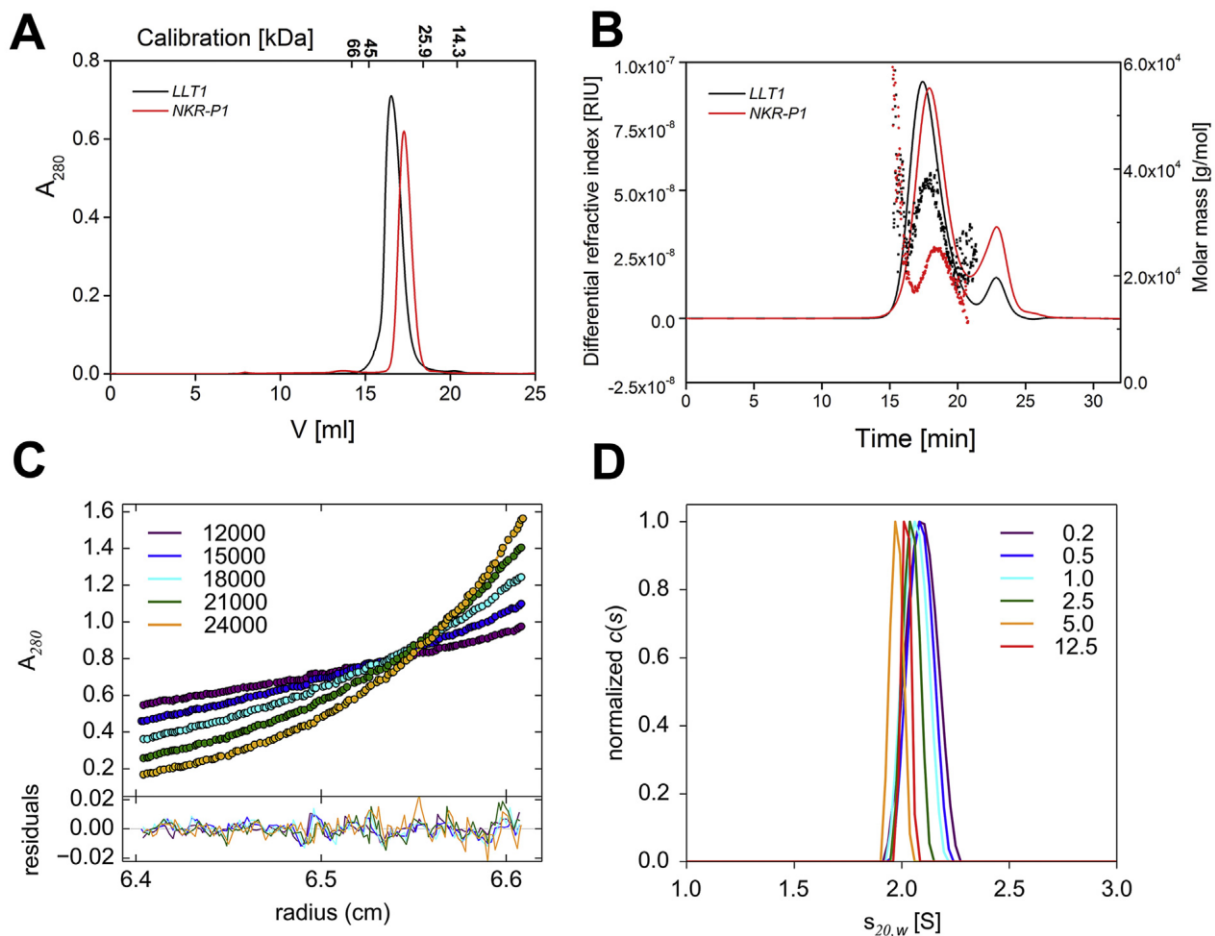
Fig. 4. Soluble NKR-P1 is monomeric in solution. (A) Comparison of size exclusion chromatography profiles of soluble LLT1 H176C mutant (black) and NKR-P1 (red). The LLT1 is forming non-covalent dimer [41] while NKR-P1 migrates rather as monomer. (B) Comparison of size exclusion chromatography with refractive index detection (line plot, left axis) and molar masses determined by multi angle light scattering (scatter plot, right axis) of soluble LLT1 H176C mutant (black) and NKR-P1 (red). (C) Sedimentation equilibrium analysis in analytical ultracentrifuge performed at 0.11 mg/ml concentration showed that NKR-P1 behaves as monomer; upper panel − absorbance data with fitted curves (single non-interacting discrete species model), lower panel − residual plot showing the goodness of fit. (D) Series of sedimentation velocity analyses in analytical ultracentrifuge at increasing protein concentration (given in mg/ml; normalized continuous size distributions of the sedimenting species) showed that NKR-P1 does not self-associate. (For interpretation of the references to colour in this figure legend, the reader is referred to the web version of this article.)

N-linked glycosylation sites occupied with the GlcNAc$_2$Man$_5$ oligosaccharide moieties (Fig. 3A). Furthermore, the prepared soluble human NKR-P1 with homogeneous GlcNAc$_2$Man$_5$ N-glycans (although still being in-homogeneous with respect to incomplete N-glycosylation site occupancy) was readily crystallized using the vapour diffusion method in sitting drop, forming bipyramidal crystals (Fig. 3B) up to 80 μm in size. These initial crystals already diffracted up to resolution of ca 2.0 Å and were later optimized leading to solution of NKR-P1 crystal structure (Bláha *et al.*, submitted).

Utilizing a mass spectrometry approach, we have identified cystic peptides in the soluble NKR-P1 ectodomain confirming canonical configuration of disulphides in CTL domain: C94-C105, C122-C210, and C189-C202 (Table S2, Fig. 1). Furthermore, we have been able to confirm presence of saccharide moieties at the three predicted N-linked glycosylation sites − N116, N157, and N169 (Table S2, Fig. 1). The incomplete occupancy of these sites accounts for the three different glycoforms observed on SDS-PAGE (Fig. 3A).

3.5. Stoichiometry of recombinant human NKR-P1 in solution

Comparison of SEC retention volumes for soluble LLT1(H176C) eluting as a non-covalent dimer [41] and for soluble NKR-P1

ectodomain suggests that soluble NKR-P1 elutes rather as a monomer (Fig. 4A). To confirm this, we repeated the analysis with multi-angle light scattering detection (Fig. 4B) providing a molecular weight of ca 22 kDa and 33 kDa for soluble NKR-P1 and LLT1(H176C) respectively, both with low polydispersity (Fig. 4B). Monomeric state of human NKR-P1 was further corroborated by sedimentation equilibrium analysis in analytical ultracentrifuge resulting in estimated molecular weight of 20.7 kDa (Fig. 4C). Sedimentation velocity experiment performed with samples of increasing protein concentration also showed no tendency to form homodimer or oligomeric species (Fig. 4D). Soluble human NKR-P1 behaves as particle with standard sedimentation coefficient $s_{20,w}$ 2.10 S and approximate dimensions of 4.5 × 3.5 nm corresponding well to expected values for monomeric protein.

Human NKR-P1 should form a covalently linked homodimer on the cell surface [19], but the produced soluble form of NKR-P1 lacks the odd cysteine residue in the stalk region implicated in such dimerization [13]. However, soluble ectodomains of the homologous subfamily of related *clec2* receptors − CD69 [61], LLT1 [40], and KACL [62] were previously reported to form stable non-covalent dimers in solution quite easily. On the other hand, recently published structure of NKp65 [62], a member of more closely related *klrf* subfamily, shows this receptor interacting with

its *clec2* ligand KACL while being in a monomeric state and its dimerization in the manner of *clec2* receptors would even hamper the interaction with its *clec2* ligand. Similarly, previously reported mouse NKR-P1A and NKR-P1C(B6) orthologues were observed in solution only as monomers [43,44]. Taken together with the presented low propensity of NKR-P1 to form a non-covalent dimer in solution, a different, less stable mode of dimerization should be expected than that of *clec2* receptors for the human NKR-P1 and its orthologues and close homologues — the *klrf* receptors; that requires covalent stabilization by a disulphide bridge(s) in the putative stalk region.

4. Conclusions

To conclude, we have recombinantly expressed soluble human NKR-P1 ectodomain in stable, deglycosylatable and crystallizable form. To our knowledge, this is the first attempt at structural characterization of human NKR-P1 immunoreceptor. The strategy of construct design described herein for NKR-P1 — i.e. the construction of stalk region deletion library — might be considered also for other C-type lectin-like receptors of NK cells, although in our case, it was rather the choice of proper expression system that was the most important factor. Selection of stably transfected HEK293 cell lines as expression host may be optimal both for protein production aimed at structural characterization and for production of soluble receptor domains that could be utilized in clinical therapy also for other NK cell CTL receptors and their ligands. Depending on the intended use, suitable HEK293 cell line with desired *N*-glycosylation profile could be chosen, i.e. HEK293S GnTI⁻ or HEK293T cell lines with simple or complex *N*-glycans, respectively.

Acknowledgements

Appendix A. Supplementary data

Supplementary data related to this article can be found at http://dx.doi.org/10.1016/j.pep.2017.07.016.

References

[1] E. Vivier, D.H. Raulet, A. Moretta, M.A. Caligiuri, L. Zitvogel, L.L. Lanier, W.M. Yokoyama, S. Ugolini, Innate or adaptive immunity? The example of natural killer cells, Science 331 (2011) 44—49.

[2] M.A. Caligiuri, Human natural killer cells, Blood 112 (2008) 461—469.

[3] E. Vivier, E. Tomasello, M. Baratin, T. Walzer, S. Ugolini, Functions of natural killer cells, Nat. Immunol. 9 (2008) 503—510.

[4] A. Cerwenka, L.L. Lanier, Natural killer cell memory in infection, inflammation and cancer, Nat. Rev. Immunol. 16 (2016) 112—123.

[5] E. Vivier, S. Ugolini, Natural killer cells: from basic research to treatments, Front. Immunol. 2 (2011) 18.

[6] M.A. Cooper, M. Colonna, W.M. Yokoyama, Hidden talents of natural killers: NK cells in innate and adaptive immunity, EMBO Rep. 10 (2009) 1103—1110.

[7] D.H. Raulet, N. Guerra, Oncogenic stress sensed by the immune system: role of natural killer cell receptors, Nat. Rev. Immunol. 9 (2009) 568—580.

[8] C.S. Brandt, M. Baratin, E.C. Yi, J. Kennedy, Z. Gao, B. Fox, B. Haldeman, C.D. Ostrander, T. Kaifu, C. Chabannon, A. Moretta, R. West, W. Xu, E. Vivier, S.D. Levin, The B7 family member B7-H6 is a tumor cell ligand for the activating natural killer cell receptor NKp30 in humans, J. Exp. Med. 206 (2009)

1495—1503.

[9] N. Anfossi, P. Andre, S. Guia, C.S. Falk, S. Roetynck, C.A. Stewart, V. Breso, C. Frassati, D. Reviron, D. Middleton, F. Romagne, S. Ugolini, E. Vivier, Human NK cell education by inhibitory receptors for MHC class I, Immunity 25 (2006) 331—342.

[10] C. Bottino, R. Castriconi, L. Moretta, A. Moretta, Cellular ligands of activating NK receptors, Trends Immunol. 26 (2005) 221—226.

[11] K. Karre, H.G. Ljunggren, G. Piontek, R. Kiessling, Selective rejection of H-2-deficient lymphoma variants suggests alternative immune defence strategy, Nature 319 (1986) 675—678.

[12] L.L. Lanier, B. Corliss, J.H. Phillips, Arousal and inhibition of human NK cells, Immunol. Rev. 155 (1997) 145—154.

[13] Y. Bartel, B. Bauer, A. Steinle, Modulation of NK cell function by genetically coupled C-type lectin-like receptor/ligand pairs encoded in the human natural killer gene complex, Front. Immunol. 4 (2013) 362.

[14] W.M. Yokoyama, B.F. Plougastel, Immune functions encoded by the natural killer gene complex, Nat. Rev. Immunol. 3 (2003) 304—316.

[15] D. Rozbesky, L. Ivanova, L. Hernychova, V. Grobarova, P. Novak, J. Cerny, Nkrp1 family, from lectins to protein interacting molecules, Molecules 20 (2015) 3463—3478.

[16] A.N. Zelensky, J.E. Gready, The C-type lectin-like domain superfamily, FEBS J. 272 (2005) 6179—6217.

[17] K.P. Kane, K.J. Lavender, B.J. Ma, Ly-49 receptors and their functions, Crit. Rev. Immunol. 24 (2004) 321—348.

[18] S. Bauer, V. Groh, J. Wu, A. Steinle, J.H. Phillips, L.L. Lanier, T. Spies, Activation of NK cells and T cells by NKG2D, a receptor for stress-inducible MICA, Science 285 (1999) 727—729.

[19] L.L. Lanier, C. Chang, J.H. Phillips, Human NKR-P1A. A disulfide-linked homodimer of the C-type lectin superfamily expressed by a subset of NK and T lymphocytes, J. Immunol. 153 (1994) 2417—2428.

[20] J. Spreu, S. Kuttruff, V. Stejfova, K.M. Dennehy, B. Schittek, A. Steinle, Interaction of C-type lectin-like receptors NKp65 and KACL facilitates dedicated immune recognition of human keratinocytes, Proc. Natl. Acad. Sci. U. S. A. 107 (2010) 5100—5105.

[21] S. Welte, S. Kuttruff, I. Waldhauer, A. Steinle, Mutual activation of natural killer cells and monocytes mediated by NKp80-AICL interaction, Nat. Immunol. 7 (2006) 1334—1342.

[22] I. Vogler, A. Steinle, Vis-a-vis in the NKC: genetically linked natural killer cell receptor/ligand pairs in the natural killer gene complex (NKC), J. Innate Immun. 3 (2011) 227—235.

[23] M. Exley, S. Porcelli, M. Furman, J. Garcia, S. Balk, CD161 (NKR-P1A) costimulation of CD1d-dependent activation of human T cells expressing invariant V alpha 24 J alpha Q T cell receptor alpha chains, J. Exp. Med. 188 (1998) 867—876.

[24] J.R. Fergusson, K.E. Smith, V.M. Fleming, N. Rajoriya, E.W. Newell, R. Simmons, E. Marchi, S. Bjorkander, Y.H. Kang, L. Swadling, A. Kurioka, N. Sahgal, H. Lockstone, D. Baban, G.J. Freeman, E. Sverremark-Ekstrom, M.M. Davis, M.P. Davenport, V. Venturi, J.E. Ussher, C.B. Willberg, P. Klenerman, CD161 defines a transcriptional and functional phenotype across distinct human T cell lineages, Cell Rep. 9 (2014) 1075—1088.

[25] B. Afzali, P.J. Mitchell, F.C. Edozie, G.A. Povoleri, S.E. Dowson, L. Demandt, G. Walter, J.B. Canavan, C. Scotta, B. Menon, P.S. Chana, W. Khamri, S.Y. Kordasti, S. Heck, B. Grimbacher, T. Tree, A.P. Cope, L.S. Taams, R.I. Lechler, S. John, G. Lombardi, CD161 expression characterizes a subpopulation of human regulatory T cells that produces IL-17 in a STAT3-dependent manner, Eur. J. Immunol. 43 (2013) 2043—2054.

[26] L. Cosmi, R. De Palma, V. Santarlasci, L. Maggi, M. Capone, F. Frosali, G. Rodolico, V. Querci, G. Abbate, R. Angeli, L. Berrino, M. Fambrini, M. Caproni, F. Tonelli, E. Lazzeri, P. Parronchi, F. Liotta, E. Maggi, S. Romagnani, F. Annunziato, Human interleukin 17-producing cells originate from a CD161+CD4+ T cell precursor, J. Exp. Med. 205 (2008) 1903—1916.

[27] E. Billerbeck, Y.H. Kang, L. Walker, H. Lockstone, S. Grafmueller, V. Fleming, J. Flint, C.B. Willberg, B. Bengsch, B. Seigel, N. Ramamurthy, N. Zitzmann, E.J. Barnes, J. Thevanayagam, A. Bhagwanani, A. Leslie, Y.H. Oo, S. Kollnberger, P. Bowness, O. Drognitz, D.H. Adams, H.E. Blum, R. Thimme, P. Klenerman, Analysis of CD161 expression on human CD8+ T cells defines a distinct functional subset with tissue-homing properties, Proc. Natl. Acad. Sci. U. S. A. 107 (2010) 3006—3011.

[28] V. Brucklacher-Waldert, K. Stuerner, M. Kolster, J. Wolthausen, E. Tolosa, Phenotypical and functional characterization of T helper 17 cells in multiple sclerosis, Brain J. Neurol. 132 (2009) 3329—3341.

[29] L. Estrada-Capetillo, B. Hernandez-Castro, A. Monsivais-Urenda, C. Alvarez-Quiroga, E. Layseca-Espinosa, C. Abud-Mendoza, L. Baranda, A. Urzainqui, F. Sanchez-Madrid, R. Gonzalez-Amaro, Induction of Th17 lymphocytes and Treg cells by monocyte-derived dendritic cells in patients with rheumatoid arthritis and systemic lupus erythematosus, Clin. Dev. Immunol. 2013 (2013) 584303.

[30] J.A. Smith, R.A. Colbert, Review: the interleukin-23/interleukin-17 axis in spondyloarthritis pathogenesis: Th17 and beyond, Arthritis & Rheumatol. 66 (2014) 231—241.

[31] A. Poggi, P. Costa, M.R. Zocchi, L. Moretta, Phenotypic and functional analysis of CD4+ NKRP1A+ human T lymphocytes. Direct evidence that the NKRP1A molecule is involved in transendothelial migration, Eur. J. Immunol. 27 (1997) 2345—2350.

[32] A. Poggi, P. Costa, M.R. Zocchi, L. Moretta, NKRP1A molecule is involved in

transendothelial migration of CD4+ human T lymphocytes, Immunol. Lett. 57 (1997) 121–123.

[33] V. Annibali, G. Ristori, D.F. Angelini, B. Serafini, R. Mechelli, S. Cannoni, S. Romano, A. Paolillo, H. Abderrahim, A. Diamantini, G. Borsellino, F. Aloisi, L. Battistini, M. Salvetti, CD161(high)CD8+T cells bear pathogenetic potential in multiple sclerosis, Brain J. Neurol. 134 (2011) 542–554.

[34] P. Chalan, J. Bijzet, M.G. Huitema, B.J. Kroesen, E. Brouwer, A.M. Boots, Expression of lectin-like transcript 1, the ligand for CD161, in rheumatoid arthritis, PLoS One 10 (2015) e0132436.

[35] H. Aldemir, V. Prod'homme, M.J. Dumaurier, C. Retiere, G. Poupon, J. Cazareth, F. Bihl, V.M. Braud, Cutting edge: lectin-like transcript 1 is a ligand for the CD161 receptor, J. Immunol. 175 (2005) 7791–7795.

[36] D.B. Rosen, J. Bettadapura, M. Alsharifi, P.A. Mathew, H.S. Warren, L.L. Lanier, Cutting edge: lectin-like transcript-1 is a ligand for the inhibitory human NKR-P1A receptor, J. Immunol. 175 (2005) 7796–7799.

[37] C. Germain, A. Meier, T. Jensen, P. Knapnougel, G. Poupon, A. Lazzari, A. Neisig, K. Hakansson, T. Dong, N. Wagtmann, E.D. Galsgaard, P. Spee, V.M. Braud, Induction of lectin-like transcript 1 (LLT1) protein cell surface expression by pathogens and interferon-gamma contributes to modulate immune responses, J. Biol. Chem. 286 (2011) 37964–37975.

[38] P. Roth, M. Mittelbronn, W. Wick, R. Meyermann, M. Tatagiba, M. Weller, Malignant glioma cells counteract antitumor immune responses through expression of lectin-like transcript-1, Cancer Res. 67 (2007) 3540–3544.

[39] C. Germain, T. Guillaudeux, E.D. Galsgaard, C. Hervouet, N. Tekaya, A.S. Gallouet, J. Fassy, F. Bihl, G. Poupon, A. Lazzari, P. Spee, F. Anjuere, C. Pangault, K. Tarte, P. Tas, L. Xerri, V.M. Braud, Lectin-like transcript 1 is a marker of germinal center-derived B-cell non-Hodgkin's lymphomas damping natural killer cell functions, Oncoimmunology 4 (2015) e1026503.

[40] T. Skalova, J. Blaha, K. Harlos, J. Duskova, T. Koval, J. Stransky, J. Hasek, O. Vanek, J. Dohnalek, Four crystal structures of human LLT1, a ligand of human NKR-P1, in varied glycosylation and oligomerization states, Acta Crystallogr. D Biol. Crystallogr. 71 (2015) 578–591.

[41] J. Blaha, P. Pachl, P. Novak, O. Vanek, Expression and purification of soluble and stable ectodomain of natural killer cell receptor LLT1 through high-density transfection of suspension adapted HEK293S GnTI(-) cells, Protein Expr. Purif. 109 (2015) 7–13.

[42] J.V. Ravetch, L.L. Lanier, Immune inhibitory receptors, Science 290 (2000) 84–89.

[43] P. Kolenko, D. Rozbesky, O. Vanek, V. Kopecky Jr., K. Hofbauerova, P. Novak, P. Pompach, J. Hasek, T. Skalova, K. Bezouska, J. Dohnalek, Molecular architecture of mouse activating NKR-P1 receptors, J. Struct. Biol. 175 (2011) 434–441.

[44] D. Rozbesky, D. Kavan, J. Chmelik, P. Novak, O. Vanek, K. Bezouska, High-level expression of soluble form of mouse natural killer cell receptor NKR-P1C(B6) in Escherichia coli, Protein Expr. Purif. 77 (2011) 178–184.

[45] J. Kamishikiryo, H. Fukuhara, Y. Okabe, K. Kuroki, K. Maenaka, Molecular basis for LLT1 protein recognition by human CD161 protein (NKRP1A/KLRB1), J. Biol. Chem. 286 (2011) 23823–23830.

[46] P.J. Reeves, N. Callewaert, R. Contreras, H.G. Khorana, Structure and function in rhodopsin: high-level expression of rhodopsin with restricted and homogeneous N-glycosylation by a tetracycline-inducible N-acetylglucosaminyltransferase I-negative HEK293S stable mammalian cell line, Proc. Natl. Acad. Sci. U. S. A. 99 (2002) 13419–13424.

[47] N.S. Berrow, D. Alderton, S. Sainsbury, J. Nettleship, R. Assenberg, N. Rahman, D.I. Stuart, R.J. Owens, A versatile ligation-independent cloning method suitable for high-throughput expression screening applications, Nucleic Acids Res. 35 (2007) e45.

[48] L.E. Bird, High throughput construction and small scale expression screening of multi-tag vectors in Escherichia coli, Methods 55 (2011) 29–37.

[49] Y. Durocher, S. Perret, A. Kamen, High-level and high-throughput recombinant protein production by transient transfection of suspension-growing human 293-EBNA1 cells, Nucleic Acids Res. 30 (2002) E9.

[50] L.E. Bird, H. Rada, J. Flanagan, J.M. Diprose, R.J. Gilbert, R.J. Owens, Application of In-Fusion cloning for the parallel construction of E. coli expression vectors, Methods Mol. Biol. 1116 (2014) 209–234.

[51] J.E. Nettleship, P.J. Watson, N. Rahman-Huq, L. Fairall, M.G. Posner, A. Upadhyay, Y. Reddivari, J.M. Chamberlain, S.E. Kolstoe, S. Bagby, J.W. Schwabe, R.J. Owens, Transient expression in HEK 293 cells: an alternative to E. coli for the production of secreted and intracellular mammalian proteins, Methods Mol. Biol. 1258 (2015) 209–222.

[52] Y. Zhao, D.A. Chapman, I.M. Jones, Improving baculovirus recombination, Nucleic Acids Res. 31 (2003) E6. E6.

[53] P. Pompach, P. Man, D. Kavan, K. Hofbauerova, V. Kumar, K. Bezouska, V. Havlicek, P. Novak, Modified electrophoretic and digestion conditions allow a simplified mass spectrometric evaluation of disulfide bonds, J. Mass Spectrom. JMS 44 (2009) 1571–1578.

[54] M.M. Young, N. Tang, J.C. Hempel, C.M. Oshiro, E.W. Taylor, I.D. Kuntz, B.W. Gibson, G. Dollinger, High throughput protein fold identification by using experimental constraints derived from intramolecular cross-links and mass spectrometry, Proc. Natl. Acad. Sci. U. S. A. 97 (2000) 5802–5806.

[55] P. Schuck, Size-distribution analysis of macromolecules by sedimentation velocity ultracentrifugation and lamm equation modeling, Biophys. J. 78 (2000) 1606–1619.

[56] P. Schuck, On the analysis of protein self-association by sedimentation velocity analytical ultracentrifugation, Anal. Biochem. 320 (2003) 104–124.

[57] C.A. Brautigam, Calculations and publication-quality illustrations for analytical ultracentrifugation data, Methods Enzym. 562 (2015) 109–133.

[58] T. Skalova, K. Kotynkova, J. Duskova, J. Hasek, T. Koval, P. Kolenko, P. Novak, P. Man, P. Hanc, O. Vanek, K. Bezouska, J. Dohnalek, Mouse Clr-g, a ligand for NK cell activation receptor NKR-P1F: crystal structure and biophysical properties, J. Immunol. 189 (2012) 4881–4889.

[59] R. Linding, R.B. Russell, V. Neduva, T.J. Gibson, GlobPlot: exploring protein sequences for globularity and disorder, Nucleic Acids Res. 31 (2003) 3701–3708.

[60] A. Drozdetskiy, C. Cole, J. Procter, G.J. Barton, JPred4: a protein secondary structure prediction server, Nucleic Acids Res. 43 (2015) W389–W394.

[61] O. Vanek, M. Nalezkova, D. Kavan, I. Borovickova, P. Pompach, P. Novak, V. Kumar, L. Vannucci, J. Hudecek, K. Hofbauerova, V. Kopecky Jr., J. Brynda, P. Kolenko, J. Dohnalek, P. Kaderavek, J. Chmelik, L. Gorcik, L. Zidek, V. Sklenar, K. Bezouska, Soluble recombinant CD69 receptors optimized to have an exceptional physical and chemical stability display prolonged circulation and remain intact in the blood of mice, FEBS J. 275 (2008) 5589–5606.

[62] Y. Li, Q. Wang, S. Chen, P.H. Brown, R.A. Mariuzza, Structure of NKp65 bound to its keratinocyte ligand reveals basis for genetically linked recognition in natural killer gene complex, Proc. Natl. Acad. Sci. U. S. A. 110 (2013) 11505–11510.

7.2 PUBLICATION NO. 2

Vaněk, O.; Celadova, P.; Skořepa, O.; Bláha, J.; Kalousková, B.; Dvorská, A.; Poláchová, E.; Pucholtová, H.; Kavan, D.; Pompach, P.; Hofbauerová, K.; Kopecký, V.; Mesci, A.; Voigt, S.; Carlyle, JR.

Production of recombinant soluble dimeric C-type lectin-like receptors of rat natural killer cells.

Sci. Rep. 2019, 9, 17836. doi: *10.1038/s41598-019-52114-8*
Erratum (publisher correction) in: Sci Rep. 2020, 10, 2828

My contribution to the publication:
Performing research (cell culture maintenance, transfection optimization, protein expression, protein purification, and quality control)

OPEN

Production of recombinant soluble dimeric C-type lectin-like receptors of rat natural killer cells

Ondřej Vaněk [1*], Petra Celadova[1], Ondřej Skořepa[1], Jan Bláha[1,6], Barbora Kalousková[1], Anna Dvorská[1], Edita Poláchová[1], Helena Pucholtová[1], Daniel Kavan[1,2], Petr Pompach[2], Kateřina Hofbauerová [2,3], Vladimír Kopecký [3], Aruz Mesci[4], Sebastian Voigt [5] & James R. Carlyle[4]

Working at the border between innate and adaptive immunity, natural killer (NK) cells play a key role in the immune system by protecting healthy cells and by eliminating malignantly transformed, stressed or virally infected cells. NK cell recognition of a target cell is mediated by a receptor "zipper" consisting of various activating and inhibitory receptors, including C-type lectin-like receptors. Among this major group of receptors, two of the largest rodent receptor families are the NKR-P1 and the Clr receptor families. Although these families have been shown to encode receptor-ligand pairs involved in MHC-independent self-nonself discrimination and are a target for immune evasion by tumour cells and viruses, structural mechanisms of their mutual recognition remain less well characterized. Therefore, we developed a non-viral eukaryotic expression system based on transient transfection of suspension-adapted human embryonic kidney 293 cells to produce soluble native disulphide dimers of NK cell C-type lectin-like receptor ectodomains. The expression system was optimized using green fluorescent protein and secreted alkaline phosphatase, easily quantifiable markers of recombinant protein production. We describe an application of this approach to the recombinant protein production and characterization of native rat NKR-P1B and Clr-11 proteins suitable for further structural and functional studies.

Natural killer (NK) cells are innate immune lymphocytes capable of recognizing and destroying a wide variety of target cells, including transformed, infected, transplanted, antibody-coated, and stressed cells[1]. In contrast to T or B cells, NK cells do not express a single dominant activation receptor on their surface. Instead, the functions of these immune effector cells are regulated by a high number of receptors that generate either inhibitory or activation signals through the large "receptor zipper"[2]. These receptors belong to two major protein families similar to members of the immunoglobulin or C-type lectin superfamilies[3]. Inhibitory C-type lectin receptors, such as Ly-49 proteins or CD94/NKG2A heterodimers, recognize MHC class I glycoproteins on the surface of healthy cells and efficiently block the natural killing of these cells. However, in pathological states, target cells often lose inhibitory "self" ligands, leading to enhanced cytotoxicity via NK cell disinhibition. This mode of detection has been termed "missing-self" recognition[4]. Conversely, stressed, transformed or infected cells often overexpress some proteins that are usually in low abundance, on healthy cells. These proteins might be recognized by activating receptors (induced-self-recognition), as in the case of the stress-induced MHC class I-like molecules MICA and MICB, which are recognized by the NKG2D activation C-type lectin-like receptor[5].

In addition to Ly-49, the NKR-P1 (CD161) receptor family, which is the second largest group of receptors encoded by distinct but closely related genes of the NK gene complex, may generate both activation and inhibitory signals in NK cells. This protein family was first identified on the surface of rat natural killer cells using

[1]Department of Biochemistry, Faculty of Science, Charles University, Hlavova 2030/8, 12840, Prague, Czech Republic. [2]Institute of Microbiology, The Czech Academy of Sciences, Vídeňská 1083, 14220, Prague, Czech Republic. [3]Institute of Physics, Faculty of Mathematics and Physics, Charles University, Ke Karlovu 5, 12116, Prague, Czech Republic. [4]Department of Immunology, University of Toronto, 1 King's College Circle, M5S 1A8, Toronto, ON, Canada. [5]Department of Infectious Diseases, Robert Koch Institute, Seestraße 10, 13353, Berlin, Germany. [6]Present address: EMBL Hamburg, c/o DESY, Building 25A, Notkestraße 85, 22603, Hamburg, Germany. *email: ondrej. vanek@natur.cuni.cz

a specific monoclonal antibody 3.2.3[6]. Subsequent studies showed that NKR-P1 (CD161) receptors consist of homodimeric type II transmembrane C-type lectin-like proteins primarily found on NK, NKT, and activated CD8^{+} T cells[7]. Genes encoding the NKR-P1 family (designated *Klrb1*) appear to be conserved amongst birds, rodents, humans, and other mammals, suggesting that the gene products play a key role in innate immunity across species boundaries[8]. The NKR-P1 receptors consist of N-terminal peptide motifs involved in receptor signalling, a single transmembrane domain, an extended stalk region that includes the putative dimerization cysteine(s), and a large C-terminal ligand binding domain similar to the carbohydrate-recognition domain of C-type lectins[9].

The discovery that physiological ligands of at least some NKR-P1 receptors belong to a family of related C-type lectin-like receptors, the C-type lectin-related (Clr) proteins, which are encoded by a family of *Clec2* genes interspersed among the *Klrb1* genes themselves, was a breakthrough in understanding NKR-P1 function[10,11]. These studies have shown that mouse NKR-P1B recognizes Clr-b and that transfected cells expressing Clr-b are partly protected from lysis by NK cells, thus suggesting that NKR-P1B:Clr-b recognition is a novel form of missing-self recognition designed to monitor the cellular levels of Clr-b. Accordingly, genetic linkage of the *Clec2* and *Klrb1* genes highlighted the importance of this system as a particularly unique self/non-self discrimination tool because the "self" ligand is always coinherited with its cognate receptor[7,12]. These findings established a new paradigm of lectin-like receptors that interact with other lectin-like proteins rather than with carbohydrates, although the role of receptor and ligand glycosylation in these interactions remains unknown.

In addition to mice, this MHC-independent self-recognition system is conserved at least in rats[13] and humans[14,15]. Similarly to MHC-I molecules, this self-recognition system is also subject to viral and tumour evasion of innate and adaptive immunity. In humans, the LLT1 receptor, an orthologue of rodent Clr proteins, is upregulated in glioblastoma[16], in prostate cancer[17] and in B-cell non-Hodgkin's lymphoma[18], in which the receptor mediates immune escape and contributes to the immunosuppressive properties of tumour cells. Conversely, rat cytomegalovirus encodes a protein named RCTL that closely resembles rat Clr-11 (a homolog of mouse Clr-b). Viral infection stimulates Clr-11 loss, which is rapidly counteracted by RCTL surface expression upregulation. RCTL inhibits NK killing of infected cells via direct interaction with NKR-P1B. Thus, RCTL functions as a decoy ligand to subvert NKR-P1B mediated missing-self recognition by NK cells[19]. Interestingly, this subversion is strain-dependent: the NKR-P1B receptor from the WAG rat strain is susceptible to RCTL binding, whereas the NKR-P1B receptor from the SD rat strain is less susceptible, thereby overcoming this decoy inhibition signal. The allelic divergence of rodent NKR-P1 receptors suggests that host genomes are evolving under selection pressure to avert this viral evasion strategy[7,20]. Similarly, in mice, Clr-b loss was observed upon murine cytomegalovirus (MCMV) infection[21]. Furthermore, the MCMV-encoded immunoevasin m12 was observed to engage the inhibitory NKR-P1B receptor, thus subverting the NKR-P1B:Clr-b immune axis. However, a similar host-pathogen evolutionary interplay is revealed by the engagement of some of the m12 alleles through the activating NKR-P1A/C receptors that avert the MCMV decoy strategy[22]. The mouse Clr-b ligand is also a very sensitive marker of cell health that is rapidly downregulated during chemotherapy-induced genotoxic and cellular stress[23] or poxvirus infection[24] or oncogenesis[25]. Concomitantly, recent studies showed that NKR-P1B:Clr-b missing-self recognition plays a key and non-redundant role in bone marrow transplantation[26,27] and cancer immunosurveillance[25] in a mouse models.

Although the structures of a few mouse NKR-P1 and Clr proteins, as well as the structure of the mouse NKR-P1B:m12 complex, were published[22,28,29], only limited structural data on the NKR-P1:Clr receptor complex are available yet. In some cases, the preparation of soluble C-type lectin-like receptor domains by recombinant expression in *E. coli* followed by *in vitro* refolding might be relatively easy[28,29]. However, this strategy also has several disadvantages. The refolding yields are often too low for structural studies, and the number of cysteine residues present in the expression constructs is usually kept as low as possible, leading to monomeric recombinant proteins (or non-covalent dimers, at best). However, native C-type lectin-like NK receptors are often homodimers linked by one or several disulphide bridges[30], and stable dimer formation might also be a prerequisite for complex formation. Moreover, the role of glycosylation in NKR-P1:Clr recognition could not be ascertained using bacterially expressed proteins.

In this report, we describe a eukaryotic expression system based on transient transfection of a human embryonic kidney 293 (HEK293) cell line to produce native dimeric NK cell C-type lectin-like receptors for structural and functional studies. In contrast to stable transfection and cell line generation, transient transfection offers a quick modularity of the expression construct regarding the purification or visualization tag(s), if necessary. Simultaneously, by using cost-effective transfection reagents, affordable cell culture media and strong expression vectors, milligram amounts of recombinant proteins can be generated within days at only moderate costs and production equipment requirements[31,32]. Moreover, successful selenomethionine incorporation and N-linked glycosylation control, which are important for structural biology, particularly for protein crystallography, were shown in HEK293 cell lines[32,33]. Here, we report the successful application of this technique to the recombinant production of rat C-type lectin-like NK cell receptors.

Results

Optimized transient transfection of suspension-adapted HEK293T cells.
Transient transfection of adherent HEK293T cell lines with several pHLsec plasmids has been successfully used for recombinant protein expression[32]. However, in our laboratory, the growth of high cell quantities in expanded surface roller bottles was rather difficult due to uneven cell attachment to the surface of the culture bottles. Moreover, the expansion of adherent culture prior to large-scale transient transfection using this method was a time-consuming, labour-intensive, and material-demanding procedure. Therefore, we decided to switch to suspension culture, which is affordable (glass bottles can be autoclaved and reused easily), scalable in a range from a few millilitres to hundreds of litres and may yield potentially higher volumetric productivity.
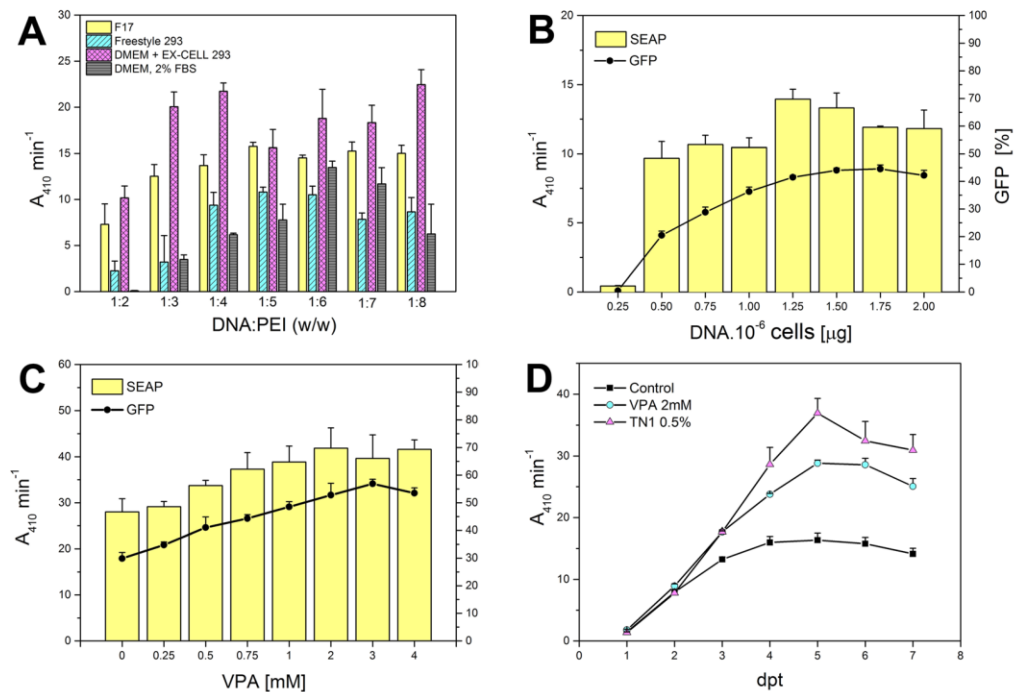
Figure 1. Optimization of transient transfection of suspension adapted HEK293T cells. (**A**) Effect of the DNA-to-PEI ratio on SEAP production in different transfection and production media. (**B**) Effect of the amount of DNA added to the cells. (**C**) Enhancement of transient expression by valproic acid addition at 3 hours post-transfection; transfections were performed in 24-well plates, as described in Materials and Methods, SEAP activity and transfection efficiency were determined 3 days post-transfection (dpt) by measuring the pNPP hydrolysis rate and by flow cytometry (GFP positive viable cells), respectively. (**D**) Transient transfection expression levels as a function of time; SEAP activity was measured each dpt in a control culture, in a culture supplemented with 2 mM VPA and in a culture fed at 2 dpt with 0.5% TN1 hydrolysate; transfections were performed in a 12-well plate, as described in the Materials and Methods section.

An aliquot of 5×10^6 adherent HEK293T cells was thawed and transferred directly into 10 ml of EX-CELL 293 serum-free media, in a 10-cm culture dish. Small floating clumps of cells resumed growth one day later. The culture was pipette-resuspended and split into fresh medium every three days, and we considered the cells fully adapted to serum-free conditions after six splits. Then, we transferred the cell suspension into a square-shaped glass bottle, which was placed on an orbital shaker inside the incubator. Cells resumed growth one day later and grew with a doubling time of approximately 24 h. The EX-CELL 293 medium supports HEK293T high-density cultivation (up to 6×10^6/ml with no apparent loss of viability) and is also suitable for freezing the cells (up to 5×10^7/ml with 5–10% DMSO tested). In contrast, EX-CELL 293 is unsuitable for polyethylenimine (PEI) mediated transfection, most likely due to the presence of negatively charged additives (such as heparin, often used to dissociate cell clumps), which disrupt DNA-PEI transfection polyplexes. We screened several other media for their transfection and production properties using secreted alkaline phosphatase (SEAP) and green fluorescent protein (GFP) as easily quantifiable reporter proteins to monitor secreted protein production and transfection efficiency, respectively. A small volume of cell suspension was transfected with a 19:1 (w/w) mixture of SEAP and GFP expression plasmids, and SEAP activity and transfection efficiency were measured 72 hours later. From the two commercial media tested, F17 medium allows the use of lower DNA:PEI ratios, thus minimizing the risk of potential cytotoxic effects of high PEI concentrations (Fig. 1A). Because the original adherent HEK293T cells were easily transfected in standard DMEM medium supplemented with 2% FBS, we assessed whether these conditions could be modified for suspension conditions. By omitting calcium chloride from the DMEM formulation and by supplementing it with 0.1% Pluronic F-68 instead, we were able to maintain the cells in suspension, although the addition of 2% FBS caused cell aggregation. Conversely, the highest SEAP activities were achieved when transfection was performed in half the desired culture volume of calcium-free DMEM, which was completed with EX-CELL 293 to the full volume 3 hours post-transfection (Fig. 1A). All subsequent transfections were performed in calcium-free DMEM/EX-CELL 293 at a 1:4 (w/w) DNA:PEI ratio.

To maximize the expression yield, we assessed the effect of the DNA amount added to the cells. As shown in Fig. 1B, the amount of DNA necessary for sufficient transfection efficiency and SEAP expression could not be reduced below 1 μg/10^6 cells under these conditions. However, both transfection efficiency and SEAP expression almost doubled when valproic acid was added 3 hours after transfection (Fig. 1C). Valproic acid is a histone deacetylase inhibitor reported to enhance transient gene expression in both HEK293 and CHO cell lines[34] by increasing the overall transcription level while simultaneously inhibiting cell growth[35]. The positive effect of
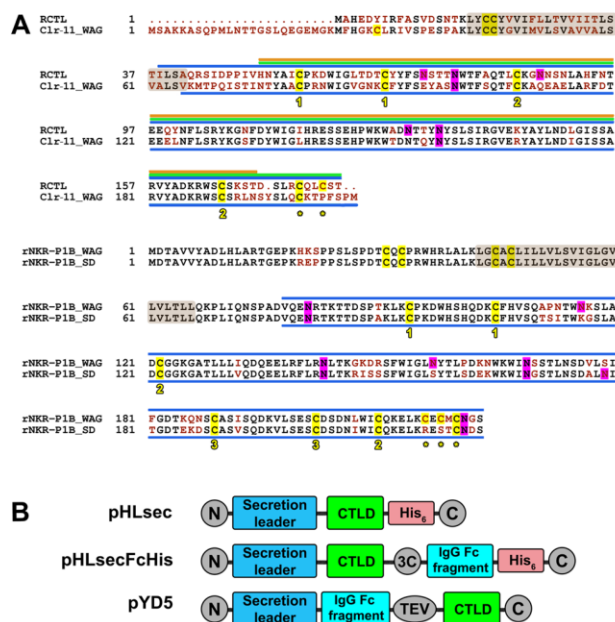
Figure 2. Sequence alignment and design of protein expression constructs. (**A**) Amino acid sequences of rat Clr-11^{WAG}, RCTL, NKR-P1B^{WAG}, and NKR-P1B^{SD} (GenBank accession nos. DQ168419.1, AF302184, EF100678, and EF100684, respectively) were aligned in ClustalW2; non-identical amino acids are indicated in red; transmembrane regions (as predicted by TMHMM 2.0 server) are highlighted in the brown box; cysteine residues are highlighted in yellow, and cysteine residues conserved among C-type lectin-like receptors and forming intramolecular disulphide bridges are numbered according to their linkage, whereas those expected to form intermolecular disulphide bridges are indicated with an asterisk; potential sites of N-glycosylation are highlighted in magenta; the recombinant protein constructs corresponding to C-type lectin-like domain (CTLD) are indicated with blue lines; the following three constructs were generated in case of RCTL: I38-T180 (blue line), H51-T180 (green line), and H51-T170 (orange line). (**B**) Schematic description of protein expression constructs designed using the three plasmids used in this work.

valproic acid (VPA) on transient SEAP expression was confirmed in a time-course study of SEAP expression levels (Fig. 1D). VPA-treated cells analysed by flow cytometry consistently showed a higher level of transfection efficiency and also much higher GFP median fluorescence intensity (data not shown), thus indicating the higher specific productivity of cells transcriptionally activated with VPA. Concurrently, we tried to further boost the expression yield by feeding the cells with casein hydrolysate Tryptone N1 during the production phase, which was previously reported to enhance the productivity of HEK293EBNA cell lines[36]. Peptone additives are often used to replenish nutrients during batch cell culture, and the positive effect of Tryptone N1 (TN1) was also shown in HEK293T cell lines (Fig. 1D). In summary, the optimal values of the transfection and expression parameters were determined for suspension-adapted HEK293T cells through a series of independent experiments, i.e., 1 µg/10^6 cells for DNA, 1:4 for DNA:PEI ratio, calcium-free DMEM and EX-CELL 293 as transfection and production media, respectively, and the expression yield was further enhanced by adding 2 mM VPA and 0.5% TN1, 3 and 48 hours post-transfection, respectively.

Construct design and recombinant expression of soluble rat NK cell lectin-like receptors. We selected rat NK cell C-type lectin-like receptors as a model system to study NKR-P1:Clr interactions. In particular, rat inhibitory NKR-P1B receptors from the WAG and SD rat strains differ in several amino acid residues (Fig. 2A), and these differences lead to differential outcomes when WAG or SD rat strains are challenged by cytomegalovirus infection due to different mechanisms of recognition of the viral RCTL decoy ligand[19]. Conversely, Clr-11 ligand from the WAG and SD rat strains differ only in a single amino acid (R192K in the WAG or SD strain, respectively, not shown) located in the C-terminus of the protein and unlikely involved in receptor binding. Therefore, we consider both Clr-11 sequences functionally equal, and we omitted Clr-11^{SD} from the present study. Clr-11^{WAG} and RCTL sequence alignment (Fig. 2A) shows a highly conserved core of the C-type lectin-like domain surrounded by more variable N- and C-terminal sequences of the extracellular portion of the receptor. The C-type lectin-like domain of NK cell receptors usually contains four to eight conserved cysteine residues responsible for intramolecular disulphide bond formation. These residues are necessary to stabilize the domain fold and several additional cysteine residues in the N- or C-terminal chains involved in dimerization by forming an intermolecular disulphide bridge(s). Furthermore, they are presumably required for stable receptor expression at the cell surface. Interestingly, all four receptors contain their proposed dimerization cysteine residues in their C-termini, suggesting that the N-terminal domain chain may not be necessary for dimer formation in these proteins.
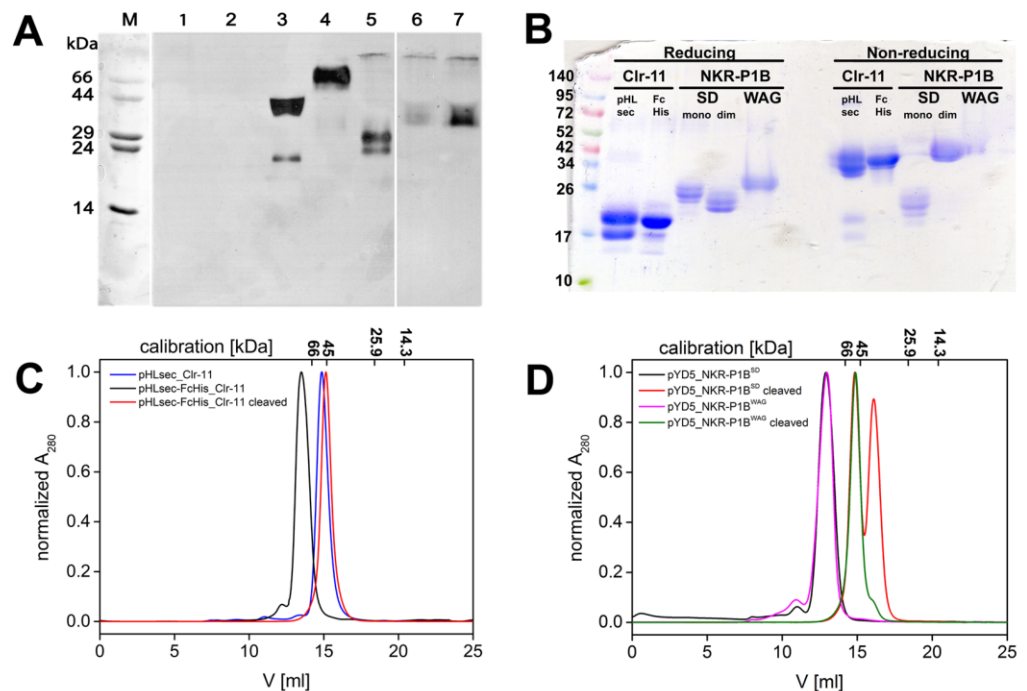
Figure 3. Expression and purification of soluble dimeric rat NK cell C-type lectin-like receptors. (**A**) Small-scale expression test of pHLsec constructs; transfection was performed in a 24-well plate, and 10 μl samples of culture supernatants were collected 3 days later and resolved by 15% SDS-PAGE under non-reducing conditions, transferred onto nitrocellulose membrane and detected by PentaHis mAb; lanes: M, marker; 1, mock transfected; 2, RCTL I38-T180; 3, Clr-11; 4, NKR-P1B^{WAG}; 5, NKR-P1B^{SD}; 6, RCTL H51-T180; 7, RCTL H51-T170. Full-size images of membranes and their photographs are available as Supplementary Information (Figure S1). (**B**) Samples of purified proteins were resolved by 4–20% SDS-PAGE under both reducing and non-reducing conditions; lanes: pHLsec_Clr-11, pHLsec-FcHis_Clr-11 cleaved off by a 3C protease, pYD5_NKR-P1B^{SD} (monomeric and dimeric fractions) and pYD5_ NKR-P1B^{WAG}, both cleaved off by TEV protease. (**C**) Gel filtration profiles of Clr-11, Clr-11-FcHis, and Clr-11 with the FcHis tag cleaved off by a 3C protease. (**D**) Gel filtration profiles of pYD5 Fc-NKR-P1B$^{SD/WAG}$ fusion proteins and NKR-P1B$^{SD/WAG}$ with the Fc tag cleaved off by TEV protease, resulting in the disulphide dimer of NKR-P1B^{WAG} and a mixture of dimer and monomer species of NKR-P1B^{SD}.

Initially, we tried to express the whole extracellular part of RCTL, Clr-11^{WAG}, and both the NKR-P1B^{WAG} and NKR-P1B^{SD} receptors with only slightly shortened N-termini, i.e., including the stalk region. Thus, four expression constructs were generated by PCR amplification from their respective receptor cDNA templates: RCTL I38-T180, Clr-11^{WAG} V65-M207, NKR-P1B^{WAG} V78-S223, and NKR-P1B^{SD} V78-S223. These constructs were cloned to pHLsec expression vector for secreted protein production (Fig. 2B). The vector adds an additional ETG and GTKHHHHHH amino acid sequences to the N- and C-termini of the construct, respectively[32]. Small-scale expression tests (Fig. 3A, lanes 2–5) showed positive expression for all except for the RCTL constructs, moreover, the NKR-P1B^{WAG} were purely dimeric, Clr-11^{WAG} was mostly dimeric, and NKR-P1B^{SD} was monomeric. To also achieve some expression level for the RCTL protein, two shorter constructs were prepared, RCTL H51-T180 and RCTL H51-T170, and the latter was expressed as a monomer, although at a much lower yield (Fig. 3A, lanes 6 and 7). When expressed by transient transfection in square-shaped bottles and purified by IMAC and gel filtration, the final yield of the pure recombinant receptors ranged from 0.2 to 5 mg per litre of production medium, and Clr-11 and RCTL were the best- and worst-produced proteins, respectively.

Generation of dimeric Clr-11^{WAG} by C-terminal Fc fusion. Regarding structural biology and protein crystallography, minor heterogeneities, such as incomplete covalent dimerization of Clr-11^{WAG} (Fig. 3B, lanes pHLsec_Clr-11), potentially leaving some flexible parts unstructured, can be detrimental to the quality and usefulness of the final protein preparation. Additionally, glycosylation heterogeneity or the differential occupation of glycosylation sites (the likely reason for the presence of two bands in Clr-11 preparations, Fig. 3B, lanes pHLsec_ Clr-11) may increase sample heterogeneity even further. To overcome the first issue, we cloned the Clr-11^{WAG} expression construct into the pHLsec-FcHis vector. In this vector, the C-terminus of the expression construct is fused to human rhinovirus (HRV) 3C protease cleavage site followed by the hinge and the Fc regions of the human IgG1 molecule, and by a hexahistidine tag (Fig. 2B). This FcHis fusion was used to promote the disulphide bond-mediated dimerization of Clr-11 because IgG is a disulphide-linked dimer itself and therefore IgG hinge dimerization may help to position the Clr-11^{WAG} dimerization cysteine residues close enough to enable disulphide
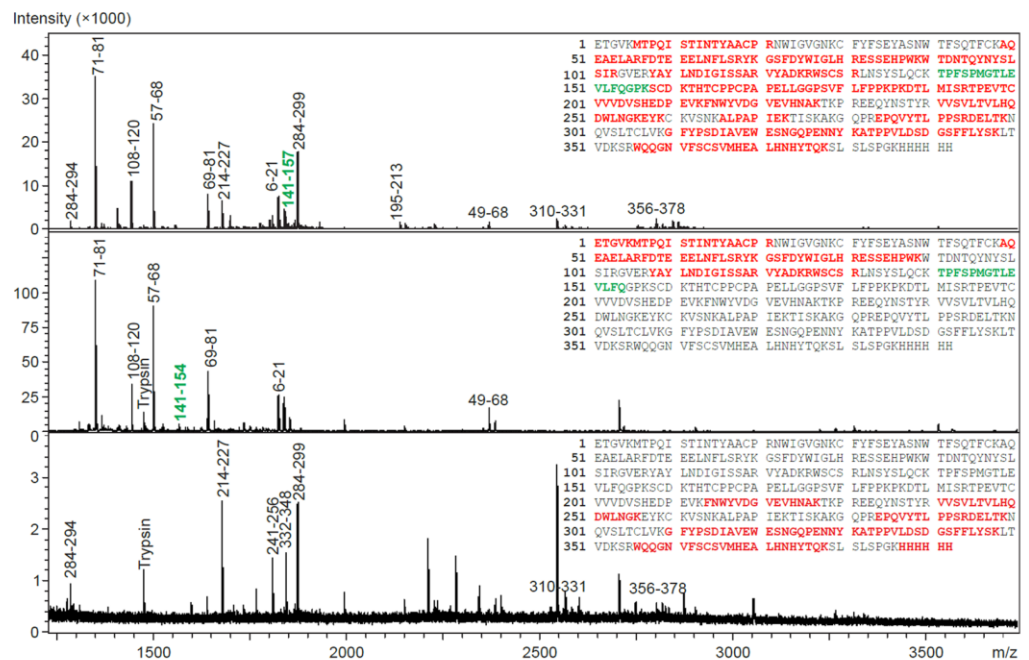
Figure 4. Mass spectrometry analysis of Clr-11-FcHis cleavage with HRV 3C protease. Reduced tryptic digests prepared from SDS-PAGE bands of Clr-11-FcHis (top), Clr-11 with the FcHis fusion cleaved off (middle) and the cleaved FcHis fusion (bottom) were analysed by MALDI-TOF/TOF mass spectrometry. Peptides identified in mass spectra are highlighted in red; peaks in mass spectra are labelled according to corresponding Clr-11-FcHis peptide sequences. The 3C protease cleavage site peptide TPFSPMGTLEVLFQ/GPK is highlighted in green.

bond formation. The expression and purification of Clr-11-FcHis protein was straightforward and at a yield similar to that of the untagged protein, resulting in a purely dimeric fusion Clr-11-FcHis preparation (Fig. 3C, black curve).

The HRV 3C protease preferably cleaves under reducing conditions; however, complete digestion may also be achieved by slightly increasing the protease amount under non-reducing conditions. When applied to the Clr-11-FcHis protein, we observed complete cleavage after one hour at room temperature (data not shown); nevertheless, we chose overnight cleavage at 4 °C for convenience and for lower protease consumption. Because both FcHis fusion and 3C protease contain the histidine tag, we were able to easily separate the cleaved fusion, protease and purely dimeric Clr-11^{WAG} by repeating the purification procedure (Fig. 3C, red curve). Interestingly, the production of Clr-11 with the FcHis fusion also leads to a reduced level of glycosylation heterogeneity, as suggested by the presence of a single band on the SDS-PAGE (Fig. 3B, lane pHLsec-FcHis_Clr-11). When required, glycosylation heterogeneity might be further reduced using N-glycosylation processing inhibitors, such as kifunensine or swainsonine[33], or the N-acetylglucosaminyltransferase I-negative (GnTI⁻) HEK293S cell line[37], which is unable to synthesize complex N-glycans.

Mass spectrometry characterization of Clr-11-FcHis cleavage and dimerization. To confirm disulphide bond status and correct covalent dimer formation, we analysed the SDS-PAGE bands of uncleaved and cleaved Clr-11-FcHis proteins by mass spectrometry. The protein bands were excised and digested by trypsin directly within the gel; the resulting peptides were extracted, reduced and analysed in MALDI-TOF/TOF mass spectrometer (Fig. 4). All three samples analysed showed good sequence coverage. The cleavage site TPFSPMGTLEVLFQ/GPK was identified in Clr-11-FcHis but not in Clr-11, where the FcHis fusion was cleaved off and replaced by the TPFSPMGTLEVLFQ peptide, corresponding to the correct fusion cleavage. When examining Clr-11-FcHis and Clr-11 tryptic and Asp-N peptides prepared under non-reducing conditions, we were able to confirm the correct intramolecular disulphide bond connection (data not shown) of all four cysteines present in the C-type lectin-like domain (CTLD), i.e., C80-C91 and C108-C190. More importantly, we were also able to distinguish a cystine dipeptide LNSYSLQCK-LNSYSLQCK, corresponding to the correct covalent intermolecular C200-C200 disulphide bond, and stable dimer formation (Fig. 5).

Generation of dimeric NKR-P1B by N-terminal Fc fusion. Subsequently, we tried to apply the same approach to NKR-P1B^{SD} and NKR-P1B^{WAG}, i.e., to produce these expression constructs as C-terminal FcHis fusions to promote their dimerization. Although we were able to express and purify these fusion proteins in a dimeric form and at a good yield (improved in comparison with the untagged proteins; data not shown), we were unable to efficiently cleave off the FcHis fusion with the 3C protease. A possible explanation is that the dimerization cysteines of the receptor and of the IgG hinge region cross-linked with each other. Thus, although
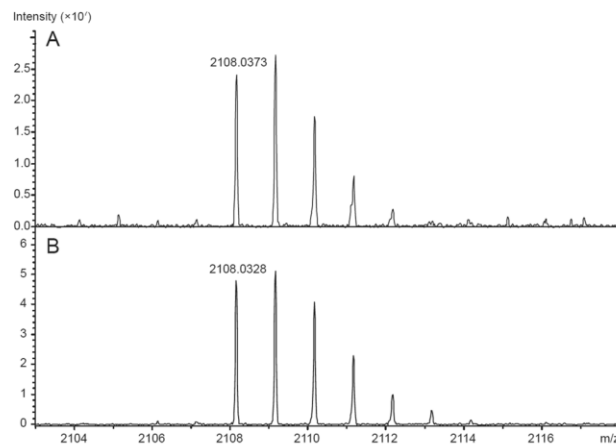
Figure 5. Mass spectrometry analysis of Clr-11 covalent dimerization. MALDI TOF/TOF analyses of tryptic digests of (**A**) Clr-11-FcHis and (**B**) Clr-11 after 3C protease cleavage, both prepared under non-reducing conditions. The m/z value 2108.03 corresponds to the dimerization cystine dipeptide LNSYSLQCK-LNSYSLQCK.

these recombinant fusion proteins are dimeric, their dimerization mode may not be physiological. Reducing the number of cysteine residues in the hinge region or completely removing them from the expression constructs may promote correct dimerization exclusively through the CTLD cysteines.

To overcome this problem, we tested the reverse arrangement of these Fc fusion constructs, i.e., we attached the IgG Fc region to the N-terminus of the NKR-P1B ectodomain using a pYD5 plasmid (Fig. 2B), enabling the subsequent cleavage of the fusion by the tobacco etch virus (TEV) protease. The expression yields of the pYD5_NKR-P1B$^{SD/WAG}$ fusion constructs were similar to those of previous FcHis constructs, and gel filtration showed their correct dimeric state (Fig. 3D, black and magenta curve). Upon cleavage with the TEV protease, we obtained the purely disulphide dimer of the NKR-P1B^{WAG} ectodomain (Fig. 3D, green curve and Fig. 3B, lanes WAG), whereas the NKR-P1B^{SD} ectodomain yielded a mixture of dimeric and monomeric species (Fig. 3D, red curve and Fig. 3B, lanes SD). This difference is likely caused by the fact that NKR-P1B^{WAG} has three cysteine residues in its C-terminus, whereas NKR-P1B^{SD} has a single cysteine in the same position; therefore, disulphide dimerization is more efficient in the NKR-P1B^{WAG} ectodomain.

For the RCTL protein, we were unable to improve its expression yield and dimeric state, even when using FcHis or pYD5 fusion constructs; therefore, we are not yet able to report the successful preparation of any stable soluble form, monomeric or dimeric, of this viral decoy protein in reasonable yield. RCTL is apparently much less stable than its host NK cell counterpart, and its preparation will require further optimization.

Sedimentation analysis confirms dimeric status of prepared proteins. To further characterize the solution behaviour of the prepared dimeric proteins, sedimentation analysis was performed in an analytical ultracentrifuge. Gel filtration suggested that Clr-11 prepared using a histidine-tagged construct (showing incomplete covalent dimerization, Fig. 3B, lanes pHLsec_Clr-11) and the purely dimeric Clr-11 cleaved from the FcHis fusion construct migrate at the same position (Fig. 3C, blue and red curve), thus suggesting that Clr-11 likely forms a stable non-covalent dimer in solution, even in absence of the stabilizing disulphide bridge. Sedimentation velocity experiments performed with the histidine-tagged Clr-11 showed a single peak in the sedimentation coefficient distribution (Fig. 6A, bottom) with an $s_{20,w}$ value of $3.04 \pm 0.2\,S$, which corresponds to a dimeric protein with a moderately elongated shape and with predicted dimensions of approximately $8-10 \times 3-4\,nm$. However, the broad shape of the peak in sedimentation coefficient distribution suggests the presence of monomer-dimer equilibrium at lower protein concentrations. The weight-average molecular weight of $40837 \pm 500\,Da$ was calculated based on the results from the sedimentation equilibrium experiment (Fig. 6B), which also matched the value expected for the glycosylated dimer ($2 \times 18211 = 36422\,Da$ for the dimeric protein itself + mass of up to 4 N-glycosylation sites occupied per dimer).

Similarly, the sedimentation velocity analyses performed for Clr-11 cleaved from pHLsec-FcHis and for both NKR-P1B^{SD} and NKR-P1B^{WAG} cleaved from pYD5 fusion constructs fully confirmed their entirely dimeric state, yielding $s_{20,w}$ values of $3.10 \pm 0.05\,S$, $3.45 \pm 0.05\,S$ and $3.68 \pm 0.1\,S$, respectively (Fig. 6C, solid coloured lines). The shift of these individual sedimentation coefficient values reflects the difference in molecular weight of the individual protein expression constructs and differences in the number of their N-glycosylation sites. Compared with histidine-tagged Clr-11 expressed from the pHLsec vector, Clr-11 cleaved from the pHLsec-FcHis construct is much more homogeneous and shows no sign of monomer-dimer equilibrium (Fig. 6C, black vs. red solid lines). We have also analysed the entire Fc-fusion proteins (Fig. 6C, dashed coloured lines). Their resulting peaks of these ca 100 kDa dimeric fusion glycosylated constructs with apparent sedimentation coefficient values ranging from 5 to 5.5 S correspond to the size and shape of expected elongated particles with estimated dimensions of $13-15 \times 4-5\,nm$. Thus, a fusion of extracellular parts of C-type lectin-like receptors to the Fc region of human IgG is not only an efficient method of preparation of disulphide dimers of these receptors, but also a strategy for the generation of immunoactive constructs with therapeutic potential.
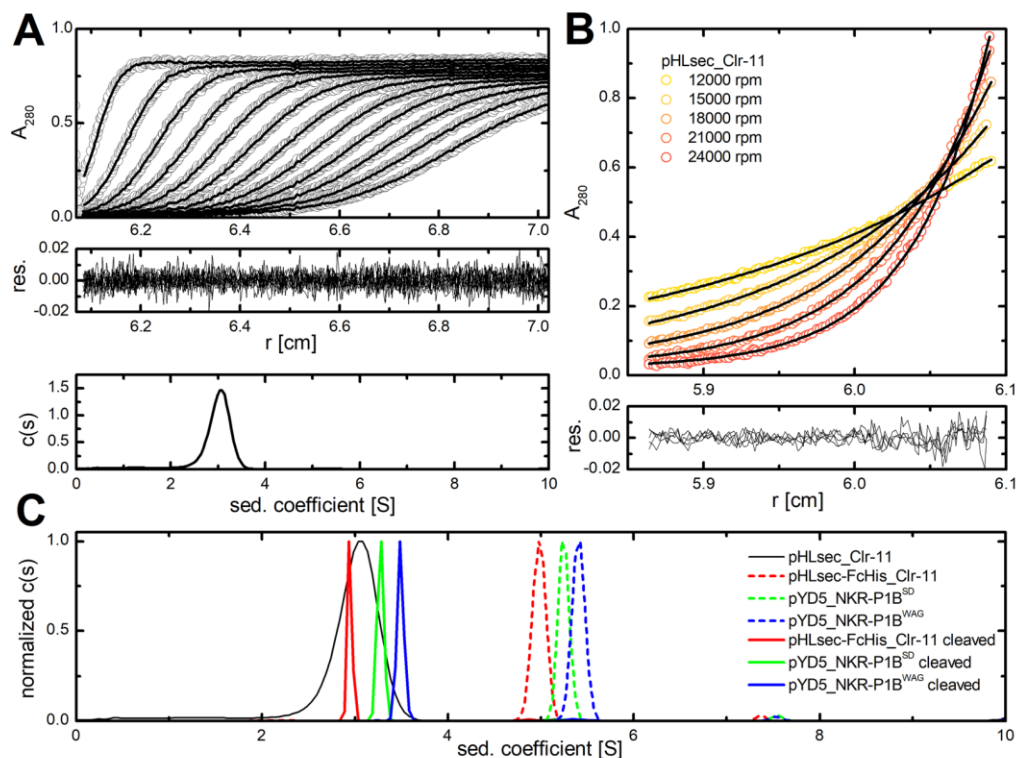
Figure 6. Sedimentation analysis of rat Clr-11 and NKR-P1B dimeric expression constructs. (**A**) pHLsec_Clr-11 protein was analysed by sedimentation velocity; panels show (from top to bottom) absorbance scans recorded at 280 nm (every fifth scan is shown, circles) together with fitted curves (lines), residuals derived from the fitted data, and the resulting c(s) continuous distribution of the sedimentation coefficient. (**B**) pHLsec_Clr-11 was spun at 12–15–18–21–24000 rpm and 4 °C and its sedimentation equilibrium was monitored at 280 nm. The upper panel shows absorbance data (circles) with fitted curves (non-interacting discrete species model, lines), whereas the lower panel shows residuals derived from the fitted data. (**C**) Normalized continuous sedimentation coefficient distributions of pHLsec_Clr-11 (black line), Clr-11 (red line) and both NKR-P1B^SD (green line) and NKR-P1B^WAG (blue line) cleaved from pHLsec-FcHis and pYD5 Fc fusion constructs, respectively, as well as the distributions of the original uncleaved Fc fusion constructs (the same colour coding, dashed lines).

FTIR spectroscopy analysis of protein secondary structure shows well-folded native proteins.

Lastly, the secondary structure of all recombinant soluble receptor constructs was examined by Fourier-transform infrared (FTIR) spectroscopy (Fig. 7 and Table 1). The FTIR spectra of all studied proteins are dominated by two broad bands corresponding to vibrations of the peptide linkage – amide I at ~1639 cm^{-1} (dominated by νCO, i.e., stretching vibrations of CO group) and amide II at ~1550 cm^{-1} (dominated by δNH, i.e., bending vibrations of the NH group, and νCN; Fig. 7A–D). The overall character of these spectra and the maximum of the amide I band correspond to proteins dominated by β-sheet structure. The intensity ratio of amide I and amide II bands, which reflects presence of aggregates, corresponds to fully soluble globular proteins, and no marks of aggregated structures are present (amide I/amide II ratio is close to 3:2 in soluble globular proteins and 1:1 in aggregated structures, whereas the band of intermolecular/aggregated β-sheets at ~1620 cm^{-1} is missing). The second derivative of Clr-11 FTIR spectra clearly shows a high content of β-sheets by the strong negative band at 1637 cm^{-1}, thus confirming that Clr-11 is structurally similar to mouse Clr-g.

The results of secondary structure analysis are summarized in Table 2. The differences between the original FTIR spectra and the fitted curves taken from the protein spectra reference set are very low (lower than 6%, not shown). This translates into reasonable estimations of the protein secondary structure because the relative sums of the estimated structures are < 110%. All estimated secondary structures are very close to each other, as expected for proteins belonging to the same structural family. The estimated secondary structures of monomeric and dimeric NKR-P1B^SD are identical, and also the NKR-P1B^WAG structure differs only very little. The secondary structure estimated for dimeric NKR-P1B^SD in solution and calculated from its crystal structure is very close and inside the margins of errors, which is also true for soluble rat Clr-11 and for the crystal structure of the closely related mouse Clr-g. The values estimated in this study for the dimeric NKR-P1B^SD are also very close to values previously estimated for a monomeric, bacterially expressed and refolded, shorter expression construct of rat NKR-P1B[38].
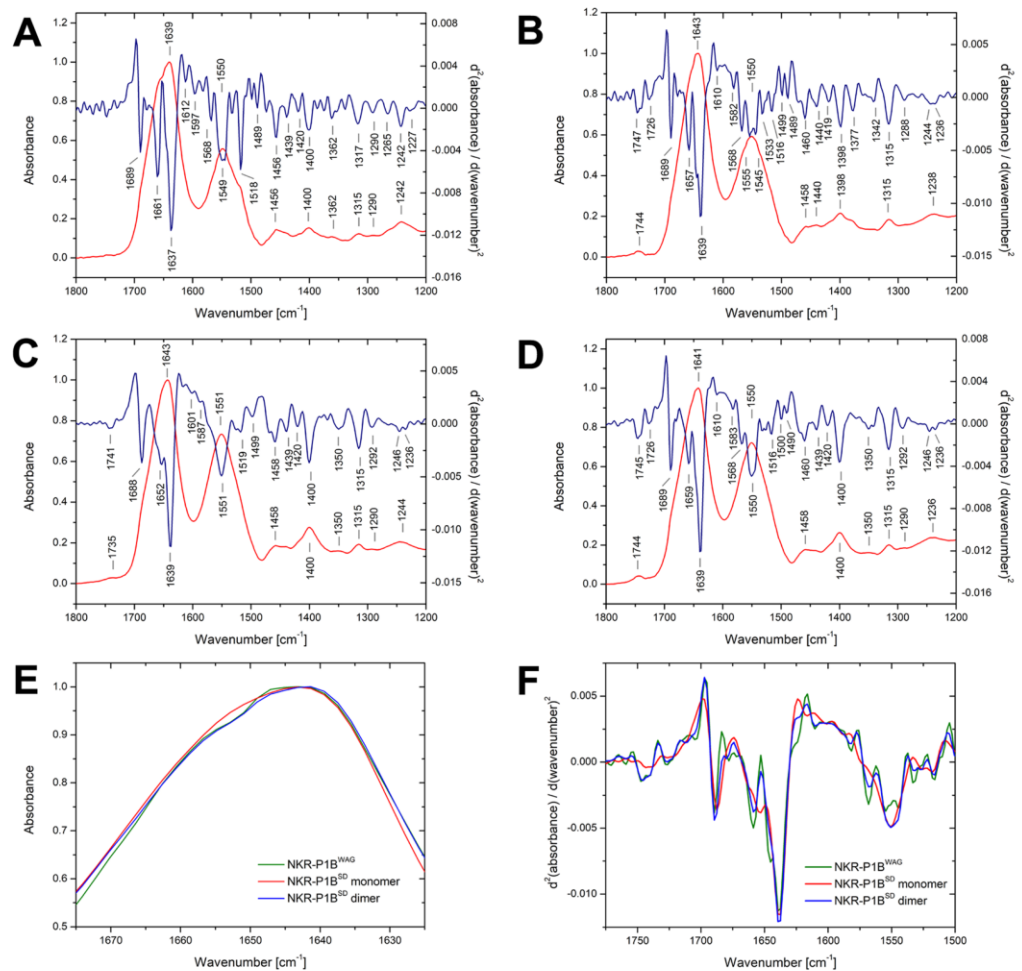
Figure 7. FTIR spectroscopy analysis of recombinant dimeric rat NK cell receptors. Fourier-transform infrared spectra of (**A**) Clr-11 cleaved from pHLsec-FcHis, (**B**) NKR-P1B^{WAG}, (**C**) monomeric, and (**D**) dimeric NKR-P1B^{SD}, all cleaved from pYD5 fusion constructs, in the region of amide I, II and III bands depicted as red curves. The blue line corresponds to the second derivative of the spectrum smoothed by Savitski-Golay function at 7 points; distinct spectral bands are labelled, and band assignment is outlined in Table 1. (**E**) Detailed comparison of the FTIR spectra and their (**F**) second derivatives for monomeric and dimeric NKR-P1B^{SD}, and NKR-P1B^{WAG} in the region of amide I and II bands.

Although the NKR-P1B^{SD} and NKR-P1B^{WAG} dimers are highly similar – both show the same pattern in amide I and II regions – a slight, yet distinct, difference between the NKR-P1B^{SD} monomer and the corresponding dimer is visible at ~1655 cm^{-1} (Fig. 7E), even though their secondary structures show no significant differences (Table 2). The differences are best observed when using the second derivatives (Fig. 7F). The band at 1652 cm^{-1} is shifted at 1659 cm^{-1} upon NKR-P1B^{SD} dimer formation. Unfortunately, this band shift might be attributed both to α-helices or disordered structures[39], or even partly to turns[40]. Slight changes in turns are observed in the region at ~1689 cm^{-1}. However, no changes in β-sheet bands are identified. Thus, β-sheets unlikely participate in NKR-P1B^{SD} dimerization, further confirming that the NKR-P1B^{SD} dimer structure in solution is the same as the crystal structure in which the dimerization interface is formed by α-helices and surrounding turns and loops without involving the β-sheet protein core.

Discussion

Although new detailed structural and functional data are revealing the functional role of NKR-P1 monomers and dimers and the nature of the NKR-P1:Clr interaction, difficulties producing stable covalent NKR-P1 homodimers require using recombinant NKR-P1 proteins from different host organisms in a different stoichiometry. Recently, Hernychová *et al.* reported that only monomeric forms of mouse NKR-P1B could bind to Clr-b on cell surface, suggesting that NKR-P1B monomers might separately participate in the interaction with Clr-b or that the interaction itself might promote NKR-P1B dimerization[41]. Although the signalling efficiency of monomeric NKR-P1B was not evaluated in this study, Hernychová *et al.* concluded that NKR-P1B homodimers are not functional, regardless of the presence of a stalk region, which did not affect the interaction and was not even crucial

Frequency (cm^{-1})	Assignment	References
1227/—/—/—	β-sheet (amide III)/His	[39,54–56]
1242/1236/1236/1236	β-sheet (amide III)/Tyr–OH	[39,54–56]
1265/1246/1246/1244	coil (amide III)/Tyr–OH	[39,54–56]
1290/1292/1292/1288	β-turns (amide III)	[54,55]
1317/1315/1315/1315	α-helix (amide III)	[54,55]
1362/1350/1350/1342	Trp	[39,56]
1400/1400/1400/1398	Asp/Glu (ν_sCOO$^-$)	[39,56]
—/—/—/1419	Trp/Pro?	[39,56]
1439/1439/1439/1440	δCH$_2$, Pro (νCN), His$^-$(δCH & δCN)	[39,56]
1456/1458/1460/1460	δCH$_2$, δCH$_3$/Tyr/Trp?	[39,56]
1489/—/1490/1489	Trp? (νCC ring & δCH)	[39,56]
—/1499/1500/1499	Phe/Tyr–O$^-$ (νCC ring)?	[39,56]
1518/1519/1516/1516	Tyr–OH (νCC ring & δCH)	[39,56]
—/—/—/1533	amide II	[40,56]
—/—/—/1545	amide II	[40,56]
1549/1551/1550/—	amide II	[40,56]
—/—/—/1555	amide II	[40,56]
1568/—/1568/1568	Asp/Glu (ν_{as}COO$^-$)	[39,56]
1597/1587/1583/1582	Tyr (νCC ring)	[39,56]
—/1601/—/—	Tyr–O$^-$ (νCC ring)?	[39,56]
—/—/1610/1610	Tyr (νCC ring)	[39,56]
1637/1639/1639/1639	β-sheet (amide I)	[40,57]
1661/1652/1659/1657	α-helix/coil/turns (amide I)	[40,57]
1689/1688/1689/1689	β-sheet antiparallel/ turns (amide I)	[40,57]
—/—/1726/1726	Asp/Glu (νC=O)	[39,54,56]
—/1741/1745/1747	Asp/Glu (νC=O)	[39,54,56]

Table 1. Assignment of the infrared bands distinguishable in the second derivatives of Clr-11/monomeric NKR-P1B^{SD}/dimeric NKR-P1B^{SD}/NKR-P1B^{WAG} receptors FTIR spectra shown in Fig. 7 (ν corresponds to stretching, δ to bending, *as* to anti-symmetrical, and *s* to symmetrical vibrations).

NKR-P1B^{WAG}		Clr-11		mouse Clr-g	
Structure	**LSA (%)**	**LSA *N* (%)**	**LSA (%)**	**LSA *N* (%)**	**crystal structure***
α-helix	21 ± 10	20	23 ± 10	22	17
β-sheet	28 ± 9	27	25 ± 9	24	27
β-turn	14 ± 4	13	13 ± 4	12	12
Bend	15 ± 4	14	14 ± 4	13	15
Disordered	27 ± 6	26	30 ± 6	29	29
Sum	105%	100%	105%	100%	100%
NKR-P1B^{SD} monomer		**NKR-P1B^{SD} dimer**		**NKR-P1B^{SD} dimer**	
Structure	**LSA (%)**	**LSA *N* (%)**	**LSA (%)**	**LSA *N* (%)**	**crystal structure***
α-helix	23 ± 10	22	23 ± 10	22	19
β-sheet	28 ± 9	26	28 ± 9	26	28
β-turn	14 ± 4	13	14 ± 4	13	15
Bend	16 ± 4	15	16 ± 4	15	13
Disordered	26 ± 6	24	26 ± 6	24	25
Sum	107%	100%	107%	100%	100%

Table 2. Estimation of the secondary structure content of the prepared proteins using the least-squares method (LSA)[51] analysing amide I & II bands in infrared spectra (*N* marks values normalized to 100%). Given standard deviations are calculated as standard deviations of the used reference set; therefore, they do not reflect the quality of the fits. *Calculated using DSSP[58] on the crystal structures of mouse Clr-g (PDB ID 3RS1)[29] and rat NKR-P1B^{SD} dimer (PDB ID 5J2S). However, in the NKR-P1B^{SD} crystal structure, only 118 amino acid residues are visible, i.e., 29 residues (20%), fewer than those present in the expressed protein construct.Given standard deviations are calculated as standard deviations of the used reference set; therefore, they do not reflect the quality of the fits.

for protein dimerization. Remarkably, in another recent publication Balaji *et al.* showed that only homodimers of mouse NKR-P1B were able to functionally engage CD3ζ-Clr-b chimeras on cells[42]. Moreover, in contrast to the Hernychová *et al.* findings, Balaji *et al.* reported that abrogation of the intermolecular cystine bond was detrimental to functional signalling, precluding the NKR-P1B self-association and higher-order cross-linking of Clr-b. However, NKR-P1B homodimers were not essential for the formation of a stable NKR-P1B:m12 viral immunoevasin complex, most likely because the NKR-P1B:m12 complex has a much higher affinity than the NKR-P1B:Clr-b complex. Unfortunately, discrepancies in the preparations of mouse NKR-P1B protein prevent direct comparisons between these results. Soluble, renatured NKR-P1B, produced in *E. coli*, which results in a mixture of monomers and multiple species of covalent homodimers, was used in the first study[41], whereas Balaji *et al.* was unable to produce covalent homodimers of NKR-P1B in HEK293 cells and instead used tetrameric NKR-P1 particles consisting of four streptavidin-bound biotinylated NKR-P1B monomers.

To meet this need, we developed a rapid method for the preparation of stable soluble covalent NKR-P1 dimers in HEK293 cells suitable for further functional studies and offering therapeutic potential thanks to the presence of IgG Fc fragment, if desired. First, we adapted HEK293T cells for growth in suspension in EX-CELL 293 medium supporting high-density cultures. When compared with adherent cultures, suspension cultures have the potential to be more economical (and ecological) due to their lower requirements for single-use plastic consumables and higher volumetric productivity. However, the likely presence of negatively charged additives (e.g., heparin) may have contributed to ineffective PEI-mediated transfection of HEK293T cells in EX-CELL 293 medium. This is however not a problem in F17 or calcium-free DMEM media in which we were able to optimize transfection parameters (i.e., $1 \mu g$ plasmid DNA/10^6 cells, 1:4 (w/w) DNA:PEI ratio, and calcium-free DMEM and EX-CELL 293 as transfection and production media, respectively), and to confirm the positive effect of 2 mM valproic acid added 3 hours post-transfection, as well as of Tryptone N1 added 48 hours post-transfection, on the yield of secreted protein.

To demonstrate the feasibility of preparing covalent disulfidic NKR-P1B dimers in our optimized expression system, we selected the rat inhibitory NKR-P1B:Clr-11 as a model receptor:ligand system – particularly because NKR-P1B receptors from WAG and SD rat strains share their native ligand Clr-11 but differ in their reactivity towards the viral decoy ligand RCTL[19]. Although we have been able to produce dimeric NKR-P1B^WAG and mostly dimeric Clr-11, we were unable to obtain covalent dimers of the NKR-P1B^SD and RCTL molecules. The RCTL viral decoy ligand proved especially difficult to express, and we obtained only low yields of its monomeric form. The varied dimerization propensity of the NKR-P1B^WAG and NKR-P1B^SD receptor ectodomains is proportional to the number of available C-terminal dimerization cysteines – the NKR-P1B^WAG has three such cysteine residues, whereas NKR-P1B^SD contains only one.

Nevertheless, to further promote the covalent dimerization of soluble Clr-11 and NKR-P1B^SD, we have prepared fusion constructs with a C-terminally attached Fc fragment of the human IgG1 molecule, cleavable with HRV 3C protease. The C-terminal fusion of Fc fragment was a successful strategy in the case of Clr-11, resulting in stable Cys200-Cys200 bound Clr-11 covalent dimer, as confirmed by mass spectrometry. However, we were unable to cleave off the C-terminal Fc fragment from both NKR-P1B isoforms, most likely due to cross-linking of IgG cysteines with the C-terminal dimerization cysteines of the receptor. This problem caused by the proximity of the C-terminal NKR-P1B to the Fc IgG cysteines was solved by fusing the Fc fragment to the N-terminus of the NKR-P1B ectodomain, thereby efficiently cleaving off the N-terminal Fc fragment and yielding pure NKR-P1B^WAG covalent dimer and a separable mixture of NKR-P1B^SD monomer and covalent dimer. Thus, we do not recommend C-terminal Fc fragment fusion for rat NKR-P1 expression because it can result in the formation of non-physiological dimers. Conversely, N-terminal Fc fragment fusion is a suitable expression strategy to quickly prepare covalent rat NKR-P1 dimers in milligram quantities.

Further gel filtration and sedimentation velocity analyses showed that monomeric Clr-11 exhibits an equilibrium of monomers and non-covalent dimers in solution, as expected because several *Clec2* orthologues, including mouse Clr-g[29] and Clr-b[42] and human LLT1[43] and CD69[44], have been shown to form non-covalent dimers in solution. Furthermore, the prepared covalent dimers of NKR-P1B^WAG, NKR-P1B^SD and Clr-11 showed no sign of monomer-dimer equilibrium, thus corroborating the efficiency of our expression strategy. The prepared receptors were also examined by FTIR spectroscopy clearly showing fully soluble globular proteins with no signs of aggregation. Furthermore, analysis of FTIR spectra confirmed the structural similarity of rat Clr-11 to mouse Clr-g. However, the comparison of FTIR spectra of monomeric and dimeric NKR-P1B^SD showed that its β-sheets are unlikely to participate in NKR-P1B^SD dimerization. This finding corroborates the crystal structure of NKR-P1B^SD (PDB ID 5J2S – Vaněk *et al.*, manuscript in preparation), wherein the dimerization interface is mainly formed by α-helices. Combined with the recently reported unconventional dimerization modes of mouse NKR-P1B[41,42], these results indicate that dimerization within the NKR-P1 receptor family differs from that observed in *Clec2* ligands.

Several factors likely hinder the effective formation of covalent dimers of soluble NKR-P1 constructs. When compared with the Clr receptor family, the weaker mode of non-covalent dimerization of NKR-P1B, as revealed in its crystal structures (Balaji *et al.*[42] and PDB ID 5J2S), has rather weak affinity. Therefore, membrane anchoring of the NKR-P1B molecule may be required for the effective formation of disulphide bonds within its stalk region. Thus, by providing such steric anchoring through N-terminal fusion to the Fc-fragment, the dimerization cysteines can be brought into functional proximity and promote the formation of disulphide bridges. The low propensity for non-covalent dimerization is apparently a common feature of NKR-P1 molecules and suggests that the weaker non-conventional mode of dimerization might be conserved throughout the NKR-P1 family. This overall conformational flexibility of NKR-P1 molecules might be also the reason why it is practically impossible to detect and measure the binding of rodent NKR-P1 receptors to their respective Clr ligands in solution. Apparently, the affinity of individual NKR-P1:Clr interaction is extremely weak and largely undetectable by standard biophysical approaches[42]. Yet such behaviour is not uncommon among immune receptor:ligand complexes where it is the

interaction avidity (provided by, e.g., cross-linking of the dimeric receptor:ligand molecules on the cell surface) that plays a major role in signal transduction to the cell.

In summary, the method described herein enables high-level expression of secreted recombinant soluble dimeric forms of rat NK cell C-type lectin-like receptors in quantity and quality sufficient for their biophysical, functional, and structural characterization. Transient transfection is an easily scalable, non-viral, fast and affordable method of recombinant protein production in HEK293 cell lines that allows us to use modular construct design. Furthermore, the fusion of receptor expression constructs to an Fc fragment of human IgG promotes receptor disulphide dimer formation and could be used for purification, detection, or therapy. This approach can be applied to generate other soluble NK cell surface antigens, thus enabling their detailed structural and functional characterization leading to detailed molecular insights necessary for successful rational design of new protein-based immunotherapeutics.

Methods

Chemicals. 25-kDa linear polyethylenimine (Polysciences, USA) was dissolved in water, neutralized with HCl, sterilized by filtration (0.22 μm), aliquoted and stored at −80 °C; a working aliquot was stored at 4 °C. Valproic acid and Pluronic F-68 (both Sigma, USA) were dissolved in water to 0.5 M and 10% (w/v), respectively, sterilized by filtration and stored at −20 °C. Casein hydrolysate Tryptone N1 (Organotechnie, France) was dissolved in F17 medium (GIBCO Invitrogen, USA) to 20% (w/v), sterilized by filtration and stored at 4 °C.

Cell culture. HEK293T cells were kindly provided by Radu A. Aricescu[32] and were maintained as adherent monolayers in standard Dulbecco's Modified Eagle's Medium (DMEM, 4.5 g/l glucose, Institute of Molecular Genetics, The Czech Academy of Sciences, Prague) supplemented with 4 mM L-glutamine, non-essential amino acids and 10% foetal bovine serum (GIBCO Invitrogen, USA) in standard flasks (TPP, Switzerland) in a humidified 37 °C, 5% CO_2 incubator. Suspension adapted HEK293T cells ($0.25–6 \times 10^6$/ml) were maintained in EX-CELL 293 serum-free medium (Sigma, USA) supplemented with 4 mM L-glutamine in standard dishes (TPP, Switzerland) or square-shaped glass bottles with gas permeable caps (DURAN, Germany) using 30–40% of the nominal volume at 135 rpm (Orbit 1000 orbital shaker, rotational diameter 19 mm; Labnet, USA; bottles were fixed with Sticky Pad adhesive mat; New Brunswick Scientific, USA) placed within the same incubator[45].

Vectors, cloning, and DNA purification. The pTTo3c-SSH and pTTo-GFPq vectors containing secreted alkaline phosphatase and green fluorescent protein, respectively, were kindly provided by Dr. Yves Durocher, as well as pYD5 vector (pTT5 derivative with N-terminal human IgG Fc fragment tag cleavable by TEV protease that was in-house modified to contain AgeI/KpnI cloning sites)[31]. The pHLsec and pHLsec-FcHis vectors were kindly provided by Dr. Radu A. Aricescu[32]. Isolation of cDNA of rat NKR-P1B, Clr-11, and RCTL receptors was previously described[19]. Briefly, PCR products were digested, purified and inserted into pHLsec, pHLsec-FcHis or pYD5 vectors using the flanking AgeI and KpnI sites. Positive clones were screened by colony PCR using TaqRed PCR master mix (Top-Bio, Czech Republic). The primers used to amplify the desired expression constructs and the vector-specific primers are listed in Supplementary Information (Table S1). All inserts were sequenced, and the plasmid transfection stocks were prepared using NoEndo JETSTAR 2.0 Plasmid Maxiprep Kit (Genomed, Germany) according to the manufacturer's recommendations. Using a single kit column, 3–4 mg of pure plasmid DNA (A_{260}/A_{280} ratio of 1.8–2.0) was usually obtained from 500 ml of *E. coli* DH5α culture grown in Luria broth medium (in our experience, cultures grown for more than 12-14 h give lower yields).

Small-scale transient transfections. Cells were centrifuged and resuspended in appropriate fresh transfection medium at a density of 0.5×10^6/ml. Transfection medium was calcium-free DMEM (as above, but calcium chloride and FBS were not used in the preparation; instead, 0.1% Pluronic F-68 was added) either supplemented with 2% FBS or completed with EX-CELL 293 post-transfection (see below). Alternatively, F17 (supplemented with 4 mM L-glutamine and 0.1% Pluronic F-68) or Glutamax-I Freestyle 293 medium (both GIBCO Invitrogen, USA) were used, as indicated in Results, and 0.5 ml of cell suspension was distributed per well in a 24-well plate (or 1×10^6/ml in case of calcium-free DMEM and 0.25 or 1 ml of cell suspension was distributed per well in a 24- or 12-well plate, respectively). The desired amount of DNA ($1 \mu g/10^6$ cells unless otherwise noted) was diluted in PBS (in a volume equivalent to one-tenth of the culture to be transfected), PEI was added to desired ratio (w/w; 1:4 unless noted otherwise), and the mixture was immediately vigorously shaken and incubated for 10–15 min at room temperature before adding it to the cells. Following a 3 h incubation with DNA-PEI complexes, the culture medium was completed to 0.5 ml (24-well plate) or 2 ml (12-well plate) with EX-CELL 293 in case of calcium-free DMEM transfections, and VPA was added (concentrations indicated in the text refer to a final culture volume).

SEAP analysis. SEAP activity (ΔA_{410}/min) was determined as previously described[31]. Briefly, culture supernatants were diluted with water as required (typically 1/100 to 1/1000), and 180 μl was transferred to a 96-well plate. The enzymatic reaction was initiated when 20 μl of SEAP assay solution (20 mM *p*-nitrophenyl phosphate; pNPP, 1 mM $MgCl_2$ and 1 M diethanolamine pH 9.8) were added, and absorbance was read at 410 nm in 1 min intervals at room temperature to determine the pNPP hydrolysis rates (Safire microplate reader, Tecan, Austria). Data are expressed as the mean of one experiment performed in triplicate with error bars representing standard deviations. Each sample was independently assayed for SEAP activity three times to minimize pipetting errors.

Flow cytometry. GFP-positive viable cells were estimated using a BD LSR II flow cytometer (BD Biosciences, USA). For each assay, 50 μl of cell suspension were transferred to a round-bottom 96-well plate, diluted with 150 μl of PBS and stained with 10 μl of propidium iodide (PI; 10 μg/ml in PBS) before analysis. Viable transfected cells were quantified using appropriate gating to exclude dead cells, debris and aggregates in a forward vs. side

scatter plot. Data are shown as mean of one experiment performed in triplicate with error bars representing standard deviations.

Transfection in square-shaped bottles.   For large-scale recombinant protein production, the respective expression plasmid (1 μg/10⁶ of cells to be transfected, typically 400 μg) was diluted in 10 ml of PBS, filter sterilized, and PEI was added at a 1:4 weight ratio (typically 1.6 mg). The mixture was then shaken and incubated for 10 min. Meanwhile, exponentially growing HEK293T cells were centrifuged and resuspended in calcium-free DMEM at a density of 2 × 10⁶/ml (typically in 200 ml of medium in a 1 l square-shaped bottle) and immediately transfected. Following a 3–4 h incubation period with DNA-PEI complexes, the culture medium was completed with an equal volume of EX-CELL 293 (typically 200 ml), and VPA was added to 2 mM concentration. Two days later, the culture was fed with 0.5% TN1. Conditioned culture medium containing secreted recombinant protein was harvested by centrifugation 4–6 days post-transfection and stored at −20 °C until protein purification.

Protein purification.   Conditioned medium was thawed, clarified by centrifugation at $25000 \times g$, and filtered through a 0.22 μm membrane (Steritop filter, Millipore, USA). The medium was diluted twofold with PBS, and the final pH was adjusted to 7.0, when necessary. IMAC purification was performed using cobalt-coated TALON beads (Clontech, USA) in batch mode using 2 l Erlenmeyer flasks. Following a 30-min incubation period with shaking at 110 rpm, the beads were collected in a gravity flow Econo column (Bio-Rad, USA), washed with PBS and the bound His-tagged protein was eluted with PBS containing 250 mM imidazole. The eluate was concentrated with Amicon Ultra device (10 kDa cut-off membrane, Millipore) and subjected to gel filtration on Superdex 200 HR 10/30 column (GE Healthcare, USA). All steps were performed at room temperature. Protein concentration was determined by Bradford assay (Bio-Rad). All pHLsec-FcHis constructs were cleaved with HRV 3C protease overnight, at 4 °C, in non-reducing conditions at a 1:5 target-to-protease mass ratio; all pYD5 constructs were captured on a Protein A column (MabSelect SuRe, GE Healthcare, USA), followed by cleavage with TEV protease and purification by gel filtration, as described above.

Electrophoresis and Western blot analysis.   For the rapid screening of new constructs, transfections were performed in 24-well plates using miniprep-purified DNA (JETQUICK Spin Kit, Genomed). Three days post-transfection, 10 μl of conditioned media was resolved on a 15% SDS-PAGE gel, which was subsequently electroblotted onto a BioTrace nitrocellulose membrane (Pall Corporation, USA), followed by Ponceau Red staining and washing with TBS buffer (10 mM Tris, pH 7.5, 150 mM NaCl). The membrane was blocked with 3% BSA in TBS for 1 h at room temperature, and thrice rinsed with TBS-T buffer (20 mM Tris, pH 7.5, 500 mM NaCl, 0.05% Tween-20, 0.2% Triton X-100). After 1 h incubation with PentaHis monoclonal primary antibody (1:1000 dilution in 3% BSA in TBS, Qiagen, Germany) and another 1 h incubation with horseradish peroxidase-conjugated goat anti-mouse IgG polyclonal antibodies (1:2000 in 10% non-fat milk in TBS; Abcam, UK), with extensive washings with the TBS-T and TBS buffers after each step, peroxidase activity was visualized by luminol chemiluminescence.

Mass spectrometry analysis.   Mass spectrometry analysis of disulphide bond linkage was performed as previously described[46]. Briefly, to avoid disulphide bond scrambling, 0.2 mM cystamine was added at all stages of sample preparation (i.e., SDS-PAGE gels, sample, running and digestion buffers). Protein bands were excised from the gel and their tryptic and Asp-N peptide digests were extracted and analysed on a MALDI-TOF/TOF mass spectrometer (ULTRAFLEX III, Bruker, Germany). Experimentally determined m/z values were compared with theoretical values created in GPMAW software[47], and cystine peptides were identified using a software LinX (freely available at http://peterslab.org/MSTools/). Routine protein identification and HRV 3C or TEV protease cleavage analysis was similarly performed with reduced tryptic digests.

Sedimentation analysis.   The native molecular size and shape as well as the molar mass of the proteins produced were analysed in an analytical ultracentrifuge ProteomeLab XL-I (Beckman Coulter, USA) using both sedimentation velocity and sedimentation equilibrium experiments. Before the experiment, protein samples were diluted with the gel filtration buffer (10 mM HEPES, pH 7.0, 150 mM NaCl, 10 mM NaN₃) to 0.2 mg/ml concentration, and the buffer was used as a reference. Sedimentation velocity experiments were conducted at 48000 rpm and at 20 °C using double-sector cells and An50-Ti rotor. Absorbance scans were recorded at 280 nm, at 5-min intervals. Buffer density, protein partial specific volume, and particle dimensions were estimated in Sednterp (www.jphilo.mailway.com). Data were analysed in Sedfit[48] using a continuous sedimentation coefficient distribution c(s) model. The sedimentation equilibrium experiment was performed with pHLsec_Clr-11 at a concentration of 0.1 mg/ml at 12–15–18–21–24000 rpm and at 4 °C in a six-sector cell, and absorbance scans were collected after 36 h (first scan) or 20 h (consecutive scans) of equilibration. The sedimentation equilibrium data were globally analysed in Sedphat[49] using a non-interacting discrete species model.

Fourier-transform infrared spectroscopy.   The proteins were transferred to 10 mM Tris, pH 7.5, 50 mM NaCl buffer using centrifugal filters (10 kDa cut-off, $12000 \times g$, Millipore, USA) at 20 mg/ml final concentration. Infrared spectra were recorded within a Vector 33 FTIR spectrometer (Bruker, Germany) using a standard MIR source, KBr beam-splitter and a DTGS detector. For each sample 4000 scans were collected with a 4 cm⁻¹ spectral resolution using a Blackman-Harris 3-term apodization function. Protein samples were measured at room temperature in a CaF₂-cell with an 8-μm path length (Chevtchenko Optics, Germany). The spectrometer was purged by dry air during all experiments. The spectral contribution of the buffer was corrected following the standard algorithm[50]. The spectrum of water vapour was subtracted; the spectra were offset at 1800 cm⁻¹ at zero and normalized to the amide I intensity maximum at one. Data were processed using the software GRAMS/AI (Thermo Electron, USA). The secondary structure of the proteins was estimated from their infrared

spectra using the Dousseau and Pézolet method[51] implemented as a Matlab routine (MathWorks, USA) in the Vibrational Spectroscopy Toolbox and Applications[52]. This method uses least-squares analysis to compare the amide I and amide II bands of a protein of unknown structure with those of the reference set of proteins of known three-dimensional structure (taken from[53]). The main advantage of this method is its independence from band assignments.

Data availability

All data generated or analysed during this study are included in this published article. Raw data, e.g., mass and FTIR spectra or AUC datasets generated in the current study are available from the corresponding author on reasonable request.

References

1. Lanier, L. L. Up on the tightrope: natural killer cell activation and inhibition. *Nature Immunology* **9**, 495–502, https://doi.org/10.1038/ni1581 (2008).
2. Vivier, E., Tomasello, E., Baratin, M., Walzer, T. & Ugolini, S. Functions of natural killer cells. *Nature Immunology* **9**, 503–510, https://doi.org/10.1038/ni1582 (2008).
3. Lanier, L. L. NK cell recognition. *Annual Review of Immunology* **23**, 225–274, https://doi.org/10.1146/annurev.immunol.23.021704.115526 (2005).
4. Karre, K., Ljunggren, H. G., Piontek, G. & Kiessling, R. Selective rejection of H-2-deficient lymphoma variants suggests alternative immune defence strategy. *Nature* **319**, 675–678, https://doi.org/10.1038/319675a0 (1986).
5. Raulet, D. H. Roles of the NKG2D immunoreceptor and its ligands. *Nature Reviews Immunology* **3**, 781–790, https://doi.org/10.1038/nri1199 (2003).
6. Chambers, W. H. *et al.* Monoclonal antibody to a triggering structure expressed on rat natural killer cells and adherent lymphokine-activated killer cells. *The Journal of Experimental Medicine* **169**, 1373–1389, https://doi.org/10.1084/jem.169.4.1373 (1989).
7. Mesci, A., Ljutic, B., Makrigiannis, A. P. & Carlyle, J. R. NKR-P1 biology: from prototype to missing self. *Immunologic Research* **35**, 13–26, https://doi.org/10.1385/IR:35:1:13 (2006).
8. Hao, L., Klein, J. & Nei, M. Heterogeneous but conserved natural killer receptor gene complexes in four major orders of mammals. *Proceedings of the National Academy of Sciences of the United States of America* **103**, 3192–3197, https://doi.org/10.1073/pnas.0511280103 (2006).
9. Giorda, R. *et al.* NKR-P1, a signal transduction molecule on natural killer cells. *Science* **249**, 1298–1300, https://doi.org/10.1126/science.2399464 (1990).
10. Iizuka, K., Naidenko, O. V., Plougastel, B. F., Fremont, D. H. & Yokoyama, W. M. Genetically linked C-type lectin-related ligands for the NKRP1 family of natural killer cell receptors. *Nature Immunology* **4**, 801–807, https://doi.org/10.1038/ni954 (2003).
11. Carlyle, J. R. *et al.* Missing self-recognition of Ocil/Clr-b by inhibitory NKR-P1 natural killer cell receptors. *Proceedings of the National Academy of Sciences of the United States of America* **101**, 3527–3532, https://doi.org/10.1073/pnas.0308304101 (2004).
12. Rahim, M. M. & Makrigiannis, A. P. Ly49 receptors: evolution, genetic diversity, and impact on immunity. *Immunological Reviews* **267**, 137–147, https://doi.org/10.1111/imr.12318 (2015).
13. Kveberg, L. *et al.* Two major groups of rat NKR-P1 receptors can be distinguished based on chromosomal localization, phylogenetic analysis and Clr ligand binding. *European Journal of Immunology* **39**, 541–551, https://doi.org/10.1002/eji.200838891 (2009).
14. Aldemir, H. *et al.* Cutting edge: lectin-like transcript 1 is a ligand for the CD161 receptor. *Journal of Immunology* **175**, 7791–7795, https://doi.org/10.4049/jimmunol.175.12.7791 (2005).
15. Rosen, D. B. *et al.* Cutting edge: lectin-like transcript-1 is a ligand for the inhibitory human NKR-P1A receptor. *Journal of Immunology* **175**, 7796–7799, https://doi.org/10.4049/jimmunol.175.12.7796 (2005).
16. Roth, P. *et al.* Malignant glioma cells counteract antitumor immune responses through expression of lectin-like transcript-1. *Cancer Research* **67**, 3540–3544, https://doi.org/10.1158/0008-5472.CAN-06-4783 (2007).
17. Mathew, S. O., Chaudhary, P., Powers, S. B., Vishwanatha, J. K. & Mathew, P. A. Overexpression of LLT1 (OCIL, CLEC2D) on prostate cancer cells inhibits NK cell-mediated killing through LLT1-NKRP1A (CD161) interaction. *Oncotarget* **7**, 68650–68661, https://doi.org/10.18632/oncotarget.11896 (2016).
18. Germain, C. *et al.* Lectin-like transcript 1 is a marker of germinal center-derived B-cell non-Hodgkin's lymphomas dampening natural killer cell functions. *Oncoimmunology* **4**, e1026503, https://doi.org/10.1080/2162402X.2015.1026503 (2015).
19. Voigt, S. *et al.* Cytomegalovirus evasion of innate immunity by subversion of the NKR-P1B:Clr-b missing-self axis. *Immunity* **26**, 617–627, https://doi.org/10.1016/j.immuni.2007.03.013 (2007).
20. Carlyle, J. R. *et al.* Molecular and genetic basis for strain-dependent NK1.1 alloreactivity of mouse NK cells. *Journal of Immunology* **176**, 7511–7524, https://doi.org/10.4049/jimmunol.176.12.7511 (2006).
21. Aguilar, O. A. *et al.* Modulation of Clr Ligand Expression and NKR-P1 Receptor Function during Murine Cytomegalovirus Infection. *Journal of Innate Immunity* **7**, 584–600, https://doi.org/10.1159/000382032 (2015).
22. Aguilar, O. A. *et al.* A Viral Immunoevasin Controls Innate Immunity by Targeting the Prototypical Natural Killer Cell Receptor Family. *Cell* **169**, 58–71 e14, https://doi.org/10.1016/j.cell.2017.03.002 (2017).
23. Fine, J. H. *et al.* Chemotherapy-induced genotoxic stress promotes sensitivity to natural killer cell cytotoxicity by enabling missing-self recognition. *Cancer Research* **70**, 7102–7113, https://doi.org/10.1158/0008-5472.CAN-10-1316 (2010).
24. Williams, K. J. *et al.* Poxvirus infection-associated downregulation of C-type lectin-related-b prevents NK cell inhibition by NK receptor protein-1B. *Journal of Immunology* **188**, 4980–4991, https://doi.org/10.4049/jimmunol.1103425 (2012).
25. Tanaka, M. *et al.* The inhibitory NKRP1B: Clr-b recognition axis facilitates detection of oncogenic transformation and cancer immunosurveillance. *Cancer Research* **78**, 3589–3603, https://doi.org/10.1158/0008-5472.CAN-17-1688 (2018).
26. Chen, P. *et al.* Genetic investigation of MHC-independent missing-self recognition by mouse NK cells using an *in vivo* bone marrow transplantation model. *Journal of Immunology* **194**, 2909–2918, https://doi.org/10.4049/jimmunol.1401523 (2015).
27. Rahim, M. M. *et al.* The mouse NKR-P1B:Clr-b recognition system is a negative regulator of innate immune responses. *Blood* **125**, 2217–2227, https://doi.org/10.1182/blood-2014-02-556142 (2015).
28. Kolenko, P. *et al.* Molecular architecture of mouse activating NKR-P1 receptors. *Journal of Structural Biology* **175**, 434–441, https://doi.org/10.1016/j.jsb.2011.05.001 (2011).
29. Skalova, T. *et al.* Mouse Clr-g, a ligand for NK cell activation receptor NKR-P1F: crystal structure and biophysical properties. *Journal of Immunology* **189**, 4881–4889, https://doi.org/10.4049/jimmunol.1200880 (2012).
30. Bartel, Y., Bauer, B. & Steinle, A. Modulation of NK cell function by genetically coupled C-type lectin-like receptor/ligand pairs encoded in the human natural killer gene complex. *Frontiers in Immunology* **4**, 362, https://doi.org/10.3389/fimmu.2013.00362 (2013).

31. Durocher, Y., Perret, S. & Kamen, A. High-level and high-throughput recombinant protein production by transient transfection of suspension-growing human 293-EBNA1 cells. *Nucleic Acids Research* **30**, E9, https://doi.org/10.1093/nar/30.2.e9 (2002).
32. Aricescu, A. R., Lu, W. & Jones, E. Y. A time- and cost-efficient system for high-level protein production in mammalian cells. *Acta Crystallographica Section D, Biological Crystallography* **62**, 1243–1250, https://doi.org/10.1107/S0907444906029799 (2006).
33. Chang, V. T. *et al.* Glycoprotein structural genomics: solving the glycosylation problem. *Structure* **15**, 267–273, https://doi.org/10.1016/j.str.2007.01.011 (2007).
34. Backliwal, G. *et al.* Valproic acid: a viable alternative to sodium butyrate for enhancing protein expression in mammalian cell cultures. *Biotechnology and Bioengineering* **101**, 182–189, https://doi.org/10.1002/bit.21882 (2008).
35. Sunley, K. & Butler, M. Strategies for the enhancement of recombinant protein production from mammalian cells by growth arrest. *Biotechnology Advances* **28**, 385–394, https://doi.org/10.1016/j.biotechadv.2010.02.003 (2010).
36. Pham, P. L. *et al.* Transient gene expression in HEK293 cells: peptone addition posttransfection improves recombinant protein synthesis. *Biotechnology and Bioengineering* **90**, 332–344, https://doi.org/10.1002/bit.20428 (2005).
37. Reeves, P. J., Callewaert, N., Contreras, R. & Khorana, H. G. Structure and function in rhodopsin: high-level expression of rhodopsin with restricted and homogeneous N-glycosylation by a tetracycline-inducible N-acetylglucosaminyltransferase I-negative HEK293S stable mammalian cell line. *Proceedings of the National Academy of Sciences of the United States of America* **99**, 13419–13424, https://doi.org/10.1073/pnas.212519299 (2002).
38. Sovova, Z. *et al.* Structural analysis of natural killer cell receptor protein 1 (NKR-P1) extracellular domains suggests a conserved long loop region involved in ligand specificity. *Journal of Molecular Modeling* **17**, 1353–1370, https://doi.org/10.1007/s00894-010-0837-y (2011).
39. Barth, A. Infrared spectroscopy of proteins. *Biochimica et Biophysica Acta* **1767**, 1073–1101, https://doi.org/10.1016/j.bbabio.2007.06.004 (2007).
40. Fabian, H. & Vogel, H. J. Fourier transform infrared spectroscopy of calcium-binding proteins. *Methods in Molecular Biology* **173**, 57–74, https://doi.org/10.1385/1-59259-184-1:057 (2002).
41. Hernychova, L. *et al.* The C-type lectin-like receptor Nkrp1b: Structural proteomics reveals features affecting protein conformation and interactions. *Journal of Proteomics* **196**, 162–172, https://doi.org/10.1016/j.jprot.2018.11.007 (2019).
42. Balaji, G. R. *et al.* Recognition of host Clr-b by the inhibitory NKR-P1B receptor provides a basis for missing-self recognition. *Nature. Communications* **9**, 4623, https://doi.org/10.1038/s41467-018-06989-2 (2018).
43. Skalova, T. *et al.* Four crystal structures of human LLT1, a ligand of human NKR-P1, in varied glycosylation and oligomerization states. *Acta Crystallographica Section D, Biological Crystallography* **71**, 578–591, https://doi.org/10.1107/S1399004714027928 (2015).
44. Vanek, O. *et al.* Soluble recombinant CD69 receptors optimized to have an exceptional physical and chemical stability display prolonged circulation and remain intact in the blood of mice. *FEBS Journal* **275**, 5589–5606, https://doi.org/10.1111/j.1742-4658.2008.06683.x (2008).
45. Muller, N., Girard, P., Hacker, D. L., Jordan, M. & Wurm, F. M. Orbital shaker technology for the cultivation of mammalian cells in suspension. *Biotechnology and Bioengineering* **89**, 400–406, https://doi.org/10.1002/bit.20358 (2005).
46. Pompach, P. *et al.* Modified electrophoretic and digestion conditions allow a simplified mass spectrometric evaluation of disulfide bonds. *Journal of Mass Spectrometry: JMS* **44**, 1571–1578, https://doi.org/10.1002/jms.1609 (2009).
47. Peri, S., Steen, H. & Pandey, A. GPMAW–a software tool for analyzing proteins and peptides. *Trends in Biochemical Sciences* **26**, 687–689, https://doi.org/10.1016/S0968-0004(01)01954-5 (2001).
48. Schuck, P. Size-distribution analysis of macromolecules by sedimentation velocity ultracentrifugation and lamm equation modeling. *Biophysical Journal* **78**, 1606–1619, https://doi.org/10.1016/S0006-3495(00)76713-0 (2000).
49. Schuck, P. On the analysis of protein self-association by sedimentation velocity analytical ultracentrifugation. *Analytical Biochemistry* **320**, 104–124, https://doi.org/10.1016/S0003-2697(03)00289-6 (2003).
50. Dousseau, F., Therrien, M. & Pezolet, M. On the Spectral Subtraction of Water from the FT-IR Spectra of Aqueous-Solutions of Proteins. *Applied Spectroscopy* **43**, 538–542, https://doi.org/10.1366/0003702894202814 (1989).
51. Dousseau, F. & Pezolet, M. Determination of the secondary structure content of proteins in aqueous solutions from their amide I and amide II infrared bands. Comparison between classical and partial least-squares methods. *Biochemistry* **29**, 8771–8779, https://doi.org/10.1021/bi00489a038 (1990).
52. Pazderka, T. & Kopecky Jr., V. Two-dimensional correlation analysis of Raman optical activity - Basic rules and data treatment. *Vibrational Spectroscopy* **60**, 193–199, https://doi.org/10.1016/j.vibspec.2011.10.002 (2012).
53. Baumruk, V., Pancoska, P. & Keiderling, T. A. Predictions of secondary structure using statistical analyses of electronic and vibrational circular dichroism and Fourier transform infrared spectra of proteins in H O. *Journal of Molecular Biology* **259**, 774–791, https://doi.org/10.1006/jmbi.1996.0357 (1996).
54. Jung, C. Insight into protein structure and protein-ligand recognition by Fourier transform infrared spectroscopy. *Journal of Molecular Recognition* **13**, 325–351. https://doi.org/10.1002/1099-1352(200011/12)13:6<325::AID-JMR507>3.0.CO;2-C (2000).
55. Cai, S. & Singh, B. R. Identification of beta-turn and random coil amide III infrared bands for secondary structure estimation of proteins. *Biophysical Chemistry* **80**, 7–20, https://doi.org/10.1016/S0301-4622(99)00060-5 (1999).
56. Barth, A. The infrared absorption of amino acid side chains. *Progress in Biophysics and Molecular Biology* **74**, 141–173, https://doi.org/10.1016/S0079-6107(00)00021-3 (2000).
57. Barth, A. & Zscherp, C. What vibrations tell us about proteins. *Quarterly Reviews of Biophysics* **35**, 369–430, https://doi.org/10.1017/S0033583502003815 (2002).
58. Kabsch, W. & Sander, C. Dictionary of protein secondary structure: pattern recognition of hydrogen-bonded and geometrical features. *Biopolymers* **22**, 2577–2637, https://doi.org/10.1002/bip.360221211 (1983).

Acknowledgements

Author contributions

O.V., P.C., O.S., J.B., B.K., A.D., E.P., H.P. and A.M. participated in cloning, recombinant protein expression and purification, cell line cultivation and transfection optimization, D.K. and P.P. performed mass spectrometry analyses, K.H. and V.K. performed FTIR spectroscopy measurements, J.B., S.V., J.R.C. and O.V. wrote the main manuscript text. All authors reviewed the manuscript.

Competing interests

The authors declare no competing interests.

Additional information

Supplementary information is available for this paper at https://doi.org/10.1038/s41598-019-52114-8.

Correspondence and requests for materials should be addressed to O.V.

Reprints and permissions information is available at www.nature.com/reprints.

Publisher's note Springer Nature remains neutral with regard to jurisdictional claims in published maps and institutional affiliations.

7.3 PUBLICATION NO. 3

Skořepa, O.; Pazicky, S.; Kalousková, B.; Bláha, J.; Abreu, C.; Ječmen, T.; Rosůlek, M.; Fish, A.; Sedivy, A.; Harlos, K.; Dohnálek, J.; Skálová, T.; Vaněk, O.

Natural Killer Cell Activation Receptor NKp30 Oligomerization Depends on Its N-Glycosylation.

Cancers 2020, 12, 1998. doi: *10.3390/cancers12071998*

My contribution to the publication:

Performing research (cloning and vector design, cell culture maintenance, transfection optimization, protein expression, protein purification, and quality control)

MDPI

Article

Natural Killer Cell Activation Receptor NKp30 Oligomerization Depends on Its *N*-Glycosylation

Ondřej Skořepa [1], Samuel Pazicky [1,†] ![ORCID], Barbora Kalousková [1] ![ORCID], Jan Bláha [1,†], Celeste Abreu [1], Tomáš Ječmen [1] ![ORCID], Michal Rosůlek [1,2] ![ORCID], Alexander Fish [3], Arthur Sedivy [4], Karl Harlos [5], Jan Dohnálek [6] ![ORCID], Tereza Skálová [6] ![ORCID] and Ondřej Vaněk [1,*] ![ORCID]

[1]   Department of Biochemistry, Faculty of Science, Charles University, Hlavova 2030,
       12840 Prague, Czech Republic; ondrej.skorepa@natur.cuni.cz (O.S.); spazicky@gmail.com (S.P.);
       barbora.kalouskova@natur.cuni.cz (B.K.); jahabla@gmail.com (J.B.); celesteabreu22@gmail.com (C.A.);
       tomas.jecmen@natur.cuni.cz (T.J.); rosulek.michal@gmail.com (M.R.)
[2]   BIOCEV, Institute of Microbiology, The Czech Academy of Sciences, Průmyslová 595,
       25250 Vestec, Czech Republic
[3]   Department of Biochemistry, Oncode Institute, Netherlands Cancer Institute, Plesmanlaan 121,
       1066 CX Amsterdam, The Netherlands; a.fish@nki.nl
[4]   Protein Technologies, Vienna Biocenter Core Facilities GmbH, Dr. Bohr-Gasse 3, 1030 Vienna, Austria;
       arthur.sedivy@vbcf.ac.at
[5]   Division of Structural Biology, Wellcome Centre for Human Genetics, University of Oxford, Roosevelt Drive,
       Oxford OX3 7BN, UK; karl@strubi.ox.ac.uk
[6]   BIOCEV, Institute of Biotechnology, The Czech Academy of Sciences, Průmyslová 595,
       25250 Vestec, Czech Republic; dohnalek@ibt.cas.cz (J.D.); t.skalova@gmail.com (T.S.)
*   Correspondence: ondrej.vanek@natur.cuni.cz
†   Present address: EMBL, Hamburg Unit c/o DESY, Notkestrasse 85, 22607 Hamburg, Germany.

✔ check for updates

Abstract: NKp30 is one of the main human natural killer (NK) cell activating receptors used in directed immunotherapy. The oligomerization of the NKp30 ligand binding domain depends on the length of the C-terminal stalk region, but our structural knowledge of NKp30 oligomerization and its role in signal transduction remains limited. Moreover, ligand binding of NKp30 is affected by the presence and type of *N*-glycosylation. In this study, we assessed whether NKp30 oligomerization depends on its *N*-glycosylation. Our results show that NKp30 forms oligomers when expressed in HEK293S GnTI⁻ cell lines with simple *N*-glycans. However, NKp30 was detected only as monomers after enzymatic deglycosylation. Furthermore, we characterized the interaction between NKp30 and its best-studied cognate ligand, B7-H6, with respect to glycosylation and oligomerization, and we solved the crystal structure of this complex with glycosylated NKp30, revealing a new glycosylation-induced mode of NKp30 dimerization. Overall, this study provides new insights into the structural basis of NKp30 oligomerization and explains how the stalk region and glycosylation of NKp30 affect its ligand affinity. This furthers our understanding of the molecular mechanisms involved in NK cell activation, which is crucial for the successful design of novel NK cell-based targeted immunotherapeutics.

Keywords: NK cell; NKp30; B7-H6; glycosylation; oligomerization

1. Introduction

Natural killer (NK) cells display spontaneous cytotoxic activity without prior sensitization in a process known as natural cytotoxicity. Accordingly, this subset of lymphocytes plays a key role in early immune defense within innate immunity [1,2]. In particular, mature NK cells recognize tumor cells and certain virus-infected cells through a number of inhibitory and activating receptors [3]. The inhibitory

receptors bind to human leukocyte antigen (HLA) molecules, which block NK cell cytotoxicity, whereas their activating receptors bind to specific molecules expressed on target cells, which activate NK cells. Hence, NK cell activation depends on the balance between inhibitory and activating signals coming from their inhibitory and activating receptors [3,4], which are classified primarily into two families: C-type lectin-like and immunoglobulin-like receptors [5].

Natural cytotoxicity receptors (NCRs), namely the natural killer cell proteins NKp30, NKp44, and NKp46 (numbers refer to their molecular weights), stand out for their role in activating NK cells and initiating tumor targeting [5]. NCRs are type I transmembrane proteins that consist of one or two extracellular immunoglobulin-like (Ig-like) domains, a transmembrane α-helix with a positively charged amino acid that facilitates the interaction with signaling adaptor proteins, and a short C-terminal intracellular chain [4].

Natural killer protein 30 (NKp30; also known as natural cytotoxicity receptor 3, NCR3; or CD337) is an Ig-like activating receptor of NK cells [4,6]. Similar to other members of CD28 protein family, the extracellular part of NKp30 consists of a single N-terminal Ig-like domain, followed by a distinct 15 amino acids long stalk region proximal to the plasma membrane, which is important for receptor signaling [7]. Most CD28 family members bind proteins of the B7 family [8]; however, the first molecules that have been shown to interact with NKp30 are heparin and heparin sulfate, that serve as co ligands and only interact with the glycosylated receptor [4,9]. On the other hand, interaction of NKp30 with viral ligands, such as hemagglutinin of the ectromelia and vaccinia virus [10] and protein pp65 released from human cytomegalovirus [10], has inhibitory effects on NK cells [4]. For example, pp65 binding to NKp30 causes NKp30-CD3ζ complex dissociation, thus disrupting the activating signaling pathway, albeit without preventing other ligands from binding to NKp30 because pp65 uses another binding site [4,11].

Further, three specific cellular ligands of NKp30 have been identified. Consistent with the other members of CD28 family, NKp30 binds a member of B7 family, in particular B7 homolog 6 (B7-H6), that is constitutively expressed on the surface of some tumor cells [12]. Another NKp30 cellular ligand, BAG-6, plays a role in DNA damage response, gene expression regulation, protein quality control, and immunoregulation in healthy cells [13], but is recruited to the cell membrane and interacts with NKp30 in some tumor cells or under the stress conditions [13]. Both B7-H6 and BAG-6 also exist on the surface of exosomes [13] and in soluble forms that result from proteolytic shedding of their membrane forms, which hinders NK cell activation [13,14]. Lastly, the most recently discovered NKp30 ligand, galectin 3, expressed on the surface of some tumors, almost completely blocks NK cell cytotoxicity [15].

Since the B7-H6:NKp30 interaction was first discovered, considerable research efforts have been made to define B7-H6 expression specificity in tumor cell lines and its underlying clinical potential [8,16,17]. Similarly to NKp30, B7-H6 is a type I transmembrane protein [12]. It consists of two extracellular Ig-like domains (IgV and IgC), an α-helical transmembrane domain, and a C-terminal sequence homologous to group-specific antigen (GAG) proteins. This C-terminal sequence has various signaling motifs, including ITIM-, SH-2-, and SH-3-binding motifs [8,12], which trigger signal transduction upon NKp30 binding. However, the signal outcome remains unknown [8]. The closest structural homologs of B7-H6 are B7-H1 (more widely known as programmed death-ligand 1 or PD-L1) and B7-H3, all of which belong to the B7 protein family [8,12].

B7-H6 is expressed in several tumor cell lines, both ex vivo and in vivo, but remains undetected in healthy cells thus far, and is therefore an excellent tumor marker [8,12]. In addition, B7-H6 expression has been induced in monocytes and neutrophils [18] using agonists of Toll-like receptors (TLR2, TLR4, TLR5, and TLR8), interleukin IL-1β, and tumor necrosis factor alpha (TNFα), with consistent B7-H6 mRNA and protein expression kinetics. In these phagocytes, B7-H6 mRNA expression peaked early, from 3 to 12 h after induction, returning to baseline within 24 h, whereas its surface expression was stable for up to 48 h after induction. Soluble or exosomal B7-H6 expression has also been induced using the same factors. In in vitro studies, both soluble and membrane forms of B7-H6 were detected in the blood of patients with systemic inflammatory response syndrome, but its cell-surface expression was only

identified in patients presenting with sepsis and selective for CD14^{+} and CD161^{+} pro-inflammatory monocytes. In contrast, the blood of patients presenting with sepsis caused by Gram-negative bacteria contains soluble or exosomal forms of B7-H6 [18].

Although crystal structures of NKp30, both unbound [19] and in a complex with B7-H6 [20], have been solved, these structures refer to NKp30 recombinantly expressed in bacteria and therefore lacking glycosylation. However, two *N*-glycosylation sites of NKp30 are crucial for its signal transduction and for B7-H6 but not BAG-6 ligand binding [21]. Moreover, NKp30 lacks the C-terminal 15 amino acids long stalk region that connects the ligand binding domain to the transmembrane helix in these structures. Importantly, both glycosylation and the stalk region affect the binding affinity of NKp30 [22]. The stalk region affects the oligomeric state of NKp30; NKp30 without the stalk region forms only monomer and dimer species in solution, whereas NKp30 with the stalk region forms higher oligomers [21]. Interestingly, the NKp30 dimer is observed in the crystal structure of its unbound (construct without the stalk region produced in *Escherichia coli*) [19] but not in that of its B7-H6-bound state [20]. Nevertheless, the presence of oligomers is positively correlated with NKp30 affinity to its ligands, as previously measured by surface plasmon resonance (SPR), although the differences in the measured affinity are rather small. This increased affinity is due to an avidity effect, which is attributed to NKp30 ectodomain oligomerization [21]. Greater changes in affinity are caused by alterations in *N*-glycosylation; glycosylation at Asn42 is essential for ligand binding, and glycosylation at Asn68 also has a substantial effect, whereas glycosylation at Asn121 does not play a key role, as determined by site-directed mutagenesis [22].

Furthermore, the analysis of NKp30 ligand binding has highlighted differences in affinity as a function of the protein expression system used. NKp30 affinity to B7-H6 ranged from 2.5 to 3.5 μM with both recombinant proteins expressed in *Escherichia coli* [19]. However, this affinity was higher (1 μM) when B7-H6 was expressed in the Sf9 insect cell line [20] and even higher (ranging from 80 to 320 nM) when NKp30-Ig fusion protein was expressed in the human cell line HEK293T (which provides a complex *N*-glycosylation pattern). In the latter case, the affinity of NKp30 to B7-H6 additionally increased with longer stalk region [22]. Even higher affinities were recorded when expressing NKp30 in Sf9 cells and B7-H6 in HEK293T cells, assessing affinities ranging from 1 to 2 nM by ELISA, depending on the oligomeric state of NKp30 [21]. Interestingly, the affinity of NKp30 expressed in HEK293T cells to BAG-6 isolated from an insect cell line was 64 nM. In contrast, its affinity to BAG-6 isolated from *Escherichia coli* was two times higher [23].

In this study, we show that NKp30 oligomerization depends on its *N*-glycosylation. NKp30 produced in HEK293S GnTI^{−} cells lacking *N*-acetylglucosaminyl-transferase I activity forms oligomers but disassembles to pure monomers after enzymatic deglycosylation. We have further characterized the binding affinity of B7-H6 to NKp30 and its dependence on glycosylation and oligomeric state using proteins expressed in human cell lines, that closely mimic the natural post-translational modifications of this receptor. Finally, we have determined the crystal structure of the NKp30:B7-H6 complex with the glycosylated receptor. Our results suggest that dimerization may be a necessary step for NKp30 oligomerization and stable signal transduction upon B7-H6 binding.

2. Results

2.1. Recombinant Expression and Purification of Stable, Soluble, Glycosylated NKp30, and B7-H6 Proteins

For our studies, we cloned the extracellular domains of NKp30 and B7-H6 into a mammalian expression vector with a C-terminal histidine tag. Both proteins were expressed either in HEK293T cell line that provides the protein with complex wild-type *N*-glycans, or in HEK293S GnTI[−] cell line that provides uniform, simple Asn-GlcNAc$_2$Man$_5$ *N*-glycans, in the latter case allowing also for a possibility of efficient enzymatic deglycosylation, when required [24–26]. Presence of the expected glycan type was verified by mass spectrometry (Figures S1–S3). Two constructs were prepared to study the effect of the C-terminal stalk region of the NKp30 extracellular domain. The NKp30_Stalk construct

4 of 24

contains the whole NKp30 extracellular domain, including the stalk region, whereas the NKp30_LBD (Ligand Binding Domain) lacks the stalk sequence, which is the C-terminal section of the extracellular domain of NKp30 (Figure 1). The entire extracellular portion of B7-H6 (Asp25–Leu245) consisting of two Ig-like domains was used. Each Ig-like domain contains one disulfide bridge, and moreover, the C-terminal domain contains one odd cysteine residue (Cys212).
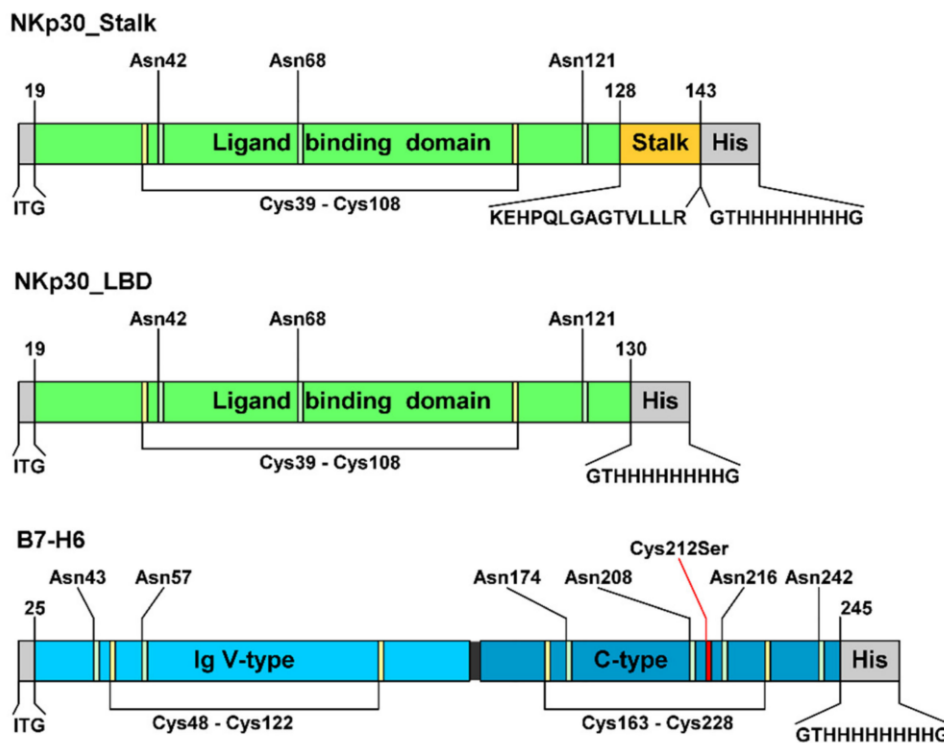
Figure 1. Recombinant NKp30 and B7-H6 expression constructs. All constructs contain three amino acids which remain after the secretion signal is cleaved at the N-terminus and a histidine tag sequence at the C-terminus. Glycosylated asparagine residues and cysteines forming disulfide bridges are indicated, as well as the mutation of the odd cysteine C212S in B7-H6.

B7-H6 expression in HEK293 cells yielded 5 mg of purified protein per liter of cell culture. However, when we analyzed fractions resulting from the SEC peak (Figure 2a, red line) by SDS-PAGE, we noticed that the protein appeared as a monomer of expected size in reducing buffer (33 kDa + N-glycosylation), but in non-reducing buffer, a band with a size corresponding to the B7-H6 dimer was identified (Figure 2b, left side, asterisk). These results suggest that the protein formed covalent dimers via its odd cysteine residue. Sedimentation analysis also showed that, although most of the protein behaved as monomers, sedimenting at 2.5 S, a small amount of putative dimer (4 S) and tetramer (6.1 S) species were also present (Figure 2c). The average fitted f/f_0 frictional ratio of 1.5 indicates an elongated shape of the molecule, in line with the published structure. However, mass spectrometry analysis confirmed that disulfide bridges of this wild-type B7-H6 expression construct were not linked correctly (Table S1).
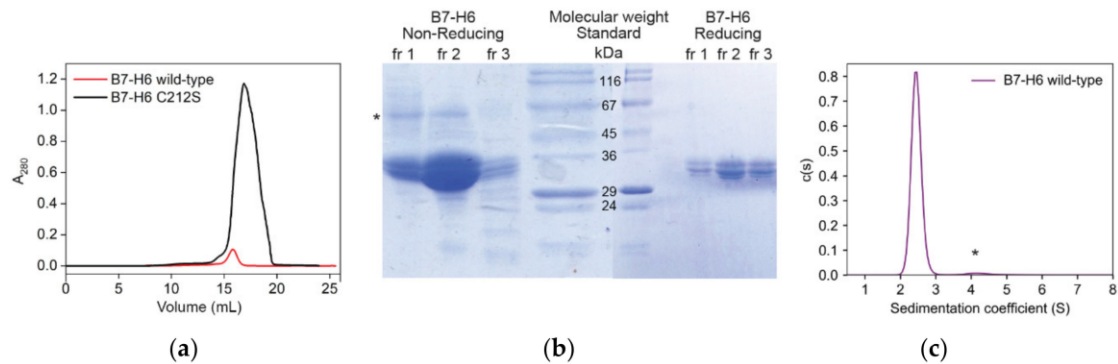
Figure 2. Recombinant B7-H6 is stabilized by the C212S mutation. (**a**) Size-exclusion chromatography (SEC) profiles of recombinantly expressed wild-type B7-H6 and its C212S mutant. (**b**) Fractions of the wild-type B7-H6 SEC peak were analyzed by 15% SDS-PAGE under non-reducing (left) and reducing (right) conditions. (**c**) Sedimentation analysis of wild-type B7-H6 at 0.5 mg/mL shown as continuous size distribution of the sedimenting species c(s). Dimeric species are marked with an asterisk in (**b,c**).

The odd cysteine that forms the unwanted covalent dimer of B7-H6 was identified as C212 according to the published structure (PDB 3PV6) [20]; therefore, we mutated this cysteine to serine (C212S). This mutation resulted in the proper folding of B7-H6 (Table S1), and strikingly, promoted the expression yield up to 50 mg per liter of cell culture (Figure 2a, black line). In the present study, only this C212S mutated form of B7-H6 was used and is henceforth referred to as B7-H6 for simplicity. The expression of both NKp30 constructs in HEK293 cell lines was straightforward, yielding 40 and 23 mg of NKp30_LBD, and 27 and 14 mg of NKp30_Stalk per liter of cell culture when expressed in HEK293T and HEK293S GnTI⁻ cell line, respectively.

2.2. Protein Deglycosylation

To assess the effect of glycosylation on NKp30 oligomerization and on its binding properties, we deglycosylated both NKp30_Stalk and NKp30_LBD. Moreover, as B7-H6 has six predicted *N*-glycosylation sites (Figure 1), the complexity of wild-type mammalian glycosylation might hinder crystallization and therefore we deglycosylated also B7-H6. Additionally, we also assessed the effect of the type of B7-H6 glycosylation on NKp30 receptor binding. The deglycosylated proteins were analyzed by SDS-PAGE (Figure 3).
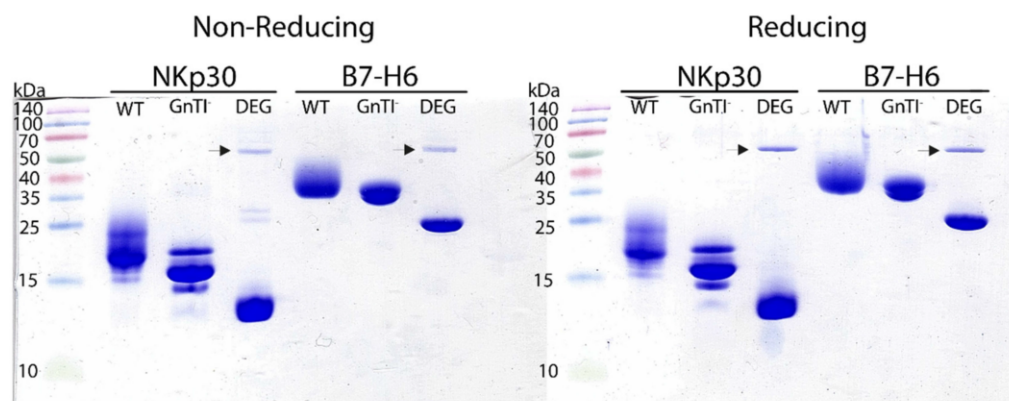
Figure 3. SDS-PAGE analysis of deglycosylated NKp30_LBD and B7-H6 C212S mutant. Different glycosylation states are marked as WT for proteins expressed in HEK293T cells with wild-type (WT) *N*-glycosylation; GnTI⁻ expressed in HEK293S GnTI⁻ cells lacking *N*-acetylglucosaminyltransferase I activity which have, therefore, uniform Asn-GlcNAc$_2$Man$_5$ *N*-glycans; and DEG for the GnTI⁻ proteins deglycosylated (DEG) with endoglycosidase Endo F1 (itself marked by an arrow).

Under standard conditions (10 mM HEPES pH 7.5, 150 mM NaCl, 10 mM NaN$_3$), B7-H6 deglycosylation caused its precipitation, most likely because of the loss of all its glycans. For this reason, we sought to improve the buffer conditions for deglycosylation and the storage of this protein by differential scanning fluorimetry. Twenty-five conditions were screened by analyzing protein melting point temperatures (Figure 4). The initial melting temperature T_m of the protein in the HEPES buffer was 50 °C and changing the pH of the buffer had no effect. Similarly, adding salts or stabilizers such as L-Arginine had virtually no effect either. Conversely, the highest T_m was recorded when adding 0.5 M saccharose (58 °C). However, at 20% glycerol, the T_m increased similarly (56 °C) and B7-H6 aggregation was completely prevented during deglycosylation. Therefore, glycerol was added to a final concentration of 20% (*v/v*) for convenience and used for further B7-H6 deglycosylation and storage at low temperatures (−20 °C). Glycerol was always removed by buffer exchange on desalting columns prior to subsequent experiments.
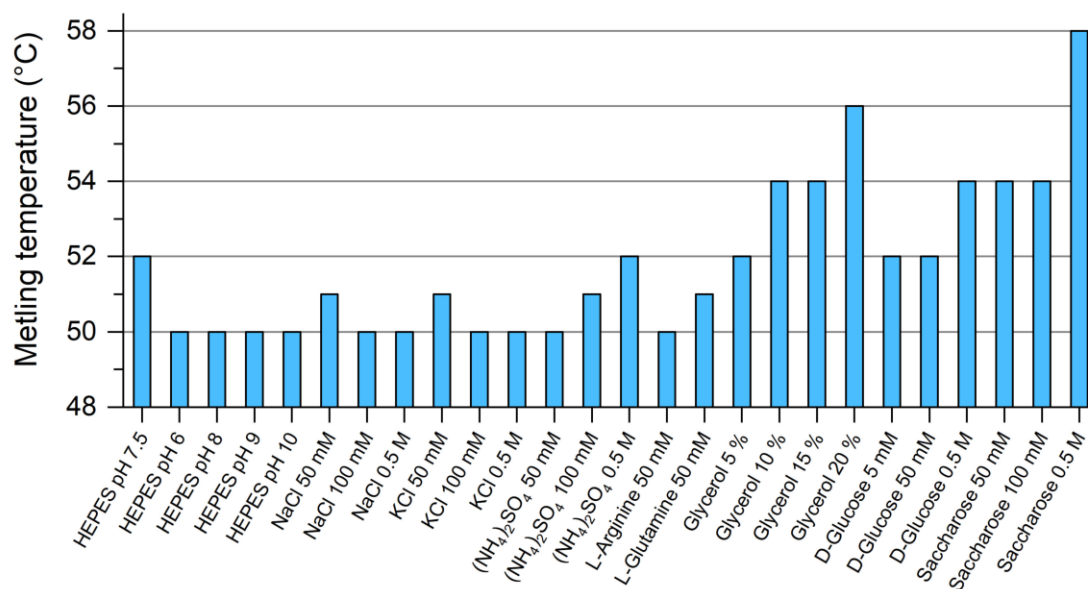
Figure 4. B7-H6 is stabilized by glycerol and saccharose addition. Differential scanning fluorimetry was used to analyze changes in protein melting temperature when adding various reagents. The concentrations given in the graph correspond to the final concentrations present in the sample.

2.3. NKp30 Glycosylation Promotes Its Oligomerization

The extracellular part of the NKp30 receptor has three *N*-glycosylation sites (Figure 1). In previous study, the presence of its *N*-glycans has been shown to enhance B7-H6 ligand binding [22] and associated cell signaling. In addition, NKp30 also forms non-covalent oligomers when the construct contains the C-terminal stalk region [21]. Accordingly, we determined the size of these oligomers by analytical ultracentrifugation (AUC) and SEC with multi-angle light scattering (MALS) detection. Notably, the NKp30_LBD construct lacking the stalk region is purely monomeric, whereas the NKp30_Stalk construct is present in both monomeric and oligomeric species (Figure 5a). Surprisingly, we could show that not only the stalk region, but also *N*-glycosylation is essential for the formation of NKp30 oligomers. Whereas NKp30_Stalk expressed in HEK293T or HEK293S GnTI$^-$ cell line contains a prominent fraction of oligomers, the deglycosylation of NKp30 with Endo F1 (leaving a single GlcNAc unit at the glycosylation site) completely depletes the sample of oligomers (Figure 5b). Elution profile of concentrated oligomeric fraction of NKp30_Stalk shows that most of the protein remains in the oligomeric form and only a minor fraction dissociates to monomers, highlighting slow kinetics of the oligomer dissociation. However, deglycosylation of the same oligomeric fraction again depletes the oligomers and only monomeric protein remains in the sample.
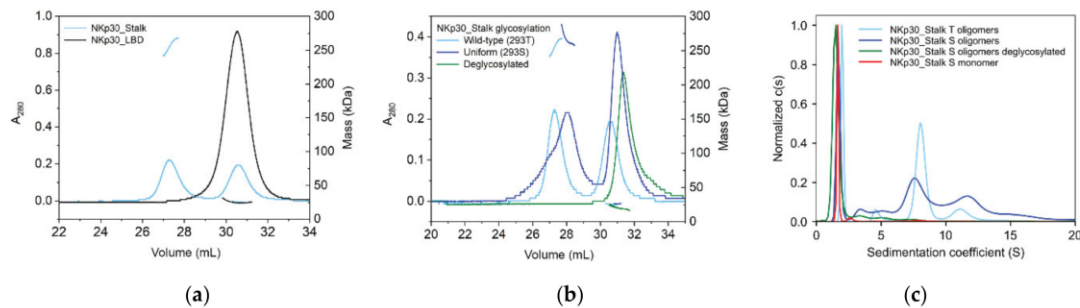
Figure 5. Glycosylation is necessary for NKp30 oligomerization. (**a**) SEC-MALS analysis of NKp30_Stalk and NKp30_LBD, confirming that the stalk region is required for oligomerization. (**b**) SEC-MALS analysis of recombinantly expressed NKp30_Stalk with wild-type glycosylation (black), uniform, simple glycans (blue), both showing non-covalent oligomers, and deglycosylated sample, which does not form oligomers (red). (**c**) Normalized continuous size distributions of sedimenting species for glycosylated and deglycosylated NKp30_Stalk oligomers and for its monomeric fraction. The main peak corresponds to the NKp30_Stalk monomer, whereas a broad distribution of oligomeric species is present in glycosylated NKp30_Stalk samples.

We repeated the same experiment and analyzed it using analytical ultracentrifugation, which led to the same conclusion; NKp30_Stalk does not form oligomers when deglycosylated (Figure 5c). Sedimentation analysis provided better resolution of the oligomeric species than SEC and thus allowed us to estimate their size. The main peak at 1.8 S, with a predicted molar mass of 18.8 kDa, matches the expected mass of the glycosylated NKp30_Stalk monomer (18.9 kDa). The molar masses predicted for the peaks corresponding to the oligomeric species indicated the presence of oligomers with 3, 5, 10, and 20 units, on average. The fitted f/f_0 ratio of 1.6 suggests that the oligomers have a considerably elongated or flattened shape. Interestingly, NKp30_Stalk with wild-type glycosylation expressed in HEK293T cells (20–25 kDa) showed a more homogeneous oligomer profile with one dominant species of ca 8 units and with secondary species of ca 16 units, based on their calculated molar masses of 180 and 320 kDa, respectively. These findings corroborate the molar masses calculated from the MALS signal (Figure 5b), which are within the same range. In summary, not only the presence of the stalk domain but also the glycosylation is essential for the formation of NKp30 oligomers.

2.4. B7-H6 Forms Equimolar Complex with Monomeric NKp30, But Not with Its Oligomeric Form

To study the impact of B7-H6 on NKp30 oligomers, we followed the NKp30:B7-H6 interaction using hydrodynamic approaches. NKp30_Stalk and B7-H6 were analyzed by SEC-MALS separately and in a complex at a 1:1 molar ratio (Figure 6a). Shifts in the elution volume and in the calculated molar mass suggest the formation of the complex in the monomeric and oligomeric fractions of the NKp30_Stalk construct. The ratio between the areas of monomeric and oligomeric peaks did not change, indicating that B7-H6 binding does not disrupt or induce NKp30 oligomerization. Subsequently, we analyzed the binding of the monomeric and oligomeric fractions separately by AUC. The monomeric fraction of glycosylated NKp30_Stalk sedimented predominantly at 1.7 S (monomer) and marginally at 3.5 S (dimeric or trimeric species). B7-H6 sedimented as monomer at 2.4 S. The equimolar mixture of these proteins sedimented as a 1:1 complex at 3.1 S, with a relatively small peak observed at 1.7 S, which is most likely an excess of the free monomer of NKp30 (Figure 6b).
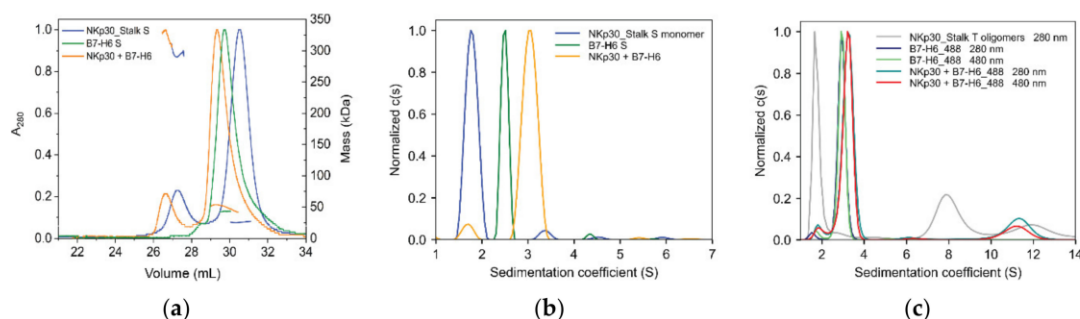
Figure 6. NKp30_Stalk oligomers cannot be saturated by B7-H6. (**a**) Normalized SEC (Size Exclusion Chromatography) elution profiles of NKp30_Stalk, B7-H6 and their equimolar mixture with MALS detection. (**b**) Sedimentation analysis of complex formation for B7-H6 and NKp30_Stalk monomeric fraction and (**c**) of NKp30_Stalk oligomeric fraction with B7-H6 labeled with ATTO488 dye performed at two wavelengths. Letters S and T denote the type of protein glycosylation (HEK293S GnTI⁻ or HEK293T *N*-glycans, respectively).

To monitor the binding of the oligomeric fraction, we labelled B7-H6 with NHS-ATTO488 fluorescent dye and performed the experiment at 280 nm (total signal) and 480 nm (B7-H6 only) wavelengths (Figure 6c). The bimodal distribution of NKp30_Stalk HEK293T oligomers changed to a single oligomeric complex upon the addition of B7-H6, with a sedimentation coefficient of 11.2 S that corresponds to ca 340 kDa at the fitted overall f/f_0 ratio of 1.7. This value is lower than expected for the fully saturated NKp30_Stalk_HEK293T putative octamer (ca 180 kDa plus eight times 30–33 kDa for each glycosylated B7-H6, i.e., approximately 420–440 kDa for the fully saturated 1:1 complex). This suggests that not all NKp30 binding sites in the oligomeric species are accessible for B7-H6 binding and that NKp30 molecules might sterically block the access to the neighboring binding sites within the oligomer itself or with the B7-H6 molecules bound to it. The modest increase in MALS-calculated molar mass for the oligomeric NKp30:B7-H6 complex (Figure 6a) supports these inferences. Indeed, the ratio between the areas of monomeric and oligomeric NKp30:B7-H6 differs between 280 nm and 480 nm, which indicates that the amount of B7-H6 present in oligomers is smaller than the amount of NKp30 in oligomers (Figure 6c). Finally, the areas under the oligomeric peak are not equal between the two wavelengths, suggesting that only approximately 60% of the NKp30 binding sites are occupied by B7-H6 in the oligomers. This matches well with the observed mass difference between the oligomeric complex (340 kDa) and the oligomers (180 kDa), resulting in ca 160 kDa of B7-H6 bound to the oligomers, or approximately five B7-H6 molecules per eight NKp30 molecules in the oligomeric complex. Hence, B7-H6 binds both monomers and oligomers of NKp30, but only sub-equimolar amount of NKp30 binding sites is available for B7-H6 binding in the oligomeric fraction.

2.5. Affinity of NKp30:B7-H6 Interaction Differs between Surface and Solution

To reevaluate the impact of glycosylation on the interaction of B7-H6 and NKp30, we measured the affinity of this interaction using proteins with different glycosylation patterns. B7-H6 has six predicted *N*-glycosylation sites, five of which were confirmed by our MS analysis (Table S1). B7-H6 in wild-type (T), simple (S), and Endo F1-deglycosylated (D) glycosylation states were immobilized on the SPR chip. The same analyte, the monomeric fraction of NKp30_Stalk, was measured in individual cells. Neither the dissociation constant K_D nor the maximal response B_{max} values significantly differed among all tested B7-H6 variants (Figure 7a). Therefore, B7-H6 glycosylation does not significantly affect the NKp30 receptor binding.
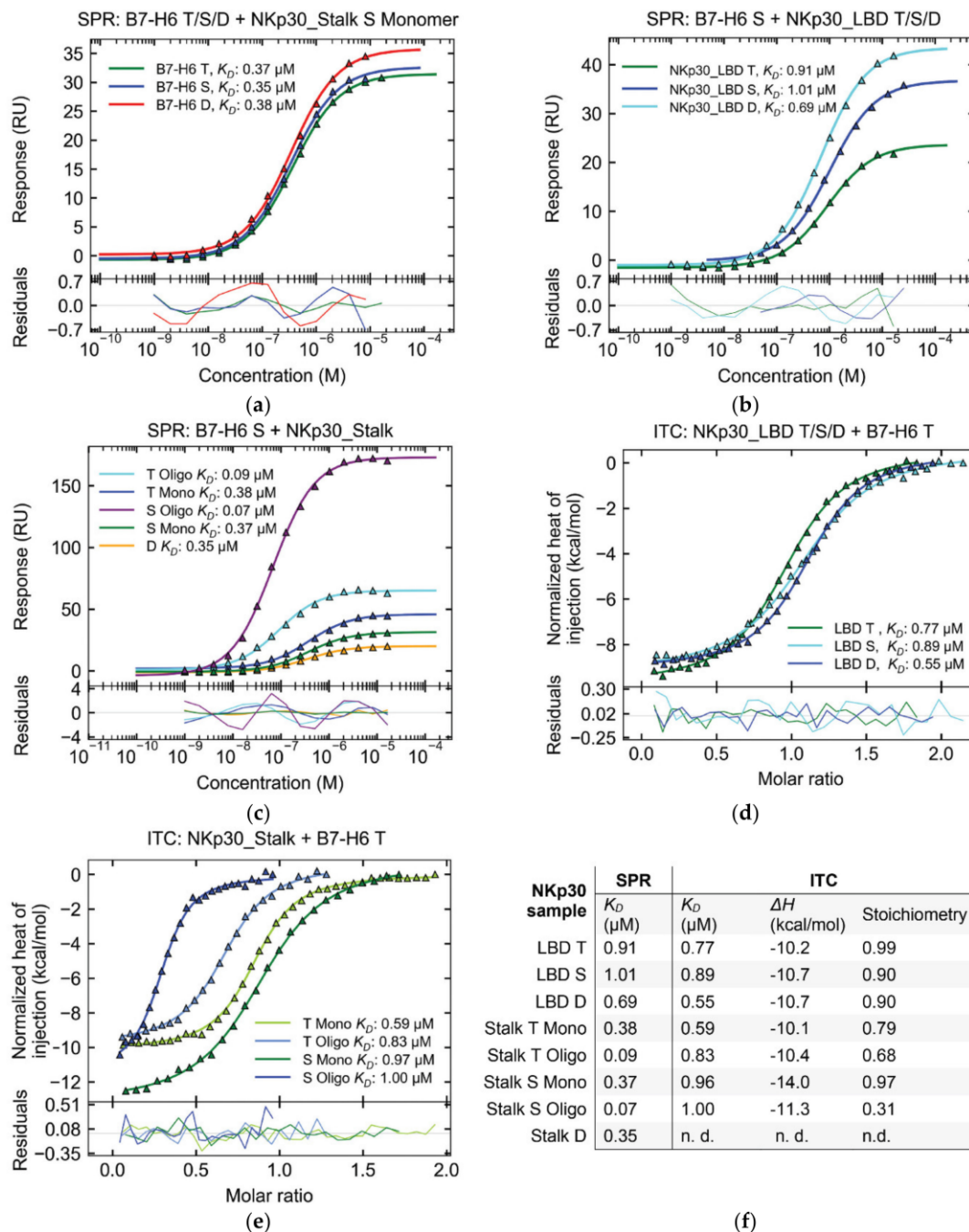
Figure 7. Characterization of the NKp30:B7-H6 interaction by SPR and ITC. Type of protein glycosylation: T—wild-type, S—uniform, D—deglycosylated, Mono—monomeric, Oligo—oligomeric fraction of NKp30_Stalk. Titles above individual graphs describe the given experiment: SPR or ITC, protein bound to SPR sensor or present in ITC cell + protein flown over the sensor or titrated into the cell, respectively. (**a**) B7-H6 glycosylation does not affect NKp30 binding. (**b,d**) Glycosylation of NKp30 weakens its interaction with B7-H6. (**c,e**) Stalk region and oligomerization of NKp30 enhance its affinity to B7-H6 in SPR but not in ITC. (**f**) Comparison of all thermodynamic parameters measured for the NKp30:B7-H6 interaction with different protein variants.

Subsequently, we investigated the effect of NKp30 deglycosylation on B7-H6 ligand binding. A previous study had already shown that the point mutation of the glycosylation site Asn68 (N68Q)

reduces the affinity for the B7-H6 ligand, whereas the N42Q mutation of the Asn42 glycosylation site almost completely abrogates binding [22]. For this reason, we performed a binding assay with NKp30 deglycosylated with Endo F1. Interestingly, in comparison with the aforementioned study, the affinity of both deglycosylated NKp30_LBD and NKp30_Stalk did not significantly differ from that of their wild-type or uniformly glycosylated counterparts in both SPR and isothermal titration calorimetry (ITC) measurements (Figure 7b–e). In fact, for NKp30_LBD, the affinity even moderately increased from uniform glycans to wild-type glycans to deglycosylated protein (Figure 7b,d). Similarly, only slight differences in affinity were found among NKp30_Stalk glycosylation variants (Figure 7c,e). However, Endo F1 treatment leaves a single GlcNAc unit at each glycosylation site, whereas point mutations completely block glycosylation. Hence, these results cannot be compared directly.

In contrast, NKp30_Stalk variants showed higher affinity than the shorter NKp30_LBD construct when analyzed by SPR (Figure 7c), thus confirming earlier observations that the stalk region contributes significantly to B7-H6 binding. The affinity of the NKp30_Stalk monomeric fraction was approximately two times higher than that of NKp30_LBD, as shown by both SPR and ITC analyses (Figure 7b,d). Even higher affinities were recorded by SPR for the NKp30_Stalk oligomeric fraction, which was bound approximately ten times more strongly than NKp30_LBD and four times more strongly than the NKp30_Stalk monomeric fraction. Simultaneously, the B_{max} was higher, as expected for oligomer binding (Figure 7c) and in line with a previous study, thus jointly concluding that the observed increase in affinity results from the avidity contribution of the oligomers [21].

Surprisingly, the affinity of the NKp30:B7-H6 interaction was similar when comparing NKp30_LBD with the monomeric and oligomeric fractions of NKp30_Stalk by ITC (Figure 7d,e), albeit with a tenfold decrease in affinity of the oligomeric fraction compared to SPR results. In addition, ITC results showed lower stoichiometry for the oligomeric fractions of NKp30_Stalk (Figure 7f), thus suggesting that not all binding sites of the oligomer are saturated and that they might be sterically blocked and inaccessible for B7-H6 binding. These findings match our results from the sedimentation analysis (Figure 6c), i.e., only 60–70% NKp30_Stalk T oligomers are accessible.

2.6. Crystal Structure of Glycosylated NKp30:B7-H6 Complex

To understand the role of glycosylation in the NKp30:B7-H6 interaction in more detail, we solved the crystal structure of NKp30 with uniform glycosylation in complex with Endo F1-deglycosylated B7-H6. Although we were unable to crystallize this complex with the oligomer-forming NKp30_Stalk construct, we obtained diffracting crystals using the NKp30_LBD monomeric protein. The structure (PDB 6YJP) was solved at 3.1 Å resolution, and the refinement parameters are summarized in Table 1. The asymmetric unit of the crystal contains two NKp30_LBD molecules (LBD_A/B) and three B7-H6 molecules (B7-H6_C/D/E), as shown in Figure 8 below. The molecules are completely localized, except for two missing loops in B7-H6 (residues 151–159 and 149–155 in chains D and E, respectively). In fact, one more NKp30_LBD chain that interacts with B7-H6 (chain E) is present in the crystal but its loose localization did not allow us to build it in the structure.

When viewing neighboring symmetry-related molecules, surrounding the asymmetric unit of the crystal, a dimer of two NKp30_LBD:B7-H6 complexes (LBD_A:B7-H6_C and LBD_B:B7-H6_D) becomes apparent (Figure 9). The interaction interfaces between NKp30 and B7-H6 are conserved and highly similar to the interaction surface observed in the 3PV6 structure; the contact between NKp30_LBD_A and B7-H6_C chains comprises four hydrogen bonds or salt bridges (chain A Gly51 N—chain C Thr127 OG1, chain A Val53 N—chain C Pro128 O, chain A Glu111 OE1—chain C Lys130 NZ and chain A Glu111 OE2—chain C Lys130 NZ), and the interface has a Pisa server complex formation significance score of 0.225 [27]. The contact between chains NKp30_LBD_B and the symmetry-related B7-H6_D comprises five hydrogen bonds or salt bridges: four analogical to the aforementioned bonds and an additionally B47 Arg NH1—D84 Asp OD1 bond. The interface has the same score, 0.225, according to the Pisa server.

Table 1. Data collection statistics and structure refinement parameters for the NKp30_LBD:B7-H6 crystal structure. Values in parentheses refer to the highest resolution shell.

PDB Code	6YJP
Data processing statistics	
Space group	C2
Unit-cell parameters a, b, c (Å); α, β, γ (°)	166.0, 86.5, 111.3; 90, 97.6 90
Resolution range (Å)	48.95-3.1 (3.29-3.1)
No. of observations	99061 (12123)
No. of unique reflections	27102 (3968)
Data completeness (%)	95 (87)
Average redundancy	3.7 (3.1)
Mosaicity (°)	0.09
Average $I/\sigma(I)$	5.7 (0.8)
Solvent content (%)	65
Matthews coefficient (Å³/Da)	3.54
Wilson B-factor (Å²)	105.5
R_{merge}	0.104 (0.971)
R_{pim}	0.081 (0.804)
CC1/2	0.995 (0.645)
Structure refinement parameters	
R_{work}	0.272
R_{free}	0.322
R_{all}	0.275
Average B-factor (Å²)	155.6
RMSD bond lengths from ideal (Å)	0.005
RMSD bond angles from ideal (°)	1.59
Number of non-hydrogen atoms	6907
Number of water molecules	0
Ramachandran statistics: residues in allowed/favored region (%)	99.5/92.9

$R_{\text{merge}} = \sum_h \sum_i |I_{\text{hi}} - \langle I_h \rangle| / \sum_h \sum_i I_{\text{hi}}$, $R_{\text{pim}} = \sum_h \sum_i (n_h - 1)^{-1/2} |I_{\text{hi}} - \langle I_h \rangle| / \sum_h \sum_i I_{\text{hi}}$, and $R = \sum_h ||F_{h,\text{obs}}| - |F_{h,\text{calc}}|| / \sum_h |F_{h,\text{obs}}|$, where I_{hi} is the observed intensity, $\langle I_h \rangle$ is the mean intensity of multiple observations of symmetry-related reflections, and $F_{h,\text{obs}}$ and $F_{h,\text{calc}}$ are the observed and calculated structure factor amplitudes. R_{work} is the R factor calculated on 95% of reflections excluding a random subset of 5% of reflections marked as "free". The final structure refinement was performed on all observed structure factors. RMSD, root-mean-square deviation, PDB, published structure.
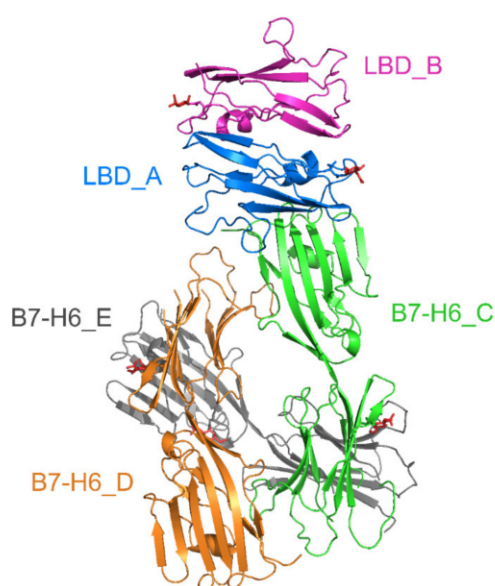
Figure 8. Crystal structure of uniformly glycosylated NKp30_LBD in complex with deglycosylated B7-H6. The asymmetric unit contains two molecules of NKp30_LBD (chains LBD_A and B) and three molecules of B7-H6 (chains B7-H6_C, D and E). Interaction interface between chains LBD_A and B7-H6_C corresponds to the interaction surface observed in the previously published structure of this complex (PDB 3PV6) [20].
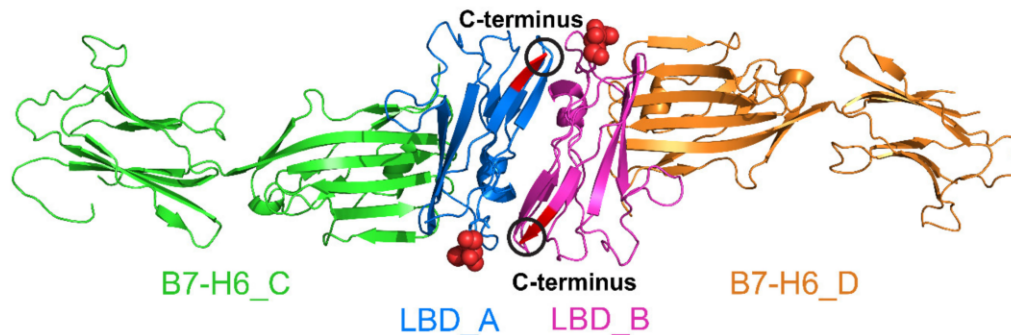
Figure 9. A dimer of the NKp30_LBD:B7-H6 complex is observed in the presented crystal structure. Within the NKp30:B7-H6 complex, both pairs of molecules bind to each other almost identically, and the binding mode of the two proteins is also very similar to that described based on the previously published structure of the complex (PDB 3PV6) [20]. However, the structure of the NKp30_LBD dimer is distinct to the previously published structure of NKp30_LBD itself (PDB 3NOI) [19]. The dimer has a two-fold rotation symmetry, and the *N*-glycosylation site at Asn42 of LBD_A (GlcNAc residue highlighted as spheres) is close to C-terminus of LBD_B (highlighted in red) and vice-versa.

In the crystal structure, electron density maps allowed us to model *N*-acetylglucosamine at NKp30_LBD asparagine residues 42 (chains A and B), and B7-H6 residues 208 (chains C and D) and 43 (chain E). Furthermore, low-quality peaks in the electron density map, corresponding to glycans, were observed near NKp30_LBD asparagine residues 68 (chain A) and 121 (chain B), and near B7-H6 residues 43 (chains C,D), 57 (chains C,D,E), 174 (chains C,D,E), 208 (chain E), and 242 (chains C,E). In the case of NKp30_LBD Asn42, the glycosylation changes the orientation of the Asn42 side chain and main chain and consequently, the placement of residue Ala43 in comparison with NKp30_LBD in PDB 3NOI and 3PV6. Noticeably, the glycosylation site at Asn42 of one NKp30_LBD molecule (LBD_A) localizes in the proximity of the C-terminus of the other NKp30_LBD molecule (LBD_B) and vice versa (Figure 9). In NKp30_Stalk or in full-length NKp30 receptor, this C-terminal part of its ligand binding domain would be followed by the 15 amino acids long stalk region. Both the glycosylation and the stalk regions are required for NKp30 oligomerization, suggesting that this NKp30_LBD dimer may be the building block of these oligomers.

NKp30_LBD chains A and B form a dimer different from that observed in the crystal structure of NKp30 itself (PDB 3NOI) [19], whereas NKp30 was only monomeric in the crystal structure of the NKp30:B7-H6 complex (PDB 3PV6) [20]. Both dimers have two-fold symmetry and a similar patch of mutual contacts (residues Arg28, Asn42, Gln45, and Glu128 participate in hydrogen bonds in both cases); however, their mutual orientation is very different: when chains A are superimposed, the positions of the same residues in chain B differ by 9–15 Å (Figure 10). The NKp30 dimer in PDB 3NOI comprises sixteen hydrogen bonds or salt bridges, and the interface scores 0.176 in the Pisa server, whereas the dimer observed in the present structure PDB 6YJP comprises eleven hydrogen bonds or salt bridges, and its interface scores 1.0 in the Pisa score, which indicates a more stable interaction and relevant interface. Interestingly, Asn42 of NKp30_LBD is positioned directly at the dimer interface in PDB 3NOI, and in close contact with Glu26 and Arg28 from the second chain, whereas GlcNAc at Asn42 in PDB 6YJP is located outside of the interface, right next to the C-terminus of the second chain—at the beginning of the stalk region.
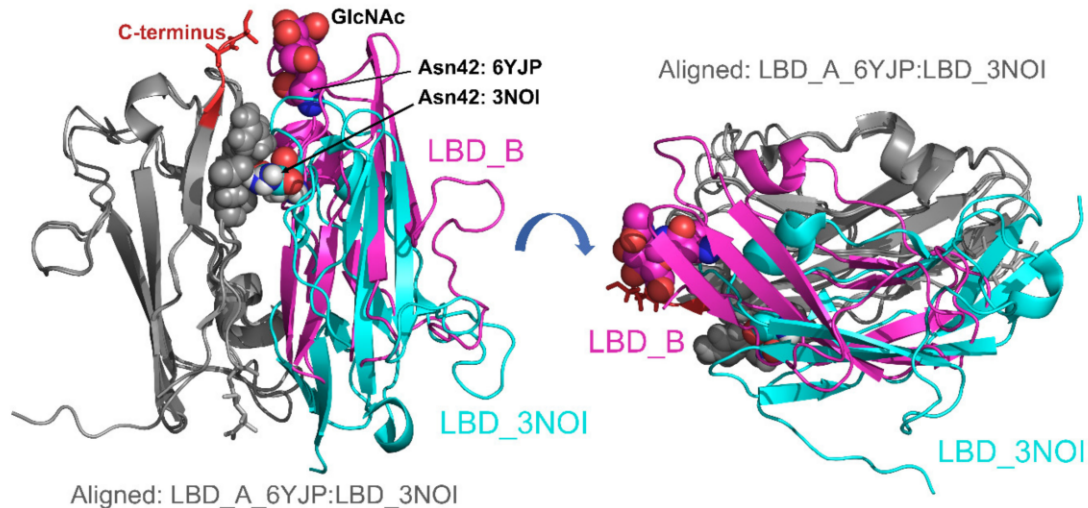
Figure 10. Glycosylation-induced NKp30 dimerization positions the glycans at Asn42 residues near the C-terminal stalk regions. The NKp30_LBD dimers observed in the present crystal structure PDB 6YJP and the PDB 3NOI [19] were aligned using molecules on one side of the dimer only (grey color). On the left —the *N*-glycosylation site at Asn42 of LBD_B, highlighted as spheres, is near the C-terminus of LBD_A (highlighted in red), whereas the Asn42 residue in LBD_3NOI is buried within the dimer interface, interacting with Glu26 and Arg28 (all highlighted as spheres). On the right—side view of the dimer interface showing the difference in arrangement of the two dimers.

3. Discussion

The first key stage of this study was the preparation of the stable, soluble, extracellular part of the B7-H6 protein. Members of the B7 family have moved to the forefront of cancer research for their underlying involvement in tumorigenesis [17] and tumor recognition [16] and for their role as regulators of immune responses and immunotherapy outcomes, such as B7-H1, also known as PD-L1, one of the most discussed checkpoint inhibitors in recent years [28]. Because B7-H6 can induce NKp30-dependent NK activation and cytokine secretion [12], therapeutic interventions based on the NKp30:B7-H6 interaction may provide a new strategy for tumor treatment. Wu et al. [29] have shown that the B7-H6-specific bispecific T cell engager (BiTE) directs host T cells to mediate cellular cytotoxicity and interferon-γ secretion, which is therefore a potential therapeutic strategy for B7-H6$^+$ hematological and solid tumors. More recently, T cells expressing B7-H6-specific human single-chain fragment variable (scFv) as chimeric antigen receptor (CAR) have been shown to induce potent anti-tumor activity in vitro and in vivo against tumors expressing high amounts of B7-H6 [30].

Although B7-H6 was the target molecule in these approaches, other strategies have been developed exploring the potential of B7-H6 as a natural ligand for the activating receptor NKp30. Kellner et al. [31,32] generated a fusion protein consisting of the ectodomain of B7-H6 and of the CD20-specific scFv 7D8. In the functional assay, the authors found that the B7-H6:7D8 fusion protein could stimulate NKp30-mediated NK cell cytotoxicity. The same strategy was successfully applied to create a HER2-specific B7-H6 fusion protein targeting HER2$^+$ tumors [33]. In our study, we initially tried to express not only the B7-H6 construct described above (Figure 1), but also a shorter construct corresponding to the N-terminal IgV B7-H6 domain (Asp25—Val140) only. However, this shorter construct could not be expressed at all, thus suggesting that, although the two Ig-like domains of B7-H6 are structurally well separated, the extracellular part of B7-H6 is stable only when expressed as a whole. Furthermore, we found that mutating the odd cysteine in the B7-H6 IgC domain (Cys212Ser) greatly stabilizes the molecule by promoting correct disulfide bond formation, reaching a ten-fold increase in yield over the wild-type B7-H6 ectodomain. Moreover, glycerol addition was optimal for long-term B7-H6 storage, both in solution and in frozen state, preventing its aggregation, especially

at higher protein concentrations. This optimized protocol for recombinant B7-H6 production may be useful for further studies involving B7-H6 fusion immunotherapeutics or requiring large-scale expression of this tumor antigen in a stable and well-folded form.

Oligomerization of the NKp30 ectodomain has been previously characterized using constructs expressed in Sf9 insect cells providing uniform, simple paucimannose *N*-glycans, similar to those present in HEK293S GnTI$^-$ cell lines. When recombinantly expressing these constructs, the authors found that both NKp30_Stalk and NKp30_LBD oligomerized in their study, although the latter to a lesser extent [21]. However, both proteins had a considerable number of additional amino acid residues at both their N- and C-termini, namely ADLGS and GSENLYFQGGS followed by a decahistidine tag, respectively. In our study, we used the same LBD and Stalk regions of the NKp30 ectodomain, but we expressed these NKp30 constructs in human cell lines, providing uniform mannose- or wild-type glycosylation, and with a limited number of flanking amino acids. Regardless of the glycosylation type or presence, at low concentration the NKp30_LBD construct showed no tendency to oligomerize. At high sample concentration, however, dimer formation has been observed for this construct in our sedimentation analysis (Figure S4). Thus, we can conclude that although the ligand binding domain of NKp30 itself shows some tendency to self-associate (as evidenced by dimer formation observed at high concentration in solution by AUC and by dimeric arrangement found in the crystal), presence of the stalk region is a prerequisite for stable NKp30 oligomerization in solution.

In addition, the ability of the NKp30_Stalk construct to oligomerize is lost upon its deglycosylation with endoglycosidase F1, thereby highlighting the unappreciated but key role of glycosylation in NKp30 oligomerization. Hermann et al. [21] observed that NKp30_Stalk oligomers bound to immobilized B7-H6-Ig have an extremely low nanomolar K_D, as assessed by SPR and ELISA (both surface-based interaction methods), and hypothesized that the increase in apparent ligand binding affinity of the oligomers is caused by the increase in the avidity of higher-molecular-order NKp30 complexes under these conditions. We noted a similar trend in our SPR analysis when using immobilized B7-H6, observing a higher affinity for NKp30_Stalk than for NKp30_LBD, and an even higher affinity for the NKp30_Stalk oligomeric fraction. In contrast, when analyzing the same system by AUC and ITC (solution-based techniques), we found that both monomeric and oligomeric fractions of NKp30_Stalk, and NKp30_LBD, showed similar thermodynamic parameters and affinity to soluble B7-H6, but the oligomers exhibited significantly lower binding stoichiometry. This suggests that interaction data on immobilized B7-H6 and oligomerizing NKp30_Stalk construct collected using surface methods might not correctly express K_D values for interactions of individual binding sites and that the NKp30 oligomers might not be completely biologically active species, at least when present in solubilized form and not on the cell surface.

Another important aspect of the NKp30:B7-H6 interaction is the glycosylation of the NKp30 ectodomain, especially on Asn42 and Asn68 sites, as shown by Hartmann et al. [22] in binding experiments with NKp30 human IgG1-Fc fusion constructs expressed in HEK293T cell lines. Interestingly, mutating these glycosylation sites affected binding to B7-H6, but not to BAG-6, as determined by SPR or ELISA, respectively. Moreover, NKp30_Stalk-Ig binding to natural ligands, in various tumor cell lines, was even stronger in the absence of glycosylation, albeit abrogated in B7-H6$^+$ reporter cell lines. This key role of glycosylation and of the stalk region in signal transduction was further corroborated by using various NKp30-transfected CD3ζ reporter cell lines stimulated by B7-H6$^+$ target cells [22]. In our study, we did not observe marked differences in NKp30:B7-H6 affinity between the NKp30_Stalk and NKp30_LBD constructs, and neither between the NKp30 variants expressed with wild-type human or uniform oligomannose *N*-glycans, or deglycosylated, independent of the method that we used to measure these interactions. The deglycosylated proteins used in our study still had a single GlcNAc residue at each glycosylation site, in contrast to the disruptive Asn-Gln mutations used in the previous study, which may account for the differences in the results. Nevertheless, our findings indicate that glycosylation most likely does not directly affect the NKp30:B7-H6 interaction and instead primarily affects the ability of NKp30 to oligomerize. Impaired oligomerization would then translate

into lower apparent binding affinities, when using surface-based methods such as SPR and ELISA, and into impaired signal transduction in cell-based experiments. The role of the stalk domain in CD3ζ-mediated activation of NK cells was thoroughly characterized by Memmer et al. [7] who showed that mutations in the stalk region close to LBD weaken the K_D of B7-H6-Fc whereas BAG-6 binding, again, remained mostly unaffected, although NKp30-Fc IgG fusions and SPR detection were used in these experiments. Subsequent reporter cell-based assays showed that Arg143 (end of the NKp30 stalk region) alignment with the aspartate of CD3ζ is required for signal transduction and that this alignment might be achieved by ligand-induced receptor clustering and/or stalk-dependent conformational changes [7]. NKp46, another member of the NCR family, exhibits similar complex behavior on the cell surface. It forms dimers and later on also clusters within the immune synapse, which activate NK cell polarization [34,35].

Although NKp30 constructs artificially dimerized through IgG-Fc fusion may not be the best tools to describe the natural behavior of this receptor at the plasma membrane of NK cells, their thorough characterization should be useful for developing immunotherapeutics. Over ten years ago, Arnon et al. [36] demonstrated using human prostate cancer cell lines that treatment with NKp30-Ig dramatically inhibits tumor growth in vivo in mice by successfully recruiting activated macrophages via antibody-dependent cellular cytotoxicity (ADCC). Strikingly, while IgG1 Fc-fusions are regularly used in NCR-related immunology research, no immunotherapy product based on them has been developed thus far.

The original motivation for our work was to understand better how NKp30 oligomers are formed and structured. To this end, we used multiple techniques, but not all of them produced conclusive results, such as structural mass spectrometry (cross-linking and H/D exchange) or cryo-electron microscopy. We also tried to crystallize the NKp30_Stalk construct and thus solve its oligomeric structure, albeit to no avail. Neither this protein nor its complex with B7-H6 formed crystals. Nevertheless, we solved the structure of the glycosylated NKp30_LBD:B7-H6 complex, which is somewhat similar to the previously known structures of NKp30_LBD (PDB 3NOI, [19]) and of the NKp30_LBD:B7-H6 complex (PDB 3PV6, [20]). However, both previously published structures were solved using bacterially expressed, non-glycosylated refolded NKp30_LBD. Therefore, our structure provides new insights into the mechanism of oligomerization of this protein.

Most interestingly, our crystal structure shows the formation of an NKp30_LBD dimer in the bound state with B7-H6. The symmetrical arrangement of Asn42 glycosylation sites, near the C-terminal stalk region beginnings on both sides of the dimer, strengthens our hypothesis of glycosylation-supported, stalk region-mediated NKp30 oligomerization. In contrast to the structure of the glycosylated NKp30_LBD dimer, in the dimer of the refolded NKp30_LBD observed in the PDB 3NOI crystal structure, the Asn42 residue is in close contact with neighboring side chains of other amino acids of the dimerization interface. With such a bulky glycan chain bound to the Asn42, this type of dimer is unlikely to exist. Therefore, we may assume that glycosylation induces the observed dimer arrangement and that this arrangement is further stabilized by the interaction between the glycan moiety and the stalk region of full-length NKp30.

Moreover, for soluble NKp30_Stalk, the stalk regions that extend on both sides of the dimer would be free to interact with stalk regions of other NKp30_Stalk dimers, thereby forming linear oligomers composed of such dimers. To acquire at least some low-resolution data on the structure of these oligomers, we have also performed SEC-SAXS analysis of the NKp30_LBD, NKp30_Stalk monomeric and oligomeric fractions, and their complexes with B7-H6 (Figure S5). Representative examples of the resultant ab initio molecular envelopes calculated from the collected SAXS data are shown in Figure S6 [37,38]. The lack of further structural data on how individual NKp30_Stalk molecules or their possible dimers are arranged in space precludes any further modelling of molecular arrangements of these oligomers. Nevertheless, the overall shape of the calculated envelopes is highly asymmetrical, that is, prolate or oblate rather than spherical, and this asymmetry is in perfect agreement not only with

the prediction based on the crystal structure but also with our sedimentation analysis of the oligomers indicating asymmetrical elongated or flattened particles.

Another interesting aspect of our crystal structure is the overall topology of the dimer of the NKp30_LBD:B7-H6 complex observed in the crystal lattice. Its arrangement is compatible with both NKp30 molecules inserted within the same NK cell membrane and B7-H6 in the cell membrane of a target tumor cell (Figure 11). Such arrangement would bring the membranes of both cells into close contact, and such an effect could be further potentiated by NKp30 oligomerization. Importantly, Xu et al. [39,40] analyzed the crystal structure of the Fab of inhibitory antibody 17B1.3 in complex with the ectodomain of B7-H6 and found that 17B1.3 could bind to a site on B7-H6 that was completely different from the binding site on NKp30 (PDB 4ZSO). Using an NKp30 reporter cell line and B7-H6-expressing P815 tumor cells, they concluded that the bulky 17B1.3 antibody acts by sterically interfering with close cell–cell contacts at the NK cell–target cell interface, thereby blocking immunological synapse formation and NK cell activation [40].
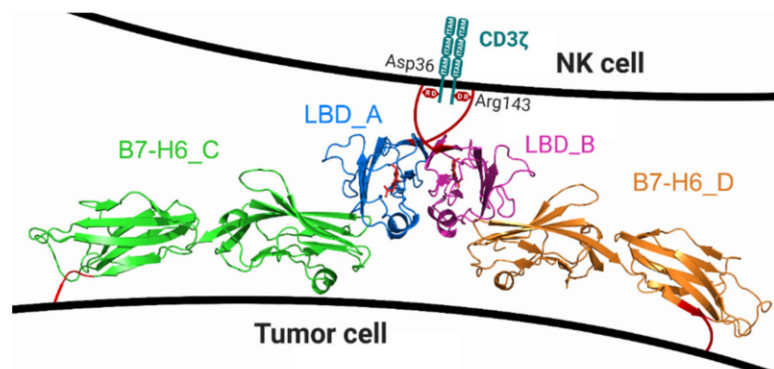
Figure 11. Model of the possible position of the NKp30_LBD:B7-H6 dimeric complex, as observed in the crystal structure (PDB 6YJP), within the NK cell immune synapse. B7-H6 has a very short stalk sequence of several amino acids only, whereas NKp30 has the 15 amino acids long stalk region at its C-terminus (red lines). The stalk is long enough to confer flexibility to the NKp30 ligand binding domain. Such an arrangement would bring the membranes of both cells into very close contact, and such an effect could be further potentiated by NKp30 oligomerization. Local deformation of the NK cell plasma membrane caused by the conformational change of the stalk region induced by ligand binding might trigger signal transduction through the CD3ζ chains associated with the NKp30 transmembrane domain thanks to the interaction of CD3ζ Asp36 residue with NKp30 Arg143 residue occurring at plasma membrane which is required for NKp30 signaling [7].

These results support the proposed close interaction mediated by the NKp30 dimer ligated with two B7-H6 monomers, as observed in the presented crystal structure. However, further studies are required to confirm such an arrangement directly on the membrane of living NK cells, as well as the oligomeric arrangement of NKp30. Considering the short length of the stalk region, it is unlikely that NKp30 forms octameric, decameric, or even larger oligomers through its stalk region on the cell surface, in contrast to its oligomerization in solution. Therefore, data on NKp30 receptor oligomers collected in solution, using its solubilized ectodomains interacting in three-dimensional (3D) space, should not be directly extrapolated to its natural habitat within the plasma membrane and to a 2.5D space on the cell surface. Moreover, all future immunotherapeutic strategies and reagents designed to target or trigger this NK cell receptor:ligand system should also allow enough flexibility with respect to the B7-H6 moiety, thus ensuring its proper orientation and interaction with NKp30.

4. Materials and Methods

4.1. Cell Culture and Vector Design

HEK293T cells were kindly provided by Radu A. Aricescu [24]. HEK293T and HEK293S GnTI⁻ cells [25] (0.3–6 × 10⁶/mL) were maintained in ExCELL293 serum-free medium (Sigma, St. Louis, MT, USA) supplemented with 4 mM L-glutamine in square-bottom glass DURAN flasks with gas permeable caps (DWK Life Sciences, Wertheim, Germany) using 30–40% of the nominal volume at 135 rpm on orbital shaker placed within the incubator at 37 °C and 5% CO_2 [26]. Transient expression in both HEK293T and HEK293S GnTI⁻ cell lines was performed using the plasmid pTW5sec, a derivative of the pTT5 plasmid backbone [41] modified in-house to contain a woodchuck hepatitis virus post-transcriptional regulatory element (WPRE) and a leader peptide of secreted alkaline phosphatase in frame with AgeI and KpnI cloning sites, followed by a C-terminal histidine tag. Therefore, proteins recombinantly expressed using this plasmid were secreted into the cell culture media and purified by immobilized metal affinity chromatography (IMAC).

4.2. Protein Expression and Purification

For high-density transfection, 800 × 10⁶ HEK293 cells were centrifuged for 5 min at 90× *g*. Cells were resuspended in 34 mL of ExCELL293 medium in an empty flask and 800 μg of DNA (1 μg/10⁶ cells) were diluted in 6 mL of phosphate-buffered saline (PBS) and filtered through a 0.22 μm filter into the flask with cells. Subsequently, linear 25 kDa polyethyleneimine (lPEI) was added in a 1:3 DNA:lPEI (*w/w*) ratio. Cells were incubated in high density on a shaker for 1.5–4 h at 37 °C. Afterwards, up to 400 mL ExCELL293 medium and 0.5 M valproic acid [42] were added to a final concentration of 2 mM. Cells were harvested after 7 days or earlier, when viability dropped below 70%, by centrifugation for 30 min at 15000× *g* at 20 °C. The supernatant was filtered through a 0.2 μm filter, diluted two-fold with PBS buffer, and loaded onto a pre-equilibrated 5 mL HiTrap TALON column using an ÄKTAprime FPLC system (GE Healthcare, Chicago, IL, USA). Protein was eluted with 250 mM imidazole in PBS, concentrated using Amicon Ultra (MWCO 10000; Sigma, St. Louis, MT, USA) concentrators, filtered using spin filter and subjected to size-exclusion chromatography on Superdex 200 Increase 10/300 GL column (GE Healthcare, USA) as a final purification step with HEPES buffer (10 mM HEPES pH 7.5, 150 mM NaCl, 10 mM NaN_3) as the mobile phase. For NKp30_Stalk, fractions were collected separately for oligomeric and monomeric species, and immediately frozen in liquid nitrogen. Protein glycosylation and disulfide bonds pairing were characterized by mass spectrometry (for details see Supplementary Methods) [43–45].

4.3. Protein Labelling

B7-H6 expressed in HEK293S GnTI⁻ cells was stained with ATTO 488 fluorescent dye (Sigma, USA) using NHS labelling chemistry according to the manufacturer's instructions. Nine volumes of B7-H6 solution in HEPES buffer were mixed with one volume of 1 M bicarbonate buffer, pH 8.5. ATTO 488-NHS ester was added to the protein solution at a molar ratio of 1:3 (protein:ATTO488-NHS). Reaction mixture was incubated for 60 min in the dark at room temperature on a roller shaker at 35 rpm. The labelled protein was purified on a HiTrap Desalting column (GE Healthcare, USA) connected to an ÄKTA basic HPLC system.

4.4. Deglycosylation

For deglycosylation of NKp30 and B7-H6 expressed in HEK293S GnTI⁻ cell lines, the proteins in HEPES buffer at 1 mg/mL concentration were mixed with recombinant GST-tagged endoglycosidase F1 (Endo F1) [46] in a 200:1 (*w/w*) ratio (target protein:Endo F1). For B7-H6, the buffer was supplemented with 20% glycerol to increase protein stability. The mixture was incubated for 3 h at 37 °C or at 4 °C overnight while mixing. Then, the solution was loaded onto a 5 mL GST-trap column (GE Healthcare, Chicago, IL, USA) connected to the fast protein liquid chromatography (FPLC) system to capture

the Endo F1, while collecting the flow-through containing deglycosylated protein. The solution was concentrated to 200 µL and loaded onto a Superdex 200 Increase 10/300 GL (GE Healthcare, Chicago, IL, USA) column for further purification and characterization of the deglycosylated proteins. Samples from collected fractions were used for SDS-PAGE analysis.

4.5. Differential Scanning Fluorimetry

Differential scanning fluorimetry was performed using SYPRO Orange Protein Gel Stain (Thermo Scientific, Waltham, MA, USA). Its 5000× DMSO stock solution was diluted to 50× concentrated solution. The samples were prepared by mixing 4 µL of B7-H6 expressed in HEK293S GnTI$^-$ cells with 10 µL of 2× concentrated screen buffer and 1 µL of 50× concentrated stain solution and complemented by HEPES buffer up to 20 µL. The sample without protein was used as a blank, and the sample with no additive was used as a reference. Data were collected on a Rotor-Gene 2000 Real Time Cycler (Corbett Research, Sydney, Australia) at an excitation wavelength of 300 nm. Fluorescence was measured at 570 nm. The temperature increased stepwise, 0.5 °C each 30 s from 25 °C to 95 °C. The data were evaluated using OriginPro 8 software (version 8.500161). Melting points can be extrapolated by finding the inflection point of sigmoid melting curves. By depicting the data as a negative derivative of relative fluorescence (−d(RF)/T), the melting points correspond to the minima of the melting curves.

4.6. Sedimentation Analysis

Sedimentation velocity measurements were performed on an analytical ultracentrifuge ProteomeLab XL-I (Beckman Coulter, Brea, CA, USA). Protein samples were purified by gel filtration, using the mobile phase buffer (10 mM HEPES pH 7.5, 150 mM NaCl, 10 mM NaN$_3$) as a reference. Sedimentation velocity experiments were conducted with 20 µM protein samples using double sector cells and An50-Ti rotor at 20 °C and 36,000 or 48,000 rpm for oligomeric or monomeric samples, respectively. Absorbance scans were recorded at 280 or 480 nm at 3–7 min intervals. Buffer density, protein partial specific volume, and particle dimensions were estimated in Sednterp (www.jphilo.mailway.com). Data were analyzed in Sedfit [47] using the continuous sedimentation coefficient distribution c(s) model. Analysis of NKp30_LBD at high concentration was performed with its 20 mg/mL sample at 50,000 rpm using 3 mm centerpiece; scans were recorded every 2 min using the interference optics. The data were fitted with the nonideal c(s) model in Sedfit [48].

4.7. Size-Exclusion Chromatography with Multi-Angle Laser Light Scattering (SEC-MALS)

SEC-MALS experiments were performed using an FPLC station equipped with miniDAWN Tristar light scattering (Wyatt Technologies, Santa Barbara, CA, USA) and Shodex RI-101 (Showa Denko K.K., Tokyo, Japan) refractive index detectors with a Superose 6 Increase 10/300 GL column (GE Healthcare, Chicago, IL, USA) equilibrated in 20 mM HEPES pH 7.5, 150 mM NaCl, 10 mM NaN$_3$ buffer. Single proteins or protein complexes, typically at 1 mg/mL concentration, were loaded onto the column. The molecular weight was estimated using the refractive index as measure of concentration. The results were analyzed using Astra software (Wyatt Technologies, Santa Barbara, CA, USA).

4.8. Isothermal Titration Calorimetry

Thermodynamic parameters of NKp30:B7-H6 interactions were determined using the PEAQ-ITC instrument (Malvern Panalytical, Westborough, MA, USA). All measurements were performed in the 10 mM HEPES pH 7.5, 150 mM NaCl, 10 mM NaN$_3$ buffer. First, control heat was determined by buffer–buffer titration. For protein interaction measurements, 200 µL of 20–30 µM NKp30 variants were loaded into the cell and 40 µL of 200–300 µM B7-H6 into the syringe (these concentrations varied slightly in different experiments). An initial injection of 0.4 µL of B7-H6 was followed by 25 injections of 1.5 µL. Injection duration was 2 s, in 120 s intervals, performing the measurements at 25 °C and stirring the cell solution at 750 rpm. The data were evaluated using NITPIC [49], Sedphat [50], and GUSSI software [51].

4.9. Surface Plasmon Resonance

Surface plasmon resonance (SPR) experiments were performed to measure NKp30_Stalk and NKp30_LBD binding, in three different *N*-glycosylation states (wild-type glycans, simple glycans, and deglycosylated with Endo F1), to B7-H6, also in three glycosylation states. Measurements were performed using the Biacore T200 system (GE Healthcare, Chicago, IL, USA) in a buffer composed of 10 mM HEPES pH 7.5, 150 mM NaCl, 1 mg/mL dextran, and 0.05% Tween-20. Three glycosylation variants of B7-H6 were biotinylated (EZ-Link NHS-Biotin; Thermo Fisher Scientific, Waltham, MA, USA) according to the manufacturer's instructions and immobilized to the streptavidin sensor. Binding experiments were performed in single cycle kinetics mode with 15 sequential injections of NKp30 samples in each cycle with concentrations ranging from 1 nM to 16.3 µM. Data from a reference flow cell with an empty channel were subtracted and fitted using the Biacore T200 evaluation software (version 3.0). Maximal fitted responses from each cycle were analyzed using Sedphat [50] software using the AB hetero-association model.

4.10. Protein Crystallization

Protein crystallization was performed at the Division of Structural Biology of the Wellcome Centre for Human Genetics, University of Oxford. Initial screening was performed using the sitting drop method in 300 nL (100 nL of protein solution and 200 nL of crystallization reagents) using the Hydra and Cartesian instruments. All crystallization plates were stored in Rock Imager (Formulatrix, Bedford, MA, USA) at 21 °C. Four commercially available screens (Index, Proplex, PACTpremier, Crystal screen) were used for the equimolar mixture of deglycosylated B7-H6 with NKp30_Stalk or NKp30_LBD, both expressed in HEK293S GnTI⁻ cells; the mixture was concentrated to 10 mg/mL before the drop set-up. Initially, needle-shaped crystals of NKp30_LBD:B7-H6 complex were obtained in 0.1 M sodium citrate pH 5.0, 20% PEG 8000. These crystals were crushed and used for seeding in optimization performed using the sitting drop method in 300 nL (200 nL of protein solution and 100 nL of crystallization reagents). The number of crystals grew in the drops that were seeded, and diffraction data were collected for a few of them. 25% glycerol was used as cryoprotectant and data were collected at 100 K. The best diffraction data were collected from crystals grown in 0.1 M sodium citrate pH 6.7, 11.7% PEG 6000.

4.11. Diffraction Data Collection

Eleven diffraction data sets were collected at the Diamond Light Source (Didcot, Oxfordshire, UK) at beamline I02 using a wavelength of 0.97949 Å and a PILATUS 6M-F detector (Dectris, Baden-Daettwil, Switzerland). The resolution of all data sets was 3–4 Å and the crystals degraded during the data collection. Eventually, three data sets from three crystals (set B7x1: images 1 to 800 (80°), set B8x5:1 to 800 (80°), and set B8x3:1 to 450 (45°)) were merged to process the data for optimal results. The data were integrated in XDS [52] and merged and scaled in AIMLESS from the CCP4 software package [53], in space group *C*2 (recommended by POINTLESS and ZANUDA) and alternatively in P1. Finally, *C*2 was selected as the correct space group based on the phase problem solution and refinement. Data suffered by strong anisotropy, with effective resolution in the direction of axis *a* being the lowest, ca. 4.4 Å. Anisotropy corrections were not applied to the data. Final data processing statistics are shown in Table 1.

4.12. Structure Solution and Refinement

The phase problem was solved in space group *C*2, using MORDA [54] and PHASER [55], data cut off 3.8 Å and already known structures of NKp30 and B7-H6 as models (PDB code 3PV6 for both molecules). The asymmetric unit in *C*2 contains three B7-H6 protein chains and two NKp30 chains. After refinement trials in REFMAC5 [56], considering manual optimization of restraints, B-values and translation, rotation, and screw-rotation (TLS) parameterization, the structures were

refined in LORESTR (automatic REFMAC5 pipeline for low-resolution structure refinement, [57]), using atomic B-factors, without TLS and with restraints to homologs optimized specially for each run of the refinement. Five percent of reflections were used as a test set (R_{free} set). Manual editing was performed in COOT [58]. Structure quality was checked using the validation tools implemented in MOLPROBITY [59]. There are four Ramachandran outliers (chain C Gly83 and Val152, chain D Gly83, and chain E Gln182), which is 0.5% of refined residues. The final structure parameters are outlined in Table 1.

4.13. Data and Structure Deposition

Diffraction data have been deposited in the SBGrid Data Bank under code 753 (doi:10.15785/SBGRID/753). The crystal structure has been deposited in the Protein Data Bank under code 6YJP.

5. Conclusions

Glycosylation is an essential post-translational modification of cell surface proteins, not only stabilizing them in the extracellular environment but also providing new functional modalities. Moreover, glycosylation is crucial for immune recognition and self-non-self discrimination, especially when involving receptors of the innate immune system, which often bind to their ligands with weak affinities. Accordingly, their ability to transduce the signal into the cell should significantly vary as a function of their glycosylation presence and its type. Glycans may help these receptors to create stable signaling complexes through dimerization and oligomerization or to organize them within complex dynamic structures of the immune synapse. In this study, we exemplified this behavior for the NK cell activation receptor NKp30, whose oligomerization depends on its *N*-glycosylation. Furthermore, we solved the first crystal structure of a glycosylated NKp30 ligand binding domain, in a complex with its tumor ligand B7-H6, highlighting why glycosylation is crucial for the NKp30 oligomerization and for signal transduction. Furthermore, our results indicate that glycosylation should not be overlooked when planning or conducting structure-function studies. In conclusion, our structure of the complex between glycosylated NKp30 and B7-H6 provides a template for designing molecules to stimulate NKp30-mediated cytolytic activity for tumor immunotherapy.

Conflicts of Interest: The authors declare no conflict of interest.

References

1. Kiessling, R.; Klein, E.; Wigzell, H. „Natural" killer cells in the mouse. I. Cytotoxic cells with specificity for mouse Moloney leukemia cells. Specificity and distribution according to genotype. *Eur. J. Immunol.* **1975**, *5*, 112–117. [CrossRef] [PubMed]

2. Herberman, R.B.; Nunn, M.E.; Holden, H.T.; Lavrin, D.H. Natural cytotoxic reactivity of mouse lymphoid cells against syngeneic and allogeneic tumors. II. Characterization of effector cells. *Int. J. Cancer* **1975**, *16*, 230–239. [CrossRef] [PubMed]

3. Pegram, H.J.; Andrews, D.M.; Smyth, M.J.; Darcy, P.K.; Kershaw, M. Activating and inhibitory receptors of natural killer cells. *Immunol. Cell Biol.* **2011**, *89*, 216–224. [CrossRef] [PubMed]

4. Kruse, P.H.; Matta, J.; Ugolini, S.; Vivier, E. Natural cytotoxicity receptors and their ligands. *Immunol. Cell Biol.* **2014**, *92*, 221–229. [CrossRef]

5. Biassoni, R. Human Natural Killer Receptors, Co-Receptors, and Their Ligands. *Curr. Protoc. Immunol.* **2009**, *84*. [CrossRef]

6. Pende, D.; Parolini, S.; Pessino, A.; Sivori, S.; Augugliaro, R.; Morelli, L.; Marcenaro, E.; Accame, L.; Malaspina, A.; Biassoni, R.; et al. Identification and Molecular Characterization of Nkp30, a Novel Triggering Receptor Involved in Natural Cytotoxicity Mediated by Human Natural Killer Cells. *J. Exp. Med.* **1999**, *190*, 1505–1516. [CrossRef]

7. Memmer, S.; Weil, S.; Beyer, S.; Zöller, T.; Peters, E.; Hartmann, J.; Steinle, A.; Koch, J. The Stalk Domain of NKp30 Contributes to Ligand Binding and Signaling of a Preassembled NKp30-CD3ζ Complex. *J. Biol. Chem.* **2016**, *291*, 25427–25438. [CrossRef]

8. Kaifu, T.; Escalière, B.; Gastinel, L.N.; Vivier, E.; Baratin, M. B7-H6/NKp30 interaction: A mechanism of alerting NK cells against tumors. *Cell. Mol. Life Sci.* **2011**, *68*, 3531–3539. [CrossRef]

9. Hershkovitz, O.; Jarahian, M.; Zilka, A.; Bar-Ilan, A.; Landau, G.; Jivov, S.; Tekoah, Y.; Glicklis, R.; Gallagher, J.T.; Hoffmann, S.C.; et al. Altered glycosylation of recombinant NKp30 hampers binding to heparan sulfate: A lesson for the use of recombinant immunoreceptors as an immunological tool. *Glycobiology* **2008**, *18*, 28–41. [CrossRef]

10. Chisholm, S.E.; Reyburn, H.T. Recognition of Vaccinia Virus-Infected Cells by Human Natural Killer Cells Depends on Natural Cytotoxicity Receptors. *J. Virol.* **2006**, *80*, 2225–2233. [CrossRef]

11. Arnon, T.I.; Achdout, H.; Levi, O.; Markel, G.; Saleh, N.; Katz, G.; Gazit, R.; Gonen-Gross, T.; Hanna, J.; Nahari, E.; et al. Inhibition of the NKp30 activating receptor by pp65 of human cytomegalovirus. *Nat. Immunol.* **2005**, *6*, 515–523. [CrossRef]

12. Brandt, C.S.; Baratin, M.; Yi, E.C.; Kennedy, J.; Gao, Z.; Fox, B.; Haldeman, B.; Ostrander, C.D.; Kaifu, T.; Chabannon, C.; et al. The B7 family member B7-H6 is a tumor cell ligand for the activating natural killer cell receptor NKp30 in humans. *J. Exp. Med.* **2009**, *206*, 1495–1503. [CrossRef] [PubMed]

13. Binici, J.; Koch, J. BAG-6, a jack of all trades in health and disease. *Cell. Mol. Life Sci.* **2014**, *71*, 1829–1837. [CrossRef] [PubMed]

14. Schlecker, E.; Fiegler, N.; Arnold, A.; Altevogt, P.; Rose-John, S.; Moldenhauer, G.; Sucker, A.; Paschen, A.; Von Strandmann, E.P.; Textor, S.; et al. Metalloprotease-Mediated Tumor Cell Shedding of B7-H6, the Ligand of the Natural Killer Cell-Activating Receptor NKp30. *Cancer Res.* **2014**, *74*, 3429–3440. [CrossRef] [PubMed]

15. Wang, W.; Guo, H.; Geng, J.; Zheng, X.; Wei, H.; Sun, R.; Tian, Z. Tumor-released Galectin-3, a Soluble Inhibitory Ligand of Human NKp30, Plays an Important Role in Tumor Escape from NK Cell Attack. *J. Biol. Chem.* **2014**, *289*, 33311–33319. [CrossRef] [PubMed]

16. Chen, Y.; Mo, J.; Jia, X.; He, Y. The B7 Family Member B7-H6: A New Bane of Tumor. *Pathol. Oncol. Res.* **2018**, *24*, 717–721. [CrossRef] [PubMed]

17. Hu, Y.; Zeng, T.; Xiao, Z.; Hu, Q.; Li, Y.; Tan, X.; Yue, H.; Wang, W.; Tan, H.; Zou, J. Immunological role and underlying mechanisms of B7-H6 in tumorigenesis. *Clin. Chim. Acta* **2020**, *502*, 191–198. [CrossRef]

18. Matta, J.; Baratin, M.; Chiche, L.; Forel, J.-M.; Cognet, C.; Thomas, G.; Farnarier, C.; Piperoglou, C.; Papazian, L.; Chaussabel, D.; et al. Induction of B7-H6, a ligand for the natural killer cell–activating receptor NKp30, in inflammatory conditions. *Blood* **2013**, *122*, 394–404. [CrossRef]

19. Joyce, M.G.; Tran, P.; Zhuravleva, M.A.; Jaw, J.; Colonna, M.; Sun, P.D. Crystal structure of human natural cytotoxicity receptor NKp30 and identification of its ligand binding site. *Proc. Natl. Acad. Sci. USA* **2011**, *108*, 6223–6228. [CrossRef]

20. Li, Y.; Wang, Q.; Mariuzza, R.A. Structure of the human activating natural cytotoxicity receptor NKp30 bound to its tumor cell ligand B7-H6. *J. Exp. Med.* **2011**, *208*, 703–714. [CrossRef]

21. Herrmann, J.; Berberich, H.; Hartmann, J.; Beyer, S.; Davies, K.E.; Koch, J. Homo-oligomerization of the Activating Natural Killer Cell Receptor NKp30 Ectodomain Increases Its Binding Affinity for Cellular Ligands. *J. Biol. Chem.* **2014**, *289*, 765–777. [CrossRef]

22. Hartmann, J.; Tran, T.-V.; Kaudeer, J.; Oberle, K.; Herrmann, J.; Quagliano, I.; Abel, T.; Cohnen, A.; Gatterdam, V.; Jacobs, A.; et al. The Stalk Domain and the Glycosylation Status of the Activating Natural Killer Cell Receptor NKp30 Are Important for Ligand Binding. *J. Biol. Chem.* **2012**, *287*, 31527–31539. [CrossRef] [PubMed]

23. Binici, J.; Hartmann, J.; Herrmann, J.; Schreiber, C.; Beyer, S.; Güler, G.; Vogel, V.; Tumulka, F.; Abele, R.; Mäntele, W.; et al. A Soluble Fragment of the Tumor Antigen BCL2-associated Athanogene 6 (BAG-6) Is Essential and Sufficient for Inhibition of NKp30 Receptor-dependent Cytotoxicity of Natural Killer Cells. *J. Biol. Chem.* **2013**, *288*, 34295–34303. [CrossRef] [PubMed]

24. Aricescu, A.R.; Lu, W.; Jones, E.Y. A time- and cost-efficient system for high-level protein production in mammalian cells. *Acta Crystallogr. Sect. D Biol. Crystallogr.* **2006**, *62*, 1243–1250. [CrossRef] [PubMed]

25. Reeves, P.J.; Callewaert, N.; Contreras, R.; Khorana, H.G. Structure and function in rhodopsin: High-level expression of rhodopsin with restricted and homogeneous N-glycosylation by a tetracycline-inducible N-acetylglucosaminyltransferase I-negative HEK293S stable mammalian cell line. *Proc. Natl. Acad. Sci. USA* **2002**, *99*, 13419–13424. [CrossRef]

26. Bláha, J.; Maraun, M.; Novák, P.; Vaněk, O. Expression and purification of soluble and stable ectodomain of natural killer cell receptor LLT1 through high-density transfection of suspension adapted HEK293S GnTI⁻ cells. *Protein Expr. Purif.* **2015**, *109*, 7–13. [CrossRef] [PubMed]

27. Krissinel, E.; Henrick, K. Inference of Macromolecular Assemblies from Crystalline State. *J. Mol. Biol.* **2007**, *372*, 774–797. [CrossRef] [PubMed]

28. Ni, L.; Dong, C. New B7 Family Checkpoints in Human Cancers. *Mol. Cancer Ther.* **2017**, *16*, 1203–1211. [CrossRef]

29. Wu, M.-R.; Zhang, T.; Gacerez, A.T.; Coupet, T.A.; Demars, L.R.; Sentman, C.L. B7H6-Specific Bispecific T Cell Engagers Lead to Tumor Elimination and Host Antitumor Immunity. *J. Immunol.* **2015**, *194*, 5305–5311. [CrossRef]

30. Gacerez, A.T.; Hua, C.K.; Ackerman, M.E.; Sentman, C.L. Chimeric antigen receptors with human scFvs preferentially induce T cell anti-tumor activity against tumors with high B7H6 expression. *Cancer Immunol. Immunother.* **2018**, *67*, 749–759. [CrossRef]

31. Kellner, C.; Maurer, T.; Hallack, D.; Repp, R.; Van De Winkel, J.G.J.; Parren, P.W.H.I.; Valerius, T.; Humpe, A.; Gramatzki, M.; Peipp, M.; et al. Mimicking an Induced Self Phenotype by Coating Lymphomas with the NKp30 Ligand B7-H6 Promotes NK Cell Cytotoxicity. *J. Immunol.* **2012**, *189*, 5037–5046. [CrossRef] [PubMed]

32. Kellner, C.; Günther, A.; Humpe, A.; Repp, R.; Klausz, K.; Derer, S.; Valerius, T.; Ritgen, M.; Brüggemann, M.; Van De Winkel, J.G.; et al. Enhancing natural killer cell-mediated lysis of lymphoma cells by combining therapeutic antibodies with CD20-specific immunoligands engaging NKG2D or NKp30. *OncoImmunology* **2016**, *5*, e1058459. [CrossRef]

33. Peipp, M.; Derer, S.; Lohse, S.; Staudinger, M.; Klausz, K.; Valerius, T.; Gramatzki, M.; Kellner, C. HER2-specific immunoligands engaging NKp30 or NKp80 trigger NK-cell-mediated lysis of tumor cells and enhance antibody-dependent cell-mediated cytotoxicity. *Oncotarget* **2015**, *6*, 32075–32088. [CrossRef] [PubMed]

34. Jaron-Mendelson, M.; Yossef, R.; Appel, M.; Zilka, A.; Hadad, U.; Afergan, F.; Rosental, B.; Engel, S.; Nedvetzki, S.; Braiman, A.; et al. Dimerization of NKp46 Receptor Is Essential for NKp46-Mediated Lysis: Characterization of the Dimerization Site by Epitope Mapping. *J. Immunol.* **2012**, *188*, 6165–6174. [CrossRef] [PubMed]

35. Hadad, U.; Thauland, T.J.; Martinez, O.M.; Butte, M.J.; Porgador, A.; Krams, S.M. NKp46 Clusters at the Immune Synapse and Regulates NK Cell Polarization. *Front. Immunol.* **2015**, *6*, 216. [CrossRef]

36. Arnon, T.I.; Markel, G.; Bar-Ilan, A.; Hanna, J.H.; Fima, E.; Benchetrit, F.; Galili, R.; Cerwenka, A.; Benharroch, D.; Sion-Vardy, N.; et al. Harnessing Soluble NK Cell Killer Receptors for the Generation of Novel Cancer Immune Therapy. *PLoS ONE* **2008**, *3*, e2150. [CrossRef]

37. Franke, D.; Petoukhov, M.V.; Konarev, P.V.; Panjkovich, A.; Tuukkanen, A.; Mertens, H.D.T.; Kikhney, A.G.; Hajizadeh, N.R.; Franklin, J.M.; Jeffries, C.M.; et al. ATSAS 2.8: A comprehensive data analysis suite for small-angle scattering from macromolecular solutions. *J. Appl. Crystallogr.* **2017**, *50*, 1212–1225. [CrossRef]

38. Pettersen, E.F.; Goddard, T.D.; Huang, C.C.; Couch, G.S.; Greenblatt, D.M.; Meng, E.C.; Ferrin, T.E. UCSF Chimera—A visualization system for exploratory research and analysis. *J. Comput. Chem.* **2004**, *25*, 1605–1612. [CrossRef]

39. Xu, X.; Li, Y.; Gauthier, L.; Chen, Q.; Vivier, E.; Mariuzza, R.A. Expression, crystallization and X-ray diffraction analysis of a complex between B7-H6, a tumor cell ligand for the natural cytotoxicity receptor NKp30, and an inhibitory antibody. *Acta Crystallogr. Sect. F Struct. Biol. Commun.* **2015**, *71*, 697–701. [CrossRef]

40. Xu, X.; Narni-Mancinelli, E.; Cantoni, C.; Li, Y.; Guia, S.; Gauthier, L.; Chen, Q.; Moretta, A.; Vély, F.; Eisenstein, E.; et al. Structural Insights into the Inhibitory Mechanism of an Antibody against B7-H6, a Stress-Induced Cellular Ligand for the Natural Killer Cell Receptor NKp30. *J. Mol. Biol.* **2016**, *428*, 4457–4466. [CrossRef]

41. Durocher, Y. High-level and high-throughput recombinant protein production by transient transfection of suspension-growing human 293-EBNA1 cells. *Nucleic Acids Res.* **2002**, *30*, 9e. [CrossRef]

42. Backliwal, G.; Hildinger, M.; Kuettel, I.; Delegrange, F.; Hacker, D.L.; Wurm, F.M. Valproic acid: A viable alternative to sodium butyrate for enhancing protein expression in mammalian cell cultures. *Biotechnol. Bioeng.* **2008**, *101*, 182–189. [CrossRef]

43. Pompach, P.; Man, P.; Kavan, D.; Hofbauerová, K.; Kumar, V.; Bezouska, K.; Havlicek, V.; Novák, P. Modified electrophoretic and digestion conditions allow a simplified mass spectrometric evaluation of disulfide bonds. *J. Mass Spectrom.* **2009**, *44*, 1571–1578. [CrossRef] [PubMed]

44. Young, M.M.; Tang, N.; Hempel, J.C.; Oshiro, C.M.; Taylor, E.W.; Kuntz, I.D.; Gibson, B.W.; Dollinger, G. High throughput protein fold identification by using experimental constraints derived from intramolecular cross-links and mass spectrometry. *Proc. Natl. Acad. Sci. USA* **2000**, *97*, 5802–5806. [CrossRef]

45. Kukačka, Z.; Rosulek, M.; Strohalm, M.; Kavan, D.; Novák, P. Mapping protein structural changes by quantitative cross-linking. *Methods* **2015**, *89*, 112–120. [CrossRef]

46. Grüninger, F.; D'Arcy, A.; D'Arcy, B.; Chène, C. Deglycosylation of proteins for crystallization using recombinant fusion protein glycosidases. *Protein Sci.* **1996**, *5*, 2617–2622. [CrossRef]

47. Schuck, P. Size-Distribution Analysis of Macromolecules by Sedimentation Velocity Ultracentrifugation and Lamm Equation Modeling. *Biophys. J.* **2000**, *78*, 1606–1619. [CrossRef]

48. Chaturvedi, S.; Ma, J.; Brown, P.H.; Zhao, H.; Schuck, P. Measuring macromolecular size distributions and interactions at high concentrations by sedimentation velocity. *Nat. Commun.* **2018**, *9*, 4415. [CrossRef] [PubMed]

49. Scheuermann, T.H.; Brautigam, C.A. High-precision, automated integration of multiple isothermal titration calorimetric thermograms: New features of NITPIC. *Methods* **2015**, *76*, 87–98. [CrossRef] [PubMed]

50. Zhao, H.; Piszczek, G.; Schuck, P. SEDPHAT—A platform for global ITC analysis and global multi-method analysis of molecular interactions. *Methods* **2015**, *76*, 137–148. [CrossRef] [PubMed]

51. Brautigam, C.A. Calculations and Publication-Quality Illustrations for Analytical Ultracentrifugation Data. *Methods Enzymol.* **2015**, *562*, 109–133. [CrossRef]

52. Kabsch, W. XDS. *Acta Crystallogr. Sect. D Biol. Crystallogr.* **2010**, *66*, 125–132. [CrossRef]

53. Winn, M.; Ballard, C.C.; Cowtan, K.; Dodson, E.J.; Emsley, P.; Evans, P.R.; Keegan, R.M.; Krissinel, E.B.; Leslie, A.G.W.; McCoy, A.; et al. Overview of the CCP4 suite and current developments. *Acta Crystallogr. Sect. D Biol. Crystallogr.* **2011**, *67*, 235–242. [CrossRef]

54. Vagin, A.; Lebedev, A. MoRDa, an automatic molecular replacement pipeline. *Acta Crystallogr. Sect. A Found. Adv.* **2015**, *71*, S19. [CrossRef]

55. McCoy, A.J.; Grosse-Kunstleve, R.W.; Adams, P.D.; Winn, M.D.; Storoni, L.C.; Read, R.J. Phaser crystallographic software. *J. Appl. Crystallogr.* **2007**, *40*, 658–674. [CrossRef] [PubMed]

56. Murshudov, G.N.; Skubak, P.; Lebedev, A.A.; Pannu, N.S.; Steiner, R.A.; Nicholls, R.; Winn, M.D.; Long, F.; Vagin, A.A. REFMAC5 for the refinement of macromolecular crystal structures. *Acta Crystallogr. Sect. D Biol. Crystallogr.* **2011**, *67*, 355–367. [CrossRef] [PubMed]

57. Kovalevskiy, O.; Nicholls, R.; Murshudov, G. Automated refinement of macromolecular structures at low resolution using prior information. *Acta Crystallogr. Sect. D Struct. Biol.* **2016**, *72*, 1149–1161. [CrossRef] [PubMed]
58. Emsley, P.; Lohkamp, B.; Scott, W.G.; Cowtan, K. Features and development of Coot. *Acta Crystallogr. Sect. D Biol. Crystallogr.* **2010**, *66*, 486–501. [CrossRef]
59. Chen, V.B.; Arendall, W.B.; Headd, J.J.; Keedy, D.; Immormino, R.M.; Kapral, G.J.; Murray, L.W.; Richardson, J.S.; Richardson, D.C. MolProbity: All-atom structure validation for macromolecular crystallography. *Acta Crystallogr. Sect. D Biol. Crystallogr.* **2010**, *66*, 12–21. [CrossRef]

7.4 PUBLICATION NO. 4

Bláha, J.; Skálová, T.; Kalousková, B.; Skořepa, O.; Cmunt, D.; Pažický, S.; Poláchová, E.; Abreu, C.; Stránský, J.; Koval', T.; Dušková, J.; Zhao, J.; Harlos, K.; Hašek, J.; Dohnálek, J.; Vaněk, O.

Crystal structure of the human NKR-P1 bound to its lymphocyte ligand LLT1 reveals receptor clustering in the immune synapse.

This article is a preprint and has not been certified by peer review.

My contribution to the publication:
Performing research (cell culture maintenance, transfection optimization, protein expression, protein purification, and quality control, cellular assays, superresolution microscopy experiment optimization, and data acquisition), data analysis, interpretation, visualization of the results

Crystal structure of the human NKR-P1 bound to its lymphocyte ligand LLT1 reveals receptor clustering in the immune synapse

Jan Bláha[1,#], Tereza Skálová[2], Barbora Kalousková[1], Ondřej Skořepa[1], Denis Cmunt[1,§], Samuel Pažický[1,#], Edita Poláchová[1], Celeste Abreu[1], Jan Stránský[2], Tomáš Kovaľ[2], Jarmila Dušková[2], Yuguang Zhao[3], Karl Harlos[3], Jindřich Hašek[2], Jan Dohnálek[2], Ondřej Vaněk[1,*]

[1] Department of Biochemistry, Faculty of Science, Charles University, Hlavova 2030, 12840 Prague, Czech Republic

[2] Institute of Biotechnology, The Czech Academy of Sciences, BIOCEV Centre, Průmyslová 595, 25250 Vestec, Czech Republic

[3] Division of Structural Biology, The Wellcome Trust Centre for Human Genetics, University of Oxford, Roosevelt Drive, OX3 7BN Oxford, United Kingdom

[#] Present address: EMBL, Hamburg Unit c/o DESY, Notkestrasse 85, 22607 Hamburg, Germany

[§] Present address: Department of Oncology, Ludwig Institute for Cancer Research, University of Lausanne, Chemin des Boveresses 155, 1066 Epalinges, Switzerland

[*] Corresponding author. Tel.: +420221951272, E-mail: ondrej.vanek@natur.cuni.cz

Abstract

Human NKR-P1 (CD161, *KLRB1*) and its ligand LLT1 (*CLEC2D*) are a prototypical inhibitory C-type lectin-like receptor:ligand pair of NK cells with a critical role in homing lymphocytes to immune-privileged sites, particularly in multiple sclerosis, rheumatoid arthritis, and Crohn's disease. Furthermore, NKR-P1:LLT1 inhibitory signaling is associated with glioblastoma, non-Hodgkin's lymphoma, breast, and prostate cancer. However, the lack of structural data on the formation of the NKR-P1:LLT1 complex limits our understanding of this signaling. We thus solved the crystal structures of NKR-P1 and the NKR-P1:LLT1 complex. NKR-P1 forms a homodimer with an unexpected arrangement that enables LLT1 binding in two modes, bridging two LLT1 molecules, thereby forming interaction clusters suggestive of an inhibitory immune synapse. Moreover, observing the formation of these clusters by SEC-SAXS analysis in solution and by dSTORM super-resolution microscopy on the cell surface, and following their role in receptor signaling using *in vitro* cytotoxicity assay with freshly isolated NK cells, we show how NKR-P1:LLT1 clustering allows these proteins to overcome the weak affinity of C-type lectin-like receptors to their ligands. Furthermore, only the ligation of both primary and secondary LLT1 binding interfaces leads to effective NKR-P1 inhibitory signaling. Therefore, our findings show how inhibitory receptor cross-linking and clustering work together to trigger signal transduction upon cellular contact in the immune synapse.

Keywords: NKR-P1; CD161; KLRB1; LLT1; CLEC2D; NK cells; C-type lectin-like; X-ray structure; SEC-SAXS; dSTORM

Introduction

Natural killer (NK) cells are innate immune lymphocytes equipped with a wide range of activating and inhibitory surface receptors, allowing them to sensitively recognize and kill malignant, infected, or other transformed cells through "missing-" and "induced-self" mechanisms and through antibody-dependent cell-mediated cytotoxicity (ADCC)[1]. In addition, NK cells also contribute to the initiation and development of the adaptive immune response, secreting several classes of cytokines, especially proinflammatory IFN-γ[1]. Interestingly, recent findings show that NK cells are even capable of maintaining a form of immunological memory[1, 2], thus further highlighting the principal roles NK cells play in immunity, particularly through their receptors.

NK receptors comprise two structurally divergent classes: the families of immunoglobulin-like receptors and C-type lectin-like receptors (CTLRs)[3, 4]. CTLRs are encoded within the natural killer gene complex (NKC, human chromosome 12), and, unlike C-type lectins, CTLRs neither bind calcium ions nor engage carbohydrate ligands[5, 6]. Instead, CTLRs are known to interact with protein ligands. For example, receptors such as Ly49, CD94/NKG2, or NKG2D recognize MHC class-I like molecules[3], whereas receptors of the NKR-P1 subfamily recognize structurally highly related Clr/Ocil CTLRs. These are encoded by *CLEC2* genes[3, 5] that are genetically tightly linked with the NKR-P1-coding *KLR* genes. This unique CTLR:CTLR interaction system is involved in both non-MHC missing-self and induced-self recognition[3, 4, 5]. Several inhibitory and activating NKR-P1 receptors have been described in mice and rats; however, the human receptor NKR-P1 (CD161, *KLRB1* gene) remains since 1994 the only human orthologue described so far[7]. Nevertheless, based on structural and functional homology to NKR-P1, the human activating CTLR:ligand pairs NKp65:KACL (*KLRF2:CLEC2A*)[8] and NKp80:AICL (*KLRF1:CLEC2B*)[9] have been proposed as the activating counterparts of human NKR-P1[4, 10].

Human NKR-P1 (CD161) was first reported as a marker of NK cells[7], in which NKR-P1 acts as an inhibitory receptor[7, 11, 12] up-regulated by IL-12[13]. However, NKR-P1 is also expressed by natural killer T (NKT) cells[14], mucosal-associated invariant T (MAIT) cells[15], and other subsets of T-lymphocytes[16], wherein NKR-P1 acts as a co-stimulatory receptor, increasing IFN-γ secretion[11, 17]. Unsurprisingly, NKR-P1 is even detected in immature CD16- CD56- NK cells[18] and in precursors of Th17 and MAIT cells in the umbilical cord blood[19]. Recently, NKR-P1 was identified in glioma-infiltrating T cells, having an inhibitory, immunosuppressive role in T cell-mediated killing of glioma cells[20]. In addition, NKR-P1 promotes

transendothelial migration to immunologically privileged niches upon interaction with its endogenous ligand, lectin-like transcript 1 (LLT1)[19, 21, 22].

LLT1 (gene *CLEC2D*) is primarily expressed on activated monocytes and B cells[23]. In these cells, LLT1 helps to maintain NK cell self-tolerance[10, 23]. However, IL-2 can induce its expression on NK and T cells[24]. Furthermore, LLT1 is up-regulated on glioblastoma[25], prostate and triple-negative breast cancer[26, 27], and B cell non-Hodgkin's lymphoma[28] cells, in which LLT1 contributes to immune evasion by dampening NK cell cytotoxicity. Interestingly, increased numbers of CD161^{+} Th17 cells have been detected in glioma tumors[29]. Concomitantly, the functions of NKR-P1 receptors on IL-17-producing regulatory T cells[30], on subsets of Tc17 cells[31], and all Th17 cells[19] are particularly relevant because these cells have been implicated in several autoimmune diseases (Crohn's disease[32], multiple sclerosis[33], rheumatoid arthritis[34], and psoriasis[35]). Therefore, the analysis of NKR-P1 receptors and ligands such as LLT1 is essential to gain a deeper insight into the structure-function relationships underlying both physiological and pathogenic processes in the immune system.

Human NKR-P1 and LLT1 are type II transmembrane glycoproteins with similar protein topology[4]: an N-terminal cytoplasmic signaling tail, a transmembrane helix, a flexible stalk region, and a C-terminal C-type lectin-like domain (CTLD)[3, 7, 36]. Moreover, both NKR-P1 and LLT1 were shown to form disulfide homodimers[7, 36], likely linked in their stalk regions. However, the structure of NKp65:KACL complex[37] is the only one among all complexes of the human CTL receptor:ligand subfamily that has been solved so far. A subsequent study further showed that the interaction between NKp65 and KACL is protein-based and independent of glycosylation[38]. Based on these data, a model of the NKR-P1:LLT1 complex was subsequently proposed, and key interaction residues were identified through surface plasmon resonance (SPR) analysis of NKR-P1 and LLT1 mutants, highlighting the fast kinetics of this interaction[39, 40]. Furthermore, the structures of related mouse NKR-P1B ectodomain complexed with murine cytomegalovirus (MCMV) immunoevasin protein m12, or with its cognate ligand Clrb, have been recently reported[41, 42]. Notwithstanding, no comprehensive model of the CTLR:ligand complexes' dimer:dimer interaction, corresponding to the natural state of these proteins when expressed on the cells' surface, is available yet.

Previously, we reported the first structure of LLT1[43] forming a non-covalent dimer following the conserved dimerization mode of *CLEC2*-encoded ligands, regardless of glycosylation[44]. Here, we investigated the structure of human NKR-P1 and examined the effects of NKR-P1 dimerization on LLT1 binding, thereby solving the structure of the human NKR-P1 receptor. Accordingly, in this study, we show that NKR-P1 forms a non-covalent dimer that differs from the dimerization mode observed for CD69[45, 46], Clrg[47], and LLT1[43], and we discuss the role of glycosylation in its dimerization. Furthermore, the crystal structure of NKR-P1 in complex

with LLT1 explains the previous in-solution interaction observations while simultaneously showing a novel assembly of this complex utilizing two different non-symmetric binding sites on LLT1. Lastly, by combining dSTORM nanoscopy cluster analysis of NKR-P1 on the cell surface with data from the obtained crystal structures, biophysical interaction and structural analyses in solution, and *in vitro* NK cell killing assays, we show for the first time that human NKR-P1 receptor overcomes its weak affinity for LLT1 by ligand binding-induced cross-linking and clustering, thus elucidating the mode of signal transduction of this receptor within the NK cell immune synapse.

Results

Structure of the human NKR-P1 ectodomain

Two crystal structures of the human NKR-P1 ectodomain were solved: the structure of glycosylated NKR-P1 possessing uniform Asn-$GlcNAc_2Man_5$ N-glycans (NKR-P1_glyco) and of deglycosylated NKR-P1 with N-glycans cleaved off after the first GlcNAc residue (NKR-P1_deglyco); statistical data on all structures are outlined in Table 1. NKR-P1 in both crystal structures follows the general fold characteristic of a CTL domain – two α-helices (α1 and α2) and two antiparallel β-sheets with the conserved hydrophobic WIGL motif within the domain core (Figs. 1 and 2a). The two β-sheets are formed by β-strands β0, β1, β1' and β5, and β2, β2′, β3, and β4, respectively (assignment according to Zelensky and Gready[5], also used to describe other related CTL structures[37, 40]). In addition, three intramolecular disulfide bonds stabilize the domain: Cys94-Cys105, Cys122-Cys210, and Cys189-Cys202.

Table 1. Data processing statistics and structure refinement parameters. Values in parentheses refer to the highest resolution shell.

Crystal structure	NKR-P1 glyco	NKR-P1 deglyco	NKR-P1:LLT1
PDB code	5MGR	5MGS	5MGT
Data processing statistics			
Space group	$P3_121$	P1	$P2_12_12_1$
Unit-cell parameters *a, b, c* (Å); α, β, γ (°)	68.24, 68.24, 127.19; 90, 90, 120	44.81, 68.40, 101.56; 101.88, 100.72, 100.64	44.58, 80.15, 272.95; 90, 90, 90
Resolution range (Å)	43.3 – 1.8 (1.84 – 1.80)	48.68 – 1.90 (1.93 – 1.90)	76.90 – 1.90 (1.94 – 1.90)
No. of observations	1287150 (76917)	610421 (26224)	1452154 (80494)
No. of unique reflections	32555 (1900)	87081 (4353)	78617 (4472)
Data completeness (%)	100 (100)	97.9 (95.1)	100 (99.9)
Average redundancy	39.5 (40.5)	7.0 (6.0)	18.5 (18.0)
Mosaicity (°)	0.08	0.09	0.05

Average $I/\sigma(I)$	41.0 (7.4)	12.9 (1.7)	14.0 (3.0)
Solvent content (%)	47	42	57
Matthews coefficient (Å³/Da)	2.32	2.13	2.32
R_{merge}†	0.061 (0.637)	0.085 (0.894)	0.153 (0.976)
R_{pim}	0.010 (0.102)	0.053 (0.618)	0.052 (0.337)
CC1/2	1.000 (0.975)	0.999 (0.671)	0.998 (0.890)
Structure refinement parameters			
R_{work}	0.167	0.157	0.166
R_{free}	0.202	0.207	0.201
R_{all}	0.168	0.157	0.166
Average B-factor (Å²)	33	32	26
RMSD bond lengths from ideal (Å)	0.016	0.018	0.019
RMSD bond angles from ideal (°)	1.7	1.8	1.8
Number of non-hydrogen atoms	2481	8344	7030
Number of dimers per asymmetric unit (chains)	1 NKR-P1 (AB)	4 NKR-P1 (AB, CD, EF, GH)	1 LLT1 (AB), 2 NKR-P1 (CD, EF)
Number of water molecules in the asymmetric unit	225	682	691
Positions of modeled GlcNAc residues	AB 116, AB 169	C 116, ABCEFGH 157, ABCDEFGH 169	AB 95, AB 147, F 116, CDF 157, CDEF 169
Ramachandran statistics: residues in favored regions (%); number of outliers[48]	98; 0	98; 0	98; 0

† $R_{merge} = \sum_h \sum_i |I_{hi} - \langle I_h \rangle| / \sum_h \sum_i I_{hi}$, $R_{p.i.m.} = \sum_h \sum_i (n_h - 1)^{-1/2} |I_{hi} - \langle I_h \rangle| / \sum_h \sum_i I_{hi}$,   and

$R = \sum_h \|F_{h,obs}| - |F_{h,calc}\| / \sum_h |F_{h,obs}|$, where I_{hi} is the observed intensity, $\langle I_h \rangle$ is the mean intensity of multiple observations of symmetry-related reflections, while $F_{h,obs}$ and $F_{h,calc}$ are the observed and calculated structure factor amplitudes, respectively. R_{work} is the R factor calculated on 95% of reflections excluding a random subset of 5% of reflections marked as "free". The final structure refinement was performed on all observed structure factors.

Human NKR-P1 homodimer is similar to murine dectin-1 homodimer

The asymmetric unit of NKR-P1_glyco contains two monomers, whereas the asymmetric unit of NKR-P1_deglyco contains eight NKR-P1 monomers. All these monomers are arranged into very similar homodimers, with pairwise RMSD on C$^\alpha$ atoms up to 0.5 Å (Fig. 2b). However, these homodimers have an unexpected configuration: they do not follow the usual dimerization mode observed for CTLDs of the *CLEC2* ligands such as CD69 or LLT1 with helix α2 at the dimerization interface. Instead, the dimerization interface of NKR-P1 is formed by helix α1, as in the murine C-type lectin-like pattern recognition receptor dectin-1[49],

5

with which human NKR-P1 shares only 32% sequence identity of the CTLD (Fig. 2c). The RMSD of the C^α atoms between NKR-P1 and dectin-1 dimers is 3.7 Å in the overlapping region (matching 196 from the total of 250 residues of the NKR-P1 dimer). The structurally distinct region mainly covers helices α2, whose positions differ up to 7 Å between NKR-P1 and dectin-1. We also observed a highly similar arrangement with helix α1-centered dimerization interface in the structure of a covalent disulfide dimer of rat NKR-P1B receptor ectodomain[50] (Fig. S1a) with 1.4 Å RMSD of the C^α atoms between these two dimers (PDB ID 5J2S, *manuscript in preparation*). On the contrary, the non-classical dimer of mouse NKR-P1B observed in the PDB ID 6E7D structure[42] has an entirely different overall arrangement (Fig. S2a).

The dimerization interface of the NKR-P1 homodimer consists of six protein-protein and several water-mediated hydrogen bonds (Tab. S1), a peptide bond interaction via delocalized electrons (Lys126-Glu127), and a small hydrophobic core comprising Leu119, Ala120, and Ile168 from both chains (Fig. S3). The contact surface area is ca. 500 Å^2. Compared with the helix α2-centered LLT1 dimer (7-12 hydrogen bonds, stronger hydrophobic core, 500-800 Å^2 contact surface area)[43], the helix α1-centered NKR-P1 dimer forms through a smaller contact surface area with fewer contact residues.
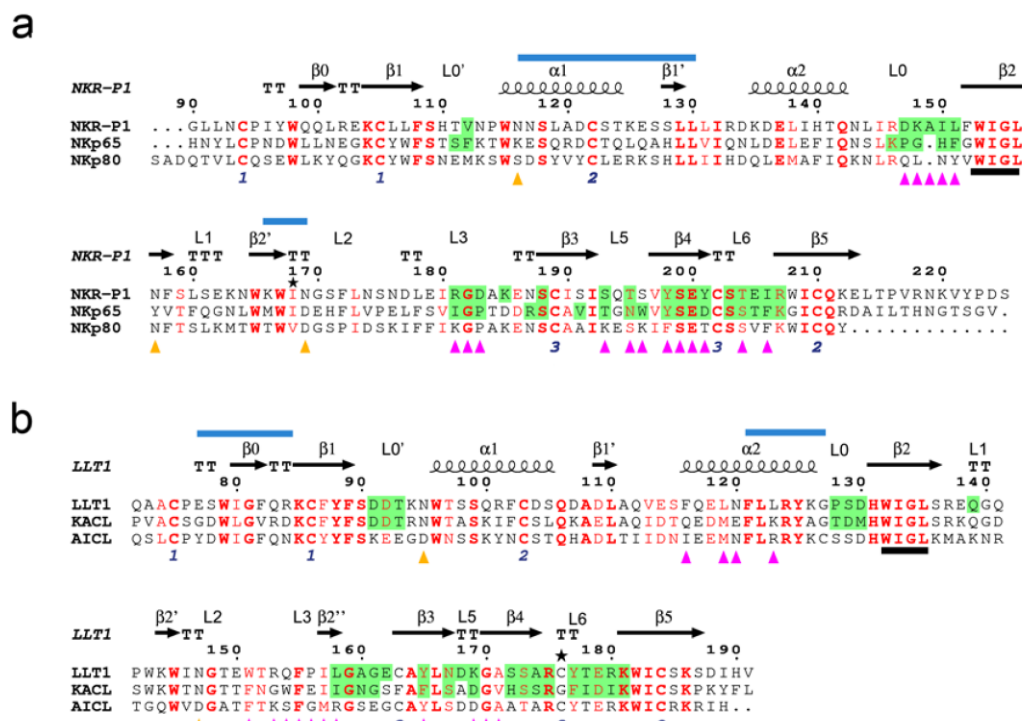
Figure 1. Sequence alignment of human NKC-encoded receptor:ligand pairs showing shared structural and functional sequence motifs. Secondary structure elements and loop regions (L) are denoted for NKR-P1 and LLT1 above the alignments. The paired numbers at the bottom indicate the disulfide pairs in the NKR-P1 and LLT1 structures; asterisks mark His176Cys mutation in LLT1 and Ile168 residue in NKR-P1. The predicted N-glycosylation sites of NKR-P1 and LLT1 are denoted with orange triangles. The conserved WIGL motifs are underlined in black. Blue lines above the sequence indicate the regions

involved in forming the non-covalent dimers of NKR-P1 or LLT1. Conserved residues are marked red; bold letters denote strictly conserved residues. (**a**) Sequence alignment of CTLDs of human NKR-P1-related NK cell receptors, i.e., human NKR-P1, NKp65, and NKp80. NKR-P1 residues contacting LLT1 in the NKR-P1:LLT1 complex in the primary binding mode, and NKp65 residues contacting KACL in the NKp65:KACL complex, are highlighted in green. Purple triangles indicate NKR-P1 residues that engage LLT1 in the NKR-P1:LLT1 complex in the secondary binding mode. (**b**) Sequence alignment of CTLDs of LLT1-related human *CLEC2* ligands, i.e., LLT1, KACL, and AICL. LLT1 residues contacting NKR-P1 in the NKR-P1:LLT1 complex in the primary binding mode, and KACL residues contacting NKp65 in the NKp65:KACL complex, are highlighted in green. Purple triangles indicate LLT1 residues that engage NKR-P1 in the NKR-P1:LLT1 complex in the secondary binding mode.
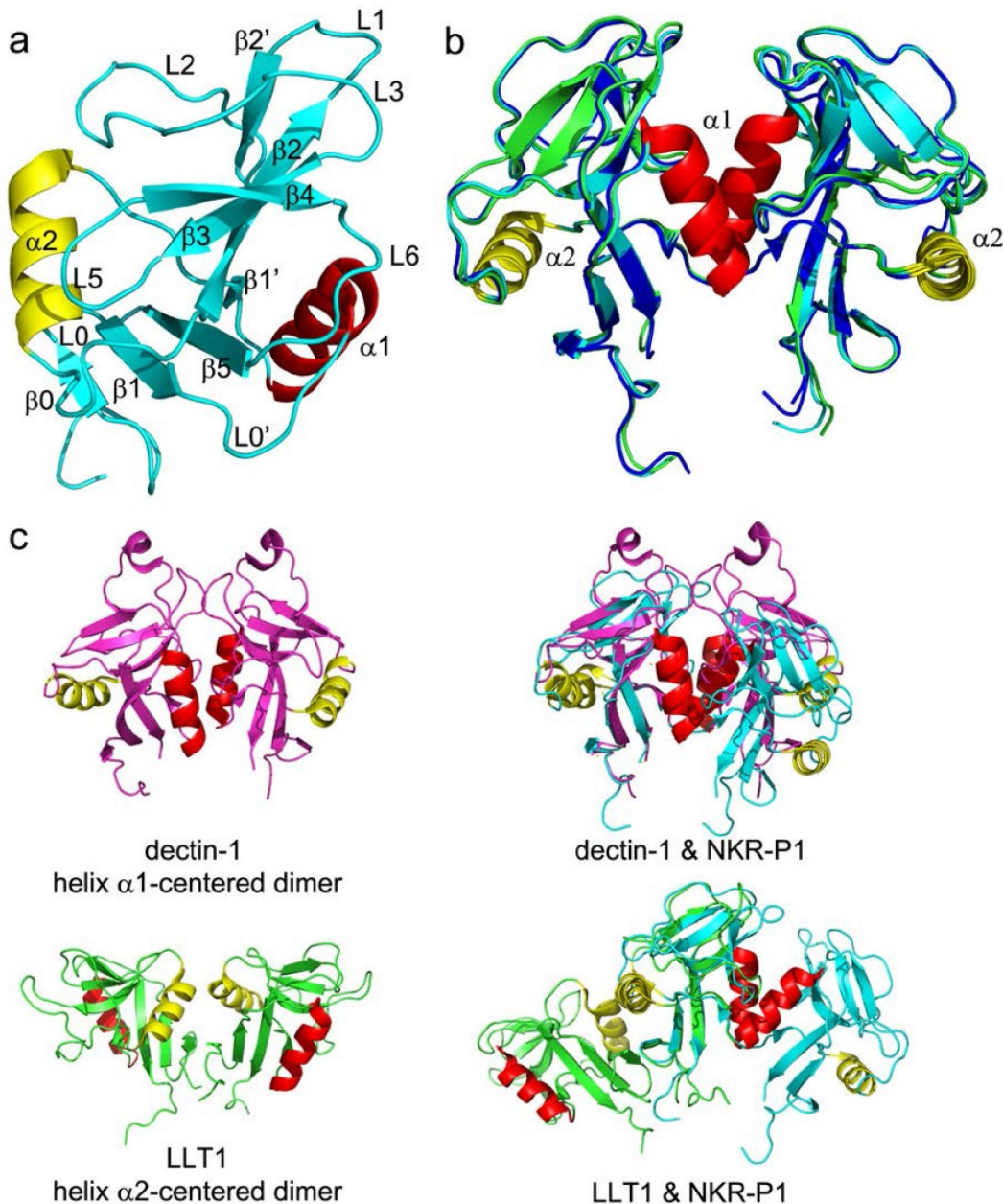
Figure 2. The structure of human NKR-P1 shows a unique dimerization interface. (**a**) Ribbon diagram of the NKR-P1 CTLD. Secondary structure elements are labeled in different colors: helix α1 is red, helix α2 is yellow, and β-strands and loops are cyan. (**b**) Comparison between NKR-P1 dimers formed by the glycosylated (cyan), deglycosylated free (green), and LLT1-bound (blue) forms of NKR-P1. (**c**) Comparison between helices α1- and α2-centered dimerization of murine dectin-1 (PDB ID 2CL8, magenta) and human LLT1 (PDB ID 4QKI, green), respectively; helices α1 and α2 are shown in red and yellow. Structural alignments of dectin-1 and NKR-P1 homodimers and LLT1 and NKR-P1 homodimers, prepared by aligning only one monomer from each dimer, are shown on the right-hand side. Although the CTLD fold is conserved in each pair of the aligned monomers, the helix α1- and helix α2-centered dimers show inverse arrangement.

Glycosylation of human NKR-P1 affects its dimerization

The NKR-P1 ectodomain contains three potential N-glycosylation sites at residues Asn116, Asn157, and Asn169 (Fig. 1a). Glycosylation at Asn169 is visible in the electron density maps of both NKR-P1_glyco and _deglyco structures: in NKR-P1_glyco, the complete $GlcNAc_2Man_5$ carbohydrate chain is localized in chain A, whereas a partial $GlcNAc_2Man_3$ chain is localized in chain B (Fig. S3a). In NKR-P1_deglyco, a single GlcNAc unit remaining at Asn169 can be well-identified in all eight NKR-P1 chains. Interestingly, the localized first GlcNAc units linked at Asn116 in NKR-P1_glyco and the overlapping GlcNAc units at Asn116 and Asn157 remaining in NKR-P1_deglyco participate in dimerization contacts with residues of helices α1 and regions β2, L1, and β2' of the opposite subunit of the NKR-P1 homodimer (Fig. S3b). In NKR-P1_glyco, five hydrogen bonds between Asn116:GlcNAc and the opposite subunit stabilize the helix α1-centered homodimer (Tab. S1). The contact surface area between the opposite chain of NKR-P1 and the localized GlcNAc unit is approximately 125 $Å^2$.

In NKR-P1_deglyco, density at the homodimer interface can accommodate the remaining GlcNAc unit of either Asn116 of one chain or Asn157 of the opposing chain of the NKR-P1 dimer (for details, see Methods, Tab. 1, and Fig. S3c). Conversely, in NKR-P1_glyco, the first GlcNAc unit at Asn116 is well defined in electron density in both chains, A and B, of the NKR-P1 dimer, while no electron density was found for glycosylation at Asn157. This suggests that although the glycosylation on either Asn116 or Asn157 can contribute to the dimer formation, dimerization might be impaired by steric hindrance if both N-glycans are present simultaneously. To test this hypothesis, we expressed NKR-P1 S159A mutant, thus abrogating glycosylation on Asn157. The overall fold of the mutant is comparable to the wild-type NKR-P1, as assessed by CD spectroscopy (Fig. S4a). Indeed, when analyzed by analytical ultracentrifugation, the mutant protein exhibited substantial levels of oligomeric species (Fig. S4b), whereas the wild-type NKR-P1 ectodomain is purely monomeric[51]. Thus, glycosylation heterogeneity may affect the propensity of human NKR-P1 to dimerize and, therefore, its ability to form multimeric complexes with LLT1.

Structure of the human NKR-P1:LLT1 complex

The crystal structure of the NKR-P1:LLT1 complex is formed by deglycosylated NKR-P1 and LLT1 ectodomains. The asymmetric unit of the crystal contains a complex of dimeric NKR-P1 with dimeric LLT1 and an extra dimer of NKR-P1 (Fig. 3a). These NKR-P1 dimers have the same helix α1-centered dimerization interface as the structures of the unbound NKR-P1 dimers described above (Fig. 2b). The LLT1 dimer retains the expected helix α2-centered dimerization mode (Fig. 2c), identical to that described previously in unbound LLT1

structures[43]. LLT1 has clearly identifiable GlcNAc units at residues Asn95 and Asn147. The NKR-P1 glycosylation observed in the electron density of the complex matches the glycosylation identified in the NKR-P1_deglyco structure.

The LLT1 homodimer engages its partner bivalently, i.e., one dimer interacts with two NKR-P1 dimers related by crystallographic symmetry: each LLT1 monomer binds to a different subunit of a distinct NKR-P1 homodimer (Fig. 3a). There is no apparent induced fit of the binding partners – the RMSD of C^α atoms between the non-interacting and the interacting NKR-P1 dimers (NKR-P1_glyco and the complex) is 0.5 Å, and that of LLT1 (PDB ID 4QKH and the current complex) is 0.7 Å. Moreover, the N-linked glycosylation chains do not directly contribute to the interaction.

LLT1 engages NKR-P1 in two distinct interaction modes

NKR-P1 and LLT1 establish two types of contact in this structure – the primary (LLT1 chain B:NKR-P1 chain D) and the secondary (LLT1 chain A:NKR-P1 symmetry-related chain C) interaction modes. The primary interaction mode matches well the structure of the homologous human NKp65:KACL complex (PDB ID 4IOP)[37] – the RMSD of C^α atoms of the two complexes is 1.3 Å (one chain of the receptor and one chain of the ligand in each case, Fig. 3b, lower left). Similarly, in the structure of mouse NKR-P1B complexed with MCMV immunoevasin m12, the observed interaction interface matches the primary mode in the present structure of the human NKR-P1 complex, although the area covered by the m12 protein is considerably larger (Fig. S1b,c)[41]. The recently described structure of the mouse NKR-P1B:Clrb complex (PDB ID 6E7D)[42] also showed an interaction interface common for both NKR-P1 receptors (Fig. S2b,c). However, the receptor:ligand arrangement observed in the second interaction mode of the NKR-P1:LLT1 complex is unique and differs from all known homologous complexes in the orientation of the ligand (Fig. 3b, lower right, Fig. S2b). The interaction interfaces of human NKR-P1 involved in both primary and secondary interaction modes are very similar. They are formed mainly by the membrane-distal residues of the L0, L3, L5, and L6 loops and by β3 and β4 strands (Fig. 3c,d) that form a flat surface for interaction with LLT1. By contrast, in LLT1, the primary and secondary interaction interfaces are substantially different, albeit sharing a small number of residues. While the loops L0', L0, L3, L5, L6 and strands β3 and β4 form the primary interaction patch of LLT1 (Fig. 3c), residues of the loops L2 and L5, strand β2" and helix α2 are involved in the second interaction interface (Fig. 3d). Both interaction modes place the membrane-proximal parts of the receptor and the ligand on opposite sides of the complex, creating a plausible model for interaction between two neighboring cells.

The primary interaction mode is established through nine direct and several water-mediated hydrogen bonds, in addition to two charge-supported and π-π stacking (Tyr201-Arg175)

interactions, with a total contact surface area of ca. 800 Å^2 (Tab. S1). The four strongest bonds occur between the NKR-P1 residues Arg181, Tyr201, Lys148, and Ser199 and the LLT1 residues Glu179, Glu162, Ser129, and Tyr177, respectively (Fig. 3c). The second interaction mode is established through five direct hydrogen bonds, two charge-supported and a hydrophobic (LLT1:Pro156 – NKR-P1:Ala149, Leu151) interaction, with a total contact surface area of ca. 550 Å^2 (Tab. S1). The three strongest bonds occur between the NKR-P1 residues Asp147, Ser199, and Arg181 and the LLT1 residues Arg153, Lys169, and Asn120, respectively (Fig. 3d).

Besides interaction with LLT1, NKR-P1 dimers bound in primary and secondary mode also have non-negligible mutual accessory contact (NKR-P1 chain D and NKR-P1 chain C in symmetry-related position). The interface area has 440 Å^2 and is established through seven direct hydrogen bonds (Tab. S1). Four residues are towering above the interface: Asn143 and Arg146 of chain D and Asn174 and Asn176 of chain Csym (none of the asparagine residues is a glycosylation site). The interface also has several water-mediated contacts.
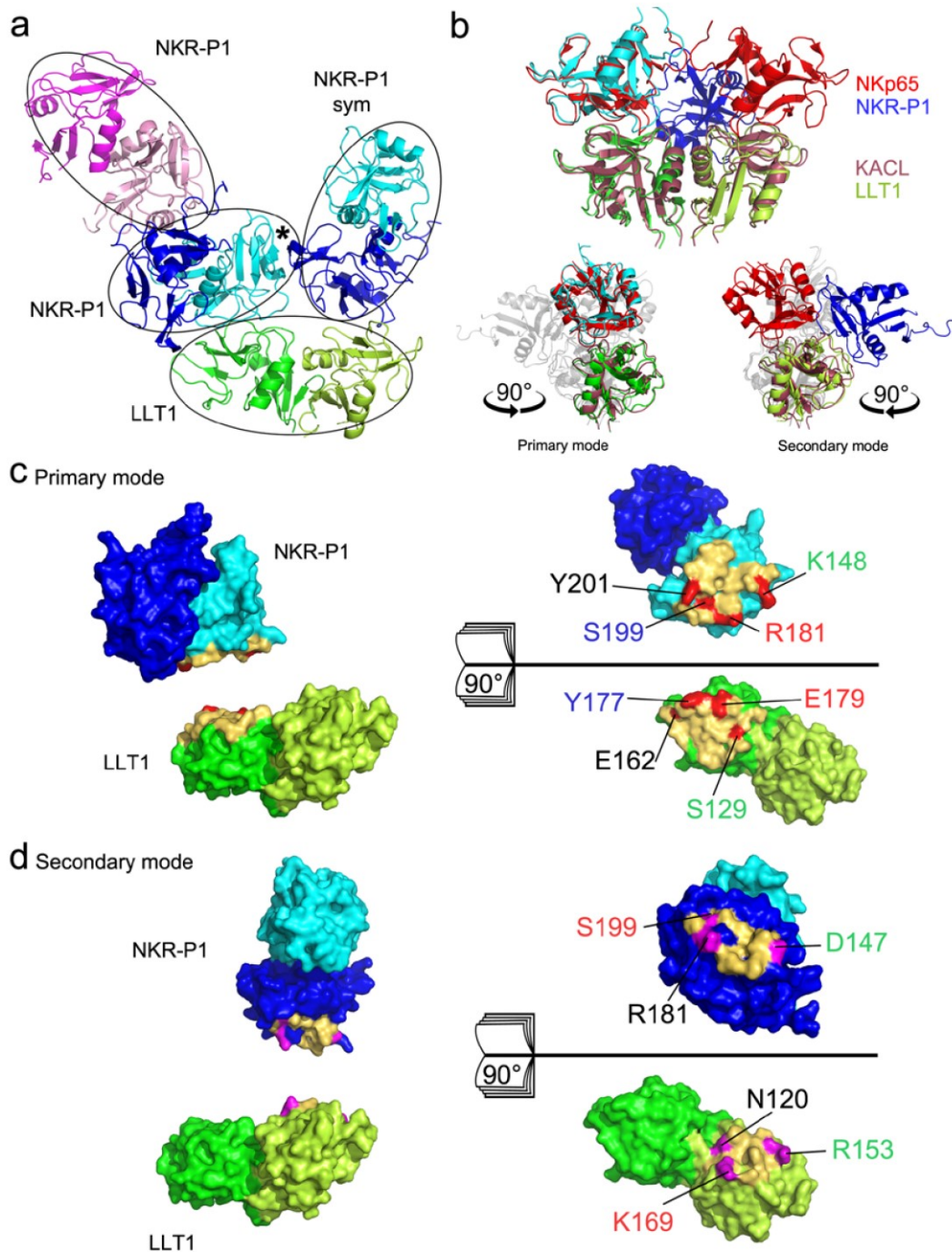
Figure 3. The structure of the NKR-P1:LLT1 complex shows two distinct binding modes. (**a**) The overall organization of the complex crystal structure. The LLT1 dimer (green/lemon) contacts the NKR-P1 dimer, formed by the blue monomer and the cyan monomer. The second blue-cyan NKR-P1 dimer is related to the first by crystal symmetry. The cyan NKR-P1 monomer interacts with LLT1 in the primary interaction mode, whereas the blue NKR-P1 monomer engages LLT1 using the secondary interaction interface. Black asterisk marks the mutual accessory contact of NKR-P1 bound in primary and secondary mode. Additionally, the asymmetric unit of the crystal contains another NKR-P1 dimer (pink/magenta) lacking contact with LLT1. (**b**) Overall comparison of the structure of dimeric KACL (purple) in complex with two NKp65 monomers (red; PDB ID 4IOP) and the structure of the LLT1 dimer (green/lemon) with the two interacting NKR-P1 molecules in the primary (cyan, left side) and secondary (blue, right side) binding modes. Comparison with only the primary or secondary NKR-P1:LLT1 interaction modes is highlighted in the lower section (both in a side view, using 90° y-axis rotation). (**c**) NKR-P1:LLT1 primary interaction interface. Contact residues within 5 Å distance are colored in yellow. Amino acids forming the four strongest contacts are highlighted in red. (**d**) NKR-P1:LLT1 secondary interaction interface. Contact residues within 5 Å distance are colored in yellow. Amino acids forming the three strongest contacts are highlighted in magenta.

NKR-P1:LLT1 complex formation in solution

To characterize the size and shape of the NKR-P1:LLT1 complex in solution, we have performed analytical ultracentrifugation (AUC), microscale thermophoresis (MST), and small-angle X-ray scattering coupled to size-exclusion chromatography (SEC-SAXS) experiments. The acquired AUC data are concentration-dependent and reflect the dynamic nature of this interacting system, similar to the results from the SEC-SAXS measurements. The free human NKR-P1 ectodomain is monomeric, with a sedimentation coefficient $s_{20,w}$ of 2.1 S corresponding to an estimated molecular mass of 18 kDa, matching the expected value of 17.5 kDa closely. The LLT1 ectodomain forms a stable non-covalent dimer (2.9 S) that does not dissociate into monomers, except in very low concentration (previously characterized in Skálová et al., 2015[43] and Bláha et al., 2017[51]). When increasing the loading concentration of the NKR-P1:LLT1 equimolar mixture, the sedimentation coefficient of the complex increases as well, reaching an $s_{20,w}$ value of 3.7 S at the highest analyzed concentration (Fig. S4c). This value, when corrected for non-ideality caused by the high protein loading concentration used (18 mg/ml), corresponds to an estimated zero-protein-concentration sedimentation coefficient $s^0_{20,w}$ value of 4.5 S, and a moderately elongated particle with approximate dimensions of 10–15 × 4–5 × 4–5 nm. That compares well with the 8–10 × 5–6 × 4–5 nm dimensions expected for the possible NKR-P1:LLT1 interaction assemblies observed in the complex's crystal structure, i.e., monomer:dimer:monomer or dimer:dimer (note that while N-glycan chains are not present in the deglycosylated complex's structure, they were present during all our analyses in solution).

Secondary interaction mode is involved in NKR-P1:LLT1 binding in solution

To understand whether the secondary interaction mode observed within the crystal structure is also utilized in the solution, we designed an N120R, R153E, K169A triple mutant of LLT1 (LLT1^{SIM}), thus abolishing the three strongest contacts in the LLT1 secondary interaction interface (Fig. 3d). The LLT1^{SIM} mutant was expressed and purified in the same way as the wild-type LLT1, and it also displayed a comparable CD spectrum (Fig. S4a). NKR-P1:LLT1^{SIM} equimolar mixture concentration series reached an $s_{20,w}$ value of 3.3 S (corresponding to an estimated $s^0_{20,w}$ value of 3.9 S), clearly showing the formation of the complex of a smaller size compared to the wild-type NKR-P1:LLT1 mixture, possibly a monomer:dimer assembly (Fig. S4d). By integrating the whole continuous size distribution c(s) curves and plotting the resulting weight-average S values against the LLT1 proteins' concentrations used, binding isotherms were constructed for both dilution series and firstly best-fit to the simplest hetero-association binding model A+B⇔AB, where A is the LLT1 dimer and B is the NKR-P1 monomer (Fig. S5a). LLT1^{SIM} showed about three-fold weaker overall affinity than the wild-

type LLT1, which was further corroborated by independent MST analysis using fluorescently labeled NKR-P1 titrated with LLT1 or LLT1^{SIM} (Fig. S5b). To analyze the difference between wild-type LLT1 and LLT1^{SIM} concerning the binding of the second NKR-P1 monomer, we also best-fit the data using the A+B⇔AB+B⇔BAB model (Fig. S5c). While for the wild-type LLT1 this improved the fit and provided two different K_D values, possibly corresponding to primary and secondary interaction modes, for LLT1^{SIM}, the fitted K_D values remained unchanged, disproving binding of the second NKR-P1 monomer. Similarly, when the AUC and MST data were globally fit together with the AUC parameters fixed at the previously best-fit values, the LLT1^{SIM} MST data could be fitted equally well with both AB and BAB model while the fit is poor for the AB model in the case of wild-type LLT1 (Fig. S5d). Taken together, our data show that the secondary interaction interface is not just a crystal contact, but it contributes significantly to the overall affinity of the NKR-P1:LLT1 interaction.

SEC-SAXS analysis confirms NKR-P1:LLT1 higher-order complex formation
The observation of assemblies of even higher-order is unlikely in the AUC sedimentation velocity experiment, given the fast kinetics of this interaction, the long time scale of the experiment, and the fact that protein concentration steadily decreases along the sedimentation boundary. However, the NKR-P1:LLT1 complex's crystal structure suggests a chain-like arrangement of receptor:ligand dimers. To determine if any such assemblies exist in the solution, we performed SEC-SAXS analysis of the NKR-P1:LLT1 equimolar mixture at 15 mg/ml loading concentration. Two distinct peaks of absorbance at 280 nm, corresponding to two distinct SAXS peaks, were observed in the SEC-SAXS experiment (Fig. 4). For analysis and *ab initio* modeling of the SAXS envelopes, we sampled and merged four data intervals from the first peak and two data intervals from the second peak (Figs. 4 and S6). The radius of gyration calculated from the SAXS signal steadily decreases with the retention volume, with two small plateaus in the main peak, suggesting a dynamic balance between complex formation and dissociation (Fig. 4). As a result, the merged scattering curves could not be fitted well to scattering curves simulated from any single structure of the NKR-P1:LLT1 complex or its components. For further analysis, we constructed models of assemblies of NKR-P1:LLT1 complex in varying lengths (number of protein chains), considering all possible permutations of the order of the molecules using only primary, only secondary, or both interaction modes in alternating fashion. The resultant library of all these models was then used by the OLIGOMER software to best-fit the observed SAXS experimental curves. By this approach, the sampled SAXS data fit reasonably well to the superimposed calculated scattering curves of groups of NKR-P1:LLT1 complex structures of higher stoichiometry (χ^2 1.29 – 3.47; note that complete glycosylation was not modeled but it contributed to the scattering; Fig. S6). Following the continuously decreasing radius of

gyration calculated from the SAXS data, the stoichiometry of the best-fit structures of the NKR-P1:LLT1 complex continuously decreases with the retention volume as well. SAXS scattering curve of the first peak is best-fit with two to three LLT1 dimers interacting in a chain-like oligomer with two to three NKR-P1 dimers, the curve of the second peak to one LLT1 dimer interacting with one NKR-P1 dimer in primary or secondary mode. The most abundant components of the superimposed structures are best-fit to the averaged *ab initio* SAXS envelopes in Fig. S6. Notably, OLIGOMER generally favored assemblies utilizing the secondary interaction mode against models with the primary mode alone.
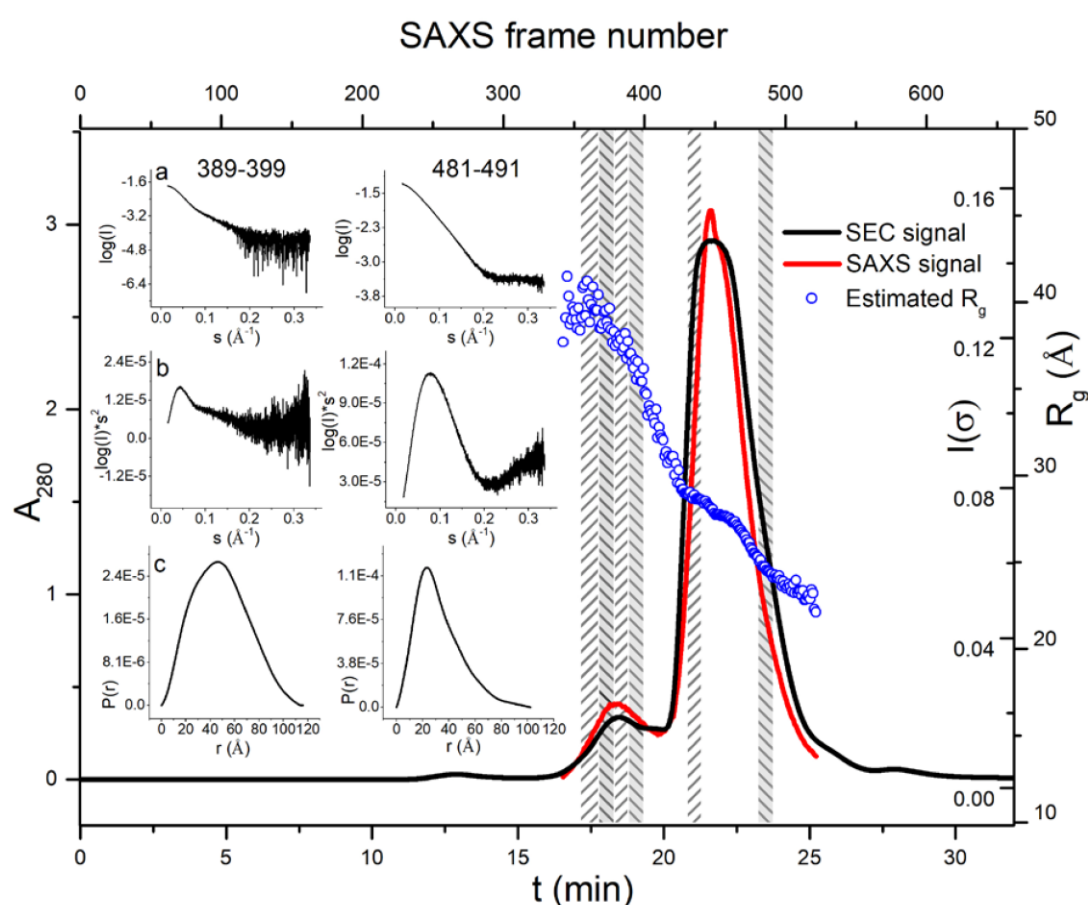
Figure 4. SEC-SAXS analysis of NKR-P1:LLT1 shows higher-order complex formation. Overlay of the size-exclusion chromatography profile (black line) and SAXS scattering signal (red line) for the NKR-P1:LLT1 equimolar mixture at 15 mg/ml loading concentration. Both signals show two distinct peaks. For each collected SAXS frame, the radius of gyration was calculated using AUTORG (blue circles). For the calculation of *ab initio* SAXS envelopes and further analysis by OLIGOMER (Fig. S6), six intervals of the SAXS data were selected and merged (frames 355-367, 368-378, 379-388, 389-399, 431-440, 481-491; denoted as columns with diagonal hatching). SAXS scattering curve (**a**), Kratky plot (**b**), and pair distance distribution function (**c**) for the intervals 389-399 and 481-491 are shown in the inset for data quality assessment of the merged data.

NKR-P1 signal transduction in live cells

To answer the question of the biological relevance of these higher-order complexes in the context of a live cell, we performed single-molecule localization microscopy studies with NKR-P1-expressing cell line and quantified the surface distribution of NKR-P1 with respect to LLT1 or LLT1[SIM] binding. Next, we analyzed the effect of soluble LLT1 or LLT1[SIM] on the inhibitory potential of native NKR-P1 expressed on the surface of freshly isolated NK cells.

LLT1 ligation induces NKR-P1 receptor clustering

Full-length NKR-P1 transfectants generated using the piggyBac system were induced to express the receptor in a limited density to allow for single-molecule localization microscopy. Cells were then incubated in the presence or absence of soluble LLT1 or LL1[SIM], fixed, and labeled with anti-NKR-P1 Alexa-647 mAb. Direct stochastic optical reconstruction microscopy (dSTORM) images were acquired, and Voronoi tessellation cluster analysis was used to assess the effect of soluble LLT1 on the nanoscale organization of NKR-P1 on the cell surface (Fig. 5a). In the absence of LLT1, we detected clusters of events with an average area of 1870 ± 777 nm^2 (Fig. 5b) and an average diameter of 41 ± 7 nm (Fig. 5c), mostly clusters with a diameter ranging from 10 to 40 nm (Fig. 5d), indicative of Alexa-647 doubly labeled NKR-P1 homodimers (ca. 6 nm + 10 nm linking error per each mAb $\pm$ 15 nm of localization precision). The addition of soluble LLT1 significantly increased the cluster diameter (to 47 ± 6 nm; $p < 0.0001$, Fig. 5c,d), the cluster area (2713 ± 1180 nm^2; $p < 0.0001$, Fig. 5b) and the number of events detected in the clusters (38.8 ± 12.3; $p < 0.0001$, Fig. 5e), whereas the density of events in clusters remained unchanged, as expected (Fig. 5f). Furthermore, the effect of LLT1[SIM] addition on NKR-P1 nanoscale organization was statistically indistinguishable from the negative control while being significantly different from the effect of LLT1 addition. Therefore, the secondary interaction interface in LLT1 is necessary for the formation of larger nanoscale NKR-P1 clusters upon interaction. No significant difference in the total density of events per inner cell surface (evaluated area) was found (Fig. 5g), pointing to stable expression levels of NKR-P1 throughout the measurement. Consequently, the size of NKR-P1 nanoclusters increases (beyond one homodimer unit) not because of differences in NKR-P1 expression levels but because LLT1 cross-links two or more NKR-P1 homodimers.
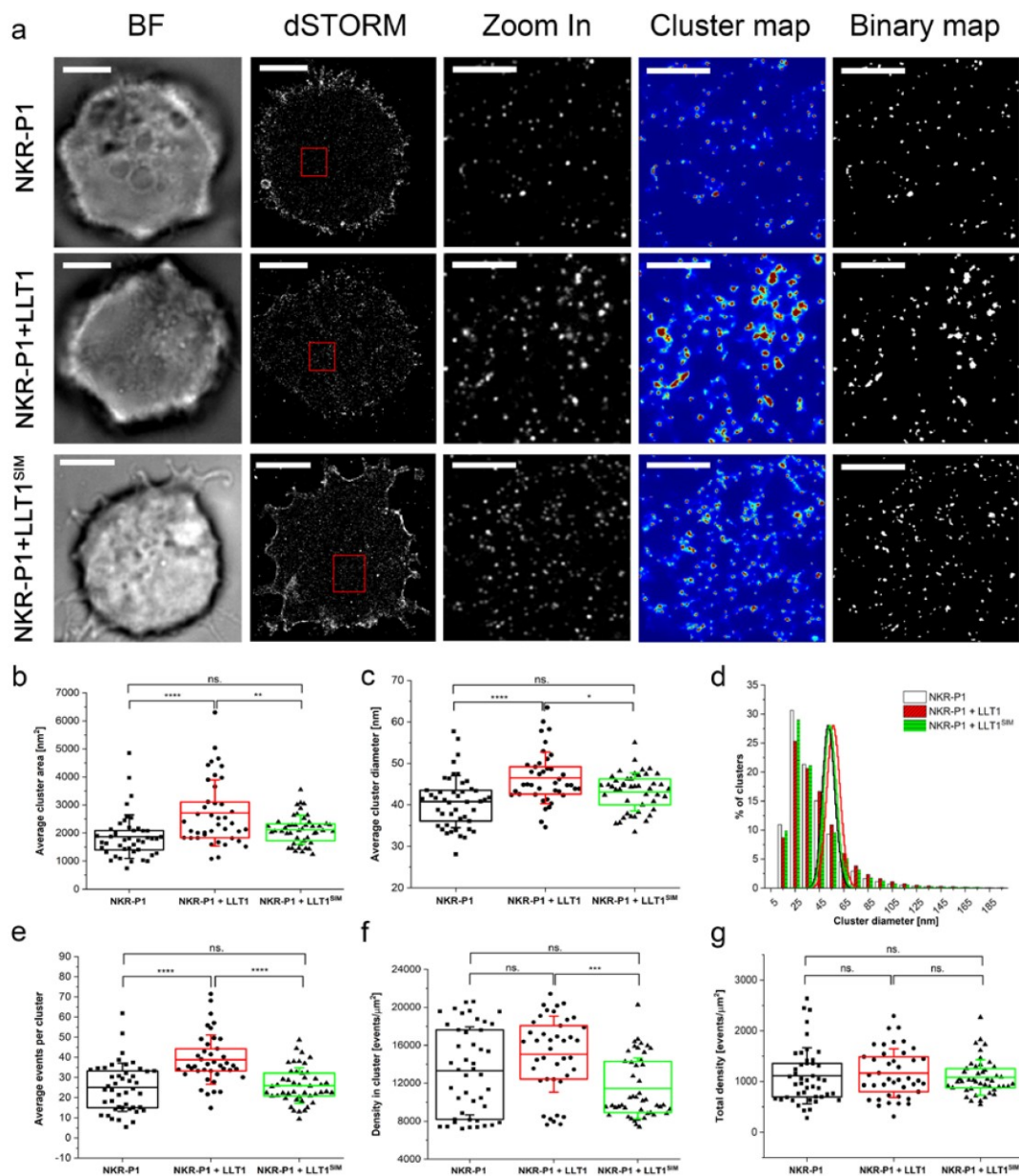
Figure 5. Soluble LLT1 affects NKR-P1 distribution on the cell surface. NKR-P1 stable transfectants were incubated in the presence or absence of soluble LLT1 or LLT1^{SIM}, and the cell surface distribution of NKR-P1 was monitored by super-resolution microscopy. (**a**) Representative brightfield (BF) and dSTORM images of full-length NKR-P1 HEK293 stable transfectants on PLL-coated slides incubated without (black) or with LLT1 (red) or LLT1^{SIM} (green), fixed and stained with Alexa-647-labeled anti-NKR-P1 mAb; scale bars represent 5 µm. The 10 µm^2 regions (red boxes in dSTORM images) are magnified and shown with corresponding cluster maps and binary maps, scale bars represent 1 µm. (**b-g**) Analysis of full-length NKR-P1 clustering: average cluster area (b), average cluster diameter (c), size distributions of cluster diameters overlaid with Poisson distribution functions (d), average events per cluster (e), density of events detected per cluster (f) and total density of the detected events (g). In (b,c) and (e,f), each plotted point represents the mean value obtained from the analysis of the total inner surface of a single cell. The horizontal bar represents the overall mean value, the box represents the interquartile range, and the error bars represent SD. Data are from 46 NKR-P1$^+$ control cells and 41 or 47 NKR-P1$^+$ cells incubated with LLT1 or LLT1^{SIM} in seven or four independent experiments, respectively. One-way ANOVA with Bonferroni correction, *$p < 0.05$, **$p < 0.01$, ***$p < 0.001$, ****$p < 0.0001$, ns. non-significant.

LLT1 secondary interaction mode is required for NKR-P1 inhibitory signaling

An NK cell-mediated cytotoxicity assay was performed to investigate further the influence of NKR-P1 cluster formation on cellular signalization. NK cells isolated from the blood of three different healthy donors were activated with IL-2 and mixed with the K562 target cells in a 40:1 effector:target cell ratio and incubated for 4 hours with PBS buffer as a negative control or with the soluble LLT1 or LLT1^{SIM} (both in two different concentrations). In the absence of NKR-P1 ligand, K562 cells are well-susceptible to NK cell-mediated lysis (Fig. 6, PBS control, less than 10% live K562 cells). The lysis was substantially blocked in the presence of soluble LLT1, as expected. By contrast, the LLT1^{SIM} variant with a mutated secondary interaction interface was incapable of blocking NK cell-mediated cytotoxicity. As observed by dSTORM on the cell surface (Fig. 5), LLT1^{SIM} does not promote NKR-P1 cluster formation. This mutant also fails to signalize via the NKR-P1 inhibitory receptor pathway. Therefore, based on both the microscopy and the cytotoxicity assay data, we conclude that NKR-P1 clustering triggered by LLT1 ligation is biologically relevant and indispensable for cellular signalization.
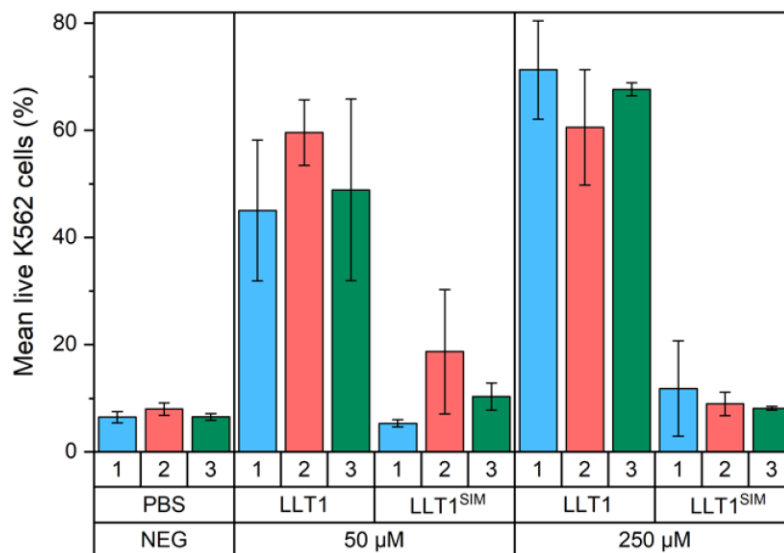
Figure 6. Inhibitory effect of soluble LLT1 on the NK cell-mediated cytotoxicity. NK cells from three different donors (blue, red, and green) and K562 target cells were incubated with PBS buffer only (negative control) or with the soluble LLT1 or LLT1^{SIM} proteins, both in 50 and 250 µM concentrations corresponding to the 1× and 5× K_D values, respectively, as analyzed by the AUC for the primary interaction mode (cf. Fig. S5). Results are represented as means of live K562 cells in each condition with standard deviation. When applicable, data were statistically evaluated by one-way ANOVA. Considering $p < 0.05$ as statistically significant, the inhibitory effect of soluble LLT1 significantly differs from LLT1^{SIM}, which does not differ from the condition without any NKR P1 ligand.

Discussion

Comparison with homologous NK cell receptor:ligand complexes

Currently, there are only two similar CTL:CTL NK cell receptor:ligand complexes with known 3D structure: human NKp65:KACL[37] and mouse NKR-P1B:Clrb[42]. These homologous complexes are topologically similar to the primary interaction mode of the NKR-P1:LLT1 complex (Fig. 3b). Sequence identity of the extracellular part of NKR-P1 with NKp65 is 33% and with murine NKR-P1B 42%, while sequence identity of the extracellular part of LLT1 with KACL is 49% and with murine Clrb 51%. The structure of the human NKp65:KACL complex comprises two monomeric NKp65 units interacting separately and symmetrically with a dimeric KACL ligand. Crystal structure of the murine NKR-P1B:Clrb complex shows two Clrb dimers interacting with one NKR-P1B dimer placed between them (each Clrb dimer interacts with one of the two NKR-P1B chains). The arrangement of the murine complex is similar to the herein presented NKR-P1:LLT1 complex's structure, apart from the fact that the murine complex is symmetric while we observe two distinct binding interfaces, the primary and the secondary interaction mode of LLT1.

Despite different oligomeric forms of NKR-P1:LLT1, NKR-P1B:Clrb, and NKp65:KACL complexes, the primary receptor:ligand interaction is similar in all three cases at the level of monomer:monomer superposition – the receptor:ligand pair of monomers overlaps basically along the whole chain. The most structurally conserved regions are generally sequentially conserved beta-sheets in the core of the proteins. Figure 7 shows in red the fragments with conserved 3D position, amino acid type, and length of at least three amino acids. Such criteria are fulfilled by these fragments: in ligands – KCFYFS (in human LLT1 residues 85-90), NWT (95-97), WIGL (132-135), WKW (143-145), and WICSK (182-186), and in receptors – WIGL (in human NKR-P1 residues 153-156) and ICQ (209-211). Therefore, it seems that for their interaction, the mutual orientation of the receptor and ligand scaffold is more important than the actual interaction interface.

We noted only three amino acid interaction pairs conserved in the interaction interface in at least two out of the three homologous complexes. They are gathered around residues Tyr165-Tyr171-Phe148, Arg175-Arg181-Arg158, and Tyr177-Tyr183-Phe160 of the ligand (Tab. S2). The arginine residues form equivalent hydrogen bonds in Clrb and KACL cases. In LLT1, the arginine assumes a different conformation and forms an intramolecular hydrogen bond with Asn183. The primary interaction mode in NKR-P1:LLT1 mainly relies on main chain contacts that enable fast k_{on}/k_{off} kinetics, thus corroborating the previously published SPR-based findings[39, 40], and our AUC analysis. Hence, a topologically similar complex is formed in all three cases, although the underlying intermolecular mechanism of recognition is semi-independent of the actual fold and amino acid composition. However, the secondary

interaction mode is unique to the NKR-P1:LLT1 complex and is not found in the other related complexes.
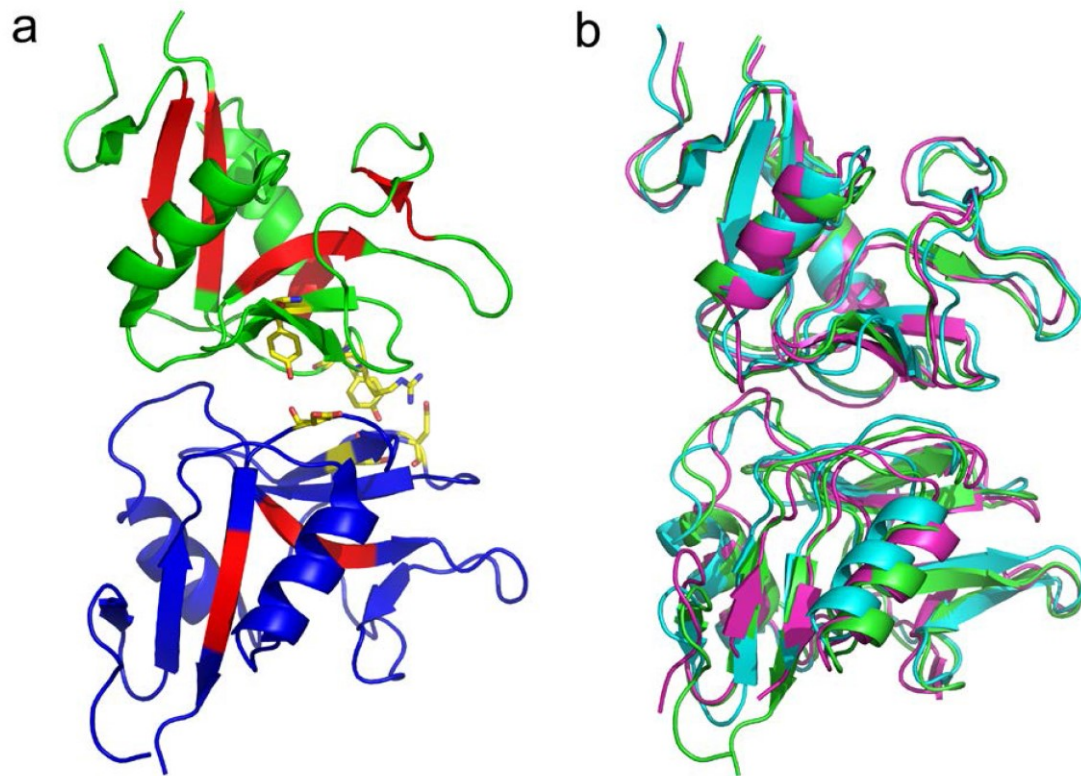

Figure 7. Anatomy of NK cell CTL receptor:ligand interactions. (**a**) The primary mode of interaction between human NKR-P1 (blue) and LLT1 (green). The residues colored red show conserved sequence fragments at least three residues long corresponding structurally in the superposition of the three receptor:ligand interaction pairs (primary mode of human NKR-P1:LLT1, murine NKR-P1B:Clrb, and human NKp65:KACL). The residues partially conserved at their interaction interface (see Tab. S2) are shown as sticks for the case of NKR-P1:LLT1. (**b**) Overlapped interaction pairs of the primary mode of human NKR-P1:LLT1 (green), murine NKR-P1B:Clrb (cyan), and human NKp65:KACL (magenta).

Effect of receptor α1-centered dimerization on complex affinity

Li *et al.*[37] reported that the orientation of NKp65 bound to its ligand precludes the putative α2-centered dimerization of NKp65. Similarly, a hypothetical NKp65 α1-centered dimer is implausible as well, based on steric hindrance and the lack of stabilizing interactions. This observation contrasts with the α1-centered dimerization of NKR-P1 present in both its unbound and complexed crystal structure. Interestingly, the single-nucleotide polymorphism (SNP) c.503T>C of the human *KLRB1* gene, causing the substitution of isoleucine 168 for threonine in the NKR-P1 CTLD, was reported to have a 37% frequency of the Thr168 allele[52]. The authors showed that the Thr168 isoform of NKR-P1 has a lower affinity to LLT1 and a weaker inhibitory effect on NK cells. They proposed that Ile168 forms a part of the interaction interface between NKR-P1 and LLT1, directly affecting LLT1 recognition by NKR-

P1[52]. However, the structure of the NKR-P1 homodimer shows that Ile168 is found at the dimerization interface rather than at the membrane-distal interaction interface – more specifically, in a small hydrophobic pocket within the dimerization interface (Fig. S3d). Therefore, we propose that the substitution of the nonpolar isoleucine residue by polar threonine caused by c.503T>C SNP indirectly affects the binding affinity because this substitution destabilizes the α1-centered NKR-P1 homodimer. Glycosylation often has a significant impact on receptor homooligomerization, as recently evidenced for, e.g., NK cell activation receptor NKp30[53]. NKR-P1 homodimerization is also regulated by its glycans, specifically the glycans present on Asn116 and Asn157 (Fig. S3b). Core glycan chains present at these residues contribute partially to the α1-centered dimerization interface, but at the same time, the glycans clash together. As a result, the stability of the α1-centered NKR-P1 homodimer is improved by abrogating N-glycosylation on Asn157, leaving only the Asn116 glycan at the dimer interface (Fig. S4b). Interestingly, a c.470A>G SNP causing N157S mutation is also listed in the human genome variation database. However, the clinical significance of N157S mutation was not yet investigated, although it could significantly affect NKR-P1 signalization via stabilizing its ligand-bound state. The oligomeric state of the receptor might thus modulate the overall NKR-P1:LLT1 binding affinity. The NKp65:KACL complex stands out for its high affinity ($K_d \sim 0.67$ nM)[37] – ca. 3000× stronger than that of NKp80:AICL ($K_d \sim 2.3$ μM)[9] and 70000–130000× than that of NKR-P1:LLT1 ($K_d \sim 48$ μM[39]; this study 90 μM). Due to the exceptionally high NKp65:KACL binding affinity, any putative ancestral α1-centered dimerization interface may have been lost in NKp65. In contrast, the NKR-P1 and NKp80 receptors may have evolved to compensate for their low affinity to their ligands by utilizing the α1-centered dimerization and enabling an increased avidity effect.

Comparison with the previously proposed NKR-P1:LLT1 binding model

The SPR analysis of single-residue mutants of both binding partners, performed by Kamishikiryo *et al.*[39, 40] and updated by Kita *et al.*[39, 40] based on the published LLT1 structure, identified several key residues of NKR-P1 and LLT1 essential for their interaction and proposed several pairs of interacting residues (Tab. S3). The mutated residues that had detrimental or moderate adverse effects on binding in these SPR studies are mainly found in the primary interaction interface (Fig. 1 and Tab. S3) – in LLT1: Tyr165, Asp167, Lys169, Arg175, Arg180, and Lys181, and in NKR-P1: Arg181, Asp183, Glu186, Tyr198, Tyr201, and Glu205. However, the proposed interaction pairs do not always agree with the mutual orientation of both proteins observed in the present crystal structure of the NKR-P1:LLT1 complex. For example, the proposed LLT1/NKR-P1 pairs Tyr177/Tyr198 and Arg175/Glu200 correspond well with our observed interaction pairs LLT1:Tyr177:OH/NKR-P1:Ser199:O and LLT1:Arg175:N/NKR-P1:Glu200:OE2, respectively. On the other hand, the proposed pairing

of Glu179 from LLT1 loop L6 with Ser193 and Thr195 from NKR-P1 loop L5 only resembles the crystal structure contacts of Glu179 with Arg181 (loop L3) and Tyr198 (strand β4), located near NKR-P1 loop L5. In contrast to the SPR studies, we observed no contact between Tyr165 and Phe152, although LLT1:Tyr165 is used in the primary interface, and Phe152 is close to the NKR-P1 L0 interaction region. Lastly, we cannot confirm the suggested direct bond between LLT1:Lys169 and NKR-P1:Glu205. Although these residues are close to each other in the primary mode (the closest distance 4.3 Å), they clearly do not form a pivotal bond of the interaction interface. Furthermore, the Lys169 side chain is rather flexible, as suggested by the low quality of its electron density map in the primary mode, in contrast to all other nearby side chains with well-defined positions.

Because the secondary binding mode observed in the NKR-P1:LLT1 structure involves a different region of LLT1 than the region used in the primary binding mode, the orientation of LLT1 and NKR-P1 in this binding mode does not match the interaction pairs proposed in the SPR studies. Notwithstanding, the NKR-P1 interaction interface is very similar in primary and secondary mode; therefore, some of the previously proposed NKR-P1 interaction residues are also involved in the secondary mode (Arg181, Asp183, Tyr198, and Tyr201). Interestingly, residue LLT1:Lys169 establishes several contacts with NKR-P1 (Arg181, Ser199, and Glu200) in secondary interaction mode. However, the pair Lys169/Glu205 proposed by Kamishikiryo et al.[39, 40] is not observed in this mode either, and these residues are even farther apart – ca 11 Å. The presence of Lys169 in both primary and secondary interaction interfaces of LLT1 suggests that this residue plays an important role in the overall complex formation. Accordingly, the reported Lys169Glu mutation of LLT1[39, 40] would lead to a co-localization of several negative side chains in the secondary interface (Glu200 and Asp183 of NKR-P1, and mutated Glu169 of LLT1), thus indicating that the disruption of the NKR-P1:LLT1 interaction observed in the previous SPR experiments most likely resulted from the weakening of the secondary rather than the primary interface. Kamishikiryo et al.[39, 40] subsequently restored binding by introducing the Glu205Lys mutation in NKR-P1. Based on our structure, this effect would be explained by the strengthening of the primary interface. Thus, the previously published SPR-based interaction data largely agree with the interaction modes observed between NKR-P1 and LLT1 in the present crystal structure, although some previously suggested interaction pairs were misassigned and are not present in either interaction interface.

Assembly of the NKR-P1:LLT1 complex on the cell surface

Several authors have previously suggested an avidity effect of multimerization upon the interaction that compensates for the low affinity of the NKR-P1:LLT1 complex[37, 40, 47]. Interestingly, in the present structure of this complex, we indeed observe the formation of a

chain of repeating NKR-P1 and LLT1 homodimers. This pseudo-linear multimer has a zigzag shape in which the membrane-proximal parts of the two proteins are on opposite sides (Fig. 8), and it is structurally based on the alternating helix α1/α2-centered NKR-P1/LLT1 homodimers (the chain-forming effect) and the simultaneous involvement of both primary and secondary interaction modes (steric effect). On the contrary, an artificially constructed multimeric model of NKR-P1:LLT1 engaged in just the primary mode shows a chain of homodimers with a non-linear, almost helical conformation (Fig. S7a). Furthermore, the NKR-P1 stalk regions sterically clash, and the LLT1 stalk regions are exposed outside the complex core in many different directions. Thus, such multimer is unlikely compatible with cell membrane anchoring and formation within the immune synapse. NKR-P1:LLT1 engaged in just the secondary mode would also form a helical multimer with both receptor and ligand stalk regions pointing in many different directions outside the complex core (Fig. S7b). At the same time, when bound to LLT1 dimer in both primary and secondary interaction mode, the neighboring NKR-P1 molecules create a mutual accessory contact of not an insignificant energetic contribution to the stability of the whole assembly (Fig. 3a, marked with a black star). This accessory contact encompasses a similar number of hydrogen bonds and size as the secondary binding interface between NKR-P1 and LLT1 itself (Fig. S8), and it could thus be considered an additional stabilizing element favoring a combination of the primary and secondary binding modes rather than a single one of them.

To determine whether such zipper-like clusters of NKR-P1:LLT1 occur not only in crystal and to some extent in solution (Fig. 4 and S6) but also on the cell surface, we used single-molecule localization microscopy to examine full-length NKR-P1 transfectants labeled with anti-NKR-P1 Alexa-647 mAb in the presence or absence of LLT1 and LLT1^{SIM} (Fig. 5). We observed a significant increase in NKR-P1 cluster size and area upon the addition of soluble LLT1, but not its secondary interaction mode mutant, LLT1^{SIM}. Additionally, our SEC-SAXS data were best-fit with multimer chains in alternating primary and secondary interaction modes (Fig. S6), even though the artificial test models discussed above were included in the analysis as well. Acceptable χ^2 values were obtained primarily for multimer models containing the alternating arrangement. Taken together, we conclude that combining both interaction modes is necessary for a biologically plausible multimeric interaction, as further supported by the NK cell-mediated cytotoxicity assay results (Fig. 6).
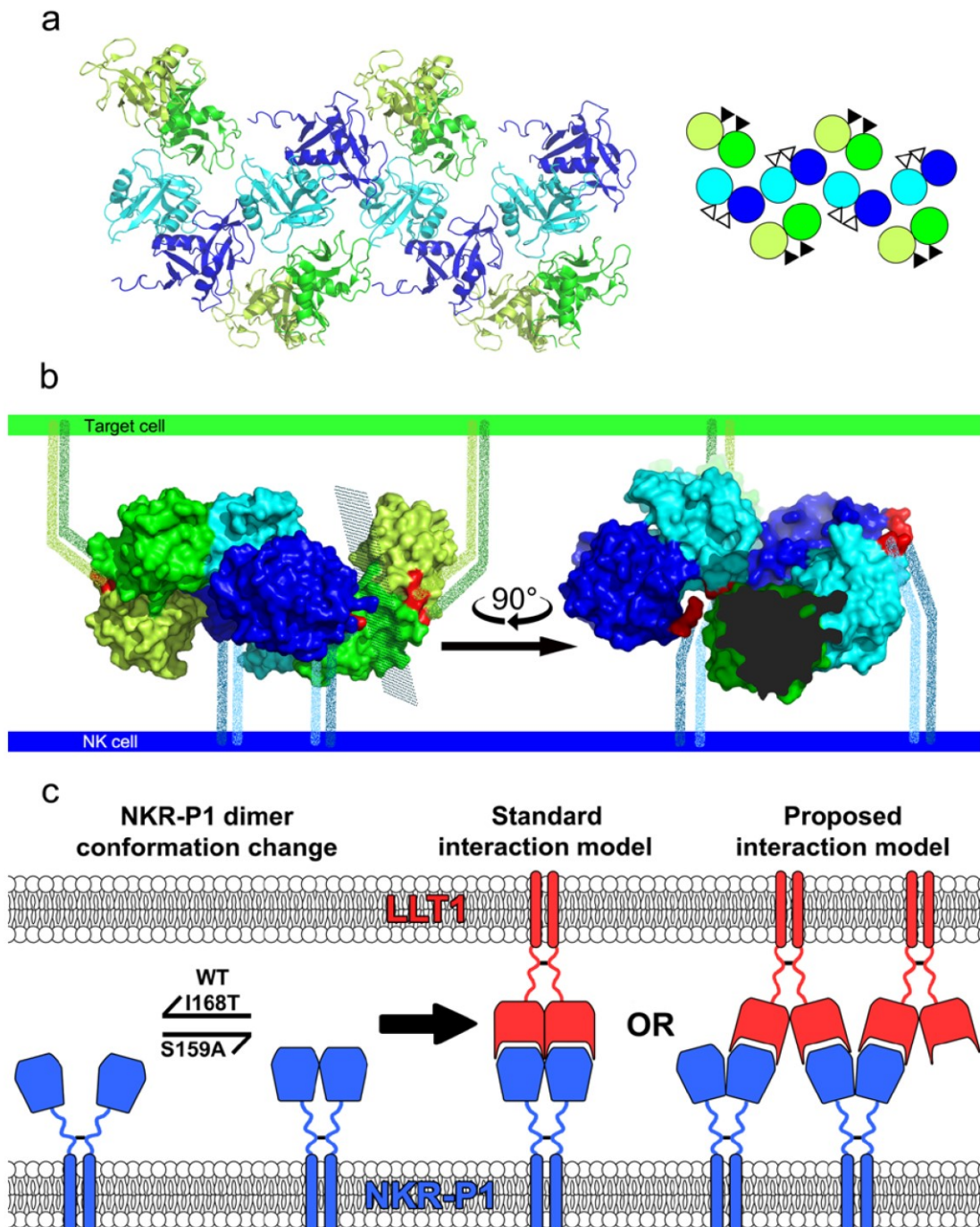
Figure 8. Organization of the NKR-P1:LLT1 complexes on the cell surface. (**a**) Representation of four adjacent asymmetric units within the NKR-P1:LLT1 complex crystal, excluding the additional unrelated NKR-P1 dimer. The NKR-P1 (blue and cyan) and LLT1 (green and lemon) dimers alternate in primary (cyan and green) and secondary (blue and lemon) interactions, forming a chain-like structure. The schematic depiction of this arrangement is shown in the inset with the same color code. The black and white triangles represent N-termini positions, pointing behind and in front of the display plane, respectively. (**b**) Depiction of the hypothetical arrangement of the chain-like structure upon contact of an NK cell (bottom, blue) with a target cell (top, green) showing the crystal structure of two NKR-P1 dimers (cyan and blue) interacting with two LLT1 dimers (green and lemon) in the primary (cyan and green) and secondary (blue and lemon) modes. The first three N-terminal residues in the structures are highlighted in red. The flexible stalk regions connecting the N-termini and cell membranes are represented as

speckled lines of the corresponding color-coding. The view on the right-hand side is clipped for clarity at the plane indicated on the left-hand side view. (c) Schematic depiction of NKR-P1 extracellular domain dynamics and possible ligand binding arrangements. NKR-P1 is expressed as a disulfide-linked homodimer; however, its CTLDs may undergo conformation change similar to monomer-dimer equilibrium. Such putative equilibrium would be shifted towards monomeric species for the wild-type protein and its I168T allelic variant[52], while a dimeric arrangement corresponding to the non-covalent dimer observed in the herein described crystal structures would be promoted for the S159A variant (left-hand side). Such NKR-P1 dimer could then interact with the cognate LLT1 ligand (itself being expressed as a disulfide-linked homodimer as well and forming stable non-covalent dimers with its CTLDs) in the previously suggested standard model of NK cell receptor – CTL ligand interaction (middle) or alternate with the dimeric ligand in the proposed chain-like arrangement based on NKR-P1:LLT1 complex crystal structure (right-hand side).

Albeit such functional multimerization of NK CTLRs has been mostly overlooked, the formation of similar nanoclusters is well described for interaction between the immunoglobulin family of KIRs and MHC class I glycoproteins[54] or for interaction between KIR2DL1 and NKG2D[55]. Moreover, a periodic zipper-like network of interacting dimers was reported in the crystal structures of the co-stimulatory immunocomplexes B7-1:CTLA-4 and B7-2:CTLA-4[56, 57]. Interestingly, B7-1 is expressed on the cell surface in a dynamic equilibrium between monomers and non-covalent dimers. Upon interaction with the co-stimulatory receptor CD28, B7-1 forms an interaction network composed of B7-1 and CD28 homodimers. The uncoupling of this interaction is facilitated by B7-1 dissociation to monomers, whereas insertion of B7-1 obligate dimer leads to prolonged, abnormal signaling between antigen-presenting cells and T cells[58].

Although as full-length proteins, both LLT1 and NKR-P1 form covalent disulfide homodimers on cell surface[7, 36], to our knowledge, the dimeric state of their CTL ectodomains has not yet been assessed in live cells. Conversely, the formation of the helix α2-centered non-covalent homodimer of soluble LLT1 ectodomain has been previously characterized[40, 43, 44] and likely occurs within the full-length protein as well. The human NKR-P1 helix α1-centered dimer uses fewer intermolecular contacts and has a smaller contact surface area than helix α2-centered dimeric CTLRs and is thus less stable. Nevertheless, its formation would expectedly increase in the context of the full-length NKR-P1 receptor disulfide homodimer. At the same time, the length of the NKR-P1 stalk region (25 amino acids) confer enough flexibility for CTLD monomer/dimer equilibrium within the disulfide homodimer of the full-length receptor itself, which would be then further regulated by polymorphism and glycosylation heterogeneity at the NKR-P1 dimerization interface (Fig. 8c, bottom left). Thus, similarly to the B7-1:CD28 system, an equilibrium between the monomeric and dimeric states of CTL ectodomains, modifying and fine-tuning the ability of NKR-P1 to form stable higher-order complexes with LLT1, may consequently regulate the strength and signaling of the NKR-P1:LLT1 system, while cross-linking of NKR-P1 by LLT1 within the immune

synapse may provide enough avidity for stable signal transduction by this low-affinity interaction complex.

In conclusion, presented data altogether show that the crystal structure of the NKR-P1:LLT1 complex constitutes a novel way of C-type lectin-like NK cell receptor:ligand multimerization on the cell surface that explains how ligand binding overcomes low affinity through receptor cross-linking within the immune synapse.

Acknowledgments

Author contributions

JB, OS, BK, SP, EP, and CA contributed to protein expression and purification; JB and YZ performed the protein crystallization; YZ and KH performed the X-ray diffraction measurements; JB, TS, JS, TK, JDu, and JDo contributed to the data processing and model refinement; OS performed the SEC-SAXS data measurement; JB and TS performed the SAXS data analysis; OV performed the analytical ultracentrifugation measurements and analysis; JB and BK acquired and analyzed the dSTORM data; BK and DC performed the NK cytotoxicity assay; JB, TS, JDo, and OV designed the experiments and wrote the manuscript with critical input from JH.

Competing financial interests

The authors declare no competing financial interests.

Methods

Protein expression and purification

Stabilized H176C form of the soluble LLT1 ectodomain (Gln72-Val191) was transiently expressed in HEK293S GnTI⁻ cells, as previously described[44]. The N120R, R153E, K169A secondary interaction mode mutant LLT1^{SIM} was cloned and produced in the same way. The C-type lectin-like domain of human NKR-P1 was produced similarly in stably transfected HEK293S GnTI⁻ cells[51]. Briefly, the expression construct corresponding to the extracellular CTL domain of NKR-P1 (Gly90-Ser225) was subcloned into the pOPINGGTneo plasmid (kindly provided by Prof. Ray Owens, University of Oxford), flanked by the N-terminal secretion leader and by the C-terminal His-tag (with the ETG and the KHHHHHH at the N- and C-termini of the secreted protein, respectively). Suspension culture of HEK293S GnTI⁻ cells[59] was transfected with a 1:3 (w/w) mixture of the expression plasmid and 25-kDa linear polyethyleneimine. The stably transfected cell pool was selected on 200 ng/µl G418 within three weeks. The secreted proteins were purified from the harvested media by two-step chromatography – an IMAC was performed on a Talon column (GE Healthcare), followed by SEC on a Superdex 200 10/300 GL (GE Healthcare) in 10 mM HEPES pH 7.5 with 150 mM NaCl and 10 mM NaN$_3$. For deglycosylation, GST-fused Endo F1[60] was added in a 1:100 weight ratio to proteins in SEC buffer with 50 mM citrate pH 5.5 and incubated for 2 hours at 37°C. The deglycosylated proteins were then purified by batch affinity chromatography on Glutathione Sepharose 4B resin (GE Healthcare) followed by SEC, as described above.

Crystallization

NKR-P1 glycosylated (structure NKR-P1_glyco) – Soluble human NKR-P1 ectodomain at 20 mg/ml in SEC buffer was crystallized using the sitting drop vapor diffusion method. Drops (100 nl of reservoir solution and 100 nl of protein solution) were set up using a Cartesian Honeybee 961 robot (Genomic Solutions) at 294 K. The reservoir consisted of 20% w/v PEG 3350, 200 mM di-sodium tartrate pH 7.2 (PEG/Ion screen, condition 36; Hampton Research). A hexagonal crystal with dimensions of 150 × 150 × 20 µm was cryoprotected by soaking in the reservoir solution with the addition of 25% (v/v) ethylene glycol.

NKR-P1 deglycosylated (structure NKR-P1_deglyco) – The Endo F1-deglycosylated soluble human NKR-P1 ectodomain was concentrated to 12 mg/ml and crystallized as described above. The reservoir consisted of 20% w/v PEG 3350, 200 mM ammonium fluoride, and 200 mM lithium chloride pH 6.2 (PEG/Ion screen, condition 3, Additive screen, condition 17; Hampton Research). A 50 × 50 × 150 µm rod-shaped crystal was cryoprotected as above by adding 25% (v/v) glycerol.

NKR-P1:LLT1 complex (structure NKR-P1:LLT1) – The Endo F1-deglycosylated soluble human NKR-P1 and LLT1 ectodomains were mixed at a 1:1 molar ratio and concentrated to 8 mg/ml of total protein concentration. The protein complex was crystallized as described above; drops (200 nl of the reservoir and 100 nl of protein solutions) were seeded with 50 nl of stock solution of crushed needle-shaped crystals of deglycosylated NKR-P1 grown in 20% w/v PEG 3350, 200 mM ammonium fluoride pH 6.2 (PEG/Ion screen, condition 3; Hampton Research). The reservoir consisted of 200 mM ammonium sulfate, 20% w/v PEG MME 5000, 100 mM Tris pH 7.5 (Proplex screen, condition 1-40; Molecular Dimensions). A tetragonal bipyramid crystal of dimensions 30 × 30 × 80 μm was cryoprotected as detailed above by adding 25% v/v glycerol.

Data collection

All diffraction data were collected at the Diamond Light Source (Harwell, UK) at beamline I03 using a wavelength of 0.97625 Å and a PILATUS3 6M detector. The crystal-detector distance was set to 340 mm, exposure time per image was 0.02 s, oscillation width was 0.1º, and the temperature was 100 K. 7200 images were collected for each dataset. In the case of the NKR-P1:LLT1 complex, only 5000 images were finally used for data processing.

Data processing and structure solution

All diffraction images were indexed and integrated using the XDS package[61], scaled using AIMLESS[62], and 5% of randomly selected reflections were used as an R_{free} set. The phase problem was solved by molecular replacement – NKR-P1_glyco: in program BALBES[63] using the structure of the human NK cell receptor KLRG1 bound to E-cadherin (PDB ID 3FF7[64]); NKR-P1_deglyco: 6 chains found in PHASER[65] using murine NKR-P1A (PDB ID 3T3A[66]) were completed with 2 chains found in MOLREP[67]; NKR-P1:LLT1: 4 chains found in BALBES as NKR-P1 chains (using the structure of murine dectin-1, PDB ID 2BPD[49]) were completed with two more chains in MOLREP, and all 6 chains were manually reinterpreted as 4 NKR-P1 chains and as 2 LLT1 chains. Refinement was performed using REFMAC5[68] and by manual editing in COOT[69]. The last cycle of refinement was performed using all reflections. The final data processing and structure parameters are outlined in Tab. 1.

Structure quality assessment

NKR-P1_glyco – The structure, comprising one dimer of the glycosylated human NKR-P1 CTLD, is overall well defined in the electron density map, corresponding to the high resolution of the structure (1.8 Å). Glycosylation at the dimerization interface does not show the overlapping features observed in the structures of deglycosylated NKR-P1 (below). GlcNAc was modeled on Asn116 with full occupancy in both chains, whereas glycosylation

at Asn157 was not observed in the electron density map. All modeled glycosylation chains ($GlcNAc_2Man_5$ at A/Asn169, $GlcNAc_2Man_3$ at B/Asn169, and GlcNAc at residues Asn116 in both chains) are well localized in the electron density map.

NKR-P1_deglyco – The asymmetric unit comprises four dimers of the human NKR-P1 CTLD deglycosylated after the first GlcNAc unit. The length of the localized part of the protein chain varies from the shortest chains A, F, and G, with modeled residues Leu91–Leu214, to the longest chain H, with residues Gly90–Arg218. GlcNAc at residue Asn169 is well localized, while GlcNAc units bound to Asn116 and Asn157 at the dimerization interface are present in alternative and overlapping positions; residue Asn116 also shows alternative conformers. GlcNAc units bound to Asn157 and Asn116 were modeled with 0.5 occupancies, and only the most distinct units from each overlapping pair were modeled (Tab. 1).

NKR-P1:LLT1 – The asymmetric unit contains two dimers of the human NKR-P1 CTLD and one dimer of the LLT1 CTLD. The structure has a well-defined electron density map, and all protein chains can be unambiguously assigned. The most distinct difference peaks correspond to non-interpretable small ligands. LLT1 has well-localized GlcNAc units at residues Asn95 and Asn147. Localized GlcNAc units of NKR-P1 are the same as those identified in the NKR-P1_deglyco structure (previous paragraph).

PDB deposition

The crystal structures were deposited in the Protein Data Bank under the codes 5MGR (NKR-P1_glyco), 5MGS (NKR-P1_deglyco), and 5MGT (NKR-P1:LLT1).

CD spectroscopy

Circular dichroism (CD) spectra of wild-type and S159A NKR-P1 and wild-type and SIM LLT1 were recorded using a Chirascan Plus CD spectropolarimeter (Applied Photophysics) and a 0.1 cm pathlength quartz cell. Spectra were recorded over the wavelength range of 195–260 nm in steps of 1 nm at room temperature. The sample concentrations were 0.2 mg/ml and 0.3 mg/ml for NKR-P1 and LLT1 protein samples, respectively; in 10 mM HEPES, 150 mM NaCl pH 7.5 sample buffer. The CD signal was expressed as ellipticity, and the resulting spectra were buffer subtracted. Secondary structure composition was analyzed using the CDNN program provided with the Chirascan Plus CD spectropolarimeter.

Analytical ultracentrifugation

NKR-P1:LLT1 complex formation and dimerization of NKR-P1 S159A mutant were analyzed in an analytical ultracentrifuge ProteomeLab XL-I equipped with an An-50 Ti rotor (Beckman Coulter, USA)[70]. For the sedimentation velocity experiment, samples of glycosylated NKR-P1, LLT1, and their equimolar mixtures with increasing concentrations in SEC buffer were

spun at 48000 rpm at 20°C, and 150 scans with 0.003 cm spatial resolution were recorded in 5-min steps using absorbance optics. Buffer density and protein partial specific volumes were estimated in SEDNTERP (www.jphilo.mailway.com). Data were analyzed with SEDFIT[71] using the continuous c(s) distribution model. Binding isotherms (and figures illustrating AUC data) were prepared in GUSSI[72] and then best-fit in SEDPHAT[73] using hetero-association models A+B⇔AB or A+B⇔AB+B⇔ABB, where A is the LLT1 dimer and B is NKR-P1 monomer, respectively. Only K_D and sedimentation coefficients of AB or ABB were floated in the fit; the other parameters were kept constant at known values.

Microscale thermophoresis

For the microscale thermophoresis (MST) measurements of NKR-P1:LLT1 and NKR-P1:LLT1^{SIM} interactions, the NKR-P1 has been fluorescently labeled with Atto 488 NHS-ester (Merck) at pH 6.5; the excess label was removed by size exclusion chromatography. Fluorescently labeled 100 nM NKR-P1 was mixed with dilution series of LLT1 or LLT1^{SIM} and analyzed in standard capillaries in an NT.115 Monolith (NanoTemper) using 30% LED excitation power and 60% MST power. Raw data were analyzed in PALMIST[74]; the exported isotherms were best-fit in SEDPHAT[73] and figures prepared in GUSSI[72].

Small-angle X-ray scattering

SEC-SAXS data for the NKR-P1:LLT1 complex were collected at the Diamond Light Source (Didcot, UK) at beamline 21 using an Agilent 1200 HPLC system with 2.4 mL Superdex 200 column (GE Healthcare), a Pilatus P3-2M detector, 12.4 keV radiation, and 4.014 m sample-to-detector distance. The human NKR-P1 and LLT1 ectodomains with $GlcNAc_2Man_5$ glycans diluted in 10 mM HEPES, 150 mM NaCl, 10 mM NaN_3, pH 7.5 were mixed at a 1:1 molar ratio. The data were collected at 293 K for buffer and protein samples at a 15 mg/ml loading concentration. The data in selected intervals (frames 355-367, 368-378, 379-388, 388-399, 431-440, 481-491) were solvent-subtracted in SCÅTTER (developed by Robert Rambo at the Diamond Light Source, http://www.bioisis.net/tutorial/9) and merged and characterized using the ATSAS[75] package. As proof of the data quality, the scattering plot, Kratky plot, and pair distance distribution function P(r) are shown in Fig. 4 for intervals 389-399 (a sample data range from the first peak) and 481-491 (a sample data range from the second peak). The scattering plot and Guinier plot for all the data ranges are shown in Fig. S6.

Using the P(r) pair distance distribution functions, twenty *ab initio* structure models were calculated with DAMMIF 2.7.2[76] for each data interval. The models were compared using the DAMSEL command and averaged using DAMAVER[77]. The final models were visualized in CHIMERA[78] as envelopes 15 Å above the beads. Agreement between the SAXS data and our 3D crystal structure of the NKR-P1:LLT1 complex was evaluated using OLIGOMER[79]. All

possible multimers of NKR-P1:LLT1 assemblies were considered (see the Results section and Fig. S6).

Super-resolution microscopy

dSTORM microscopy – Full-length NKR-P1 stable transfectants were generated in HEK293S GnTI⁻ cell line using the piggyBac transposon-based system with doxycycline-inducible protein expression[80]. Microscopy samples were prepared from cells treated with 5 ng/ml doxycycline overnight. Cells were washed with PBS and incubated with 8.4 mg/ml LLT1 or LLT1^SIM, or PBS, for 1 hour at 37 °C. After incubation, cells were allowed to settle on the surface of PLL-coated slides for 25 min at 37 °C. Cells were then fixed with 4% PFA and 0.2% GA for 10 min at room temperature and washed three times with PBS. For antibody staining, cells were first blocked with 5% BSA for 30 min and stained with Alexa Fluor® 647 anti-human CD161 antibody (clone HP-3G10; BioLegend) at 10 µg/ml in blocking solution for 60 min. Samples were washed five times with PBS before post-fixation with 4% PFA and 0.2% GA for 10 min. Finally, cells were treated with 15 mM NH_4Cl and washed two times with PBS.

dSTORM images were acquired with Carl Zeiss Elyra PS.1 in the Laboratory of Confocal and Fluorescence Microscopy (Faculty of Science, Charles University). Fiducial markers were added to the buffer and allowed to settle on the sample for 1 hour. Before measurement, the buffer was exchanged to glucose oxidase/catalase/MEA-based imaging buffer and sealed with cover glass and silicon to prevent buffer oxidation. For each cell, 2×10^4 raw images were acquired in HP TIRF illumination mode with an exposure time of 15 ms, using 100% of 642 nm laser power and 100×, 1.46 numerical aperture, oil immersion objective.

Image data analysis – Super-resolution dSTORM images were reconstructed from raw image sequences with the ThunderSTORM plug-in[81] for the ImageJ processing software[82]. Sub-pixel localization of molecules was performed by fitting an integrated Gaussian point-spread function models using the maximum likelihood estimation fitting method[83]. Reconstructed dSTORM images were corrected for drift using fiducial markers and for multiple localizations from a single source by merging events within 20 nm appearing in subsequent frames (with an off-gap of 5 frames).

Voronoi tessellation cluster analysis was performed in ClusterViSu[84] on a whole inner cell surface. A threshold value of 250 was chosen by comparing the distribution of Voronoi polygon surface values between localizations in experimental regions and randomized regions of the same density of events. Clusters containing less than two events were discarded from the data set.

Statistical analysis – Multiple means were compared with one-way analysis of variance (ANOVA) with Bonferroni correction in OriginPro 2018 (v. b9.5.1.195). Graphs show mean values, and error bars represent the SD. Values of $p > 0.05$ are indicated as not significant; statistically significant p values are indicated with asterisks ($* p < 0.05$, $** p < 0.01$, $*** p < 0.001$, $**** p < 0.0001$).

NK cell-mediated cytotoxicity assay

The influence of LLT1 or LLT1^{SIM} on inhibition of the cytotoxic activity of primary NK cells was assessed by flow cytometry. Primary NK cells were isolated by negative selection using an NK cell isolation kit (Miltenyi Biotec) according to the manufacturer's protocol. Purified NK cells were cultured overnight at 1×10^6 cells/ml in RPMI 1640 supplemented with 10% FCS, 100 units/ml penicillin, 100 µg/ml streptomycin, and 80 ng/ml IL-2 (Sigma-Aldrich) for their activation. K562 target cells were stained with CellTrace Violet Proliferation Kit (Thermo Fisher). Following the staining, 1×10^4 target cells were mixed with activated NK cells in a 40:1 (E:T) ratio. Various concentrations of LLT1 protein variants were added, keeping the final reaction volume at 20 µl. After 4 hours of incubation, the cell mixture was centrifuged at $300 \times g$ and stained with 1 µg/ml 7-AAD. Cells were analyzed using a BD LSR II flow cytometer (BD Biosciences). Three independent cytotoxicity assays using NK cells from three different healthy donors were performed in triplicates (or duplicates if PBMC fraction did not provide enough NK cells). Data are presented as a mean of measurements with SD. When applicable, data were statistically evaluated by one-way ANOVA with values of $p < 0.05$ considered statistically significant.

References

1. Vivier, E. *et al.* Innate or adaptive immunity? The example of natural killer cells. *Science* **331**, 44-49 (2011).

2. Cerwenka, A. & Lanier, L.L. Natural killer cell memory in infection, inflammation and cancer. *Nature reviews. Immunology* **16**, 112-123 (2016).

3. Yokoyama, W.M. & Plougastel, B.F. Immune functions encoded by the natural killer gene complex. *Nature reviews. Immunology* **3**, 304-316 (2003).

4. Bartel, Y., Bauer, B. & Steinle, A. Modulation of NK cell function by genetically coupled C-type lectin-like receptor/ligand pairs encoded in the human natural killer gene complex. *Frontiers in immunology* **4**, 362 (2013).

5. Zelensky, A.N. & Gready, J.E. The C-type lectin-like domain superfamily. *The FEBS journal* **272**, 6179-6217 (2005).

6.   Rozbesky, D. *et al.* Re-evaluation of binding properties of recombinant lymphocyte receptors NKR-P1A and CD69 to chemically synthesized glycans and peptides. *International journal of molecular sciences* **15**, 1271-1283 (2014).

7.   Lanier, L.L., Chang, C. & Phillips, J.H. Human NKR-P1A. A disulfide-linked homodimer of the C-type lectin superfamily expressed by a subset of NK and T lymphocytes. *Journal of immunology* **153**, 2417-2428 (1994).

8.   Spreu, J. *et al.* Interaction of C-type lectin-like receptors NKp65 and KACL facilitates dedicated immune recognition of human keratinocytes. *Proceedings of the National Academy of Sciences of the United States of America* **107**, 5100-5105 (2010).

9.   Welte, S., Kuttruff, S., Waldhauer, I. & Steinle, A. Mutual activation of natural killer cells and monocytes mediated by NKp80-AICL interaction. *Nature immunology* **7**, 1334-1342 (2006).

10. Vogler, I. & Steinle, A. Vis-a-vis in the NKC: genetically linked natural killer cell receptor/ligand pairs in the natural killer gene complex (NKC). *Journal of innate immunity* **3**, 227-235 (2011).

11. Aldemir, H. *et al.* Cutting edge: lectin-like transcript 1 is a ligand for the CD161 receptor. *Journal of immunology* **175**, 7791-7795 (2005).

12. Rosen, D.B. *et al.* Cutting edge: lectin-like transcript-1 is a ligand for the inhibitory human NKR-P1A receptor. *Journal of immunology* **175**, 7796-7799 (2005).

13. Poggi, A., Costa, P., Tomasello, E. & Moretta, L. IL-12-induced up-regulation of NKRP1A expression in human NK cells and consequent NKRP1A-mediated down-regulation of NK cell activation. *European journal of immunology* **28**, 1611-1616 (1998).

14. Exley, M., Porcelli, S., Furman, M., Garcia, J. & Balk, S. CD161 (NKR-P1A) costimulation of CD1d-dependent activation of human T cells expressing invariant V alpha 24 J alpha Q T cell receptor alpha chains. *The Journal of experimental medicine* **188**, 867-876 (1998).

15. Ussher, J.E. *et al.* CD161++ CD8+ T cells, including the MAIT cell subset, are specifically activated by IL-12+IL-18 in a TCR-independent manner. *European journal of immunology* **44**, 195-203 (2014).

16. Fergusson, J.R. *et al.* CD161 defines a transcriptional and functional phenotype across distinct human T cell lineages. *Cell reports* **9**, 1075-1088 (2014).

17. Germain, C. *et al.* Induction of lectin-like transcript 1 (LLT1) protein cell surface expression by pathogens and interferon-gamma contributes to modulate immune responses. *The Journal of biological chemistry* **286**, 37964-37975 (2011).

18. Bennett, I.M. *et al.* Definition of a natural killer NKR-P1A+/CD56-/CD16- functionally immature human NK cell subset that differentiates in vitro in the presence of interleukin 12. *The Journal of experimental medicine* **184**, 1845-1856 (1996).

19. Cosmi, L. *et al.* Human interleukin 17-producing cells originate from a CD161+CD4+ T cell precursor. *The Journal of experimental medicine* **205**, 1903-1916 (2008).

20. Mathewson, N.D. *et al.* Inhibitory CD161 receptor identified in glioma-infiltrating T cells by single-cell analysis. *Cell* **184**, 1281-1298 e1226 (2021).

21. Poggi, A., Costa, P., Zocchi, M.R. & Moretta, L. Phenotypic and functional analysis of CD4+ NKRP1A+ human T lymphocytes. Direct evidence that the NKRP1A molecule is involved in transendothelial migration. *European journal of immunology* **27**, 2345-2350 (1997).

22. Chalan, P. *et al.* Expression of Lectin-Like Transcript 1, the Ligand for CD161, in Rheumatoid Arthritis. *PloS one* **10**, e0132436 (2015).

23. Rosen, D.B. *et al.* Functional consequences of interactions between human NKR-P1A and its ligand LLT1 expressed on activated dendritic cells and B cells. *Journal of immunology* **180**, 6508-6517 (2008).

24. Boles, K.S., Barten, R., Kumaresan, P.R., Trowsdale, J. & Mathew, P.A. Cloning of a new lectin-like receptor expressed on human NK cells. *Immunogenetics* **50**, 1-7 (1999).

25. Roth, P. *et al.* Malignant glioma cells counteract antitumor immune responses through expression of lectin-like transcript-1. *Cancer research* **67**, 3540-3544 (2007).

26. Mathew, S.O., Chaudhary, P., Powers, S.B., Vishwanatha, J.K. & Mathew, P.A. Overexpression of LLT1 (OCIL, CLEC2D) on prostate cancer cells inhibits NK cell-mediated killing through LLT1-NKRP1A (CD161) interaction. *Oncotarget* **7**, 68650-68661 (2016).

27. Marrufo, A.M. *et al.* Blocking LLT1 (CLEC2D, OCIL)-NKRP1A (CD161) interaction enhances natural killer cell-mediated lysis of triple-negative breast cancer cells. *Am J Cancer Res* **8**, 1050-1063 (2018).

28. Germain, C. *et al.* Lectin-like transcript 1 is a marker of germinal center-derived B-cell non-Hodgkin's lymphomas dampening natural killer cell functions. *Oncoimmunology* **4**, e1026503 (2015).

29. Zambrano-Zaragoza, J.F., Romo-Martinez, E.J., Duran-Avelar Mde, J., Garcia-Magallanes, N. & Vibanco-Perez, N. Th17 cells in autoimmune and infectious diseases. *International journal of inflammation* **2014**, 651503 (2014).

30. Afzali, B. *et al.* CD161 expression characterizes a subpopulation of human regulatory T cells that produces IL-17 in a STAT3-dependent manner. *European journal of immunology* **43**, 2043-2054 (2013).

31. Billerbeck, E. *et al.* Analysis of CD161 expression on human CD8+ T cells defines a distinct functional subset with tissue-homing properties. *Proceedings of the National Academy of Sciences of the United States of America* **107**, 3006-3011 (2010).

32. Smith, J.A. & Colbert, R.A. Review: The interleukin-23/interleukin-17 axis in spondyloarthritis pathogenesis: Th17 and beyond. *Arthritis & rheumatology* **66**, 231-241 (2014).

33. Brucklacher-Waldert, V., Stuerner, K., Kolster, M., Wolthausen, J. & Tolosa, E. Phenotypical and functional characterization of T helper 17 cells in multiple sclerosis. *Brain : a journal of neurology* **132**, 3329-3341 (2009).

34. Estrada-Capetillo, L. *et al.* Induction of Th17 lymphocytes and Treg cells by monocyte-derived dendritic cells in patients with rheumatoid arthritis and systemic lupus erythematosus. *Clinical & developmental immunology* **2013**, 584303 (2013).

35. Michalak-Stoma, A. *et al.* Serum levels of selected Th17 and Th22 cytokines in psoriatic patients. *Disease markers* **35**, 625-631 (2013).

36. Germain, C. *et al.* Characterization of alternatively spliced transcript variants of CLEC2D gene. *The Journal of biological chemistry* **285**, 36207-36215 (2010).

37. Li, Y., Wang, Q., Chen, S., Brown, P.H. & Mariuzza, R.A. Structure of NKp65 bound to its keratinocyte ligand reveals basis for genetically linked recognition in natural killer gene complex. *Proceedings of the National Academy of Sciences of the United States of America* **110**, 11505-11510 (2013).

38. Bauer, B., Spreu, J., Rohe, C., Vogler, I. & Steinle, A. Key residues at the membrane-distal surface of KACL, but not glycosylation, determine the functional interaction of the keratinocyte-specific C-type lectin-like receptor KACL with its high-affinity receptor NKp65. *Immunology* **145**, 114-123 (2015).

39. Kamishikiryo, J., Fukuhara, H., Okabe, Y., Kuroki, K. & Maenaka, K. Molecular basis for LLT1 protein recognition by human CD161 protein (NKRP1A/KLRB1). *The Journal of biological chemistry* **286**, 23823-23830 (2011).

40. Kita, S. *et al.* Crystal structure of extracellular domain of human lectin-like transcript 1 (LLT1), the ligand for natural killer receptor-P1A. *European journal of immunology* **45**, 1605-1613 (2015).

41. Aguilar, O.A. *et al.* A Viral Immunoevasin Controls Innate Immunity by Targeting the Prototypical Natural Killer Cell Receptor Family. *Cell* **169**, 58-71 e14 (2017).

42. Balaji, G.R. *et al.* Recognition of host Clr-b by the inhibitory NKR-P1B receptor provides a basis for missing-self recognition. *Nat Commun* **9**, 4623 (2018).

43. Skalova, T. *et al.* Four crystal structures of human LLT1, a ligand of human NKR-P1, in varied glycosylation and oligomerization states. *Acta crystallographica. Section D, Biological crystallography* **71**, 578-591 (2015).

44. Blaha, J., Pachl, P., Novak, P. & Vanek, O. Expression and purification of soluble and stable ectodomain of natural killer cell receptor LLT1 through high-density transfection of suspension adapted HEK293S GnTI(-) cells. *Protein expression and purification* **109**, 7-13 (2015).

45. Vanek, O. *et al.* Soluble recombinant CD69 receptors optimized to have an exceptional physical and chemical stability display prolonged circulation and remain intact in the blood of mice. *The FEBS journal* **275**, 5589-5606 (2008).

46. Kolenko, P. *et al.* The high-resolution structure of the extracellular domain of human CD69 using a novel polymer. *Acta Crystallogr Sect F Struct Biol Cryst Commun* **65**, 1258-1260 (2009).

47. Skalova, T. *et al.* Mouse Clr-g, a ligand for NK cell activation receptor NKR-P1F: crystal structure and biophysical properties. *Journal of immunology* **189**, 4881-4889 (2012).

48. Lovell, S.C. *et al.* Structure validation by Calpha geometry: phi,psi and Cbeta deviation. *Proteins* **50**, 437-450 (2003).

49. Brown, J. *et al.* Structure of the fungal beta-glucan-binding immune receptor dectin-1: implications for function. *Protein science : a publication of the Protein Society* **16**, 1042-1052 (2007).

50. Vanek, O. *et al.* Production of recombinant soluble dimeric C-type lectin-like receptors of rat natural killer cells. *Scientific reports* **9**, 17836 (2019).

51. Blaha, J. *et al.* High-level expression and purification of soluble form of human natural killer cell receptor NKR-P1 in HEK293S GnTI- cells. *Protein expression and purification* **140**, 36-43 (2017).

52. Rother, S. *et al.* The c.503T>C Polymorphism in the Human KLRB1 Gene Alters Ligand Binding and Inhibitory Potential of CD161 Molecules. *PloS one* **10**, e0135682 (2015).

53. Skorepa, O. *et al.* Natural Killer Cell Activation Receptor NKp30 Oligomerization Depends on Its N-Glycosylation. *Cancers (Basel)* **12** (2020).

54. Davis, D.M. *et al.* The human natural killer cell immune synapse. *Proceedings of the National Academy of Sciences of the United States of America* **96**, 15062-15067 (1999).

55. Pageon, S.V. *et al.* Superresolution microscopy reveals nanometer-scale reorganization of inhibitory natural killer cell receptors upon activation of NKG2D. *Science signaling* **6**, ra62 (2013).

56. Stamper, C.C. *et al.* Crystal structure of the B7-1/CTLA-4 complex that inhibits human immune responses. *Nature* **410**, 608-611 (2001).

57. Schwartz, J.C., Zhang, X., Fedorov, A.A., Nathenson, S.G. & Almo, S.C. Structural basis for co-stimulation by the human CTLA-4/B7-2 complex. *Nature* **410**, 604-608 (2001).

58. Bhatia, S., Sun, K., Almo, S.C., Nathenson, S.G. & Hodes, R.J. Dynamic equilibrium of B7-1 dimers and monomers differentially affects immunological synapse formation and T cell activation in response to TCR/CD28 stimulation. *Journal of immunology* **184**, 1821-1828 (2010).

59. Reeves, P.J., Callewaert, N., Contreras, R. & Khorana, H.G. Structure and function in rhodopsin: high-level expression of rhodopsin with restricted and homogeneous N-glycosylation by a tetracycline-inducible N-acetylglucosaminyltransferase I-negative HEK293S stable mammalian cell line. *Proceedings of the National Academy of Sciences of the United States of America* **99**, 13419-13424 (2002).

60. Grueninger-Leitch, F., D'Arcy, A., D'Arcy, B. & Chene, C. Deglycosylation of proteins for crystallization using recombinant fusion protein glycosidases. *Protein science : a publication of the Protein Society* **5**, 2617-2622 (1996).

61. Kabsch, W. Xds. *Acta crystallographica. Section D, Biological crystallography* **66**, 125-132 (2010).

62. Evans, P.R. & Murshudov, G.N. How good are my data and what is the resolution? *Acta crystallographica. Section D, Biological crystallography* **69**, 1204-1214 (2013).

63. Long, F., Vagin, A.A., Young, P. & Murshudov, G.N. BALBES: a molecular-replacement pipeline. *Acta crystallographica. Section D, Biological crystallography* **64**, 125-132 (2008).

64. Li, Y. *et al.* Structure of natural killer cell receptor KLRG1 bound to E-cadherin reveals basis for MHC-independent missing self recognition. *Immunity* **31**, 35-46 (2009).

65. McCoy, A.J. *et al.* Phaser crystallographic software. *Journal of applied crystallography* **40**, 658-674 (2007).

66. Kolenko, P. *et al.* Molecular architecture of mouse activating NKR-P1 receptors. *Journal of structural biology* **175**, 434-441 (2011).

67. Vagin, A. & Teplyakov, A. Molecular replacement with MOLREP. *Acta crystallographica. Section D, Biological crystallography* **66**, 22-25 (2010).

68. Murshudov, G.N. *et al.* REFMAC5 for the refinement of macromolecular crystal structures. *Acta crystallographica. Section D, Biological crystallography* **67**, 355-367 (2011).

69. Emsley, P., Lohkamp, B., Scott, W.G. & Cowtan, K. Features and development of Coot. *Acta crystallographica. Section D, Biological crystallography* **66**, 486-501 (2010).

70. Rozbesky, D. *et al.* High-level expression of soluble form of mouse natural killer cell receptor NKR-P1C(B6) in Escherichia coli. *Protein expression and purification* **77**, 178-184 (2011).

71. Schuck, P. Size-distribution analysis of macromolecules by sedimentation velocity ultracentrifugation and Lamm equation modeling. *Biophysical journal* **78**, 1606-1619 (2000).

72. Brautigam, C.A. Calculations and Publication-Quality Illustrations for Analytical Ultracentrifugation Data. *Methods in enzymology* **562**, 109-133 (2015).

73. Schuck, P. On the analysis of protein self-association by sedimentation velocity analytical ultracentrifugation. *Analytical biochemistry* **320**, 104-124 (2003).

74. Scheuermann, T.H., Padrick, S.B., Gardner, K.H. & Brautigam, C.A. On the acquisition and analysis of microscale thermophoresis data. *Analytical biochemistry* **496**, 79-93 (2016).

75. Petoukhov, M.V. *et al.* New developments in the program package for small-angle scattering data analysis. *Journal of applied crystallography* **45**, 342-350 (2012).

76. Franke, D. & Svergun, D.I. DAMMIF, a program for rapid ab-initio shape determination in small-angle scattering. *Journal of applied crystallography* **42**, 342-346 (2009).

77. Svergun, D.I. Restoring low resolution structure of biological macromolecules from solution scattering using simulated annealing. *Biophysical journal* **76**, 2879-2886 (1999).

78. Pettersen, E.F. *et al.* UCSF Chimera--a visualization system for exploratory research and analysis. *Journal of computational chemistry* **25**, 1605-1612 (2004).

79. Konarev, P.V., Volkov, V.V., Skolova, A.V., Koch, M.H.J. & Svergun, D.I. PRIMUS: a Windows PC-based system for small-angle scattering data analysis. *Journal of applied crystallography* **36**, 1277-1282 (2003).

80. Li, Z., Michael, I.P., Zhou, D., Nagy, A. & Rini, J.M. Simple piggyBac transposon-based mammalian cell expression system for inducible protein production. *Proceedings of the National Academy of Sciences of the United States of America* **110**, 5004-5009 (2013).

81. Ovesny, M., Krizek, P., Borkovec, J., Svindrych, Z. & Hagen, G.M. ThunderSTORM: a comprehensive ImageJ plug-in for PALM and STORM data analysis and super-resolution imaging. *Bioinformatics* **30**, 2389-2390 (2014).

82. Schneider, C.A., Rasband, W.S. & Eliceiri, K.W. NIH Image to ImageJ: 25 years of image analysis. *Nature methods* **9**, 671-675 (2012).

83. Thompson, R.E., Larson, D.R. & Webb, W.W. Precise nanometer localization analysis for individual fluorescent probes. *Biophysical journal* **82**, 2775-2783 (2002).

84. Andronov, L., Orlov, I., Lutz, Y., Vonesch, J.L. & Klaholz, B.P. ClusterViSu, a method for clustering of protein complexes by Voronoi tessellation in super-resolution microscopy. *Scientific reports* **6**, 24084 (2016).

7.5 PUBLICATION NO. 5

Kalousková, B.; Skořepa, O.; Cmunt, D.; Abreu, C.; Krejčová, K.; Bláha, J.; Sieglová, I.; Král, V.; Fábry, M.; Pola, R.; Pechar, M.; Vaněk O.

Tumor marker B7-H6 bound to the coiled coil peptide-polymer conjugate enables targeted therapy by activating human natural killer cells.

My contribution to the publication: performing research (cloning and vector design, cell culture maintenance, transfection optimization, protein expression, protein purification, and quality control, cellular assays, flow cytometry), data collection, data analysis, interpretation, manuscript writing.

biomedicines   MDPI

Article

Tumor Marker B7-H6 Bound to the Coiled Coil Peptide-Polymer Conjugate Enables Targeted Therapy by Activating Human Natural Killer Cells

Barbora Kalousková [1], Ondřej Skořepa [1], Denis Cmunt [1,†], Celeste Abreu [1], Kateřina Krejčová [1], Jan Bláha [1,‡], Irena Sieglová [2], Vlastimil Král [2], Milan Fábry [2], Robert Pola [3], Michal Pechar [3] and Ondřej Vaněk [1,*]

1   Department of Biochemistry, Faculty of Science, Charles University, Hlavova 2030, 12840 Prague, Czech Republic; barbora.kalouskova@natur.cuni.cz (B.K.); ondrej.skorepa@natur.cuni.cz (O.S.); cmuntd@seznam.cz (D.C.); desousac@natur.cuni.cz (C.A.); krejcova.katerina27@gmail.com (K.K.); jahabla@gmail.com (J.B.)

2   Institute of Molecular Genetics, Czech Academy of Sciences, Vídeňská 1083, 14220 Prague, Czech Republic; sieglova@img.cas.cz (I.S.); kral@img.cas.cz (V.K.); fabry@img.cas.cz (M.F.)

3   Institute of Macromolecular Chemistry, Czech Academy of Sciences, Heyrovského nám. 2, 16206 Prague, Czech Republic; pola@imc.cas.cz (R.P.); pechar@imc.cas.cz (M.P.)

*   Correspondence: ondrej.vanek@natur.cuni.cz

†   Present address: Department of Oncology, Ludwig Institute for Cancer Research, University of Lausanne, Chemin des Boveresses 155, 1066 Epalinges, Switzerland.

‡   Present address: EMBL, Hamburg Unit c/o DESY, Notkestrasse 85, 22607 Hamburg, Germany.

Abstract: Targeted cancer immunotherapy is a promising tool for restoring immune surveillance and eradicating cancer cells. Hydrophilic polymers modified with coiled coil peptide tags can be used as universal carriers designed for cell-specific delivery of such biologically active proteins. Here, we describe the preparation of pHPMA-based copolymer conjugated with immunologically active protein B7-H6 via complementary coiled coil VAALEKE (peptide E) and VAALKEK (peptide K) sequences. Receptor B7-H6 was described as a binding partner of NKp30, and its expression has been proven for various tumor cell lines. The binding of B7-H6 to NKp30 activates NK cells and results in Fas ligand or granzyme-mediated apoptosis of target tumor cells. In this work, we optimized the expression of coiled coil tagged B7-H6, its ability to bind activating receptor NKp30 has been confirmed by isothermal titration calorimetry, and the binding stoichiometry of prepared chimeric biopolymer has been characterized by analytical ultracentrifugation. Furthermore, this coiled coil B7-H6-loaded polymer conjugate activates NK cells *in vitro* and, in combination with coiled coil scFv, enables their targeting towards a model tumor cell line. Prepared chimeric biopolymer represents a promising precursor for targeted cancer immunotherapy by activating the cytotoxic activity of natural killer cells.

Keywords: coiled coil; HPMA polymer; NK cell; NKp30; B7-H6; immunotherapy

Publisher's Note: MDPI stays neutral with regard to jurisdictional claims in published maps and institutional affiliations.

1. Introduction

The immune system is defending our body not only from external threats (e.g., pathogens, toxins) but also from the harm that may come from the inside (e.g., malignant growth of transformed cells) in a process called immunosurveillance [1]. As healthy cells undergo malignant transformation, the dynamic mutual communication with immune cells turns into immunoediting [2–4]. Despite all efforts of numerous lymphocyte populations, this process is not always leading to tumor suppression, but may instead result in tumor escape [3,5,6]. This immune system failure is caused by the tumor's ability to surround itself with a tumor-suppressing microenvironment [7]. Cancer treatment with immunotherapy strikes tumor barriers and facilitates restoration of immunosurveillance.

The key cellular players in immunotherapy are cytotoxic effector cells, such as T-cells (as well as their subpopulations NKT lymphocytes, Tc-lymphocytes, or γδT-lymphocytes)

and NK cells [8]. NK cells tend to be overlooked, as they represent 'only' around 12% of the blood lymphocytes [9]. However, they have a unique ability to rapidly identify and eliminate transformed or stressed cells [10]. They participate in tumor immunosurveillance and could be used in targeted immunotherapy [11–16]. Therapeutic approaches targeting NK cell activation in cancer treatment are based on native NK cell recognition mechanisms. Alternatively, mAbs can be used for immune checkpoint blockade to prevent NK cell suppression [17]. Moreover, NK cells can be harnessed in various adoptive cell therapies where they are *in vitro* activated, re-educated, or genetically modified with tumor-specific chimeric antigen receptors (CARs) [18–20].

Another therapeutic strategy is the mediation of the cellular contact between NK cells and cancer cells. Such interaction could be promoted by mAbs that target tumor markers and at the same time activate NK cells via Fcγ receptor (CD16) in antibody-dependent cell-mediated cytotoxicity (ADCC) [21]. Moreover, this interaction may be enhanced using antiCD16 scFv in fusion with antitumor scFv (targeting, for example, CD19, CD33, CD22, or EpCAM); such a molecule is then called bispecific killer engager (BiKE) [22,23]. The BiKE could be further extended with another recognition domain or with the addition of activating IL-15 (TriKE) [24,25]. This concept could be developed and generalized, such immunoactive therapeutics could also consist of the extracellular domains of NK cell receptors (targeting NK cells activating ligands as markers of tumor cells) [26] or with the NK cells activating ligands (targeting different NK cells activating pathways) [27].

NK cells activating receptors play a critical role in triggering NK cells as anti-cancer therapeutic agents; some of them are dominant in this task, namely NKG2D, 2B4, NKp30, or NKp80 [28]. Receptor NKp30 belongs to the natural cytotoxicity receptor (NCR) family, as well as receptors NKp46 and NKp44 [29]. NKp30 is a type I transmembrane protein consisting of an N-terminal immunoglobulin-like domain, stalk region (15 amino acids), transmembrane helix, and C-terminal cytoplasmic domain enabling signalization through association with CD3ζ chain [30]. Structurally, NKp30 is part of the CD28 family of proteins [31]. Three specific cellular ligands of NKp30 have been identified so far: BAG6, B7-H6, and galectin-3, all of which could be found on the tumor surface, but while BAG6 and B7-H6 activate NK cell cytotoxicity, galectin-3 blocks it completely [31–34].

Protein B7-H6 is expressed exclusively on the surface of tumor cells, which makes this tumor-induced self-molecule a valuable tumor marker triggering NK cells [31,35]. Like other members of the B7 family, B7-H6 is an immunoglobulin-like type I transmembrane protein. Its extracellular part is composed of a membrane-distal IgV-like domain and a membrane-proximal IgC-like domain [5]. Several crystal structures of NKp30:B7-H6 immunocomplex have been published so far, revealing structural features of this interaction [36–38].

The potential of NKp30:B7-H6 interaction in immunotherapy has already been explored. One of the first therapeutic constructs successfully triggering NK cells via ADCC was the NKp30-Fc IgG fusion construct, targeting B7-H6 on prostate cancer cells and resulting in *in vivo* tumor removal in mice [39]. Coating lymphomas or breast cancer cells with B7-H6 and thus mimicking an "induced-self" phenotype for NK cell recognition has also been reported as a therapeutic strategy. To this end, B7-H6 in fusion with single-chain fragment variable (scFv) of the 7D8 mAb, that targets CD20+ cells, has been used in *in vitro* cytotoxicity assay alone, in combination with similar ULBP2:7D8 construct or with antiCD20 mAb rituximab, demonstrating the synergy among the two [40] or three [41] various activation pathways. Furthermore, B7-H6:antiHER2-scFv fusion protein can also promote targeted killing of breast cancer cells [42]. B7-H6+ tumors could also be targeted with NKp30-based CARs composed of NKp30 extracellular domain and T cell receptor activation motifs [43], or CARs engineered with antiB7-H6 scFv [44,45].

Although strategy with bivalent fusion proteins seems promising, expression of such molecules is limited to a single polypeptide chain, and some targets may be expressed with difficulty (protein stability, expression yield) when fused with the partner. However, recombinant therapeutic proteins must be of exceptional purity and stability, even in

blood circulation [46]. One possible strategy to improve both the recombinant protein therapeutic presentation and its stability *in vivo* is the use of polymeric carriers. Polymers tailored for specific applications have various uses in biosciences, ranging from biomaterials used to prepare medical devices and tissue-engineering scaffolds or improved protein crystallization reagents [47] to smart drug-delivery agents optimized for cancer vaccination and immunotherapy [48–51]. Among the latter, the N-(2-hydroxypropyl)methacrylamide (pHPMA)-based copolymers are especially widely studied and developed for various purposes in biomedical applications, primarily as drug carriers. They are water-soluble, non-toxic, non-immunogenic, and biocompatible. Moreover, due to their intrinsic "stealth properties", the pHPMA copolymers are invisible to major blood plasma proteins and thus avoid unwanted aggregation [52].

The polymeric carrier must be appropriately modified to deliver biologically active molecules into various parts of the organism. In cancer treatment, these molecules could be small drug compounds or more complex and delicate therapeutic proteins. The choice of a linker is crucial in both cases, but could be more problematic for proteins, as the recombinant expression does not offer the possibility to use the same reactive organic chemistries. One possibility is to use a peptide heptad repeat pattern $(abcdefg)_n$ forming helical and supra-helical structures, i.e., so-called coiled coil motifs [53]. Although there are many naturally occurring coiled coil-based protein domains, these polypeptides could also be synthesized *de novo* with enhanced drug delivery properties [54]. Moreover, pHPMA copolymers could carry more than only a single species cargo, which makes them a versatile tool for biomedical applications, as in the case of targeting BCL-1 cells with pHPMA-(VAALEKE)$_4$ bearing doxorubicin and scFv of monoclonal antibody B1 attached via complementary (VAALKEK)$_4$ sequence [55].

The major advantage of the coiled coil peptide-bearing polymeric carrier is its versatility—practically any biologically active protein equipped with a suitable coiled coil peptide sequence can be attached to the polymeric carrier. Moreover, the coiled coil anchoring system allows attachment of more than one protein ligand to the polymeric carrier, thus providing bispecific or even multi-specific constructs capable of biorecognition with more than one biological target. To our best knowledge, such a polymer-based bispecific system is described in this work for the first time.

It has been repeatedly demonstrated [56–61] that polymer systems with coiled coil peptides enable the use of the so-called pre-targeting strategy. This means that first, a tumor-specific targeting protein equipped with a coiled coil tag is administered to the body, followed by a multivalent polymer containing the complementary coiled coil sequence. Kopecek et al. has shown [59] that careful adjustment of the time interval between the administration of the cancer-specific protein and the polymer significantly improves the efficacy of treatment of non-Hodgkin's lymphomas based on cross-linking CD20 antigens.

Very recent work has reported [62] that treatment of the malignant lymphomas with a combination of two different targeting ligands (antiCD20 and antiCD38 Fab antibody fragments) induces apoptosis resulting from cross-linking of the corresponding receptors after administration of a multivalent albumin-based cross-linking effector. The combination of the two ligands led to a higher level of apoptosis than applying either one of the two proteins. This result suggests that the combination of two ligands attached to one polymeric carrier might increase the therapeutic potential of similar types of nanomedicines.

In this work, the same complementary (VAALEKE)$_4$ and (VAALKEK)$_4$ coiled coil motifs forming stable heterodimers were used to prepare protein-polymer complexes targeting cancer cells and activating NK cells simultaneously. Malignant cells could be targeted with monoclonal antibodies recognizing common tumor markers, like carbonic anhydrase IX (CAIX), a sign of cellular hypoxia [63]. scFv fragment of such monoclonal antibody M75 with coiled coil motif has been reported as a targeting molecule for solid hypoxic tumors [64]. Therefore, we have functionalized the pHPMA copolymer not only with the coiled coil M75 scFv but also with a newly prepared coiled coil version of the NK

cell-activating ligand B7-H6, thus enabling tumor targeting and direct activation of human NK cells.

The binding of activating ligands on peptide-polymer conjugates represents a promising strategy to directed cancer immunotherapy because the described pHPMA copolymers could deliver more than a single bioactive moiety, enabling activation and targeting at the same time. Moreover, the polymer itself represents a promising precursor for targeted cancer immunotherapy due to possibly improved pharmacokinetics such as reduced catalytic degradation, prolonged blood circulation, and enhanced permeation and retention (EPR) effect that conjugation with polymer is usually associated with [65].

2. Materials and Methods

2.1. Preparation of Polymer-Peptide Conjugates

Synthesis and characterization of the coiled coil peptide bearing polymer (PolCC) have been previously described [64]. Peptides (VAALEKE)$_4$, complementary to the (VAALKEK)$_4$ peptides present on the recombinant proteins and forming together a coiled coil structure, were attached to HPMA copolymer via azide-alkyne cycloaddition ("click" chemistry). Reactive propargyl groups (13 mol.%) on the polymeric carrier were modified with the VAALEKE peptide (3.9 mol.%) and biotin (0.86 mol.%), resulting in a 56 kDa PolCC conjugate (Scheme 1, left-hand side) with approximately eight coiled coil peptides on each polymer chain (40% *w/w*). The newly synthesized conjugate based on HPMA copolymer of increased length (PolCC+, Scheme 1, right-hand side) was prepared similarly, except for using RAFT polymerization and copper-free click chemistry—full details of PolCC+ conjugate synthesis and characterization are given in Supplementary Materials (File S1). Reactive groups (2.5 mol.%) on the polymeric carrier were modified with the VAALEKE peptide (1.6 mol.%) and biotin (1 mol.%), resulting in a 130 kDa PolCC+ conjugate with approximately ten coiled coil peptides on each polymer chain (26% *w/w*). The obtained polymer conjugates were purified by size-exclusion chromatography (SEC).
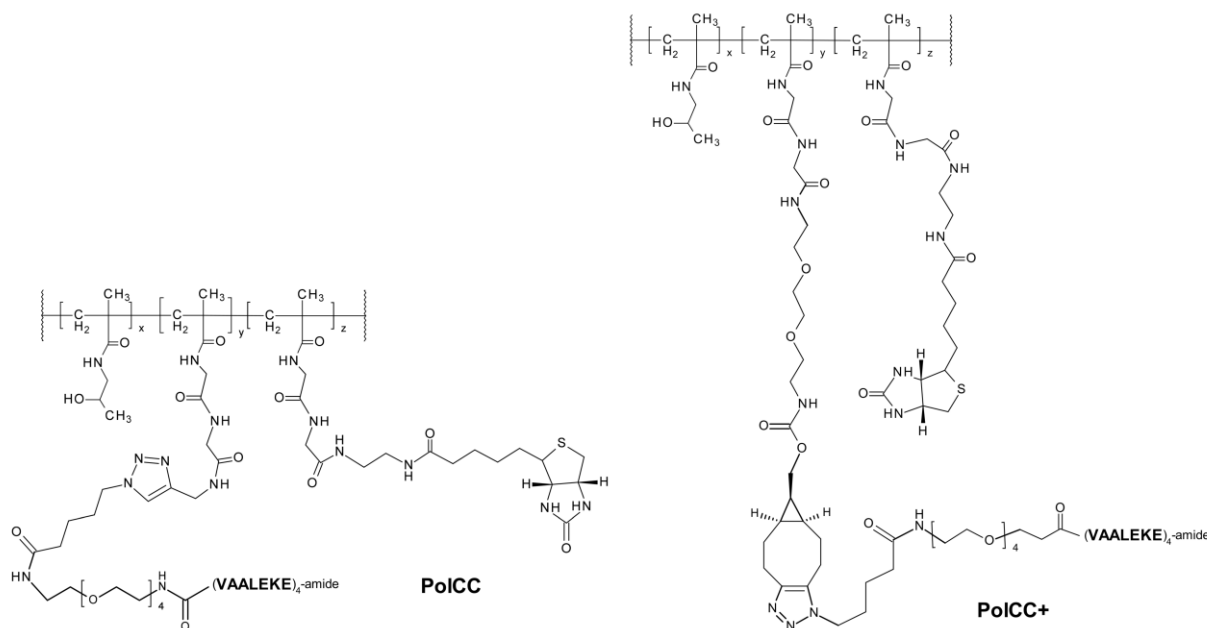
Scheme 1. Representation of PolCC and PolCC+ conjugates' chemical composition.

2.2. Cell Lines

HEK293T cells were a kind gift from Prof. Radu A. Aricescu [66]. Cells were adapted for cultivation in suspension in EX-CELL 293 serum-free medium (Sigma, St. Louis, MO, USA) supplemented with 4 mM L-glutamine. Cells were maintained in the square-shaped glass bottles placed on an orbital shaker in a humidified incubator (37 °C, 5% CO_2) [67].

HT-29 cells were provided by the Institute of Molecular Genetics, Czech Academy of Science, Prague. C33 cell line transfected with CAIX gene (C33_CAIX) or with a control vector containing neomycin resistance gene (C33_Neo) were kindly provided by Dr. Eliška Švastová (Institute of Virology, Slovak Academy of Sciences) [68]. Cells were cultivated in high glucose DMEM medium supplemented with 10% FBS, 100 U/mL penicillin, and 100 µg/mL streptomycin. For splitting, cells were treated with trypsin/EDTA. Both C33 transfectants were maintained under 900 µg/mL of G418 antibiotics. If not mentioned otherwise, all cell-culture media and supplements were purchased from Sigma, St. Louis, MO, USA.

2.3. Vector Design

The extracellular domain of NKp30-activating ligand B7-H6 was expressed using pTW5sec plasmid, a derivative of pTT5 plasmid backbone [69,70]. This vector contains secretion leader, the extracellular domain of B7-H6 (residues D25–T244 with stabilizing mutation C212S [37]), coiled coil motif consisting of four VAALKEK sequence repeats, a histidine tag, and WPRE element increasing mRNA stability and protein yield. The expressed coiled coil B7-H6 protein thus contains an additional ITG- amino acid sequence at its N-terminus and a -GT(VAALKEK)$_4$H$_8$G sequence on its C-terminus.

The extracellular domain of B7-H6 without the coiled coil tag (residues D25–L245 with C212S mutation) and ligand-binding domain of NKp30 (residues L19-E130 representing receptor ectodomain without stalk region) were cloned as described previously [37]. Additionally, vectors for a high-affinity variant of both B7-H6 and B7-H6CC proteins, harboring the recently published S60Y, F82W, L129Y mutations enhancing the affinity towards NKp30 [71], were also prepared.

2.4. Protein Expression and Purification

Coiled coil B7-H6 (B7-H6CC), high-affinity coiled coil B7-H6 (haB7-H6CC), high-affinity B7-H6 (haB7-H6), wild-type B7-H6, and NKp30 ligand-binding domain were expressed in suspension-adapted HEK293T cells using a high-density transient transfection protocol and 25 kDa linear polyethyleneimine (PEI; Polysciences, Warrington, PA, USA) as a transfection reagent [69]. On the day of transfection, cells were harvested by centrifugation (5 min, 100× *g*, 25 °C) and diluted with fresh EX-CELL 293 medium (Sigma, St. Louis, MO, USA). Next, DNA (1 µg of DNA per 1×10^6 cells) was diluted into PBS, sterilized using a 0.22 µm syringe filter, and added directly to the cell culture. The medium volume was adjusted to reach a cell density of 20×10^6 cells/mL. Transfection reagent in weight ratio 4:1 (4 µg of PEI per 1 µg of DNA) was added immediately to the high-density cell culture with DNA. The cell suspension was incubated at high density for 2 h on the shaker in the humidified incubator at 37 °C and then diluted with fresh medium to the final production density of 2×10^6 cells/mL. After the dilution, antibiotics (penicillin, streptomycin) and valproic acid (2 mM final concentration) were added.

Cell culture was harvested by centrifugation (30 min, 10,000× *g*, 20 °C) 5–7 days post-transfection. The medium was filtered using 0.22 µm Steritop filters (Merck Millipore, Burlington, MA, USA) and stored at −20 °C for subsequent purification. Proteins were purified by immobilized metal ion affinity chromatography followed by buffer exchange and size-exclusion chromatography. Before affinity purification on a HisTrap Talon column (GE Healthcare, Chicago, IL, USA), the medium was diluted (1:1) with binding buffer (50 mM Na$_2$HPO$_4$, 300 mM NaCl, 10 mM NaN$_3$, pH 7.5). The column was connected to the ÄKTAprime FPLC system (GE Healthcare, Chicago, IL, USA). After loading, the column was washed with binding buffer, and the protein was eluted using the binding

buffer with 250 mM imidazole. Buffer exchange into a size-exclusion buffer (10 mM HEPES, 150 mM NaCl, 10 mM NaN$_3$, pH 7.5) was done by HiPrep 26/10 desalting column (Cytiva, Marlborough, MA, USA). Protein was concentrated using Amicon Ultra (MWCO 10,000) concentrators at 3900× g at 20 °C to reach a suitable sample volume for size-exclusion chromatography (SEC) on the Superdex 200 10/300 column (GE Healthcare, Chicago, IL, USA) with SEC buffer as the mobile phase. Representative analytical SEC elution profiles were acquired with the Superdex Increase 200 10/300 column (GE Healthcare, Chicago, IL, USA). Protein was frozen in liquid nitrogen and stored at −80 °C.

Production of the antiCAIX antibody M75 scFv fragment with (VAALKEK)$_4$ coiled coil sequence (scFvCC) was described elsewhere [64]. Briefly, the coiled coil-tagged scFv was expressed in *E. coli* strain BL21(DE3) with translocation of the product into periplasmic space. Protein was then purified separately from the periplasmic and cytosolic cell lysate fractions using a pentahistidine tag on Ni-CAM and ion-exchange chromatography on MonoS columns. The scFvCC purified from the cytosolic fraction showed better purity and was used in all subsequent experiments. The binding activity of the prepared scFvCC towards CAIX was verified by ELISA assay as described previously [64].

2.5. Isothermal Titration Calorimetry

Thermodynamic interaction parameters were determined using isothermal titration calorimetry (ITC). All measurements were performed in the SEC buffer. For each run, control heat was determined by a buffer–buffer titration.

The interaction of B7-H6CC, haB7-H6, and haB7-H6CC with NKp30 was measured on MicroCal iTC200 (Malvern Panalytical, Westborough, MA, USA). The measurement of B7-H6CC: NKp30 was initiated by 0.4 µL injection of 182 µM NKp30 into a cell containing 25.0 µM B7-H6CC, followed by 15 injections of 2.3 µL volume with the duration of 4 s with 180 s intervals. Similarly, the measurement of haB7-H6: NKp30 was initiated by 0.4 µL injection of 150 µM NKp30 into a cell containing 15.6 µM haB7-H6, followed by 19 injections of 1.8 µL volume with the duration of 3.6 s with 150 s intervals. The measurement of haB7-H6CC: NKp30 was also initiated by 0.4 µL injection of 124 µM NKp30 into a cell containing 22.4 µM haB7-H6CC, followed by 18 injections of 1.8 µL volume with the duration of 3.6 s with 150 s intervals. The interaction of wild-type B7-H6 with NKp30 was measured on MicroCal PEAQ-ITC (Malvern Panalytical). Initial injection of 0.4 µL NKp30 (179 µM) into a cell containing 24.0 µM B7-H6CC was followed by 25 injections of 1.5 µL volume with the duration of 3 s with 150 s intervals. All measurements were performed at 25 °C while stirring the cell at 750 rpm. The data were evaluated using NITPIC (version 1.2.7, University of Texas Southwestern Medical Center, Dallas, TX, USA; [72]), Sedphat (version 15.2c, by Peter Schuck, National Institute of Health, Bethesda, MD, USA; [73]), and GUSSI software (version 1.4.2, University of Texas Southwestern Medical Center, Dallas, TX, USA; [74]). ITC data were interpreted as A + B <=> AB hetero-association, fitting log(Ka), ΔH, and the incompetent fraction of A (B7-H6; stoichiometry N = 1 − incfA) using the Marquardt–Levenberg algorithm.

2.6. Sedimentation Analysis

Sedimentation velocity experiments were conducted on an analytical ultracentrifuge ProteomeLab XL-I (Beckman Coulter, Brea, CA, USA) using an An50-Ti rotor and double sector cells [75]. Proteins and their mixtures at various loading concentrations were spun at 20 °C and 48,000 rpm. One hundred absorbance scans per measurement were recorded at 280 nm using the SEC buffer as a reference. Time intervals between scans for B7-H6CC mixtures with polymer or NKp30 were 7.5 min or 9 min, respectively. PolCC+ was analyzed at 50,000 rpm and 226 nm (400 scans per 2 min), and its mixtures with B7-H6CC at 42,000 rpm and 280 nm (100 scans per 7 min). Buffer density, protein partial specific volumes, and particle dimensions were estimated in Sednterp (www.jphilo.mailway.com, accessed on 28 July 2021). Data were analyzed in Sedfit (version 16.35r, by Peter Schuck, National Institute of Health, Bethesda, MD, USA; [76]) using the continuous sedimentation

coefficient distribution c(s) model [77]. Figures were prepared in GUSSI (version 1.4.2, University of Texas Southwestern Medical Center, Dallas, TX, USA; [74]).

2.7. NK Cell Activation Assay

NK cells were isolated from the blood samples of healthy donors collected at the transfusion station of the Institute of Hematology and Blood Transfusion (IHBT, Prague, Czech Republic) using the RosetteSep NK cell enrichment cocktail (STEMCELL Technologies, Vancouver, BC, Canada) according to the manufacturer's protocol. Blood was incubated with polyvalent antibodies cocktail, diluted with PBS, topped on the Ficoll high-density medium, and centrifuged ($1200\times g$, 25 °C, 20 min) in SepMate tubes (STEMCELL Technologies). Buffy coat zone depleted from non-NK cell lymphocytes was collected. Isolated cells were washed with PBS, then in 5 mL of red blood cell lysis buffer (eBioscience, San Diego, CA, USA) and PBS again; each washing step was followed by centrifugation ($300\times g$, 25 °C, 10 min). Finally, cells were resuspended in RPMI medium (Sigma, St. Louis, MO, USA) supplemented with 20% heat-inactivated FBS, 100 U/mL penicillin, 100 μg/mL streptomycin, 160 ng/mL IL-2 and kept overnight in a humidified incubator (37 °C, 5% CO_2).

Histidine-tagged proteins were immobilized on the Ni^{2+} chelate-coated 96-well plates (Thermo Fisher Scientific, Waltham, MA, USA). For one well, the total amount of protein (0.04, 0.2, 1, 5, or 50 pmol) was diluted into 50 μL of sterile PBS buffer (cell-culture grade), transferred to the plate, and incubated for one hour on an orbital shaker. An unbound protein was washed away with PBS. NK cells were transferred to the wells in 100 μL of the complete medium. Each well contained the same number of cells in a given experiment, but the total number of cells varied between $1.5–2.5 \times 10^5$ in individual experiments depending on the blood donor. NK cells were incubated with the proteins on the plate for 4 h (orbital shaker, humidified incubator, 37 °C, 5% CO_2).

NK cells were then transferred into a clean U-bottom-shaped 96-well plate, centrifuged ($300\times g$, 4 °C, 5 min), and the medium was discarded. Cells were stained for 30 min on ice with antiCD107a antibody conjugated with APC and washed three times with staining buffer (PBS supplemented with 1% FBS, centrifugation $300\times g$, 4 °C, 5 min). After the final wash, cells were resuspended in 120 μL of staining buffer and analyzed by flow cytometer BD LSR II (BD Biosciences, San Jose, CA, USA) using HTS sample mode. Data were analyzed using FlowJo software (version 10.8.0, Becton, Dickinson and Company, Ashland, OR, USA). The Mann–Whitney U test with a two-tailed hypothesis was used to compare the means.

2.8. Cell Staining with Polymer–Protein Complexes

First, expression of CAIX on the cell surface of HT-29 cells and C33 transfectants was verified using recombinant M75 primary antibody (kind gift from Vlastimil Král) and goat anti-mouse IgG secondary antibody with AlexaFluor405 fluorescent label (Thermo Fisher Scientific, Waltham, MA, USA) with standard staining protocol.

To perform flow cytometry measurements with direct detection of polymer–protein complexes bound to the cell surface (HT-29 and C33 transfectants), we coupled coiled coil proteins with fluorescent probes using NHS-chemistry; more precisely, scFvCC was labeled with AlexaFluor488 and B7-H6CC with AlexaFluor647 (both labels from Life Technologies, Carlsbad, CA, USA). Cells were detached from culture flasks with accutase solution (Capricorn Scientific, Ebsdorfergrund, Hesse, Germany), washed, and then resuspended in the staining buffer. Cells were labeled for 45 min on ice with polymer–protein particles; the pHPMA polymer concentration in staining solution was 1 μM, the ratio between scFvCC:PolCC:B7-H6CC was 2:1:2, controls such as PolCC alone, scFvCC:PolCC or PolCC:B7H6CC were also included. Cells were washed twice (centrifugation $300\times g$, 4 °C, 5 min) with the staining buffer before fluorescent labeling. Samples were analyzed with the flow cytometer BD LSR II (BD Biosciences, San Jose, CA, USA) and FlowJo software (version 10.8.0, Becton, Dickinson and Company, Ashland, OR, USA).

3. Results and Discussion

3.1. Design and Production of Coiled Coil B7-H6

The expression construct of NKp30 activating ligand B7-H6 fused with coiled coil motif is based on the soluble B7-H6 construct described before [37] comprising the entire B7-H6 extracellular domain (residues D25–T244) and harboring C212S mutation relieving the molecule of an odd cysteine, a trait known to destabilize recombinant proteins [37,78]. This construct, referred to as wild-type B7-H6 in the following text, was then extended with 28 amino acids (VAALKEK)$_4$ coiled coil motif [64] followed by a polyhistidine tag on its C-terminus to create the coiled coil B7-H6 (B7-H6CC; Figure 1a,b). As B7-H6 is a single-pass type I membrane protein [31], this arrangement respects its natural structural features, leaving the N-terminal domain containing an interaction interface with the NKp30 receptor unmodified, while C-terminus, which is in the full-length B7-H6 oriented towards cell membrane, contains the coiled coil sequence. We attempted to produce a B7-H6 construct with the coiled coil motif on its N-terminus, but protein expression was unsuccessful, confirming the need to respect natural receptor arrangement.
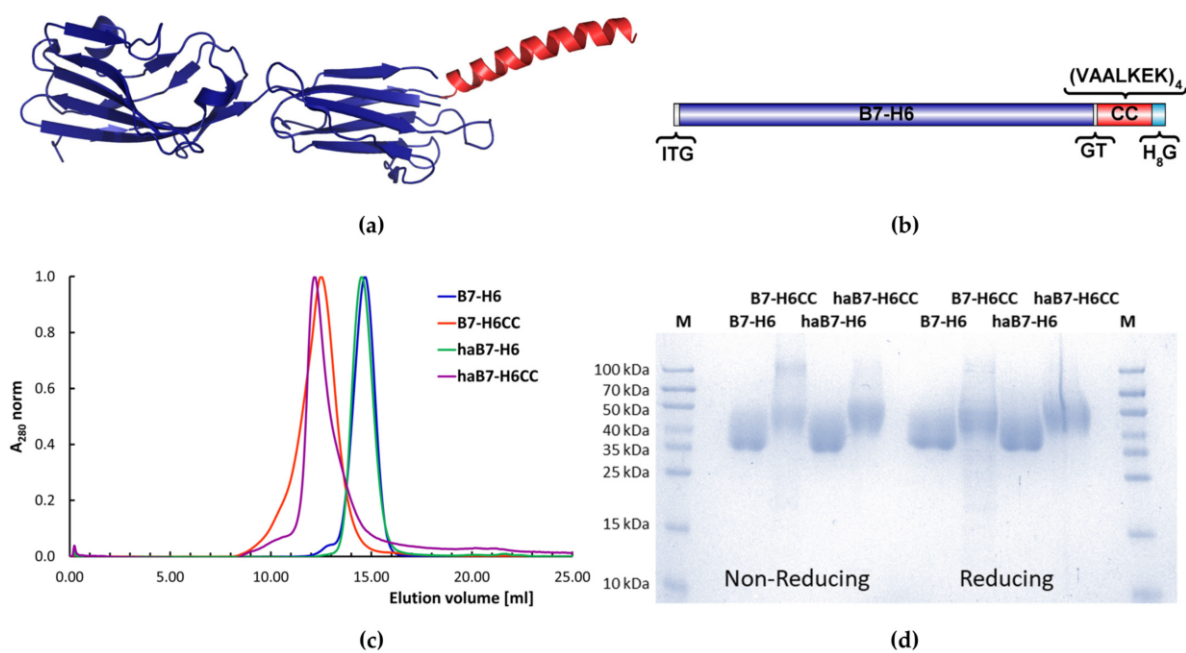

Figure 1. Molecular design and recombinant expression of B7-H6CC. (**a**) A model of B7-H6CC based on the crystal structure of B7-H6:NKp30 complex (PDB 6YJP, [37]); (**b**) schematic representation of B7-H6CC amino acid sequence highlighting the coiled coil motif; (**c**) Comparison of normalized (ha)B7-H6 and (ha)B7-H6CC SEC elution profiles; (**d**) SDS-PAGE electrophoresis as quality control of the expressed proteins, M refers to molecular weight standard.

The interaction interface between the NKp30 receptor and B7-H6 involves the N-terminal IgV-like domain of B7-H6, which is sufficient for binding [79]. Recently, point mutations increasing B7-H6 binding affinity towards NKp30 have been identified [71]. To include this high-affinity variant of B7-H6 in our study, we chose an S60Y, F82W, L129Y B7-H6 triple mutant reported having the potential to improve NKp30 receptor recognition and thus antitumor properties of B7-H6-based recombinant immunotherapeutics [71].

Although stable cell line generation is required to produce some NK cell receptors or ligands [80], for B7-H6CC, a sufficient yield was achieved by transient expression in the HEK293T cell line using a high-density transfection protocol. The protein was secreted into medium and purified by immobilized metal ion affinity chromatography (IMAC) followed by buffer exchange and size exclusion chromatography (SEC). Immediate buffer exchange on a desalting column was necessary because B7-H6CC protein tends to precipitate in

the IMAC elution buffer containing imidazole when being concentrated before SEC. This protocol led to sufficient protein production yields of up to 20 mg per liter of cell culture, which is less than previously reported for the wild-type B7-H6 [37], pointing to a negative impact of the coiled coil tag on the protein stability.

Representative profiles of analytical size-exclusion chromatography and SDS-PAGE gel showing the quality of the prepared B7-H6CC protein are shown in Figure 1c,d, respectively. In both figures, B7-H6CC is compared with the wild-type B7-H6. The expected molecular weight of B7-H6CC is approximately 43 kDa as it possesses six N-glycosylation sites resulting in several glycoforms and blurred bands on the SDS-PAGE gel (Figure 1d). During SEC, B7-H6CC is eluted as a single peak but with a different elution volume than the wild-type B7-H6. This shift could not be explained solely by the increase in protein mass caused by the coiled coil sequence, which itself has only 3 kDa, but it might result from non-covalent dimerization of B7-H6CC driven by the nature of the coiled coil sequence. Indeed, homodimerization of (VAALKEK)$_4$ coiled coil motif has been described previously for the scFvCC fragment of the M75 mAb [64]. This interpretation is indirectly supported by the SDS-PAGE (Figure 1d), where the majority of the coiled coil B7-H6 variants migrate as a monomer under non-reducing conditions and directly by the sedimentation velocity analysis discussed below.

3.2. Coiled Coil B7-H6 Binds NKp30 Receptor with an Undisturbed Affinity

To verify that the addition of the coiled coil sequence to B7-H6 did not alter the binding affinity towards its cognate receptor NKp30, we performed control isothermal titration calorimetry (ITC) measurements. We determined the binding parameters of the wild-type B7-H6 to NKp30 first (Figure 2a). The obtained parameters (K_D = 668 nM, ΔH = −11.5 kcal/mol, ΔS = −10.4 cal/mol·K, N = 0.88) did not differ significantly from previously published data [36,37,71]. Next, we performed ITC titration for B7-H6CC (Figure 2b). The observed thermodynamic parameters (K_D = 787 nM, ΔH = −11.2 kcal/mol, ΔS = −9.6 cal/mol·K, N = 0.74) match reasonably well those of the wild-type B7-H6.

Similarly, we performed ITC measurements with the high-affinity B7-H6 variant containing mutations S60Y, F82W, L129Y (haB7-H6) (Figure 2c,d), which according to a previous publication, significantly increased the affinity for NKp30 [71]. The authors of this study used biolayer interferometry (BLI) to determine the thermodynamic parameters. As the reference interacting pair for evaluating the affinity-matured IgV domain variants of B7-H6, they used wild-type IgV domain bound to the humanized Fab of cetuximab in an effector-silenced IgG1 SEED backbone. The measured K_D was then 409 nM, which is in reasonably good agreement with our ITC measurements. On the other hand, the affinity values of haB7-H6 differ significantly in our measurements. Compared to the published value of 9.06 nM for affinity-matured B7-H6, we observed more than ten times weaker affinity for haB7-H6, i.e., 115 nM, and for haB7-H6CC even more, 259 nM. The discrepancy in the measured values could be because, in the mentioned publication, the affinity-matured B7-H6 domain is bound not to the natural IgC domain, but to the humanized Fab of cetuximab. Even minor changes in the haB7-H6 IgV domain backbone could affect the binding site for NKp30, and thus the two systems are not directly comparable.

At the same time, however, it is worth noting that BLI is a technique that measures the interaction on the surface, similar to surface plasmon resonance (SPR), which has been previously shown to be impractical for measuring binding partners that may oligomerize [37], as the apparent increase in affinity may be due to avidity contribution of oligomers. In this case, NKp30 can oligomerize when glycosylated [37] and if the C-terminal stalk domain is present [81]. However, the BLI in the aforementioned publication was measured with the soluble extracellular part of NKp30 (L19-T138), which contained a non-negligible part of the stalk domain (ten from the total of fifteen amino acids). Considering that there is no available study that would characterize the oligomeric state of the NKp30 variants with truncated stalk domain, we cannot dismiss the possibility that the contribution of avidity biased the measured BLI values.
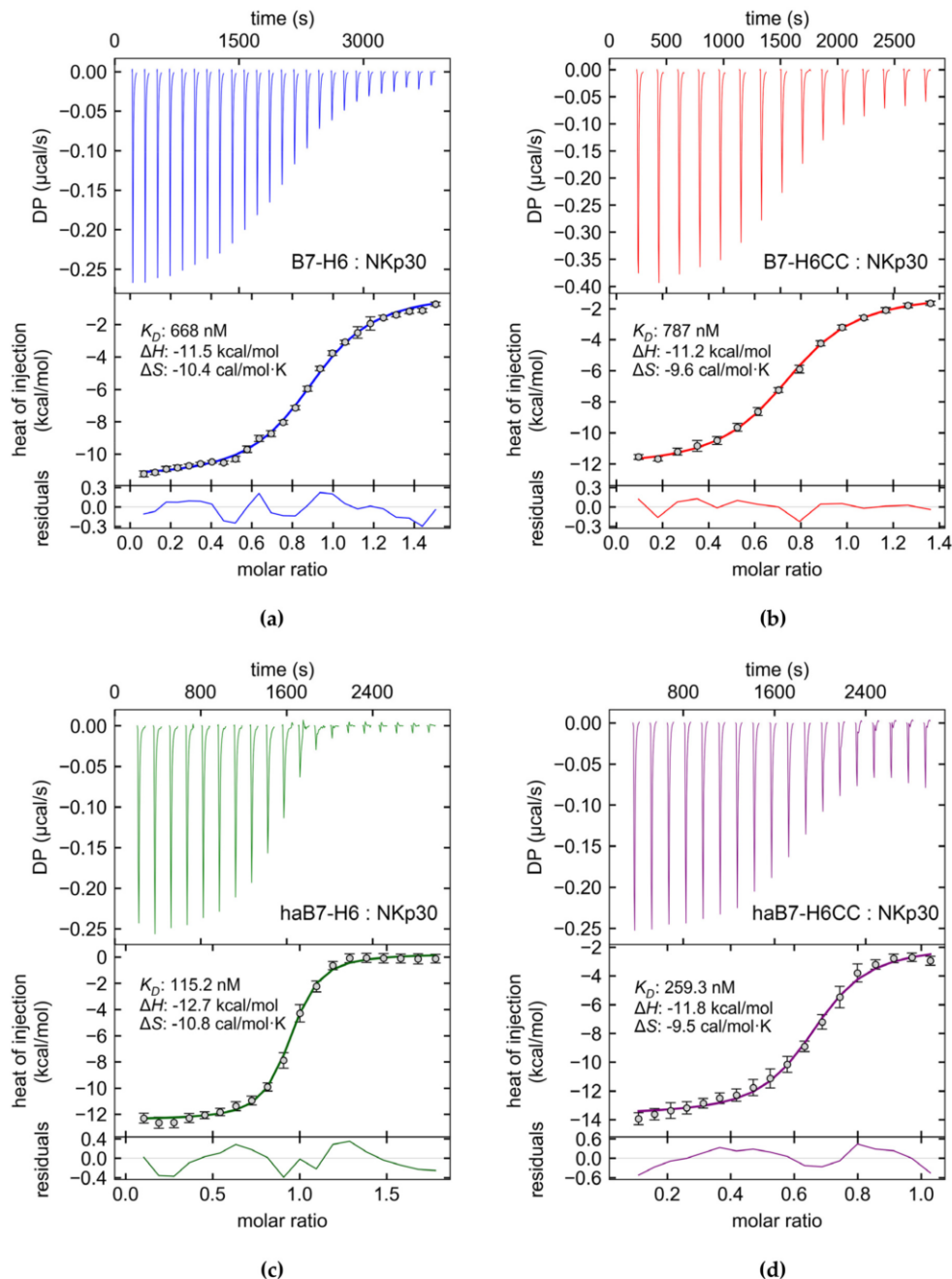
Figure 2. Wild-type and coiled coil B7-H6 proteins bind NKp30 receptor with comparable affinity. The binding of (**a**) wild-type B7-H6 or (**b**) its coiled coil variant to the NKp30 receptor was compared by isothermal titration calorimetry, confirming that adding the coiled coil sequence to the C-terminus of B7-H6 does not substantially alter its binding properties in solution. Next, haB7-H6 (**c**) and haB7-H6CC (**d**) high-affinity B7-H6 constructs were analyzed to assess whether the previously reported mutations indeed increase the affinity. For haB7-H6, the affinity was almost six-fold higher compared to wild-type B7-H6, but more than ten times lower than published previously for the affinity-matured B7-H6 IgG1 SEED fusion constructs [71]. Similarly to B7-H6CC, we observed lower stoichiometry and affinity values for the haB7-H6CC than for the untagged haB7-H6.

The thermodynamic parameters measured for the two high-affinity B7-H6 variants interacting with NKp30 in our ITC analysis were K_D = 115 nM, ΔH = −12.7 kcal/mol,

$\Delta S = -10.8$ cal/mol·K, N = 0.91 for the haB7-H6, and $K_D = 259$ nM, $\Delta H = -11.8$ kcal/mol, $\Delta S = -9.5$ cal/mol·K, N = 0.65 for the haB7-H6CC. Noteworthy is the difference in measured stoichiometry for the coiled coil modified variants relative to B7-H6 lacking the coiled coil tag. This shift in stoichiometry might be caused by dimer formation mediated by the coiled coil sequence, as observed previously [64,82] and also confirmed within this study by analytical ultracentrifugation (AUC) analysis (Figure 3a, following page). It is possible that dimerization of B7-H6 partially sterically hinders the access of NKp30 to the binding site on the second B7-H6 unit in the dimer. Such steric barrier would affect the association and dissociation (k_{on}/k_{off}) of NKp30:B7-H6CC complex, thus explaining lower affinities observed for the B7-H6 coiled coil constructs compared to the untagged proteins.

3.3. B7-H6CC Binds to the Polymer-Peptide Conjugate

To analyze the hydrodynamic behavior of B7-H6CC as well as its interaction with the pHPMA polymer modified with the complementary (VAALEKE)$_4$ coiled coil peptide (PolCC), we employed sedimentation velocity analysis in an analytical ultracentrifuge (SV-AUC). The B7-H6CC protein alone showed two significant peaks in its sedimentation coefficient distribution (Figure 3a, purple curve) with $s_{20,w}$ values of 2.88 S and 4.17 S corresponding to B7-H6CC monomer and dimer, respectively. The peaks are not resolved well in the distribution, which is typical for a monomer-dimer equilibrium. Wild-type B7-H6 is a monomer in solution [37]; thus, we may attribute the dimer formation to the presence of the coiled coil tag. As mentioned above, we observed a similar effect of the (VAALKEK)$_4$ coiled coil tag before in the case of the scFvCC fragment of the mAb M75 [64]. The fitted ratio of the frictional coefficients f/f_0 of 1.6 corresponds to an elongated particle, suggesting the antiparallel orientation of peptides in the coiled coil dimer.

Next, we analyzed the hydrodynamic states of B7-H6CC with respect to receptor binding. To this end, we titrated B7-H6CC with the soluble ligand-binding domain of the NKp30 receptor and analyzed if the interaction affects the oligomeric state of B7-H6CC or vice versa. As shown in Figure 3a, both monomeric and dimeric B7-H6CC binds NKp30, and this interaction does not disrupt the coiled coil homodimer. Figure 3b shows weight-average S values for the whole sedimentation coefficient distributions plotted against the NKp30 receptor concentration (sw isotherm). The maximum of this curve corresponds to the maximal complex formation observed at 16 μM NKp30 concentration, thus confirming the expected 1:1 overall stoichiometry of this protein-protein interaction. The data could be fitted with the A + B <=> AB binding model, keeping the known values of B7-H6CC and NKp30 sedimentation and extinction coefficients constant while fitting the affinity and sed. coefficient of the resultant complex. In this way, we obtained an average 4.88 S value for the complex and a K_D value of 895 nM (N = 0.78), matching reasonably well the ITC results described above (Figure 2b).
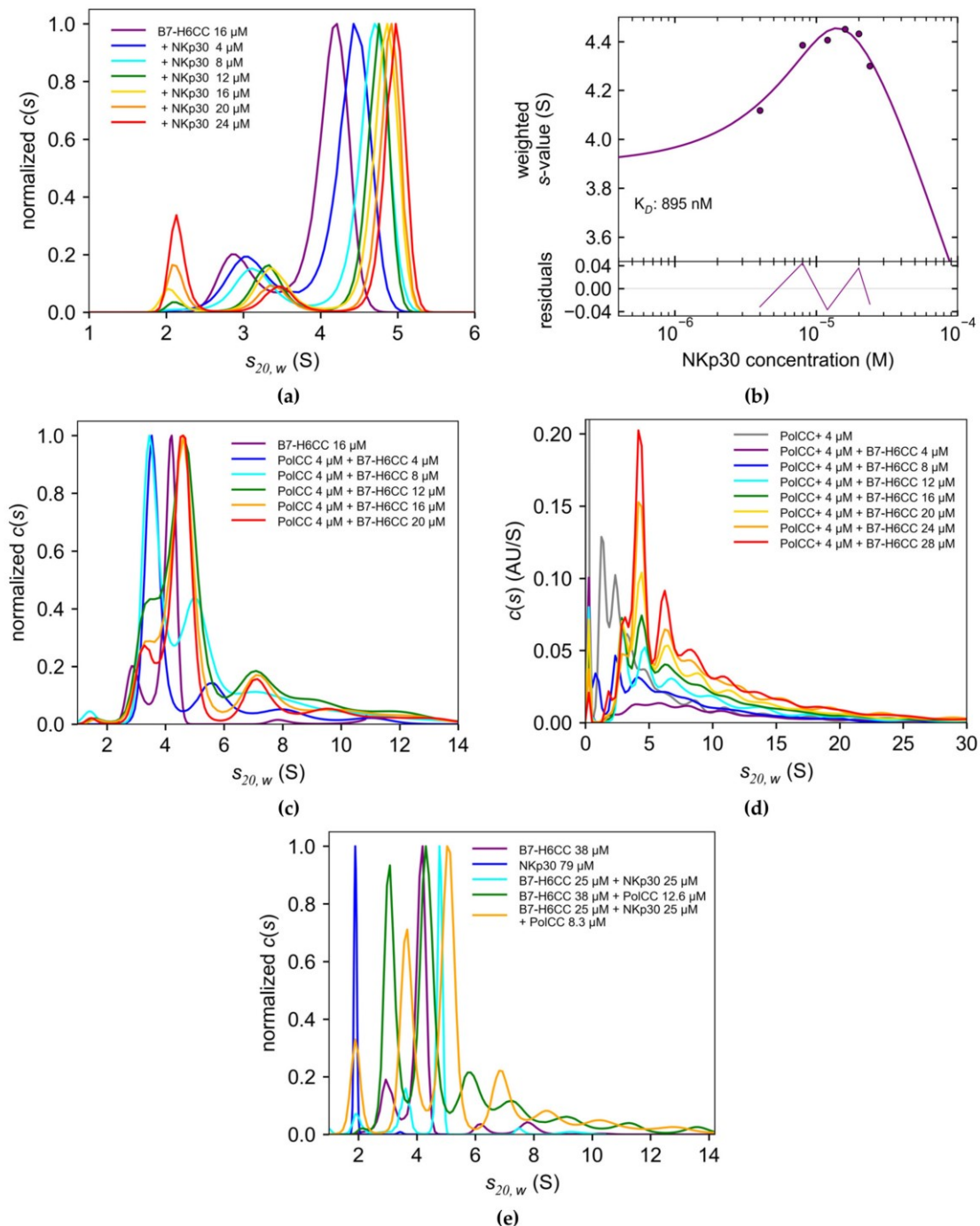
Figure 3. B7-H6CC binds both to the coiled coil peptide-polymer conjugate and to the receptor NKp30. (**a**) Sedimentation velocity analytical ultracentrifugation analysis of B7-H6CC titration with NKp30 shows that both monomeric and dimeric B7-H6CC bind NKp30; (**b**) Binding isotherm from (**a**) fitted with A + B <=> AB binding model; (**c**) PolCC titration with B7-H6CC shows successful hetero-association of the coiled coil peptide pair leading to polyvalent polymer–protein complexes; (**d**) PolCC+ titration with B7-H6CC shows a significantly larger proportion of PolCC+:B7-H6CC polymer–protein complexes with higher stoichiometries than observed for PolCC in (**c**). (**e**) NKp30 receptor binds both to the free and polymer-bound forms of B7-H6CC.

As shown previously, the (VAALKEK)$_4$ coiled coil homodimer is relatively weak and is easily disrupted in the presence of the complementary (VAALEKE)$_4$ peptide bearing opposite charges [64]; therefore, it should not represent any hurdle in the intended use of the B7-H6CC protein. To test if this is also true for B7-H6CC, we mixed PolCC with an increasing molar excess of B7-H6CC and analyzed the resulting polymer–protein complexes (Figure 3c). The equimolar mixture showed a complete absence of the B7-H6CC homodimer (Figure 3c, compare the purple and blue curve), confirming the preferred hetero-association of the used coiled coil peptide pair. Upon increase of the molar ratio between the polymer and the protein, the observed distributions shift from a 1:1 (3.5 S species) to higher stoichiometries, mostly 1:2 (4.5 S), 1:3 (5.6 S), and 1:4 (7.2 S) and only limited number of even larger polymer–protein complexes.

Considering that there are on average eight (VAALEKE)$_4$ peptides per PolCC conjugate, these results show that not all these peptides are accessible for B7-H6CC binding. To improve this and create genuinely multivalent polymer–protein complexes, we synthesized a new version of the coiled coil peptide-polymer conjugate (for details, see Supplementary Materials). This novel conjugate, PolCC+, has a similar number of (VAALEKE)$_4$ peptides per polymer chain; however, the length of the pHPMA polymer backbone was increased more than twofold, resulting in a lower density of the (VAALEKE)$_4$ peptides on the polymer chain and thus potentially fewer sterical clashes between the neighboring bound B7-H6CC molecules. When titrated with B7-H6CC and analyzed by SV-AUC, the new PolCC+ conjugate indeed displayed a considerably higher proportion of larger polymer–protein complexes (Figure 3d).

Finally, we analyzed the interaction of the NKp30 receptor with B7-H6CC when bound to the PolCC (Figure 3e). We prepared the polymer–protein complexes in a 1:3 molar ratio and analyzed them in the presence or absence of NKp30, equimolar to the B7-H6CC. Comparison of the resultant sedimentation coefficient distribution curves clearly shows a significant shift of the observed S values when NKp30 was added, relative to both B7-H6CC:PolCC only (green vs. orange curve) and B7-H6CC:NKp30 only (cyan vs. orange curve). This shift proves the simultaneous complex formation between PolCC, B7-H6CC, and NKp30. Furthermore, NKp30 binds to all species present in the PolCC:B7-H6CC mixture, thus confirming the potential for receptor clustering induced by interaction with such polyvalent polymer–ligand complexes.

3.4. B7-H6CC and B7-H6CC:PolCC Complexes Activate NK Cells

The biological activity of the prepared haB7-H6 and haB7-H6CC proteins was tested in the NK cell degranulation assay. Recombinant proteins were immobilized on the Ni^{2+} chelate-coated plates and incubated with human NK cells isolated from the blood samples of healthy donors. Activation was analyzed by flow cytometry, detecting CD107a on the NK cell surface as a degranulation marker (Figure 4). Statistical analysis of the data is given in Supplementary Materials (Supplementary Figure S1).

After isolation, NK cells were pre-activated by overnight cultivation in the presence of 160 ng/mL IL-2. Recombinant proteins were attached via their polyhistidine tag to the well's surface in different concentrations, resulting in various activating conditions. The total amount of the protein varied from 0.04 up to 50 pmol, which were chosen as sub-saturating and over-saturating, respectively, according to the manufacturer´s declaration of the wells' binding capacity. The excess of the protein was washed away with PBS, so unbound NK cell-activating ligand B7-H6 could not block NK cell activation, as described for soluble B7-H6 escaping in the blood circulation due to its proteolytic shedding from the surface of tumor cells [83].

In the first experiment, we tested multiple concentrations of B7-H6 and B7-H6CC in the presence or absence of the coiled coil peptide-polymer conjugate (Figure 4a). In the second experiment, we compared a limited dilution series of B7-H6CC and its high-affinity variant haB7-H6CC to compare the capacity of both proteins to induce NK cell degranulation (Figure 4b).
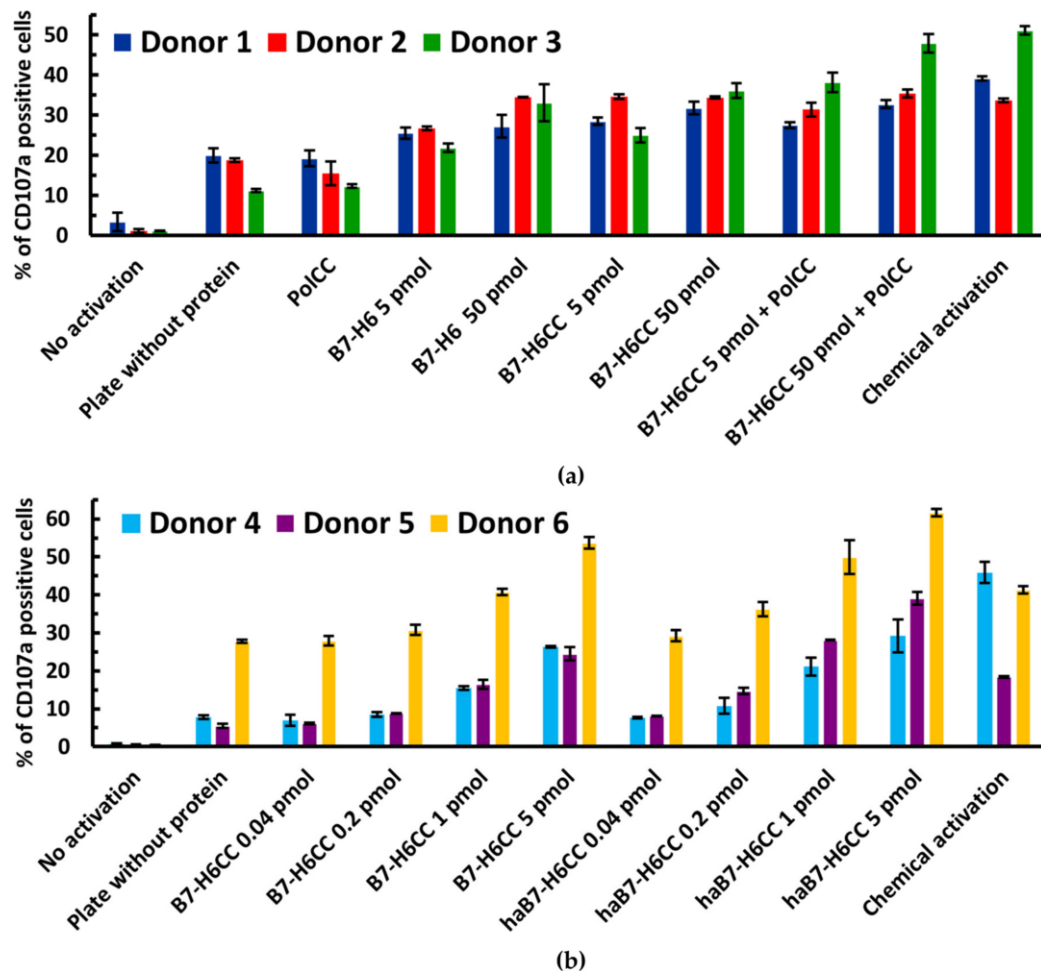
Figure 4. Both B7-H6 and B7-H6CC activate NK cells in the plate activation assay. (**a**) NK cells were incubated in various conditions with B7-H6, B7-H6CC, and polymer–protein complexes and in the control conditions. (**b**) Comparison between activation potential of B7-H6CC and haB7-H6CC proteins. Activation of NK cells was assessed with flow cytometry as the surface expression of CD107a molecule, an NK cell degranulation marker.

As presented in Figure 4a, the biological activity of B7-H6CC does not significantly differ ($p < 0.05$) from the activity of non-modified B7-H6 or is even higher. Moreover, the biological activity of the B7-H6CC is not disturbed when bound to the PolCC. We may also conclude that the (VAALKEK)$_4$ peptide linker does not interfere with the B7-H6 binding to NKp30, both in solution and on the NK cell surface, and thus is suitable for attachment of the protein to the pHPMA coiled coil peptide-polymer conjugate. Next, we compared the NK cell-activating potential of B7-H6CC with its haB7-H6CC high-affinity version (Figure 4b). The appropriate concentration range to observe the differences was assessed by dilution from 5 pmol to the lower values (1, 0.2, 0.04 pmol), as the differences were better distinguishable in under-saturated conditions. Significant differences ($p < 0.05$) were observed in conditions with 1 or 0.2 pmol of added protein where haB7-H6CC exhibited higher biological activity than B7-H6CC. In this study, we observed significant differences between the response capability of NK cells from different donors. Thus, the NK cell activation level (expressed as a percentage of CD107a positive cells upon stimulation) was always compared only for the single given donor. Data are presented for each donor separately; global trends of donor-averaged data are presented in Supplementary Figure S2

for illustration only. The variation might correlate with the current state of health or intrinsic differences between the donors.

3.5. Polymer–Protein Complexes Bind to the Target Tumor Cell Line

To analyze if the prepared polymer–protein complexes could be targeted to a cancer cell line, we used the previously described scFvCC fragment of the M75 mAb recognizing the carbonic anhydrase IX tumor marker (CAIX) [64]. As CAIX expression is regulated by hypoxia-inducible factor-1 (HIF-1), the amount of gene transcript correlates with the oxygen supply; thus, routinely used cancer cell lines such as HeLa or A549 cultivated in normoxia exhibit no or very low expression levels of CAIX [84,85]. Therefore we used colorectal carcinoma cell line HT-29, CAIX-positive in normoxic conditions, and C33 cell line transfected with the CAIX gene (C33_CAIX) and a control C33 line transfected with the same vector carrying only the same resistance gene (C33_Neo) [68]. Cells were cultivated at normal oxygen levels. The expression of CAIX was verified with M75 antibody resulting in CAIX-high cells (C33_CAIX), CAIX-medium cells (HT-29), and CAIX-low cells (CAIX_Neo) (Figure 5a).
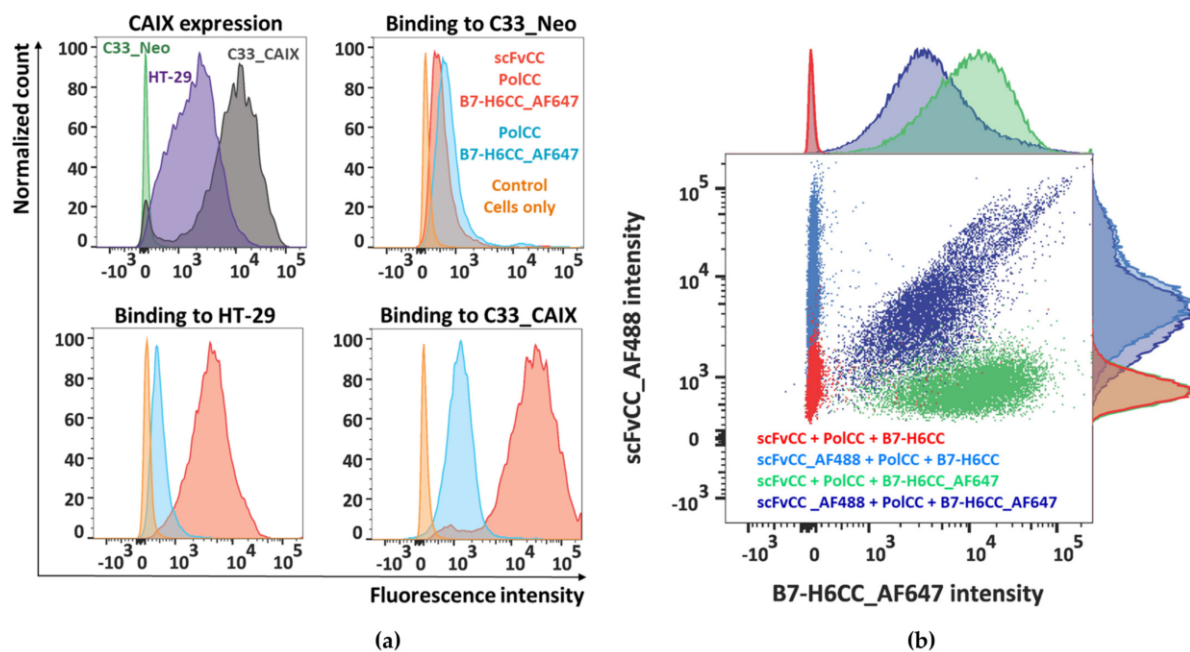

Figure 5. Binding of the polymer–protein complexes to the surface of cell lines with different levels of CAIX expression. (**a**) Cells were first characterized for the CAIX expression levels by M75 mAb (first histogram), then HT-29, C33_Neo, and C33_CAIX cells were stained with polymer–protein complexes (scFvCC + PolCC + B7-H6CC, in red), or with control complexes lacking the targeting scFvCC (PolCC + B7-H6CC, in blue), or were analyzed unstained (in orange). (**b**) HT-29 cells were stained with polymer–protein complexes always containing both scFvCC and B7-H6CC proteins; additionally, proteins were combined with their fluorescently labeled variants (AlexaFluor488 labeled scFvCC, AlexaFluor647 labeled B7-H6CC) to show the double color labeling and thus binding of complete particles to the cell surface.

PolCC was mixed with either B7-H6CC alone or with both B7-H6CC and scFvCC at a 1:1 molar ratio simultaneously, and binding of polymer–protein complexes to the CAIX-expressing cell lines was assessed by flow cytometry with direct detection by using an AlexaFluor647-labeled B7-H6CC. As seen from the histogram comparison in Figure 5a, scFvCC:PolCC:B7-H6CC binds specifically on the HT-29 and C33_CAIX cell surface while PolCC:B7-H6CC, lacking the CAIX-targeting scFvCC moiety, shows only a low background signal. The signal intensity of scFvCC:PolCC:B7-H6CC-labeled cells correlates with CAIX expression levels, and in the case of the C33_Neo cell line, only the background signal was

observed. This analysis confirms that both coiled coil modified proteins, scFvCC and B7-H6CC, are bound to the complementary coiled coil peptide-polymer conjugate simultaneously.

To directly visualize the simultaneous presence of B7-H6CC and scFvCC on the coiled coil peptide-polymer conjugate, both proteins were fluorescently labeled, scFvCC with AlexaFluor488, and already used B7-H6CC with AlexaFluor647. HT-29 cells were decorated with polymer–protein complexes that always contained the targeting and activating moiety, but different combinations of labeled and non-modified protein variants (Figure 5b). This staining resulted in non-stained cells defining experimental background (Figure 5b, in red); single stained cells in the blue channel, when only scFv_AF488 was detectable (Figure 5b, in light blue); single stained cells in the red channel, when by contrast only B7-H6CC_AF647 was detectable; and finally, the cells labeled in both channels proving that the polymer carries both proteins (Figure 5b, in dark blue).

A minor population of the cells labeled with both colors (using scFv_AF488 + PolCC + B7-H6CC_AF647) and having the signal positive only in the red channel for B7-H6_AF647 could be seen as well. These cells are most likely still labeled with complete polymer–protein complexes, which, however, contain residual unstained scFvCC remaining in the NHS-labelling mixture.

To conclude the binding experiments, scFvCC derived from M75 antibody and modified with (VAALKEK)$_4$ coiled coil sequence could be bound to the complementary coiled coil peptide-polymer conjugate. Moreover, it can also target this carrier to the cell surface and bring to the membrane proximity the carrier cargo. Such cargo was in this study NK cell-activating ligand B7-H6, also modified with (VAALKEK)$_4$ coiled coil sequence, with undisturbed biological activity to trigger the degranulation of NK cells. These properties make the coiled coil peptide-polymer conjugate suitable for delivering bispecific immunoactive complexes targeting the surface of cancer cells.

4. Conclusions

Biocompatible pHPMA copolymers loaded with bioactive protein compounds are a promising tool for targeted cancer immunotherapy. This study describes that such a bioactive protein, NK cell-activating ligand B7-H6, could be recombinantly expressed with a coiled coil motif for polymer attachment. We have also expressed a variant of B7-H6 with a slightly enhanced affinity towards the receptor NKp30. Finally, we have tested the binding of the polymer bearing both targeting moiety (scFvCC targeting carbonic anhydrase IX, a metabolic marker of cancer cells) and the immunoactive moiety (B7-H6CC activating NK cells) to the surface of the cancer cells. Described polymer–protein complexes could be a versatile tool for targeted anti-cancer therapy, as proteins could be easily exchanged or combined to profit from the synergic effect. However, the best stoichiometry, uniform complexes' composition, and stability must be further investigated before the direct cellular cytotoxicity assays.

Author Contributions: Conceptualization, B.K., V.K., M.P., and O.V.; Methodology, B.K., D.C., J.B., M.P., and O.V.; Validation, B.K., V.K., and O.V.; Formal analysis, B.K., O.S., and O.V.; Investigation, B.K., O.S., D.C., C.A., K.K., J.B., I.S., V.K., M.F., R.P., M.P., and O.V.; Resources, I.S., V.K., M.F., R.P., and M.P.; Writing—original draft preparation, B.K., O.S., M.P., and O.V.; Writing—review and editing, B.K., O.S., D.C., V.K., M.P., and O.V.; Visualization, B.K., O.S., and O.V.; Supervision, J.B., M.F., M.P., and O.V.; Project administration, V.K., M.P., and O.V.; Funding acquisition, D.C. and O.V. All authors have read and agreed to the published version of the manuscript.

Conflicts of Interest: The authors declare no conflict of interest. The funders had no role in the study's design, in the collection, analyses, or interpretation of data, in the writing of the manuscript, or in the decision to publish the results.

References

1. Vesely, M.D.; Kershaw, M.H.; Schreiber, R.D.; Smyth, M.J. Natural Innate and Adaptive Immunity to Cancer. *Annu. Rev. Immunol.* **2011**, *29*, 235–271. [CrossRef]
2. Dunn, G.P.; Bruce, A.T.; Ikeda, H.; Old, L.J.; Schreiber, R.D. Cancer immunoediting: From immunosurveillance to tumor escape. *Nat. Immunol.* **2002**, *3*, 991–998. [CrossRef]
3. Smyth, M.J.; Dunn, G.P.; Schreiber, R.D. Cancer Immunosurveillance and Immunoediting: The Roles of Immunity in Sup-pressing Tumor Development and Shaping Tumor Immunogenicity. *Adv. Immunol.* **2006**, *90*, 1–50. [CrossRef] [PubMed]
4. Aguilar, O.A.; Mesci, A.; Ma, J.; Chen, P.; Kirkham, C.L.; Hundrieser, J.; Voigt, S.; Allan, D.S.; Carlyle, J.R. Modulation of Clr Ligand Expression and NKR-P1 Receptor Function during Murine Cytomegalovirus Infection. *J. Innate Immun.* **2015**, *7*, 584–600. [CrossRef]
5. Chen, D.S.; Mellman, I. Elements of cancer immunity and the cancer-immune set point. *Nature* **2017**, *541*, 321–330. [CrossRef]
6. Zitvogel, L.; Tesniere, A.; Kroemer, G. Cancer despite immunosurveillance: Immunoselection and immunosubversion. *Nat. Rev. Immunol.* **2006**, *6*, 715–727. [CrossRef]
7. Liu, Y.; Cao, X. Immunosuppressive cells in tumor immune escape and metastasis. *J. Mol. Med.* **2015**, *94*, 509–522. [CrossRef]
8. Dunn, G.P.; Old, L.J.; Schreiber, R.D. The Three Es of Cancer Immunoediting. *Annu. Rev. Immunol.* **2004**, *22*, 329–360. [CrossRef]
9. Pascal, V.; Schleinitz, N.; Brunet, C.; Ravet, S.; Bonnet, E.; Lafarge, X.; Touinssi, M.; Reviron, D.; Viallard, J.F.; Moreau, J.F.; et al. Comparative analysis of NK cell subset distribution in normal and lymphoproliferative disease of granular lymphocyte conditions. *Eur. J. Immunol.* **2004**, *34*, 2930–2940. [CrossRef] [PubMed]
10. Bryceson, Y.T.; Björkström, N.K.; Mjösberg, J.; Ljunggren, H. Natural Killer Cells. In *The Autoimmune Diseases*; Elsevier: Amsterdam, The Netherlands, 2020; pp. 229–242.
11. Morvan, M.; Lanier, L.L. NK cells and cancer: You can teach innate cells new tricks. *Nat. Rev. Cancer* **2015**, *16*, 7–19. [CrossRef] [PubMed]
12. Shimasaki, N.; Jain, A.; Campana, D. NK cells for cancer immunotherapy. *Nat. Rev. Drug Discov.* **2020**, *19*, 200–218. [CrossRef]
13. Hu, W.; Wang, G.; Huang, D.; Sui, M.; Xu, Y. Cancer Immunotherapy Based on Natural Killer Cells: Current Progress and New Opportunities. *Front. Immunol.* **2019**, *10*, 1205. [CrossRef]
14. Habif, G.; Crinier, A.; André, P.; Vivier, E.; Narni-Mancinelli, E. Targeting natural killer cells in solid tumors. *Cell. Mol. Immunol.* **2019**, *16*, 415–422. [CrossRef] [PubMed]
15. Farkona, S.; Diamandis, E.P.; Blasutig, I.M. Cancer immunotherapy: The beginning of the end of cancer? *BMC Med.* **2016**, *14*, 73. [CrossRef]
16. Vivier, E.; Ugolini, S.; Blaise, D.; Chabannon, C.; Brossay, L. Targeting natural killer cells and natural killer T cells in cancer. *Nat. Rev. Immunol.* **2012**, *12*, 239–252. [CrossRef]
17. Chauhan, S.K.S.; Koehl, U.; Kloess, S. Harnessing NK Cell Checkpoint-Modulating Immunotherapies. *Cancers* **2020**, *12*, 1807. [CrossRef]
18. Dahlberg, C.I.M.; Sarhan, D.; Chrobok, M.; Duru, A.; Alici, E. Natural Killer Cell-Based Therapies Targeting Cancer: Possible Strategies to Gain and Sustain Anti-Tumor Activity. *Front. Immunol.* **2015**, *6*, 605. [CrossRef]
19. Pfefferle, A.; Huntington, N.D. You Have Got a Fast CAR: Chimeric Antigen Receptor NK Cells in Cancer Therapy. *Cancers* **2020**, *12*, 706. [CrossRef]
20. Liu, E.; Marin, D.; Banerjee, P.; Macapinlac, H.A.; Thompson, P.; Basar, R.; Kerbauy, L.N.; Overman, B.; Thall, P.; Kaplan, M.; et al. Use of CAR-Transduced Natural Killer Cells in CD19-Positive Lymphoid Tumors. *N. Engl. J. Med.* **2020**, *382*, 545–553. [CrossRef] [PubMed]

21.   Nigro, C.L.; Macagno, M.; Sangiolo, D.; Bertolaccini, L.; Aglietta, M.; Merlano, M.C. NK-mediated antibody-dependent cell-mediated cytotoxicity in solid tumors: Biological evidence and clinical perspectives. *Ann. Transl. Med.* **2019**, *7*, 105. [CrossRef] [PubMed]

22.   Tay, S.S.; Carol, H.; Biro, M. TriKEs and BiKEs join CARs on the cancer immunotherapy highway. *Hum. Vaccines Immunother.* **2016**, *12*, 2790–2796. [CrossRef]

23.   Gleason, M.K.; Ross, J.A.; Warlick, E.D.; Lund, T.C.; Verneris, M.R.; Wiernik, A.; Spellman, S.; Haagenson, M.D.; Lenvik, A.J.; Litzow, M.R.; et al. CD16xCD33 bispecific killer cell engager (BiKE) activates NK cells against primary MDS and MDSC CD33+ targets. *Blood* **2014**, *123*, 3016–3026. [CrossRef] [PubMed]

24.   Felices, M.; Lenvik, T.R.; Davis, Z.B.; Miller, J.S.; Vallera, D.A. Generation of BiKEs and TriKEs to Improve NK Cell-Mediated Targeting of Tumor Cells. In *Natural Killer Cells*; Humana Press: New York, NY, USA, 2016; Volume 1441, pp. 333–346. [CrossRef]

25.   Sarhan, D.; Brandt, L.; Felices, M.; Guldevall, K.; Lenvik, T.; Hinderlie, P.; Curtsinger, J.; Warlick, E.; Spellman, S.R.; Blazar, B.R.; et al. 161533 TriKE stimulates NK-cell function to overcome myeloid-derived suppressor cells in MDS. *Blood Adv.* **2018**, *2*, 1459–1469. [CrossRef] [PubMed]

26.   Märklin, M.; Hagelstein, I.; Koerner, S.P.; Rothfelder, K.; Pfluegler, M.S.; Schumacher, A.; Grosse-Hovest, L.; Jung, G.; Salih, H.R. Bispecific NKG2D-CD3 and NKG2D-CD16 fusion proteins for induction of NK and T cell reactivity against acute myeloid leukemia. *J. Immunother. Cancer* **2019**, *7*, 143. [CrossRef]

27.   Han, Y.; Sun, F.; Zhang, X.; Wang, T.; Jiang, J.; Cai, J.; Gao, Q.; Hezam, K.; Liu, Y.; Xie, J.; et al. CD24 targeting bi-specific antibody that simultaneously stimulates NKG2D enhances the efficacy of cancer immunotherapy. *J. Cancer Res. Clin. Oncol.* **2019**, *145*, 1179–1190. [CrossRef] [PubMed]

28.   Chester, C.; Fritsch, K.; Kohrt, H.E. Natural Killer Cell Immunomodulation: Targeting Activating, Inhibitory, and Co-stimulatory Receptor Signaling for Cancer Immunotherapy. *Front. Immunol.* **2015**, *6*, 601. [CrossRef]

29.   Koch, J.; Steinle, A.; Watzl, C.; Mandelboim, O. Activating natural cytotoxicity receptors of natural killer cells in cancer and infection. *Trends Immunol.* **2013**, *34*, 182–191. [CrossRef]

30.   Memmer, S.; Weil, S.; Beyer, S.; Zöller, T.; Peters, E.; Hartmann, J.; Steinle, A.; Koch, J. The Stalk Domain of NKp30 Contributes to Ligand Binding and Signaling of a Preassembled NKp30-CD3ζ Complex. *J. Biol. Chem.* **2016**, *291*, 25427–25438. [CrossRef]

31.   Brandt, C.S.; Baratin, M.; Yi, E.C.; Kennedy, J.; Gao, Z.; Fox, B.; Haldeman, B.; Ostrander, C.D.; Kaifu, T.; Chabannon, C.; et al. The B7 family member B7-H6 is a tumor cell ligand for the activating natural killer cell receptor NKp30 in humans. *J. Exp. Med.* **2009**, *206*, 1495–1503. [CrossRef]

32.   Binici, J.; Koch, J. BAG-6, a jack of all trades in health and disease. *Cell. Mol. Life Sci.* **2013**, *71*, 1829–1837. [CrossRef] [PubMed]

33.   Kruse, P.H.; Matta, J.; Ugolini, S.; Vivier, E. Natural cytotoxicity receptors and their ligands. *Immunol. Cell Biol.* **2013**, *92*, 221–229. [CrossRef]

34.   Wang, W.; Guo, H.; Geng, J.; Zheng, X.; Wei, H.; Sun, R.; Tian, Z. Tumor-released Galectin-3, a Soluble Inhibitory Ligand of Human NKp30, Plays an Important Role in Tumor Escape from NK Cell Attack. *J. Biol. Chem.* **2014**, *289*, 33311–33319. [CrossRef] [PubMed]

35.   Kaifu, T.; Escalière, B.; Gastinel, L.N.; Vivier, E.; Baratin, M. B7-H6/NKp30 interaction: A mechanism of alerting NK cells against tumors. *Cell. Mol. Life Sci.* **2011**, *68*, 3531–3539. [CrossRef]

36.   Li, Y.; Wang, Q.; Mariuzza, R.A. Structure of the human activating natural cytotoxicity receptor NKp30 bound to its tumor cell ligand B7-H6. *J. Exp. Med.* **2011**, *208*, 703–714. [CrossRef]

37.   Skořepa, O.; Pazicky, S.; Kalousková, B.; Bláha, J.; Abreu, C.; Ječmen, T.; Rosůlek, M.; Fish, A.; Sedivy, A.; Harlos, K.; et al. Natural Killer Cell Activation Receptor NKp30 Oligomerization Depends on Its *N*-Glycosylation. *Cancers* **2020**, *12*, 1998. [CrossRef]

38.   Xu, X.; Narni-Mancinelli, E.; Cantoni, C.; Li, Y.; Guia, S.; Gauthier, L.; Chen, Q.; Moretta, A.; Vély, F.; Eisenstein, E.; et al. Structural Insights into the Inhibitory Mechanism of an Antibody against B7-H6, a Stress-Induced Cellular Ligand for the Natural Killer Cell Receptor NKp30. *J. Mol. Biol.* **2016**, *428*, 4457–4466. [CrossRef] [PubMed]

39.   Arnon, T.I.; Markel, G.; Bar-Ilan, A.; Hanna, J.; Fima, E.; Benchetrit, F.; Galili, R.; Cerwenka, A.; Benharroch, D.; Sion-Vardy, N.; et al. Harnessing Soluble NK Cell Killer Receptors for the Generation of Novel Cancer Immune Therapy. *PLoS ONE* **2008**, *3*, e2150. [CrossRef]

40.   Kellner, C.; Maurer, T.; Hallack, D.; Repp, R.; Van De Winkel, J.G.J.; Parren, P.W.H.I.; Valerius, T.; Humpe, A.; Gramatzki, M.; Peipp, M.; et al. Mimicking an Induced Self Phenotype by Coating Lymphomas with the NKp30 Ligand B7-H6 Promotes NK Cell Cytotoxicity. *J. Immunol.* **2012**, *189*, 5037–5046. [CrossRef] [PubMed]

41.   Kellner, C.; Günther, A.; Humpe, A.; Repp, R.; Klausz, K.; Derer, S.; Valerius, T.; Ritgen, M.; Brüggemann, M.; Van De Winkel, J.G.; et al. Enhancing natural killer cell-mediated lysis of lymphoma cells by combining therapeutic antibodies with CD20-specific immunoligands engaging NKG2D or NKp30. *OncoImmunology* **2015**, *5*, e1058459. [CrossRef]

42.   Peipp, M.; Derer, S.; Lohse, S.; Staudinger, M.; Klausz, K.; Valerius, T.; Gramatzki, M.; Kellner, C. HER2-specific immunoligands engaging NKp30 or NKp80 trigger NK-cell-mediated lysis of tumor cells and enhance antibody-dependent cell-mediated cytotoxicity. *Oncotarget* **2015**, *6*, 32075–32088. [CrossRef]

43.   Zhang, T.; Wu, M.-R.; Sentman, C.L. An NKp30-Based Chimeric Antigen Receptor Promotes T Cell Effector Functions and Antitumor Efficacy *In Vivo*. *J. Immunol.* **2012**, *189*, 2290–2299. [CrossRef]

44.   Wu, M.-R.; Zhang, T.; Demars, L.R.; Sentman, C.L. B7H6-specific chimeric antigen receptors lead to tumor elimination and host antitumor immunity. *Gene Ther.* **2015**, *22*, 675–684. [CrossRef] [PubMed]

45. Hua, C.K.; Gacerez, A.T.; Sentman, C.L.; Ackerman, M.E. Development of unique cytotoxic chimeric antigen receptors based on human scFv targeting B7H6. *Protein Eng. Des. Sel.* **2017**, *30*, 713–721. [CrossRef]

46. Vaněk, O.; Nálezková, M.; Kavan, D.; Borovičková, I.; Pompach, P.; Novák, P.; Kumar, V.; Vannucci, L.; Hudeček, J.; Hofbauerová, K.; et al. Soluble recombinant CD69 receptors optimized to have an exceptional physical and chemical stability display prolonged circulation and remain intact in the blood of mice. *FEBS J.* **2008**, *275*, 5589–5606. [CrossRef]

47. Kolenko, P.; Skálová, T.; Vaněk, O.; Štěpánková, A.; Dušková, J.; Hašek, J.; Bezouška, K.; Dohnálek, J. The high-resolution structure of the extracellular domain of human CD69 using a novel polymer. *Acta Crystallogr. Sect. F Struct. Biol. Cryst. Commun.* **2009**, *65*, 1258–1260. [CrossRef]

48. Deming, T.J.; Klok, H.-A.; Armes, S.P.; Becker, M.L.; Champion, J.A.; Chen, E.Y.-X.; Heilshorn, S.C.; van Hest, J.C.M.; Irvine, D.J.; Johnson, J.A.; et al. Polymers at the Interface with Biology. *Biomacromolecules* **2018**, *19*, 3151–3162. [CrossRef]

49. Jo, S.D.; Nam, G.-H.; Kwak, G.; Yang, Y.; Kwon, I.C. Harnessing designed nanoparticles: Current strategies and future perspectives in cancer immunotherapy. *Nano Today* **2017**, *17*, 23–37. [CrossRef]

50. Aikins, M.E.; Xu, C.; Moon, J.J. Engineered Nanoparticles for Cancer Vaccination and Immunotherapy. *Accounts Chem. Res.* **2020**, *53*, 2094–2105. [CrossRef]

51. Thangam, R.; Patel, K.D.; Kang, H.; Paulmurugan, R. Advances in Engineered Polymer Nanoparticle Tracking Platforms towards Cancer Immunotherapy—Current Status and Future Perspectives. *Vaccines* **2021**, *9*, 935. [CrossRef] [PubMed]

52. Janisova, L.; Gruzinov, A.; Zaborova, O.V.; Velychkivska, N.; Vaněk, O.; Chytil, P.; Etrych, T.; Janoušková, O.; Zhang, X.; Blanchet, C.; et al. Molecular Mechanisms of the Interactions of N-(2-Hydroxypropyl)methacrylamide Copolymers Designed for Cancer Therapy with Blood Plasma Proteins. *Pharmaceutics* **2020**, *12*, 106. [CrossRef] [PubMed]

53. Apostolovic, B.; Danial, M.; Klok, H.-A. Coiled coils: Attractive protein folding motifs for the fabrication of self-assembled, responsive and bioactive materials. *Chem. Soc. Rev.* **2010**, *39*, 3541–3575. [CrossRef]

54. Utterström, J.; Naeimipour, S.; Selegård, R.; Aili, D. Coiled coil-based therapeutics and drug delivery systems. *Adv. Drug Deliv. Rev.* **2020**, *170*, 26–43. [CrossRef]

55. Pola, R.; Laga, R.; Ulbrich, K.; Sieglová, I.; Král, V.; Fábry, M.; Kabešová, M.; Kovář, M.; Pechar, M. Polymer Therapeutics with a Coiled Coil Motif Targeted against Murine BCL1 Leukemia. *Biomacromolecules* **2013**, *14*, 881–889. [CrossRef]

56. Wu, K.; Liu, J.; Johnson, R.N.; Yang, J.; Kopeček, J. Drug-Free Macromolecular Therapeutics: Induction of Apoptosis by Coiled-Coil-Mediated Cross-Linking of Antigens on the Cell Surface. *Angew. Chem. Int. Ed.* **2010**, *49*, 1451–1455. [CrossRef]

57. Wu, K.; Yang, J.; Liu, J.; Kopeček, J. Coiled-coil based drug-free macromolecular therapeutics: *In vivo* efficacy. *J. Control. Release* **2012**, *157*, 126–131. [CrossRef]

58. Chu, T.-W.; Yang, J.; Zhang, R.; Sima, M.; Kopeček, J. Cell Surface Self-Assembly of Hybrid Nanoconjugates via Oligonucleotide Hybridization Induces Apoptosis. *ACS Nano* **2014**, *8*, 719–730. [CrossRef] [PubMed]

59. Chu, T.-W.; Zhang, R.; Yang, J.; Chao, M.P.; Shami, P.J.; Kopeček, J. A Two-Step Pretargeted Nanotherapy for CD20 Cross-linking May Achieve Superior Anti-Lymphoma Efficacy to Rituximab. *Theranostics* **2015**, *5*, 834–846. [CrossRef] [PubMed]

60. Zhang, L.; Fang, Y.; Yang, J.; Kopeček, J. Drug-free macromolecular therapeutics: Impact of structure on induction of apoptosis in Raji B cells. *J. Control. Release* **2017**, *263*, 139–150. [CrossRef]

61. Zhang, L.; Fang, Y.; Li, L.; Yang, J.; Radford, D.C.; Kopeček, J. Human Serum Albumin-Based Drug-Free Macromolecular Therapeutics: Apoptosis Induction by Coiled-Coil-Mediated Cross-Linking of CD20 Antigens on Lymphoma B Cell Surface. *Macromol. Biosci.* **2018**, *18*, e1800224. [CrossRef] [PubMed]

62. Gambles, M.T.; Li, J.; Wang, J.; Sborov, D.; Yang, J.; Kopeček, J. Crosslinking of CD38 Receptors Triggers Apoptosis of Malignant B Cells. *Molecules* **2021**, *26*, 4658. [CrossRef]

63. Pastorekova, S.; Gillies, R.J. The role of carbonic anhydrase IX in cancer development: Links to hypoxia, acidosis, and beyond. *Cancer Metastasis Rev.* **2019**, *38*, 65–77. [CrossRef] [PubMed]

64. Pechar, M.; Pola, R.; Laga, R.; Ulbrich, K.; Bednárová, L.; Maloň, P.; Sieglová, I.; Král, V.; Fábry, M.; Vaněk, O. Coiled Coil Peptides as Universal Linkers for the Attachment of Recombinant Proteins to Polymer Therapeutics. *Biomacromolecules* **2011**, *12*, 3645–3655. [CrossRef]

65. Kissel, M.; Peschke, P.; Šubr, V.; Ulbrich, K.; Strunz, A.M.; Kühnlein, R.; Debus, J.; Friedrich, E. Detection and cellular localisation of the synthetic soluble macromolecular drug carrier pHPMA. *Eur. J. Nucl. Med. Mol. Imaging* **2002**, *29*, 1055–1062. [CrossRef]

66. Aricescu, A.R.; Lu, W.; Jones, E.Y. A time- and cost-efficient system for high-level protein production in mammalian cells. *Acta Crystallogr. Sect. D Biol. Crystallogr.* **2006**, *62*, 1243–1250. [CrossRef] [PubMed]

67. Vaněk, O.; Celadova, P.; Skořepa, O.; Bláha, J.; Kalousková, B.; Dvorská, A.; Poláchová, E.; Pucholtová, H.; Kavan, D.; Pompach, P.; et al. Production of recombinant soluble dimeric C-type lectin-like receptors of rat natural killer cells. *Sci. Rep.* **2019**, *9*, 17836. [CrossRef]

68. Csaderova, L.; Debreova, M.; Radvak, P.; Stano, M.; Vrestiakova, M.; Kopacek, J.; Pastorekova, S.; Svastova, E. The effect of carbonic anhydrase IX on focal contacts during cell spreading and migration. *Front. Physiol.* **2013**, *4*, 271. [CrossRef]

69. Bláha, J.; Pachl, P.; Novák, P.; Vaněk, O. Expression and purification of soluble and stable ectodomain of natural killer cell receptor LLT1 through high-density transfection of suspension adapted HEK293S GnTI⁻ cells. *Protein Expr. Purif.* **2015**, *109*, 7–13. [CrossRef] [PubMed]

70. Durocher, Y. High-level and high-throughput recombinant protein production by transient transfection of suspension-growing human 293-EBNA1 cells. *Nucleic Acids Res.* **2002**, *30*, E9. [CrossRef] [PubMed]

71. Pekar, L.; Klausz, K.; Busch, M.; Valldorf, B.; Kolmar, H.; Wesch, D.; Oberg, H.-H.; Krohn, S.; Boje, A.S.; Gehlert, C.L.; et al. Affinity Maturation of B7-H6 Translates into Enhanced NK Cell–Mediated Tumor Cell Lysis and Improved Proinflammatory Cytokine Release of Bispecific Immunoligands via NKp30 Engagement. *J. Immunol.* **2020**, *206*, 225–236. [CrossRef]

72. Scheuermann, T.H.; Brautigam, C.A. High-precision, automated integration of multiple isothermal titration calorimetric thermograms: New features of NITPIC. *Methods* **2014**, *76*, 87–98. [CrossRef] [PubMed]

73. Zhao, H.; Piszczek, G.; Schuck, P. SEDPHAT—A platform for global ITC analysis and global multi-method analysis of molecular interactions. *Methods* **2015**, *76*, 137–148. [CrossRef]

74. Brautigam, C.A. Calculations and Publication-Quality Illustrations for Analytical Ultracentrifugation Data. *Methods Enzym.* **2015**, *562*, 109–133. [CrossRef]

75. Rozbeský, D.; Kavan, D.; Chmelík, J.; Novák, P.; Vaněk, O.; Bezouška, K. High-level expression of soluble form of mouse natural killer cell receptor NKR-P1C(B6) in *Escherichia coli*. *Protein Expr. Purif.* **2011**, *77*, 178–184. [CrossRef] [PubMed]

76. Schuck, P. Size-Distribution Analysis of Macromolecules by Sedimentation Velocity Ultracentrifugation and Lamm Equation Modeling. *Biophys. J.* **2000**, *78*, 1606–1619. [CrossRef]

77. Skálová, T.; Kotýnková, K.; Dušková, J.; Hašek, J.; Koval', T.; Kolenko, P.; Novák, P.; Man, P.; Hanč, P.; Vaněk, O.; et al. Mouse Clr-g, a Ligand for NK Cell Activation Receptor NKR-P1F: Crystal Structure and Biophysical Properties. *J. Immunol.* **2012**, *189*, 4881–4889. [CrossRef] [PubMed]

78. Skálová, T.; Bláha, J.; Harlos, K.; Dušková, J.; Koval', T.; Stránský, J.; Hašek, J.; Vaněk, O.; Dohnálek, J. Four crystal structures of human LLT1, a ligand of human NKR-P1, in varied glycosylation and oligomerization states. *Acta Crystallogr. Sect. D Biol. Crystallogr.* **2015**, *71*, 578–591. [CrossRef]

79. Joyce, M.G.; Tran, P.; Zhuravleva, M.A.; Jaw, J.; Colonna, M.; Sun, P.D. Crystal structure of human natural cytotoxicity receptor NKp30 and identification of its ligand binding site. *Proc. Natl. Acad. Sci. USA* **2011**, *108*, 6223–6228. [CrossRef]

80. Bláha, J.; Kalousková, B.; Skořepa, O.; Pažický, S.; Novák, P.; Vaněk, O. High-level expression and purification of soluble form of human natural killer cell receptor NKR-P1 in HEK293S GnTI⁻ Cells. *Protein Expr. Purif.* **2017**, *140*, 36–43. [CrossRef]

81. Herrmann, J.; Berberich, H.; Hartmann, J.; Beyer, S.; Davies, K.; Koch, J. Homo-oligomerization of the Activating Natural Killer Cell Receptor NKp30 Ectodomain Increases Its Binding Affinity for Cellular Ligands. *J. Biol. Chem.* **2014**, *289*, 765–777. [CrossRef]

82. Pechar, M.; Pola, R.; Laga, R.; Braunova, A.; Filippov, S.K.; Bogomolova, A.; Bednarova, L.; Vanek, O.; Ulbrich, K. Coiled coil peptides and polymer-peptide conjugates: Synthesis, self-assembly, characterization and potential in drug delivery systems. *Biomacromolecules* **2014**, *15*, 2590–2599. [CrossRef]

83. Matta, J.; Baratin, M.; Chiche, L.; Forel, J.M.; Cognet, C.; Thomas, G.; Farnarier, C.; Piperoglou, C.; Papazian, L.; Chaussabel, D.; et al. Induction of B7-H6, a ligand for the natural killer cell-activating receptor NKp30, in inflammatory conditions. *Blood* **2013**, *122*, 394–404. [CrossRef] [PubMed]

84. Wykoff, C.C.; Beasley, N.J.; Watson, P.; Turner, K.J.; Pastorek, J.; Sibtain, A.; Wilson, G.; Turley, H.; Talks, K.L.; Maxwell, P.; et al. Hypoxia-inducible expression of tumor-associated carbonic anhydrases. *Cancer Res.* **2000**, *60*, 7075–7083. [PubMed]

85. Sowa, T.; Menju, T.; Chen-Yoshikawa, T.F.; Takahashi, K.; Nishikawa, S.; Nakanishi, T.; Shikuma, K.; Motoyama, H.; Hijiya, K.; Aoyama, A.; et al. Hypoxia-inducible factor 1 promotes chemoresistance of lung cancer by inducing carbonic anhydrase IX expression. *Cancer Med.* **2016**, *6*, 288–297. [CrossRef] [PubMed]

86. Ulbrich, K.; Šubr, V.; Strohalm, J.; Plocová, D.; Jelínková, M.; Říhová, B. Polymeric Drugs Based on Conjugates of Synthetic and Natural Macromolecules. I. Synthesis and Physico-Chemical Characterisation. *J. Control. Release* **2000**, *64*, 63–79. [CrossRef]

87. Pola, R.; Král, V.; Filippov, S.K.; Kaberov, L.; Etrych, T.; Sieglová, I.; Sedláček, J.; Fábry, M.; Pechar, M. Polymer Cancerostatics Targeted by Recombinant Antibody Fragments to Gd2-Positive Tumor Cells. *Biomacromolecules* **2019**, *20*, 412–421. [CrossRef]

88. Perrier, S.; Takolpuckdee, P.; Westwood, J.; Lewis, D.M. Versatile Chain Transfer Agents for Reversible Addition Fragmentation Chain Transfer (RAFT) Polymerization to Synthesize Functional Polymeric Architectures. *Macromolecules* **2004**, *37*, 2709–2717. [CrossRef]

89. Green, N.M. A Spectrophotometric Assay for Avidin and Biotin Based on Binding of Dyes by Avidin. *Biochem. J.* **1965**, *94*, 23C–24C. [CrossRef]

90. Wood, C.W.; Woolfson, D.N. CCBuilder 2.0: Powerful and accessible coiled-coil modeling. *Protein Sci.* **2018**, *27*, 103–111. [CrossRef]

8   LIST OF PUBLICATIONS

1. Bláha, J.; **Kalousková, B.**; Skořepa, O.; Pažický, S.; Novák, P.; Vaněk, O. High-level expression and purification of soluble form of human natural killer cell receptor NKR-P1 in HEK293S GnTI⁻ cells. *Protein Expr. Purif.* **2017**, *140*, 36–43.

2. Sumová, P.; Šíma, M.; **Kalousková, B.**; Polanská, N.; Vaněk, O.; Oliveira, F.; Valenzuela, J. G.; Volf, P. Amine-binding properties of salivary yellow-related proteins in phlebotomine sand flies. *Insect Biochem. Mol. Biol.* **2019**, *115*, 103245.

3. Willen, L.; Leštinová, T.; **Kalousková, B.**; Sumová, P.; Spitzová, T.; Velez, R.; Domenech, E.; Vaněk, O.; Gállego, M.; Mertens, P.; Volf, P. Field study of the improved rapid sand fly exposure test in areas endemic for canine leishmaniasis. *PLoS Negl. Trop. Dis.* **2019**, *13*, e0007832.

4. Vaněk, O.; Celadová, P.; Skořepa, O.; Bláha, J.; **Kalousková, B.**; Dvorská, A.; Poláchová, E.; Pucholtová, H.; Kavan, D.; Pompach, P.; Hofbauerová, K.; Kopecký, V. Jr.; Mesci, A.; Voigt, S.; Carlyle, J. R. Production of recombinant soluble dimeric C-type lectin-like receptors of rat natural killer cells. *Sci. Rep.* **2019**, *9*, 17836.

5. Skořepa, O.; Pažický, S.; **Kalousková, B.**; Bláha, J.; Abreu, C.; Ječmen, T.; Rosůlek, M.; Fish, A.; Sedivy, A.; Harlos, K.; Dohnálek, J.; Skálová, T.; Vaněk, O. Natural Killer Cell Activation Receptor NKp30 Oligomerization Depends on Its N-Glycosylation. *Cancers* **2020**, *12*, 1998.

6. Sumová, P.; Polanská, N.; Leštinová, T.; Spitzová, T.; **Kalousková, B.**; Vaněk, O.; Volf, P.; Rohoušová, I. *Phlebotomus perniciosus* Recombinant Salivary Proteins Polarize Murine Macrophages Toward the Anti-Inflammatory Phenotype. *Front. Cell. Infect. Microbiol.* **2020**, *10*, 427.

7. Bláha, J.; Skálová, T.; **Kalousková, B.**; Skořepa, O.; Cmunt, D.; Pažický, S.; Poláchová, E.; Abreu, C.; Stránský, J.; Koval', T.; Dušková, J.; Zhao, Y.; Harlos, K.; Hašek, J.; Dohnálek, J.; Vaněk, O. Crystal structure of the human NKR-P1 bound to its lymphocyte ligand LLT1 reveals receptor clustering in the immune synapse. *bioRxiv* **2021,** 2021.06.16.448687, Preprint.

8. **Kalousková, B.**; Skořepa, O.; Cmunt, D.; Abreu, C.; Krejčová, K.; Bláha, J.; Sieglová, I.; Král, V.; Fábry, M.; Pola, R.; Pechar, M.; Vaněk O. Tumor marker B7-H6 bound to the coiled coil peptide-polymer conjugate enables targeted therapy by activating human natural killer cells. *Biomedicines* **2021**, *9,* 1598.